



The  
University  
Of  
Sheffield.

Department of Automatic Control and Systems Engineering

# Modelling, Simulation and Control of Turbulent Flows

A thesis submitted in partial satisfaction of the requirements for the degree  
Doctor of Philosophy in Automatic Control and Systems Engineering

by

**Peter Hywel Heins**

Supervisor: Dr Bryn Ll. Jones

JUNE 2015



*Dedicated to my parents,*

*thank you for your love and support.*

# Vita

- 1989 Born in Chester, United Kingdom
- 2007-2011 MEng in Aeronautical Engineering,  
Imperial College London, United Kingdom
- 2011-2015 PhD Student,  
Department of Automatic Control and Systems Engineering,  
The University of Sheffield, United Kingdom

## Publications and Presentations

**P. H. Heins**, B. Ll. Jones, and A. S. Sharma. ‘Passivity-based output-feedback control of turbulent channel flow’. *Automatica*, accepted for publication.

B. Ll. Jones, **P. H. Heins**, E. C. Kerrigan, J. F. Morrison, and A. S. Sharma. ‘Modelling for robust feedback control of fluid flows’. *Journal of Fluid Mechanics*, 769:687-722, 2015.

**P. H. Heins**, ‘Robust control of wall-bounded turbulent fluid flows’, oral presentation at *UKACC PhD Presentation Showcase, London, U.K., 23rd October 2014*.

**P. H. Heins**, B. Ll. Jones, and A. S. Sharma. ‘Passivity-based feedback control of a channel flow for drag reduction’, *UKACC 10th International Conference on Control, Loughborough, U.K., 9th-11th July 2014*, pp. 226-231 (Won award for “Best Applications Paper”).

**P. H. Heins**, B. Ll. Jones, and A. S. Sharma. ‘Drag reduction in a turbulent channel flow using a passivity-based approach’, oral presentation at *APS 66th Annual Meeting of the Division of Fluid Dynamics, Pittsburgh, U.S.A., 24th-26th November 2013*.

# Abstract of Thesis

Most real-world fluid flows around aircraft, ground vehicles and water craft are predominantly turbulent. It is well-known that turbulent flows induce much higher skin-friction drag relative to laminar flows. For streamlined bodies such as ships and passenger aircraft, skin-friction drag can be the main contributor to the total drag on those vehicles. In this thesis, two different linear time-invariant output-feedback control methods will be investigated which aim to reduce skin-friction drag in turbulent wall-bounded flow. Both methods use wall-based sensing and actuation arrangements, and are evaluated upon direct numerical simulations (DNS) of turbulent channel flow.

Spectral discretisation is used to produce highly accurate linear control models which are derived from the governing equations. The open-source DNS code used in the current work is outlined, and a procedure for modifying the boundary conditions at the walls is presented.

The first control methodology investigated, passivity-based control, inhibits the ability of the flow to produce energy. Passive systems can only store and dissipate energy. It is shown how the nonlinear dynamics in the equations that govern turbulent flows are passive, and can be considered as a feedback forcing to the linearised dynamics. The linear spatial modes of the flow which are capable of producing the most energy are identified. Controllers are then developed which make these modes closer to passive, resulting in restricted turbulent energy production, and consequently, reduced skin-friction drag.

$\mathcal{H}_\infty$  loop-shaping control is also investigated as a means of reducing turbulent skin-friction drag. This method offers *a priori* guarantees of closed-loop robustness to uncertainty and performance in terms of input disturbance rejection. Controllers are synthesised with the objective of minimising perturbation streamwise wall-shear stress in turbulent channel flow. It is shown that when enough spatial modes of a flow are controlled using this method, significant reductions in skin-friction drag can be achieved.



# Acknowledgements

I certainly would not have achieved a fraction of what I have been able to achieve if it were not for the help, support and insight of those around me at the University of Sheffield. I would first and foremost like to thank Dr Bryn Jones, who went above and beyond what any PhD student can expect from their supervisor. I am incredibly lucky to have had the support and academic opportunities offered to me by Bryn, and for that I will be forever grateful. I would also like to thank Dr Ati Sharma, who was my other supervisor during the first year of my PhD. Ati has continued to give me help and guidance since leaving Sheffield, and his input has been fundamental to my work.

I found being part of a research group invaluable. It was a great environment to exchange ideas and to get feedback on your research. I would like to thank members past and present of our small research group, in particular Oliver Dellar and Dr Paul Towers - I learned a lot from both of you. I am also grateful to Dr Pierre Ricco and Daniel Wise from the Department of Mechanical Engineering; their help with *Channelflow* was integral to my PhD.

Finally, I would like to thank all the staff and research students in the Department of Automatic Control and Systems Engineering. I feel blessed to have worked in such a friendly, supportive and welcoming atmosphere, and I know the last three and a half years would have been no way near as enjoyable in any other place.



# Contents

<b>Abstract of Thesis</b>	<b>iii</b>
<b>Acknowledgements</b>	<b>v</b>
<b>List of Figures</b>	<b>xi</b>
<b>List of Symbols</b>	<b>xix</b>
<b>List of Acronyms</b>	<b>xxiii</b>
<b>1 Introduction</b>	<b>1</b>
1.1 Motivation . . . . .	1
1.2 Wall-Bounded Turbulence . . . . .	1
1.2.1 Governing Equations . . . . .	3
1.3 Coherent Structure and Motion . . . . .	5
1.3.1 Turbulent Boundary Layers . . . . .	5
1.3.2 Turbulence Regeneration . . . . .	8
1.4 Flow Control . . . . .	12
1.5 Previous Research into ACL Drag Reduction . . . . .	15
1.5.1 Opposition Control . . . . .	15
1.5.2 Model-Based Control . . . . .	17
1.6 Thesis Layout and Publications . . . . .	22
<b>2 Modelling</b>	<b>25</b>
2.1 Orr-Sommerfeld Squire Equations . . . . .	26
2.2 Spectral Discretisation . . . . .	28
2.2.1 Streamwise and Spanwise Discretisation . . . . .	29
2.2.2 Wall-Normal Discretisation . . . . .	30
2.2.3 Spectra and Pseudospectra . . . . .	37
2.2.4 Incorporating Wall Actuation . . . . .	39
<b>3 Simulation</b>	<b>43</b>
3.1 Introduction . . . . .	43
3.2 Direct Numerical Simulation of Channel Flow . . . . .	44
3.2.1 Time-Stepping Algorithm . . . . .	47

3.2.2	The Influence-Matrix Method . . . . .	48
3.3	General Inhomogeneous Boundary Conditions . . . . .	53
3.4	Validation of Implemented Boundary Conditions . . . . .	54
3.4.1	Linear Validation . . . . .	54
3.4.2	Nonlinear Validation . . . . .	55
3.5	Controller Implementation . . . . .	59
<b>4</b>	<b>Passivity-Based Control</b>	<b>63</b>
4.1	Introduction . . . . .	63
4.2	Dissipativity, Passivity and Positive Realness . . . . .	64
4.2.1	Mathematical Preliminaries . . . . .	64
4.2.2	Dissipativity . . . . .	65
4.2.3	Passivity . . . . .	66
4.2.4	Positive-Realness . . . . .	67
4.2.5	The Passivity Theorem . . . . .	68
4.3	Passivity of Channel Flow . . . . .	69
4.3.1	Perturbation Energy Balance . . . . .	70
4.3.2	Passivity of the Nonlinear System . . . . .	71
4.3.3	Passivity of the Linear System . . . . .	73
4.3.4	Passivity of the Interconnected System . . . . .	78
4.4	Passivity-Based Control of Channel Flow . . . . .	80
4.4.1	Positive-Real Control Method . . . . .	81
4.4.2	Controller Synthesis . . . . .	83
4.4.3	Controller Dimension . . . . .	87
4.4.4	Linear Analysis . . . . .	90
4.4.5	DNS Testing . . . . .	95
4.5	Summary . . . . .	111
<b>5</b>	<b><math>\mathcal{H}_\infty</math> Loop-Shaping Control</b>	<b>113</b>
5.1	Introduction . . . . .	113
5.2	Uncertainty in Fluid Flows . . . . .	113
5.2.1	Coprime Factor Uncertainty . . . . .	116
5.3	Model Refinement . . . . .	117
5.3.1	The $\nu$ -Gap Metric . . . . .	118
5.3.2	Model Refinement Procedure . . . . .	119
5.4	$\mathcal{H}_\infty$ Loop-Shaping Control of Channel Flow . . . . .	120
5.4.1	Controller Design Procedure . . . . .	120
5.4.2	DNS Testing . . . . .	124
5.5	Summary . . . . .	138
<b>6</b>	<b>Discussion, Conclusions and Future Work</b>	<b>143</b>
6.1	Discussion . . . . .	143
6.1.1	Passivity-Based Control V.s. $\mathcal{H}_\infty$ Loop-Shaping Control . .	143

---

6.1.2 Implementation of Controllers in the Real-World . . . . .	145
6.2 Conclusions . . . . .	148
6.3 Novel Contributions . . . . .	152
6.4 Future Work . . . . .	153
<b>Bibliography</b>	<b>157</b>
<b>A Positive Real Control Method - Controller Synthesis</b>	<b>167</b>



# List of Figures

1.1	A study on turbulence by Leonardo da Vinci - a free water jet issuing from a square hole into a pool. . . . .	2
1.2	A schematic of channel flow. . . . .	4
1.3	A schematic of a spatially-developing boundary layer over a flat plate [28]. . . . .	5
1.4	Turbulent boundary layer mean-velocity profile, with different layers/sublayers annotated [34]. . . . .	6
1.5	Plots of mean velocity profiles for laminar (—) and $Re = 2230$ turbulent (—) channel flow. . . . .	7
1.6	Diagrams of Smith's model for streak breakdown in a turbulent boundary layer. <i>Top</i> - Plan and side views of a developing hairpin vortex [102]. <i>Bottom</i> - Sketch of the formation and breakdown of a hairpin vortex [4]. . . . .	10
1.7	A schematic of the four classifications of flow control strategies. . . . .	13
2.1	Spectra (black dots) and $\epsilon$ - <i>pseudospectra</i> (coloured contours) for Orr-Sommerfeld Squire dynamics matrix $\mathbb{L}$ , for wavenumber pair $(\alpha = 1, \beta = 1)$ , $Re = 1000$ . . . . .	38
3.1	Table of error-norms between <i>Channelflow</i> and OSS simulations. . . . .	55
3.2	Profiles of $(\alpha = 0, \beta = 1)$ velocity Fourier coefficients $\hat{u}$ , $\hat{v}$ and $\hat{w}$ from <i>Channelflow</i> simulation ( $\Delta$ - real part, $\circ$ - imaginary part) and OSS simulation (thick line - real part, dashed line - imaginary part) for $t = 0, 10, 60$ , for $Re = 10^4$ and validation boundary conditions (3.41). . . . .	56
3.3	Profiles of $(\alpha = 1, \beta = 0)$ velocity Fourier coefficients $\hat{u}$ , $\hat{v}$ and $\hat{w}$ from <i>Channelflow</i> simulation ( $\Delta$ - real part, $\circ$ - imaginary part) and OSS simulation (thick line - real part, dashed line - imaginary part) for $t = 0, 10, 60$ , for $Re = 10^4$ and validation boundary conditions (3.41). . . . .	57

3.4	Profiles of ( $\alpha = 1, \beta = 1$ ) velocity Fourier coefficients $\hat{u}$ , $\hat{v}$ and $\hat{w}$ from <i>Channelflow</i> simulation ( $\Delta$ - real part, $\circ$ - imaginary part) and OSS simulation (thick line - real part, dashed line - imaginary part) for $t = 0, 10, 60$ , for $Re = 10^4$ and validation boundary conditions (3.41). . . . .	58
3.5	Plots of energy spectra from $Re = 10^3$ <i>Channelflow</i> simulation for times $t = 0, 2, 10$ , and validation boundary conditions (3.41) applied to mode ( $\alpha = 0, \beta = 2$ ) only. N.b. plots are symmetrical about $\beta = 0$ , therefore, spectra only plotted for $\beta \geq 0$ . . . . .	60
3.6	Block diagram of controller $\hat{\mathbf{K}}$ in feedback with <i>Channelflow</i> plant $\hat{\mathbf{C}}\mathbf{F}$ for a single Fourier mode. . . . .	62
4.1	A schematic displaying the index of passivity $\varepsilon$ of a system. . . . .	68
4.2	The negative feedback interconnection of systems $\Sigma_1$ and $\Sigma_2$ . . . . .	69
4.3	Block diagram representation of the dynamics of channel flow. . . . .	70
4.4	Colour map of modal critical energy Reynolds number $Re_c$ in wavenumber space, computed using wall-normal resolution $N_y = 60$ . . . . .	76
4.5	Colour maps of $\varepsilon$ in wavenumber space. N.b. a) and c) show contours of $\log_{10}  \varepsilon $ , in a) all contours represent positive $\varepsilon$ , in c) all contours represent negative $\varepsilon$ . Wall-normal resolution $N_y = 80$ . . . . .	77
4.6	Plots of $\beta$ vs. $ \varepsilon $ for $Re = 10^2$ ( $-$ ), $Re = 10^3$ ( $--$ ), $Re = 10^4$ ( $- \cdot$ ), $Re = 10^5$ ( $\cdot \cdot$ ), for streamwise-constant modes ( $\alpha = 0$ ). Wall-normal resolution $N_y = 80$ . . . . .	79
4.7	Table of least passive modes for different Reynolds numbers. . . . .	79
4.8	Block diagram of channel flow system in feedback with a controller. . . . .	83
4.9	Plots of residual closed-loop index of passivity for controllers generated using control models discretised via the collocation and Galerkin methods with <b>sensing arrangement 1</b> , for wavenumber pairs ( $\alpha = 0, \beta = 1$ ) - ( $\cdot$ ), ( $\alpha = 0, \beta = 2$ ) - ( $\times$ ), and ( $\alpha = 0, \beta = 10$ ) - ( $\circ$ ). . . . .	88
4.10	Plots of residual closed-loop index of passivity for controllers generated using control models discretised via the collocation and Galerkin methods with <b>sensing arrangement 2</b> , for wavenumber pairs ( $\alpha = 0, \beta = 1$ ) - ( $\cdot$ ), ( $\alpha = 0, \beta = 2$ ) - ( $\times$ ), and ( $\alpha = 0, \beta = 10$ ) - ( $\circ$ ). . . . .	89
4.11	Plot of $ \varepsilon_L $ (thick line) and $ \varepsilon_{L, K_{\min}} $ for both collocation ( $\cdot$ ) and Galerkin ( $\times$ ) discretised control models, for sensing arrangement 1 (S1) and sensing arrangement 2 (S2); all controllers have penalties $\epsilon_c = \epsilon_d = 0.001$ , and actuator time-constant $\tau_\phi = 0.01$ . . . . .	91
4.12	Spectra (black dots) and $\varepsilon$ - <i>pseudospectra</i> (coloured contours) for open-loop and closed-loop ( $\alpha = 0, \beta = 2$ ) system with <b>sensing arrangement 1</b> , $\epsilon_c = \epsilon_d = 0.001$ , $\tau_\phi = 0.01$ . . . . .	93

4.13 Spectra (black dots) and $\epsilon$ - <i>pseudospectra</i> (coloured contours) for open-loop and closed-loop ( $\alpha = 0, \beta = 2$ ) system with <b>sensing arrangement 2</b> , $\epsilon_c = \epsilon_d = 0.001$ , $\tau_\phi = 0.01$ . . . . .	94
4.14 Plots of transient energy growth from linear simulations of open-loop (black solid line), and collocation (--) and Galerkin (·-) closed-loop ( $\alpha = 0, \beta = 2$ ) systems with sensing arrangement 1 (black) and sensing arrangement 2 (red), all started from “optimal” initial condition, $\epsilon_c = \epsilon_d = 0.001$ , $\tau_\phi = 0.01$ , $N_{y,c} = 250$ . . . . .	95
4.15 Table detailing the resolution checks for the uncontrolled simulation. The final two columns list the percentage change in skin-friction coefficient and mean total perturbation energy with respect to the first row which corresponds to the grid spacings used for all testing. . . . .	97
4.16 Table detailing the resolution checks for the $K_{G250}$ -controlled simulation. Columns 6 and 7 list the percentage change in skin-friction coefficient and mean total perturbation energy with respect to the first row which corresponds to the grid spacings used for all testing. The final two columns list the percentage reductions in skin-friction drag and total perturbation energy with respect to the uncontrolled simulation with corresponding grid spacings. All reported results are for simulations with wall-normal resolution $N_y = 151$ . . . . .	97
4.17 Plots of perturbation energy for mode ( $\alpha = 0, \beta = 1$ ) over time for the uncontrolled (–) and $K_{G250}$ -controlled (--) simulations, with control penalties $\epsilon_c = \epsilon_d = \mathbf{0.001}$ . . . . .	98
4.18 Plots of total perturbation energy over time for the uncontrolled (–) and $K_{G250}$ -controlled (--) simulations, with control penalties $\epsilon_c = \epsilon_d = \mathbf{0.001}$ . . . . .	99
4.19 Plots of total skin-friction drag over time at the upper and lower walls for the uncontrolled (–) and $K_{G250}$ -controlled (--) simulations, with control penalties $\epsilon_c = \epsilon_d = \mathbf{0.001}$ . . . . .	99
4.20 Plots of perturbation energy for mode ( $\alpha = 0, \beta = 1$ ) over time for the uncontrolled (–) and $K_{G250}^*$ -controlled (--) simulations, with control penalties $\epsilon_c = \epsilon_d = \mathbf{0.01}$ . . . . .	100
4.21 Temporal-mean perturbation energies for modes ( $\alpha = 0, \beta \leq 10$ ) from uncontrolled (·) and $K_{G250}^*$ -controlled (×) simulations, with control penalties $\epsilon_c = \epsilon_d = \mathbf{0.01}$ . . . . .	101
4.22 Plots of total perturbation energy over time for the uncontrolled (–) and $K_{G250}^*$ -controlled (--) simulations, with control penalties $\epsilon_c = \epsilon_d = \mathbf{0.01}$ . . . . .	102
4.23 Plots of total skin-friction drag over time at the upper and lower walls for the uncontrolled (–) and $K_{G250}^*$ -controlled (--) simulations, with control penalties $\epsilon_c = \epsilon_d = \mathbf{0.01}$ . . . . .	102

4.24	Temporal-mean perturbation energies for modes ( $\alpha = 0, \beta \leq 10$ ) from uncontrolled ( $\cdot$ ), $K_{C168}$ -controlled ( $\times$ ), and $K_{C250}$ -controlled ( $\times$ ) simulations. . . . .	103
4.25	Plots of perturbation energy for Fourier mode ( $\alpha = 0, \beta = 2$ ) from uncontrolled ( $-$ ), $K_{C168}$ -controlled ( $--$ ), and $K_{C250}$ -controlled ( $---$ ) simulations. Also included are dash-dot lines representing the uncontrolled (upper black), $K_{C168}$ -controlled (lower black), and $K_{C250}$ -controlled (red) moving mean values. . . . .	104
4.26	Plots of total perturbation energy over time for the uncontrolled ( $-$ ), $K_{C168}$ -controlled ( $--$ ), and $K_{C250}$ -controlled ( $---$ ) simulations. Also included are dash-dot lines representing the uncontrolled (upper black), $K_{C168}$ -controlled (lower black), and $K_{C250}$ -controlled (red) moving mean values. . . . .	105
4.27	Plots of total skin-friction drag over time for the upper and lower walls for the uncontrolled flow ( $-$ ), $K_{C168}$ -controlled flow ( $--$ ), and $K_{C250}$ -controlled flow ( $---$ ). Also included are dash-dot lines representing the uncontrolled (upper black), $K_{C168}$ -controlled (lower black), and $K_{C250}$ -controlled (red) moving mean values. . . . .	105
4.28	Summary table of the % reduction in mean total energy and mean skin-friction drag achieved by each passivity-based controller tested. The first 300 time units of controlled data are not included in the calculation of these values in order to remove the transient effects of the controllers. . . . .	106
4.29	Profiles of Reynolds stress ( $-\overline{u'v'}$ ) (thick lines) and FIK-weighted Reynolds stress ( $y\overline{u'v'}$ ) (dashed lines) for the uncontrolled flow (black) and $K_{C250}$ -controlled flow (red), displayed for the bottom half of the channel only. . . . .	106
4.30	Table of skin-friction coefficient values calculated using the FIK identity (first three columns of data) and the actual skin-friction coefficient (last column of data). . . . .	106
4.31	Table showing the power required to push the fluid $\mathcal{P}_x$ , the power saved due to drag reduction $\Delta\mathcal{P}_x$ , the approximate actuation power $\mathcal{P}_\phi^*$ , and the power efficiency $\mathcal{P}_\%$ for each controller. For the uncontrolled flow, $\mathcal{P}_x = -0.2203$ . . . . .	107
4.32	Colour maps of streamwise velocity $\hat{u}$ overlaid with contours of streamwise vorticity $\hat{\eta}_x$ from uncontrolled and $K_{C168}$ -controlled simulations for wavenumber pair ( $\alpha = 0, \beta = 2$ ) and $T = 1100$ . . . . .	108
4.33	Isosurface plots of $\mathbf{Q} = 0.1$ at the bottom wall, underlaid with colour maps of streamwise velocity $u$ at $y^+ = 15$ for uncontrolled and $K_{C168}$ -controlled simulations for time $t = 1300$ . . . . .	110

4.34	Plots of $\langle \mathbf{w}, \mathbf{w} \rangle$ vs. $\langle \mathbf{z}, \mathbf{w} \rangle$ for wavenumber pairs $(\alpha = 0, \beta = 1)$ (black) and $(\alpha = 0, \beta = 2)$ (red), from uncontrolled (—) and $K_{C168}$ -controlled (--) simulations. . . . .	111
5.1	Block diagram of linear system $\mathcal{P}$ in feedback with controller $K$ , under forcing from nonlinearity $\mathbf{n}$ and modelling uncertainty $\mathbf{w}$ . . . . .	115
5.2	Block diagram represented the perturbed system $\mathcal{P}_p$ , shaded box, in feedback with a controller $K$ . $\mathbf{v}_1$ , $\mathbf{v}_2$ , $\mathbf{w}_1$ and $\mathbf{w}_2$ represent disturbance inputs. . . . .	116
5.3	Block diagrams illustrating the loop-shaping procedure. (a) System $\mathcal{P}$ is augmented with precompensator matrix $\mathcal{W}$ to form shaped system $\mathcal{P}_{\mathcal{W}}$ with desirable loop shape. (b) When implementing the final controller, precompensator matrix $\mathcal{W}$ is absorbed back into $K$ to form the weighted controller $K_{\mathcal{W}}$ . . . . .	118
5.4	Plots of maximum singular values vs. frequency for (a) uncompensated system $\mathcal{P}_{N_y}$ , and (b) compensated system $\mathcal{P}_{\mathcal{W}N_y}$ , for $N_y = 30$ (--) and $N_y = 100$ (—), for mode $(\alpha = 0, \beta = 2)$ . . . . .	122
5.5	Plots of $\delta_{\nu}(\mathcal{P}_{\mathcal{W}N_y}, \mathcal{P}_{\mathcal{W}N_y+1}) - (\cdot)$ , and sequence $\{1.7(0.82)^{N_y}\} - (\times)$ vs. grid resolution $N_y$ , for $(\alpha = 0, \beta = 2)$ . . . . .	123
5.6	Plots of maximum singular values vs. frequency for uncompensated $\mathcal{P}_{60}$ (—) and compensated $\mathcal{P}_{\mathcal{W}60}$ (--) systems for (a) mode $(\alpha = 1, \beta = 0)$ , and (b) mode $(\alpha = 1, \beta = 1)$ , $N_y = 60$ . Also displayed are the precompensator matrices $\mathcal{W}$ used and the resulting robust stability margins $\mathcal{R}$ . . . . .	125
5.7	Plots of streamwise wall-shear stress $\hat{\tau}_{yx}$ for mode $(\alpha = 0, \beta = 2)$ , from uncontrolled (—) and controlled (--) simulations. . . . .	126
5.8	Plots of streamwise wall-shear stress $\hat{\tau}_{yx}$ for modes $(\alpha = 2, \beta = 0)$ and $(\alpha = 2, \beta = 2)$ , from uncontrolled (—) and controlled (--) simulations. . . . .	127
5.9	Colour map representing % rms reductions in perturbation streamwise wall-shear stress for all controlled modes from $K_{(\alpha 2, \beta 12)}$ -controlled simulation. . . . .	128
5.10	Colour maps of streamwise velocity $\hat{u}$ overlaid with contours of streamwise vorticity $\hat{\eta}_x$ for mode $(\alpha = 0, \beta = 2)$ , for time $t = 1100$ . . . . .	129
5.11	Colour maps of streamwise velocity $\hat{u}$ overlaid with arrows representing in-plane velocity vectors at the lower wall for <b>uncontrolled</b> mode $(\alpha = 0, \beta = 2)$ , at times $t = 0, 20$ and $50$ . . . . .	130
5.12	Colour maps of streamwise velocity $\hat{u}$ overlaid with arrows representing in-plane velocity vectors at the lower wall for <b>controlled</b> mode $(\alpha = 0, \beta = 2)$ , at times $t = 0, 20$ and $50$ . . . . .	131

5.13	Table detailing the resolution checks for the $K_{(\alpha 2, \beta 4)}$ -controlled simulation. Column 6 lists the percentage change in skin-friction coefficient with respect to the first row which corresponds to the grid spacings used for all testing. The final column lists the percentage reductions in skin-friction drag with respect to the uncontrolled simulation with corresponding grid spacings. . . . .	132
5.14	Plots of total skin-friction drag from uncontrolled (—) and $K_{(\alpha 2, \beta 4)}$ -controlled (—) simulations. . . . .	133
5.15	Plots of total skin-friction drag from uncontrolled (—) and $K_{(\alpha 2, \beta 8)}$ -controlled (—) simulations, plots of the moving mean values (·—) are also included. . . . .	133
5.16	Plots of total skin-friction drag from uncontrolled (—) and $K_{(\alpha 2, \beta 12)}$ -controlled (—) simulations, plots of the moving mean values (·—) are also included. . . . .	134
5.17	Table of mean total drag reductions from each of the controlled simulations ran. The first 300 time units of controlled data are not included in the calculation of drag reductions so as to remove the transient effects of the controllers. N.b. that for $K_{(\alpha 2, \beta 12)}$ , the simulation is still running. . . . .	134
5.18	Plots of mean velocity profiles $\overline{\langle U \rangle}$ for laminar (—), uncontrolled turbulent (—) and $K_{(\alpha 4, \beta 12)}$ -controlled (—) turbulent flows. . . . .	135
5.19	Profiles of Reynolds stress ( $-\overline{\langle u'v' \rangle}$ ) (thick lines) and FIK-weighted Reynolds stress ( $y\overline{\langle u'v' \rangle}$ ) (dashed lines) for the uncontrolled flow (black) and $K_{\alpha 2, \beta 12}$ -controlled flow (red), displayed for the bottom half of the channel only. . . . .	136
5.20	Table of skin-friction coefficient values calculated using the FIK identity (first three columns of data) and the actual skin-friction coefficient (last column of data). . . . .	136
5.21	Table showing the power required to push the fluid $\mathcal{P}_x$ , the power saved due to drag reduction $\Delta\mathcal{P}_x$ , the approximate actuation power $\mathcal{P}_\phi^*$ , and the power efficiency $\mathcal{P}_\%$ for each controller. For the uncontrolled flow, $\mathcal{P}_x = -0.2203$ . . . . .	136
5.22	Isosurface plots of $\mathbf{Q} = 0.1$ , underlaid with colour maps of perturbation streamwise wall-shear stress $\frac{\partial u}{\partial y}$ at the lower wall for uncontrolled and $K_{(\alpha 2, \beta 12)}$ controlled simulations, for time $t = 500$ . . . . .	137
5.23	Greyscale maps of wall-normal forcing at the lower wall for $K_{(\alpha 4, \beta 12)}$ controlled flow. . . . .	139
6.1	Block diagram depicting how the controllers developed in this thesis could be implemented on a real channel flow. . . . .	146

---

6.2	Table of minimum dimensional sensor/actuator spacings $\Delta S^*$ based on channel half-height $h^*$ and sensor/actuator resolution per wavelength $N_s$ . . . . .	147
6.3	Table of dimensional actuator bandwidths for controlling air ( $\nu = 1.5 \times 10^{-5}$ ) and water ( $\nu = 1 \times 10^{-6}$ ) $Re = 2230$ channel flows. . .	148



# List of Symbols

$\nabla$	gradient operator
$\nabla \cdot$	divergence operator
$\nabla^2$	Laplacian operator
$i = \sqrt{-1}$	
$I$	identity matrix
$\mathbb{C}$	set of complex numbers
$\mathbb{R}$	set of real numbers
$\mathbb{Z}$	set of natural numbers
$\Re$	real part
$\Im$	imaginary part
$\ \cdot\ $	vector norm
$\lambda$	spectra
$\cdot \rightarrow \frac{\partial}{\partial t}$	
$' \rightarrow \frac{\partial}{\partial y}$	
$t$	time
$x, y, z$	cartesian coordinates
$\langle \cdot, \cdot \rangle$	inner product
$k_x, k_z$	streamwise and spanwise wavenumber indices
$\alpha, \beta$	streamwise and spanwise wavenumbers
$k^2 := \alpha^2 + \beta^2$	
$\hat{\cdot}$	Fourier coefficient
$\bar{\cdot}$	temporal mean
$\bar{\sigma}$	maximum singular value
$\cdot^\top$	matrix conjugate transpose
$\cdot^{-1}$	matrix inverse
$\cdot^*$	dimensional variable

## Fluid Dynamics

$Re_\tau = \frac{u_\tau h}{\nu}$	skin-friction velocity Reynolds number
$u_\tau$	skin-friction velocity
$\nu$	fluid kinematic viscosity
$h$	channel half height
$Re = \frac{U_{cl} h}{\nu}$	centreline velocity Reynolds number
$U_{cl}$	channel centreline velocity
$\tau_w$	wall-shear stress
$\rho$	fluid density
$\cdot+$	wall units
$\bar{D}$	skin-friction drag
$\mathbf{V}$	total velocity
$U, V, W$	streamwise, wall-normal and spanwise velocity
$P$	total pressure
$\mathbf{v}$	perturbation velocity
$u, v, w$	streamwise, wall-normal and spanwise perturbation velocity
$p$	perturbation pressure
$\Omega$	flow domain
$\partial\Omega$	flow domain boundary
$\chi$	point in flow domain
$\tilde{\mathbf{V}}$	base velocity
$\tilde{P}$	base pressure
$\mathbf{n}$	Nonlinear forcing
$\mathbf{d}$	exogenous disturbance forcing
$\boldsymbol{\eta}$	vorticity
$\mathbb{L}_{OS}, \mathbb{L}_C, \mathbb{L}_{Sq}$	Orr-Sommerfeld, coupling and Squire operators
$N_x, N_y, N_z$	no. of domain grid points in x, y and z directions
$L_x, L_z$	streamwise and spanwise domain dimensions
$\mathbf{a}$	Chebyshev spectral coefficients
$\gamma$	weighting function
$\mathbf{T}$	Chebyshev polynomials
$\Phi$	wall-normal velocity basis functions
$\Psi$	wall-normal vorticity basis functions
$\tilde{D}^n$	Chebyshev collocation differentiation matrix
$f_u, f_l$	lifting functions
$q_u, q_l$	control signals
$U_{bulk}$	bulk velocity
$E$	perturbation energy
$Q$	energy matrix
$V$	volume of domain
$Re_c$	local critical energy Reynolds number
$Re_E$	global critical energy Reynolds number

$\tau_{yx}, \tau_{yz}$	streamwise and spanwise wall-shear stress
$\bar{D}_R$	drag reduction
$L(\cdot)$	linear Navier-Stokes operator
$\mathcal{N}(\cdot)$	nonlinear Navier-Stokes operator
$\mathbf{Q}$	Q-criterion

## Control Systems

$A, B, C, D, E$	state-space matrices
$C_s$	sensor matrix
$\mathbf{y}, \mathbf{z}$	system output vectors
$\mathbf{u}, \mathbf{w}$	system input vectors
$\mathbf{x}$	state vector
$\varepsilon$	index of passivity
$\bar{\varepsilon}$	feed-through energy
$\Sigma$	system
$A_K, B_K, C_K, D_K$	LTI controller matrices
$\tau_\phi$	actuator time-constant
$\epsilon_c, \epsilon_d$	control and measurement penalties
$K$	controller
$\Delta$	uncertainty model
$\delta_\nu$	$\nu$ -gap metric
$\mathcal{W}$	precompensator matrix
$b_{\mathcal{P}, K}$	robust stability margin
$\mathcal{R}$	robustness margin
$\mathcal{P}, \mathbf{L}$	linear system/plant
$s := \sigma + i\omega$	complex frequency
$\mathcal{H}_\infty$	the set of functions with finite infinity-norm
$\mathcal{H}_2$	the set of functions with finite 2-norm



# List of Acronyms

<b>ACL</b>	active closed-loop
<b>AOL</b>	active open-loop
<b>ARE</b>	algebraic Riccati equation
<b>CFD</b>	computational fluid dynamics
<b>CFL</b>	Courant-Friedrichs-Lewy
<b>DNS</b>	direct numerical simulation
<b>FIK</b>	Fukagata Iwamoto Kasagi
<b>IFP</b>	input feed-forward passivity
<b>LES</b>	large eddy simulation
<b>LTI</b>	linear time-invariant
<b>LTR</b>	loop transfer recovery
<b>LQG</b>	linear quadratic Gaussian
<b>LQR</b>	linear quadratic regulator
<b>MEMS</b>	micro-electrical-mechanical systems
<b>MWR</b>	mean-weighted residual
<b>OFF</b>	output feedback passivity
<b>OSS</b>	Orr-Sommerfeld Squire
<b>PBC</b>	passivity-based control
<b>PCL</b>	passive closed-loop
<b>PDAE</b>	partial differential algebraic equation
<b>POL</b>	passive open-loop
<b>PR</b>	positive real
<b>RANS</b>	Reynolds-averaged Navier Stokes
<b>SBDF3</b>	3rd-order semi-implicit backward differentiation
<b>SIP</b>	strictly input passive
<b>SOP</b>	strictly output passive
<b>SPR</b>	strictly positive real
<b>VSP</b>	very strictly passive



# Chapter 1

## Introduction

### 1.1 Motivation

Controlling turbulent wall-bounded fluid flows for the purposes of reducing skin-friction drag is of great scientific, economical and environmental interest. Most real-world fluid flows around aircraft, buildings, ships, submarines and ground vehicles are turbulent. It is well-known that turbulent boundary layers induce much higher skin friction drag on bodies than laminar boundary layers and that for streamlined bodies, skin friction drag can be the highest contributor to the total drag on that body. If a control system could reduce the wall-shear stress in, suppress the turbulent intensity of, or even relaminarise a turbulent flow, potentially large reductions in drag could be achieved. For example, approximately 45% of the total drag on a commercial aircraft is due to skin friction [30]. It is estimated that a 10-15% total drag reduction could be achieved if the flow over the wings and fin were to be relaminarised [30]. As the airline industry consumes around 1.5 billion barrels of jet fuel per year [67] and current jet fuel prices currently stand at approximately \$100 per barrel [52], this drag reduction would save billions of dollars for this sector. International shipping consumes approximately 300 million tonnes of fuel per year [2] and so is another transport sector that would benefit greatly from drag reduction - skin-friction accounts for between 50 – 80% of the drag experienced by large naval vessels [2]. Combined, the shipping and aviation industries emit 4.6% of the world’s CO<sub>2</sub> emissions [2]. Therefore, as well as the obvious economical benefits, reducing skin-friction drag via flow control could also help the global effort to reduce greenhouse gas emissions.

### 1.2 Wall-Bounded Turbulence

Most wall-bounded flows under natural conditions are predominantly turbulent. As J. D. Anderson eloquently put it, “*Nature, when let to herself, always goes to the state of maximum disorder*” [64]. Turbulent flows are characterised by their chaotic and stochastic property changes and highly nonlinear multi-scale interac-



Figure 1.1: A study on turbulence by Leonardo da Vinci - a free water jet issuing from a square hole into a pool.

tions, this is in contrast to laminar flows where changes in properties are smooth and deterministic and perturbations decay over time. Turbulence has been studied for hundreds of years; Leonardo da Vinci observed its multiple scales and structures five hundred years ago (see Figure 1.1). However, turbulence remains one of the last great unsolved problems in classical physics, as although the equations that model the dynamics of turbulence are known — the Navier-Stokes equations — many questions remain: Is there a general solution to the Navier-Stokes equations? What are the precise structures and motions within turbulent boundary layers, and what part do they play in the turbulence regeneration process?

Turbulence can be viewed as advantageous in some scenarios and disadvantageous in others. Advantageous for mixing of fluids, reduced profile drag on bluff bodies and transferring heat; disadvantageous for increased skin-friction drag, increased noise due to acoustic vibration and increased aerodynamic heating. Control systems that promote turbulence where it is advantageous and mitigate turbulence where it is disadvantageous would have an enormous impact in many engineering situations. Being able to control something as chaotic and complex as turbulence may seem near-impossible, but in order to control anything, all one needs is a model of the system you wish to control, a control law and a means of implementing the control (i.e. practically implementable actuators and/or sensors); for turbulence, all three exist.

There are a number of different canonical wall-bounded shear flows studied in the literature, these include boundary layer flow, pipe flow, Couette flow and plane channel flow (also referred to as plane Poiseuille flow). These all differ in their wall geometry and prescribed boundary conditions. In the current work, the focus will be restricted to turbulent plane channel flow (also referred to as just *channel flow*). Channel flow is the uni-directional flow between two flat plates of infinite spatial dimensions with periodic boundary conditions in the streamwise and spanwise directions and Dirichlet boundary conditions in the wall-normal di-

rection. A schematic of channel flow is shown in Figure 1.2. The majority of research into ACL flow control for skin-friction drag reduction has used channel flow as a “test bed”. This is because its geometry and boundary conditions allow for both the synthesis of highly accurate low-order linear models, and moderate Reynolds number direct numerical simulations. However, all wall-bounded turbulent flows have similar coherent structures and motions, and regenerative processes. Section 1.3 outlines previous research into the coherent structures and motions in wall-bounded turbulent flows. However, firstly, the governing equations for turbulent flows will be presented.

### 1.2.1 Governing Equations

The dynamics of all fluids are described by the Navier-Stokes equations. These are statements on the conservation of mass and momentum within a fluid. The general Navier-Stokes equations are of high complexity, therefore, in the current work a number of assumptions will be made to simplify them. Firstly, it will be assumed that all flows studied will be incompressible. This means that the density of the fluid will not change over time, which is a sound assumption as long as the Mach number of the flow does not exceed  $M = 0.3$ . Secondly, it shall be assumed that all fluids studied will be Newtonian. Newtonian fluids have a linear viscosity model; most fluids of engineering interest such as air and water are Newtonian. Thirdly, it will be assumed that the mass flow rate within the channel is constant. The incompressible Navier-Stokes equations for a Newtonian channel flow non-dimensionalised by the channel half-height  $h^* \in \mathbb{R}$  and  $U_{cl}^* \in \mathbb{R}$ , the maximum laminar centreline velocity for a constant mass flow rate, are:

$$\frac{\partial \mathbf{V}}{\partial t} = \frac{1}{\text{Re}} \nabla^2 \mathbf{V} - \nabla P - \mathbf{V} \cdot \nabla \mathbf{V} + \mathbf{f}, \quad (1.1a)$$

$$\nabla \cdot \mathbf{V} = 0, \quad (1.1b)$$

with initial and boundary conditions:

$$\mathbf{V}(\chi, 0) = \mathbf{V}_0(\chi) \quad \forall \chi \in \Omega, \quad (1.2a)$$

$$\mathbf{V}(\chi, t) = \mathbf{g}(\chi, t) \quad \forall (\chi, t) \in \partial\Omega \times [0, t_f], \quad (1.2b)$$

where  $\mathbf{V} : \Omega \times \mathbb{R}_+ \rightarrow \mathbb{R}^3$  is the velocity vector field,  $P : \Omega \times \mathbb{R}_+ \rightarrow \mathbb{R}$  is the pressure scalar field,  $\mathbf{f} : \Omega \times \mathbb{R}_+ \rightarrow \mathbb{R}^3$  is a vector of external forces,  $\mathbf{g} : \partial\Omega \times \mathbb{R}_+ \rightarrow \mathbb{R}^3$  is a vector of boundary conditions,  $\mathbf{V}_0 \in \mathbb{R}^3$  is an initial velocity vector for time  $t = 0$ ,  $\nabla^2$  is the Laplacian operator, and  $\nabla$  is the gradient operator. Reynolds number is defined  $\text{Re} := U_{cl}^* h^* / \nu^*$ , and  $\nu^* \in \mathbb{R}$  denotes kinematic viscosity. The endpoint of the time interval is  $t_f \in \mathbb{R}_+$ ,  $\Omega \subset \mathbb{R}^3$  is a domain in three spatial dimensions with boundary  $\partial\Omega$ , and  $\chi \in \Omega$  is a point within the domain. The superscript  $*$  is used to denote dimensional variables.

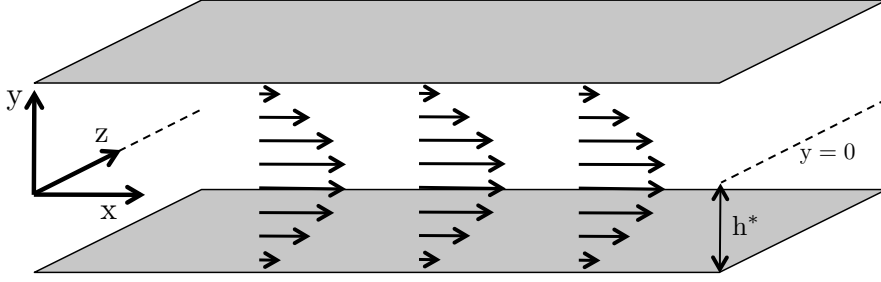


Figure 1.2: A schematic of channel flow.

The following notation shall be adopted in the following for mathematical description of channel flow -  $\{x, y, z\} \in \chi$  represent cartesian descriptions of the streamwise, wall-normal and spanwise directions respectively, and  $\{U, V, W\} \in \mathbf{V}$  denote the streamwise, wall-normal and spanwise components of velocity respectively. This cartesian notation is illustrated in the schematic of channel flow in Figure 1.2.

### Boundary Conditions

For un-actuated channel flow (i.e. no wall transpiration) with dimensions  $[L_x \times 2 \times L_z]$ , the vector  $\mathbf{g}$  is chosen such that the following boundary conditions are imposed:

$$\mathbf{V}(x, \pm 1, z, t) = 0, \quad (1.3a)$$

$$\mathbf{V}(x, y, z, t) = \mathbf{V}(x + L_x, y, z, t), \quad (1.3b)$$

$$\mathbf{V}(x, y, z, t) = \mathbf{V}(x, y, z + L_z, t). \quad (1.3c)$$

Dirichlet boundary condition (1.3a) corresponds to the impermeability and no-slip conditions at the walls, and (1.3b)-(1.3c) correspond to the periodic boundary conditions imposed in the streamwise and spanwise directions respectively.

### Wall Units and Averaging Definitions

When analysing turbulent flows, it is good practice to use wall units, whereby lengths and velocities are normalised by viscous length ( $\nu^*/u_\tau^*$ ) and velocity ( $u_\tau^*$ ) scales. Skin-friction velocity is defined:  $u_\tau^* := \sqrt{\tau_w^*/\rho^*}$ , where  $\rho^*$  is fluid density,  $\nu^*$  denotes kinematic viscosity, and  $\tau_w^*$  is the spatially and temporally averaged wall-shear stress defined as:

$$\tau_w^* := \mu^* \frac{\partial \langle U^* \rangle}{\partial y^*}, \quad (1.4)$$

where a spatial average is defined as:

$$\langle U \rangle := \frac{1}{L_x L_z} \int_0^{L_x} \int_0^{L_z} U \, dx dz, \quad (1.5)$$

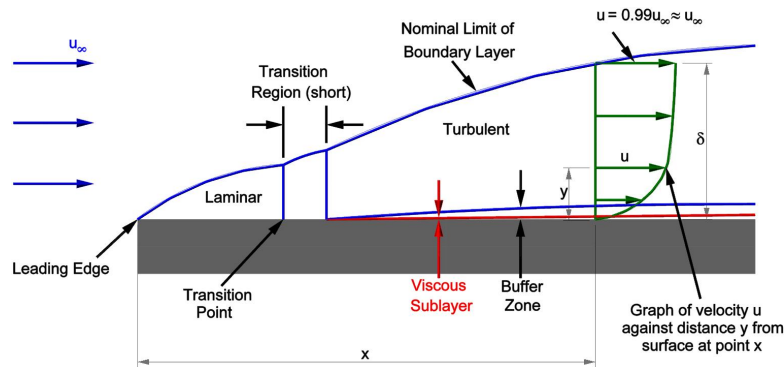


Figure 1.3: A schematic of a spatially-developing boundary layer over a flat plate [28].

and a temporal average is defined as:

$$\bar{U} := \frac{1}{t_i - t_f} \int_{t_i}^{t_f} U \, dt \quad (1.6)$$

Values normalised by wall units are given  $^+$  notation. A Reynolds number based on skin-friction velocity is defined as:

$$Re_\tau := \frac{u_\tau^* h^*}{\nu^*}. \quad (1.7)$$

## 1.3 Coherent Structure and Motion

### 1.3.1 Turbulent Boundary Layers

When a fluid travels over a solid surface, a near-wall layer develops where viscous forces become important; this layer is known as a boundary layer. Boundary layers develop due to the velocity no-slip condition on solid surfaces. When fluid passes over a flat plate for instance, a boundary layer forms at the front edge of the plate and then develops as it moves downstream. The boundary layer in the region close to the front of the plate is laminar, as the local Reynolds number is low. Downstream, the boundary layer will undergo transition to turbulence as local Reynolds number increases. A schematic of this process is shown in Figure 1.3. Channel flow, due to its periodic boundary conditions, develops only in time.

A turbulent boundary layer contains an inner layer and an outer layer. Within the inner layer viscous effects dominate and the rate of turbulent kinetic energy production exceeds dissipation. Turbulent kinetic energy can be produced by fluid shear, friction or buoyancy [64]. Therefore, the eddies created by wall-bounded vortices and the fluid shear caused by the no-slip condition at the wall all produce turbulent kinetic energy in the inner layer. In the outer layer inertial effects dominate and turbulent dissipation exceeds production. In between the

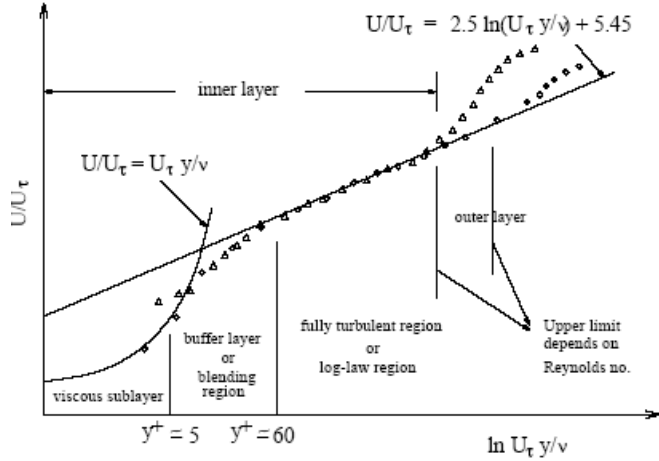


Figure 1.4: Turbulent boundary layer mean-velocity profile, with different layers/sublayers annotated [34].

two layers is the log-law region, where turbulent energy production equals dissipation. Figure 1.4 shows the mean-velocity profile of a typical turbulent boundary layer. As can be seen, the inner layer is comprised of a viscous sublayer, a buffer layer and a log-law region. The mean-velocity profile in the viscous sublayer is linear. The log-law region is so-called because the mean-velocity profile in this region obeys the semi-empirical model:  $U^+ = \frac{1}{k} \log y^+ + C$ , where  $k$  is the Von Karman constant (thought to be universal at  $k \approx 0.4$ ) and  $C$  is a constant specific to a boundary layer. The log-law region is where both viscous effects and inertial effects play an important role. In channel flow, the outer layers from the upper and lower walls meet in the centre of the channel and interact. However, both walls still have their own inner layer velocity profiles as in Figure 1.4, although their shape may be influenced by the interaction of the outer layers. Control via wall-based actuation will have the greatest effect on the region of the flow closest to the wall, i.e. the inner layer.

Figure 1.5 shows mean velocity profiles for laminar and turbulent channel flows, where the channel walls are located at  $y = \pm 1$ . The mean velocity profile for laminar channel flow is an exact solution to the Navier-Stokes equations, and is parabolic. The skin-friction drag at each wall is proportional to the wall-normal gradient of the spatial-mean velocity profile which for a non-dimensionalised channel flow is defined as:

$$\bar{D}_{\pm 1} := \frac{1}{\text{Re}} \left. \frac{\partial \langle U \rangle}{\partial y} \right|_{y=\pm 1}. \quad (1.8)$$

Figure 1.5 shows that the gradient of the turbulent mean velocity profile at the walls is much larger than for the laminar flow. Hence why turbulent flows have higher skin-friction drag. Therefore, for constant Reynolds number flow, the only way to reduce skin-friction drag is by reducing the gradient of the mean velocity profile, either directly or (usually) indirectly.

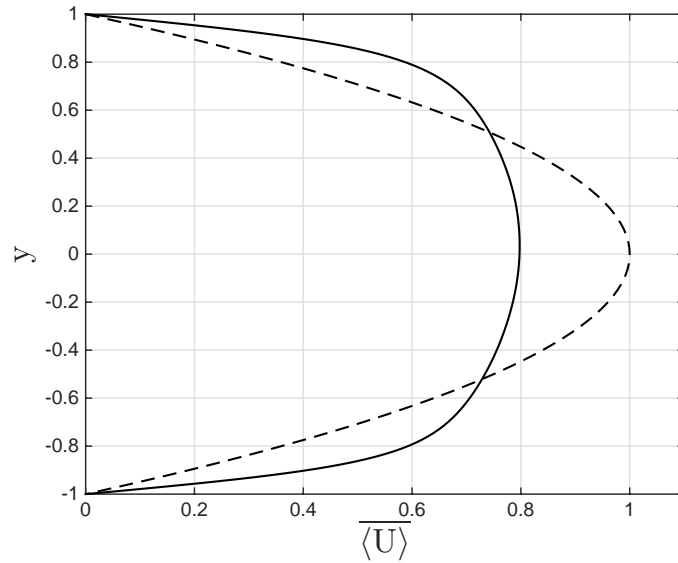


Figure 1.5: Plots of mean velocity profiles for laminar (---) and  $\text{Re} = 2230$  turbulent (—) channel flow.

The skin-friction coefficient for a turbulent channel flow is defined as [37]:

$$C_f := \frac{\tau_w^*}{\frac{1}{2}\rho^*U_b^{*2}}, \quad (1.9)$$

where  $U_b^*$  is bulk velocity which is defined as:

$$U_b^* := \frac{1}{2h^*} \int_{-h^*}^{h^*} \langle U^* \rangle dy^*. \quad (1.10)$$

Fukagata et al. [37] derived an equation, commonly known as the FIK identity, which expresses the skin-friction coefficient as a sum of the laminar and turbulent contributions to skin-friction drag. The FIK identity for a fully-developed channel flow is given as [37]:

$$C_f = \underbrace{\frac{12}{\text{Re}_b}}_{\text{Laminar}} + 12 \underbrace{\int_{-1}^1 (-y)(-\langle u'v' \rangle) dy}_{\text{Turbulent}}, \quad (1.11)$$

where  $\text{Re}_b$  is bulk Reynolds number defined as:

$$\text{Re}_b := \frac{U_b^* h^*}{\nu^*}, \quad (1.12)$$

and  $\langle u'v' \rangle$  is a Reynolds stress, where  $u' := (U^* - \overline{U^*})/U_b^*$  and  $v' := V^*/U_b^*$ . As a constant mass flow rate is assumed, bulk velocity non-dimensionalised by  $U_{cl}^*$  will be  $U_b = 2/3$ . From (1.11) we see that the laminar contribution to skin-friction drag is inversely proportional to the bulk Reynolds number, whereas the

turbulent contribution is a weighted integral of the Reynolds stress term  $-\overline{u'v'}$ . The weightings are such that the turbulent drag contribution is largest nearest the walls. The FIK identity shall be used in later chapters to analyse the effects of wall-based controllers on turbulent channel flow.

### 1.3.2 Turbulence Regeneration

In turbulent wall-bounded flows, kinetic energy from the free-stream is converted into turbulent velocity perturbations and then dissipated by viscous effects into internal energy [95]. This process of near-wall turbulence production and dissipation is self-sustaining and there are various theories and models that try to explain this phenomenon, although there is no general agreed consensus. It is apparent that coherent motions in turbulent boundary layers are responsible for the self-sustaining mechanism. Robinson [95] defines coherent motion as “*a three-dimensional region of the flow over which at least one fundamental flow variable (velocity component, density, temperature etc.) exhibits significant correlation with itself or with another variable over a range of space and/or time that is significantly larger than the smallest local scales of the flow*”. The majority of research into the identification of structures in turbulent wall-bounded flows has been done at moderately low Reynolds number and it is thought that at higher Reynolds numbers, turbulent boundary layers may exhibit very different structures and motions [39]. Only research findings for low Reynolds number turbulent boundary layers will be discussed in the following.

There are some coherent motions that are known to exist and are easily observable. In the viscous sublayer and buffer layer of a turbulent boundary layer, thin, sinuous, streamwise-elongated alternating regions of low-speed and high-speed fluid lie parallel to one another; the low-speed regions are known as streaks. Many researchers have observed a mean spanwise streak-spacing of  $\lambda_z^+ \approx 100$  [19, 66, 70] and streamwise length of  $\lambda_x^+ \approx 1000$  [57], although these are dependent on wall-normal distance and Reynolds number. As streaks travel downstream, they “burst” ejecting low-speed fluid into the outer layers, this is coupled with “sweeps” of high-speed fluid towards the wall from the outer layers [95]. There is no consensus on how streaks form, how they break-up (burst), the mechanisms of energy transfer between the inner and outer layers and the relation between vortical structures and streaks.

Kline et al. [70] were one of the first research groups to observe and study streaks experimentally. Through flow observations and hot-wire anemometry of a turbulent boundary layer they found coherent motions of the streaks. They found that the low-speed streaks slowly move away from the wall as they move downstream and at a certain distance from the wall, violently eject to the outer layers. These

ejections, named “bursts”, were thought to be the primary mechanism for turbulent energy production in the inner layers and were responsible for transporting kinetic energy to the outer layers. Their experiments showed that nearly half of the turbulent energy production happened in the regions close to the wall (up to the log-law region), with the outer layers only producing around a fifth. Quasi-streamwise vortices, slightly tilted away from the wall, in counter-rotating pairs were also observed straddling the streaks and high-speed fluid in regions close to the wall.

Kim et al. [66] proposed a three stage cyclic model of the burst process. In the first stage, a low-speed streak lifts away from the wall as it moves downstream due to the streamwise vortex between the regions of low-speed and high-speed fluid and at a certain distance rapidly ejects upwards - “streak-lifting”. In the second stage, the rapid movement away from the wall creates an instantaneous inflectional velocity profile which is inviscidly unstable to disturbances within a band of frequencies. In the third stage, the streak oscillates due to the instability and breaks down into a chaotic state - “break up”. After break up, the original instantaneous velocity profile returns and the streaks return to the wall for the cycle to begin again. The researchers found that nearly all turbulent energy production occurred during these bursting events.

There have been numerous conceptual models regarding the structure of vortices present in near-wall turbulence; a summary is given in Robinson [95]. The majority of conceptual models include horseshoe [12] or hairpin-shaped [104] vortices that straddle streaks, to explain their observed lift-up and breakdown. An example of such a model is that given by Smith [102]; a model proposing the formation of hairpin vortices near the wall ( $y^+ < 100$ ) in a turbulent boundary layer. The model describes the kinematics and dynamics of hairpin vortices and their interactions with streaks, bursting and the near-wall shear layers. Smith postulated that the observed breakdown of a streak is the signature of vortex roll-up in the unstable shear layer that forms atop and astride streaks. On formation, a vortex loop moves outwards and downstream via self-induction and the streamwise velocity gradient respectively. The trailing “legs” of the vortex loop remain near the wall but are elongated, forming counterrotating streamwise vortices that eject fluid away from the wall and accumulate low-speed fluid between the legs. Streaks are preserved or redeveloped during the bursting process via the coalescence of the stretched legs of multiple “nested” hairpin vortices. The larger scale bulges in the outer layers of a turbulent boundary layer may be due to the streamwise array of vortices that comprise a burst growing outward and collating. Diagrams of these processes are shown in Figure 1.6. In the current work, visualisations of turbulent flow fields in Figures 4.33 and 5.22 show horseshoe-like vortical structures as described in the conceptual models mentioned. This shows that they exist at least

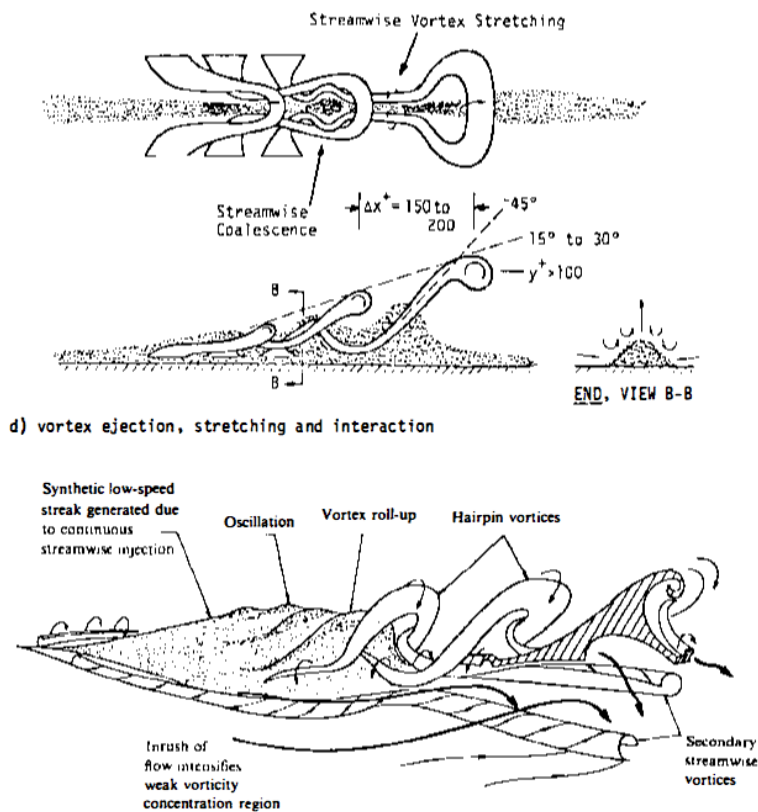


Figure 1.6: Diagrams of Smith's model for streak breakdown in a turbulent boundary layer. *Top* - Plan and side views of a developing hairpin vortex [102]. *Bottom* - Sketch of the formation and breakdown of a hairpin vortex [4].

in low Reynolds number simulated flow.

Recently, Sharma and McKeon [100] used resolvent analysis of the linearised Navier-Stokes equations to predict packets of hair pin vortices as coherent structures in turbulent pipe flow. By performing singular value decompositions on the resolvent operator for certain combinations of spatial Fourier modes and superposing the leading singular vectors, they found the resulting swirl fields to be qualitatively very similar to packets of hairpin vortices found from previous DNS studies. This is the first time such structures have been found from analytical analysis of the linearised Navier-Stokes equations.

Chernyshenko and Baig [22] investigated two generalised conceptual models of streak formation using numerical experiments. The first conceptual model stated that the pattern of streaks is dictated by the pattern of wall-normal motions i.e. streamwise vortices, hairpin vortices etc. The second model stated that the pattern of streaks is dictated by the pattern-forming properties of the combined action of lift-up, shear and diffusion described by the linearised Navier Stokes equations. In this model, wall-normal motions can occur via a variety of mechanisms. Using DNS with a modified passive-scalar form of the Navier-Stokes equations, unstructured wall-normal motions were enforced at the wall. They found that streaks still appeared. This finding supported the second conceptual model, suggesting wall-normal motions do not have to have any particular pattern for streaks to form. This contradicts the ideas behind conceptual models previously discussed. The authors also suggested that streaks may be a primary structure, meaning they form initially before generating vorticity and starting the regeneration cycle.

Another issue regarding wall-bounded turbulence is how energy and momentum is transferred between the inner and outer layers; is energy needed from the outer layers to sustain near-wall turbulence? Jimenez and Pinelli [57] used numerical experiments to determine whether near-wall turbulence is self-sustaining or whether it requires energy input from the outer flow. By artificially filtering out fluctuations above a certain distance from the wall, they found that turbulence still remained close to the wall, suggesting wall-bounded turbulence at low Reynolds number is self-sustaining and does not require input from the outer layers to persist. Using similar filtering techniques, they filtered out streaks in a turbulent boundary layer below a certain distance from the wall, to see whether streaks are required to sustain turbulence. They found that the flow relaminarised as long as streaks were filtered below at least  $y^+ \approx 60$ , thus showing that streaks are an important structure in the self-sustaining process.

This brief overview of research into turbulent boundary layer structure shows some important themes. Firstly, streak structures near the wall play an important role

in the self-sustaining cycle of near-wall turbulence. Secondly, the regeneration cycle of streaks involves streamwise vortices that may or may not be part of larger horseshoe or hairpin vortices. Finally, the bursting process of streak breakdown and regeneration is responsible for the majority of turbulent energy production. Therefore, to reduce skin-friction drag in a turbulent boundary layer via control, the streaks and/or wall-bounded vortices need to be attenuated.

## 1.4 Flow Control

*Flow control* is the art and science of altering the dynamics of a fluid flow in order to obtain a desired outcome. Besides reducing skin-friction drag, flow control has been used to delay transition to turbulence in transitional flows [7], to reduce noise emanating from jets [71], to stabilise structures that experience aerodynamic loads [80], to prevent boundary layers from separating [6] and to enhance the mixing of chemical reagents in industry [29]; to name only a few examples. Any flow control strategy that is capable of delivering one of these effects can be defined as being either open-loop or closed-loop, active or passive. An active control method requires an external energy input to provide actuation. Examples include wall transpiration (actuation via wall-normal velocity jets located at a wall), wall oscillation [94], plasma actuation [27, 24] and synthetic jets [43]. Passive control methods requires no such energy input. Closed-loop methods require real-time information relating to the flow fed to them in order to compute the required actuation. For example, this information could be wall-shear stress, wall pressure or wall temperature. Open-loop strategies require no information whilst online and the nature of their output is decided before their operation. These classifications mean that any method of flow control will fall into one of the following quadrants:

- active-open-loop (AOL)
- active-closed-loop (ACL)
- passive-open-loop (POL)
- passive-closed-loop (PCL)

These are illustrated in Figure 1.7.

Currently, POL methods seem the more viable solution for skin-friction drag reduction in turbulent wall-bounded flows. As they have no power requirements and tend to have no moving parts, they are relatively simple to test experimentally and are relatively straight-forward to implement and maintain when applied. One notable example of a POL control method is that of surface riblets which have been shown to achieve drag reductions of approximately 10% [40]. These are small grooves in the wall that are aligned in the free-stream direction. They are thought

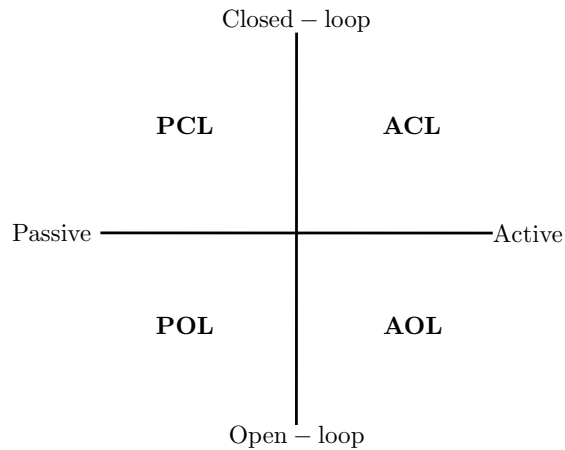


Figure 1.7: A schematic of the four classifications of flow control strategies.

to work by inhibiting streamwise vortices close to the wall which are known to be important structures in the turbulence regeneration process [39]. There is little theoretical basis for the majority of POL methods and their designs tend to be dictated by physical experimentation [39]. Therefore, even though a method may achieve an impressive drag reduction for a specific flow regime, it cannot always be known a priori whether the same method will work outside of that regime.

AOL flow control strategies focus both on the type of active control actuation and the amplitude and phase of the control signal used to drive the actuators. A lot of attention has been given to in-plane wall motion as an actuation force. Streamwise-travelling waves of spanwise wall velocity have been found to achieve drag reductions of 48% and flow relaminarisation in a turbulent channel flow [91]; the drag reduction achievable was found to depend heavily on the spanwise forcing frequency, the streamwise wavenumber of the travelling wave and Reynolds number. Unlike most POL methods, analytical methods to estimate the drag reduction achievable by spanwise oscillating walls exist [94]. This can inform the designer of which flow regimes this strategy is optimum without extensive practical testing. Other notable AOL examples include Lorentz force actuation which has been shown to achieve drag reductions of 10% [16], and plasma actuation which has been shown to be capable of replicating the effects of in-plane wall motion [24]. AOL methods are capable of significant drag reductions and even flow relaminarisation. However, due to the high power input required for some of these strategies, the net energy saving resulting from these methods can be small if not negative.

Of the four quadrants in Figure 1.7, it would seem there has been the least research into PCL methods for skin-friction drag reduction. These are methods that have no power source yet still provide a feedback input forcing to the flow. A notable PCL method of reducing drag in turbulent wall-bounded flows is that of compli-

ant wall coatings. Compliant walls are designed so that they interfere favourably with the fluid moving over them [39]. One of the first studies into the use of compliant coatings for skin-friction drag reduction was by Choi et al. [25]. Using single-layer viscoelastic compliant surfaces composed of silicone rubber, they found they could achieve a skin-friction drag reduction of 7% in a turbulent water flow around an axisymmetric body. More recently, Boiko et al. [14] used wind tunnel experiments to assess the turbulent skin-friction drag reducing properties of various “stiff” compliant coatings. They found that their best performing coating consistently achieved drag reductions of between 4-5%. This is a promising area of flow control, but much more work needs to be done before the potential drag reducing abilities of compliant surfaces can be realised.

The remainder of this thesis will focus purely on ACL methods of flow control for skin-friction drag reduction. These methods aim to harness the large drag reductions shown to be capable by AOL methods but with the added robustness and efficiency properties offered by feedback control. However, the use of feedback adds an additional layer of complexity in the forms of sensing/estimation, modelling, control objective and computing; problems in all four of these need to be overcome before ACL control can become a practical option for drag reduction. Presently, another difficulty with ACL flow control is with its ability to be implemented practically. That is, whether sensors and actuators can be manufactured that are small enough to measure and control the smaller scales of a flow (especially at high Reynolds number) if required but are also reliable when faced with adverse environmental conditions. The most likely solution to this problem comes in the form of micro-electrical-mechanical systems (MEMS) technology. MEMS are devices with characteristic length scales of between  $1\mu m$  and  $1mm$  that combine mechanical and electrical components [39]. They are capable of being produced in large arrays cheaply and to tight tolerances. Current MEMS sensors include hot-wire anemometers for flow speed measurement [56], shear-stress sensors [55], pressure sensors [35] and temperature sensors [74]. Wall-normal forcing MEMS actuators include pulsed jets [61] and synthetic jets [110]; for in-plane forcing, micro-scale technology is unlikely to be required. However, it may be the case that micro-sensing and -actuation is not required at all in some cases. As will be demonstrated in the current work, it is the largest scales of a flow that are responsible for the vast majority of turbulent energy production. Therefore, when controlling to mitigate turbulent energy, sensing and actuation on the macro-scale may only be required.

The following section details a comprehensive literature review into previous studies on ACL flow control for skin-friction drag reduction. To ensure the focus of this review remains on drag reduction of turbulent flow, research into transition delay has been purposefully omitted; except for a few notable exceptions.

## 1.5 Previous Research into ACL Drag Reduction

In the author's opinion, research into ACL drag reduction can be split into two categories - opposition control and model-based control. Opposition control methods tend to be simple, linear and based on intuition. Control laws are constructed which mitigate certain structures in a flow that are thought to be responsible for high skin-friction drag. These could include coherent structures such as streamwise vortices and streaks which were discussed in Section 1.3. Model-based control methods on the other hand, use dynamical flow models to synthesise control laws which aim to minimise some measurable flow variable such as wall-shear stress or kinetic energy. However, it is not always simple to categorise a control method as either one or the other. With this in mind, the research outlined in the following has been assigned to the most appropriate category in the opinion of the author.

### 1.5.1 Opposition Control

Arguably one of the first successful ACL control strategies to reduce skin-friction drag in a turbulent wall-bounded flow was the opposition control method of Choi et al. [23]. Their control law functioned by setting one or more components of velocity at the wall (the actuation) to be equal in magnitude but opposite in sign to the corresponding components of velocity at a fixed wall-normal distance from the wall. The reasoning being that this would result in the weakening of wall-bounded streamwise vortices which are known to be important in the cycle of turbulence regeneration. In their work, they investigated various components of velocity at the wall as actuation and different wall-normal sensing planes and evaluated their control through direct numerical simulation (DNS) of  $Re_\tau = 180$  turbulent channel flow; where Reynolds number is based on skin-friction velocity  $u_\tau$ . For wall-normal actuation, they found maximum drag reductions of approximately 25% and for spanwise actuation they achieved drag reductions of approximately 30%; in both cases the wall-normal sensing plane was located at distance  $y^+ = 10$  from the wall. The aforementioned results were achieved when the components of velocity at the sensing plane were measured directly, something which cannot easily be done in practice. When wall measurements were used to estimate velocity values at the sensing plane, they found that for both components of velocity, the maximum drag reduction achievable was 6%. This highlights the difficulty of gaining accurate flow estimates away from the wall.

More recently, Deng et al. [31] showed they could improve the drag reduction capabilities of Choi et al.'s [23] method. By increasing the magnitude of their actuation signals and implementing a low-pass filter on the actuator dynamics, they showed they could achieve drag reductions of up to 33% in a  $Re_\tau = 180$  turbulent channel flow. Again, they used DNS to gain their results. It should be noted that velocity values at the detection plane were measured directly and

therefore it would be difficult to replicate these results experimentally.

Lee et al. [76] developed adaptive controllers for reducing drag in  $Re_\tau = 100 - 180$  turbulent channel flow using neural networks. Their controllers used measurements of spanwise wall-shear stress to calculate required actuation in the form of blowing and suction at the walls. Control using an off-line trained controller and an on-line trained controller gave similar skin friction reductions of around 20%. From observations of the distribution of weights in their on-line trained neural network controller, they designed a simple control law that could achieve a similar drag reduction. This simpler controller effectively acts as an opposition control scheme and reduces skin friction by counteracting streamwise vortex motion in a similar fashion to that of Choi et al. [23]. As this scheme only uses wall measurements, the drag reduction is much greater than the 6% reduction achieved by Choi et al.'s comparable controller.

Koumoutsakos [73] devised an opposition control strategy to control a  $Re_\tau = 180$  turbulent channel flow by measurement and manipulation of the wall vorticity flux using blowing and suction at the wall. A simple opposition control scheme was used, where blowing and suction which generated spanwise vorticity fluxes opposite in sign to those measured at the wall was used as actuation. The controller yielded a skin friction drag reduction on the order of 40% which for a control scheme using only wall information, is an impressive result.

In the previous research, sensors and actuators are assumed to be infinitely small and arranged in dense arrays over the walls which is at best an impractical assumption. In their work, Endo et al. [33] employed finite-dimensional and sparsely populated arrays of shear-stress sensors and simple deformable wall actuators to reduce drag in a turbulent channel flow. Wall-shear-stress measurements were used to detect streamwise vortices and streaks downstream of the sensors. Their opposition control law was then able to mitigate these structures to the extent where they achieved a drag reduction of approximately 10%. It is also worth noting that the power requirements of this control method is one order of magnitude lower than if actuation was instead via fluid injection.

Lee et al. [77] derived an opposition control law using a suboptimal approach to reduce drag in  $Re_\tau = 110$  turbulent channel flow. From the observations that the control in Choi et al.'s [23] investigation increased both spanwise pressure gradient and spanwise wall-shear stress, two simple control laws that maximised these were found which used wall-pressure and spanwise shear-stress measurements respectively. Actuation was via wall transpiration. The spanwise shear-stress controller was able to reduce drag by as much as 22%. They attempted to generate a similar control law that would minimise streamwise shear stress which is proportional to

drag. However, their resulting control law was unstable.

Fukagata and Kasagi [38] used a similar approach to Lee et al. [77] to find a suboptimal control law that uses streamwise shear-stress measurements to suppress near-wall Reynolds stresses via wall transpiration in a  $Re_\tau = 180$  turbulent pipe flow. The FIK identity [54] states that Reynolds stresses close to the wall are major contributors to turbulent skin-friction drag. They achieved maximum drag reductions of approximately 12%.

Frohnapfel et al. [36] developed an opposition control scheme to dampen the near-wall spanwise velocity fluctuations in  $Re_\tau = 150 - 450$  turbulent channel flow. They used measurements of streamwise wall-shear stress to compute a body-forcing on spanwise velocity fluctuations in a damping region close to the wall; they suggested this forcing could be implemented via plasma or Lorentz actuation. They suggested that dampening near-wall spanwise velocity would weaken streamwise vortices and reduce the Reynolds stresses close to the wall. Their control scheme achieved maximum drag reductions of 20%, thought to be the highest to date for this choice of sensing. When they modelled their sensors and actuators as having finite-dimension, in a similar fashion to Endo et al. [33], they achieved drag reductions of around 13%.

Opposition control has been shown to be a simple and effective strategy for reducing drag in turbulent flows. Through knowledge of the relevant flow physics and intuition, considerable drag reductions have been achieved even when sensing is restricted to the walls. Opposition control appears to be a good contender for successful drag reduction in laboratory experiments. Notably, the approaches of Endo et al. [33] and Frohnapfel et al. [36] which use sparsely distributed and finite-dimensional sensors and actuators.

### 1.5.2 Model-Based Control

One of the earliest attempts at model-based ACL flow control was by Joshi et al. [62]. They used Systems Theory to synthesise a proportional-integral controller based on a two-dimensional linearised Navier-Stokes model to attenuate disturbances in a channel flow. Streamwise wall-shear stress was sensed and wall transpiration was used as actuation. The controller was able to stabilise all of the linear model's unstable right-half plane poles for Reynolds numbers up to ten thousand.

There has been a considerable amount of research into the use of optimal and robust control strategies for reducing skin-friction drag. The control objective of these strategies is to find a control signal that minimises a user-defined cost

function which includes some measurement of the system as well as the magnitude of the control signal itself. Joslin et al. [63] were the first to apply optimal control to wall-bounded flow. Their controller, which used wall-shear stress measurements and actuation via wall transpiration, was successful at suppressing Tollmien-Schlichting waves in a transitional boundary layer.

Arguably the first comprehensive study into the use of optimal and robust control methodologies for flow control was conducted by Bewley and Liu [10] using strictly linear analyses. They used a linear model based on the Orr-Sommerfeld Squire equations to synthesise  $\mathcal{H}_2$  and  $\mathcal{H}_\infty$  controllers to attenuate flow perturbation energy in a channel flow; both state-feedback and output-feedback control were investigated. The two control methods differ on how they model disturbances -  $\mathcal{H}_2$  control models disturbances as Gaussian white noise whereas  $\mathcal{H}_\infty$  control models “worst-case” disturbances. Flow perturbation energy was used in their cost function to be minimised and wall transpiration was used as actuation. For the output-feedback cases, the streamwise and spanwise wall-shear stresses were measured. Two types of  $\mathcal{H}_2$  controller were tested; a linear quadratic regulator (LQR) controller and a linear quadratic Gaussian (LQG) controller. The LQR controller requires full state information to determine its output, whilst the LQG controller uses only information at the wall to estimate the states of the system and is thus more practically implementable. Full state information and state-estimator  $\mathcal{H}_\infty$  controllers were tested likewise. Their in-depth study compared transfer function norms of disturbances to states and disturbances to inputs, and transient energy growth of the uncontrolled and controlled plants for a subcritical Reynolds number case ( $Re = 5,000$ ) and a supercritical Reynolds number case ( $Re = 10,000$ ), where Reynolds number is based on the channel’s maximum laminar centreline velocity for constant mass flow rate. They generated controllers with differing combinations of three tuning parameters  $\{\gamma, \alpha, l\}$  in order to see what effect this had on their performance. The  $\gamma$  parameter is a weighting of the amount of disturbance noise included in the cost function to be minimised, for  $\mathcal{H}_2$  control:  $\gamma \rightarrow \infty$ . The  $\alpha$  parameter quantifies the relative level to which the controller’s measurements are corrupted by noise. The  $l$  parameter can be interpreted as the cost of the control and is also included in the cost function to be minimised; reducing  $l$  results in larger control magnitudes (i.e. control is cheap). They found that both  $\mathcal{H}_2$  and  $\mathcal{H}_\infty$  controllers perform well compared to classical proportional controllers; with wall information only they could both detect and stabilise the plant. Both controllers could minimise their respective disturbance transfer function norms and greatly reduce transient energy growth. However, the results varied widely depending on the choice of tuning parameters.

Lee et al. [78] designed two-dimensional LQG/LTR (loop-transfer recovery) controllers to control the eight lowest spanwise-constant Fourier modes of three-

dimensional  $Re_\tau = 100$  channel flow. The two-dimensional controllers were evenly spaced along the spanwise direction of the channel. By transforming their linear channel flow model into Jordan canonical form and retaining dynamics corresponding to equally well controllable and observable states, they reduced the order of their control model to 2.5% of their original model. Wall transpiration was used as actuation and streamwise wall-shear stress was measured for inclusion into the cost function to be minimised. The two-dimensional controllers managed to reduce skin friction in a fully-developed channel flow by 10%. They then designed a simple spanwise *ad hoc* control scheme to suppress spanwise as well as streamwise shear stress fluctuations. This new control scheme was able to reduce skin friction by 17%. The authors noted that even though their controllers could minimise wall-shear stress perturbations, they could not minimise the flow's mean wall-shear stress. They suggested that different cost functions be investigated. This study demonstrates that reduced-order control models are still able to achieve significant results. Since then, many other model reduction techniques have been applied to flow control problems, such as balanced proper orthogonal decomposition [96], balanced truncation [97] and model refinement [58] (discussed in Chapter 5).

Kim and Lim [68] employed numerical DNS-based experiments to study what effect the linear coupling term in the Orr-Sommerfeld Squire equations (presented in Chapter 2) has on turbulence regeneration. In their experiments, they found that when the linear coupling term was artificially suppressed, near-wall turbulence decayed for  $Re_\tau = 100$  channel flow. This shows that even though turbulence is a nonlinear process, it requires linear mechanisms for its maintenance. Based on this result, Lim [79] designed LQR and LQG controllers to attenuate the linear coupling term and compared their performance to controllers with different cost function objectives - state, perturbation energy and skin friction. The controllers were able to reduce the effect of the coupling term, but not suppress it entirely. All LQR controllers gave a similar mean drag reduction of around 20% and all LQG controllers gave a similar mean drag reduction of around 15%. These results show how difficult it is to find a cost function that will have a significant effect on the mean drag. Spectral controllers are unable to control the mean drag directly because in wavenumber space, mean drag corresponds to zero-valued wavenumbers for which wall transpiration is ineffective; actuation at zero-valued wave numbers would involve movement of the wall.

Högberg et al. [50] used gain scheduling of LQR controllers to relaminarise  $Re_\tau = 100$  turbulent channel flow. Full-state information was used and actuation was via wall transpiration. Flow perturbation energy was included in the cost function to be minimised. In this study, gain scheduling involved synthesising a number of controllers using different mean velocity profiles in their flow models — a turbulent

mean velocity profile, a laminar mean velocity profile and a smooth distribution of velocity profiles between the two. Each mean velocity profile was included in the Orr-Sommerfeld Squire equations to create controllers for several Fourier modes which could then be inverse-Fourier transformed into physical space to create a convolution kernel. In application, the turbulent mean velocity profile controller is used to reduce perturbation energy as much as it can. When it reaches its reduction limit, the controller based on the next mean velocity profile is used until it reaches its reduction limit and so on until the flow is relaminarised. It was found that flow relaminarisation using gain scheduling could be achieved for flows that have undergone transition from a variety of initial conditions, suggesting that in this case, initial condition has little effect on the steady-state turbulent flow. This study has shown that flow relaminarisation can be achieved via linear control methods. However, full-state information was used making the current approach unimplementable.

Bewley et al. [11] used optimal control theory in a model predictive control setting to relaminarise  $Re_\tau = 100 - 180$  turbulent channel flow. Actuation was via wall transpiration and full flow field information was used. Their control strategy made use of adjoint flow fields for a gradient-based optimisation strategy conducted over finite time horizons to minimise their cost function. For each controller time step  $dt$ , their controller integrated the full nonlinear Navier-Stokes equations forward a finite time horizon  $dT$  from  $t_a$  to  $t_a + dT$  and then computed the adjoint field from  $t_a + dT$  to  $t_a$  using DNS. Using a gradient-based optimisation strategy, the optimal actuation signal that would minimise their cost function was computed and applied between  $t_a$  and  $t_a + dt$ , where  $dt \ll dT$ . Cost functions including terminal turbulent kinetic energy, time-averaged turbulent kinetic energy and drag were all tested. Drag reductions of 50% and flow relaminarisation were achieved when terminal turbulent kinetic energy was included in their cost function. Drag reductions were not as impressive for the other cost functions tested. The control scheme used in this study cannot be implemented in reality due to the amount of computer time needed to calculate the optimal actuation at each time step (in this study it took approximately fifty times the time needed to perform a standard DNS time step). However, this study acts as a “best case” benchmark for controllers employing wall-based actuation.

Balogh et al. [8] derived a control law using a Lyapunov stability argument to globally stabilise a two-dimensional channel flow using tangential actuation at the walls and sensing of wall-shear stress. In this case, global stability implies that irrespective of initial condition, all perturbations to the laminar mean flow will decay for time  $t \rightarrow \infty$ . In practice, this leads to flow relaminarisation. It is claimed that their approach applies to the three-dimensional case also, although this is not proven. The main limitation of their method is that it is applicable

only to “sufficiently low Reynolds number flows”.

Sharma et al. [101] used the framework of passivity to design a globally stabilising controller capable of relaminarising  $Re_\tau = 100$  channel flow. Their controller required sensing of, and actuation via, the wall-normal component of velocity throughout the flow domain. In their approach, they decomposed the Navier-Stokes equations for a channel flow into the linear dynamics under feedback forcing from the nonlinearity. The passivity theorem states that the feedback interconnection of two passive systems is passive. Therefore, noting that the nonlinearity acts as a passive operator, control is only required to make the linear dynamics passive in order to ensure passivity of the entire system. A passive system can only store and dissipate energy, and is therefore globally stable. When testing their controller using DNS, they found that flow relaminarisation could be achieved when Fourier wavenumber pairs with indices less than five were made passive. This suggests that it is the larger spatial scales of a channel flow which are important for turbulent energy production.

The sensing and actuation used by Sharma et al. [101] would be incredibly difficult to implement in practice. Martinelli et al. [84] investigated whether it is possible to enforce passivity on a channel flow’s linear dynamics when actuation is restricted to the walls. They proved analytically that this is not possible for any Reynolds number and any velocity component used as actuation. Using full flow field information and all three components of velocity at the wall as actuation separately, they then designed controllers to minimise the upper bound on transient energy growth within the channel using a linear matrix inequality approach. The effect of the controllers is to make the linear dynamics of the flow closer to passive. They evaluated their controllers using DNS initialised by oblique waves and streamwise vortices. It was found that using the wall-normal component of velocity as wall actuation resulted in better transition delay. The work of Sharma et al. [101] and Martinelli et al. [84] will be extended in Chapter 4, where control using wall-based sensing and actuation is used to make turbulent channel flow closer to passive.

Although model-based control is more complex than the majority of opposition control strategies, it has been proven to be effective. Especially as in a number of cases, model-based control has managed to relaminarise turbulent flow, something which is surely one of the “holy grails” of flow control. It should be noted that all of the control strategies that have achieved flow relaminarisation use impractical sensing and/or actuation arrangements. For a controller to be seen as practical, sensing and actuation need to be both located at the wall. The previous research highlights important areas of consideration - control methodology (e.g. LQG), control objective (e.g. perturbation energy minimisation) and choice of sensing

measurement. The majority of model-based flow control research has used wall transpiration as actuation. The wall-normal component of velocity has proven to be most effective for wall actuation, at least for passivity-based control [84]. However, more research needs to be done in finding the optimal choice of actuation.

The review papers by Collis et al. [26], Kim and Bewley [67], Lumley and Blossey [81] and Zhou and Bai [116], and books by Aamo and Krstić [3], Barbu [9] and Gad-el-Hak [39] provide further insight into flow control for skin-friction drag reduction.

## 1.6 Thesis Layout and Publications

The remainder of this thesis is structured as follows:

In Chapter 2, a linearised form of the Navier-Stokes equations will be derived known as the Orr-Sommerfeld Squire equations. It will then be shown how these equations can be spectrally discretised to form highly accurate, low-order models. These models will be used for controller synthesis in later chapters.

In Chapter 3, the open-source DNS program used for evaluating controllers in this work will be outlined, and the method by which the Navier-Stokes equations are marched forward in time shall be derived. It will also be shown how this program was modified by the author to allow for the inclusion of wall-normal actuation at the boundaries - the control actuation used by all controllers developed in this thesis.

In Chapter 4, the energy-based framework of passivity will be outlined, and then used to analyse the passivity of turbulent channel flow. Based on this analysis, feedback controllers will be synthesised, with different wall-sensing arrangements, to alter the passivity of certain scales within a flow with the aim of reducing perturbation energy. Controllers will then be tested upon DNS of turbulent channel flow to evaluate their ability to reduce skin-friction drag. A linear analysis of the passivity-based controllers developed in this chapter was presented at the UKACC 10th International Conference on Control, 2014 [46]. Results from DNS testing of the controllers have been included in an article for *Automatica*, which has been accepted for publication.

In Chapter 5, the  $\mathcal{H}_\infty$  loop-shaping control method will be presented, and it will be shown how this method provides *a priori* guarantees of robustness and performance. This method will then be applied to turbulent channel flow with the aim of minimising streamwise wall-shear stress perturbations. Again, controllers will be tested upon DNS of turbulent channel flow in order to evaluate their ability to reduce skin-friction drag.

Finally, in Chapter 6, the findings from previous chapters will be discussed, and final conclusions presented. Also, avenues of future work identified from the current work will be outlined, and the novel contributions to the field contained within this thesis will be highlighted.



## Chapter 2

# Modelling

The Navier-Stokes equations in (1.1) are a set of continuous nonlinear infinite dimensional partial differential algebraic equations (PDAEs). A large portion of modern control theory requires spatially discrete linear time-invariant (LTI) state-space models for controller synthesis. All controllers developed in the current thesis will be of this form. At first glance, it may seem inappropriate to use linear control on a system as highly nonlinear as turbulent flow. However, as will be shown in Chapters 4 and 5, controlling only the linear dynamics is justifiable as long as the nonlinearity is modelled appropriately.

LTI descriptor systems have the form [5]:

$$E \frac{d\mathbf{x}(t)}{dt} = A\mathbf{x}(t) + B\mathbf{u}(t), \quad (2.1a)$$

$$\mathbf{y}(t) = C\mathbf{x}(t) + D\mathbf{u}(t), \quad (2.1b)$$

where  $\mathbf{x} \in \mathbb{R}^m$  is a vector of system states,  $\mathbf{u} \in \mathbb{R}^p$  is a vector of system inputs,  $\mathbf{y} \in \mathbb{R}^q$  is a vector of system outputs, and  $A \in \mathbb{R}^{m \times m}$ ,  $B \in \mathbb{R}^{m \times p}$ ,  $C \in \mathbb{R}^{q \times m}$ ,  $D \in \mathbb{R}^{q \times p}$  and  $E \in \mathbb{R}^{m \times m}$  are all time-invariant matrices. In order to convert the system in (2.1) into a standard state-space system, the matrix  $E$  has to be nonsingular. As will be demonstrated, the Navier-Stokes equations in the form of (1.1), once linearised, cannot be transformed into a state-space model. This is because the divergence-free condition in (1.1b) results in the system having a singular  $E$  matrix. Controller design for such systems is less straightforward than for standard state-space systems. Therefore, a number of analytic formulations of the linearised Navier-Stokes equations have been devised which satisfy the divergence-free condition *implicitly*; namely the stream-function formulation and the Orr-Sommerfeld Squire equations. It is also possible to find a divergence-free basis numerically [59]. Because the resulting model has more physically relevant states, the Orr-Sommerfeld Squire equations shall be used as a basis for all control models in this thesis.

## 2.1 Orr-Sommerfeld Squire Equations

In order to gain a linear model, the Navier-Stokes equations (1.1) need to be linearised around a time-invariant base flow. This can be achieved by first decomposing the velocity vector  $\mathbf{V}$  into the summation of a time-independent base flow  $\tilde{\mathbf{V}}(y)$  and time-dependent perturbations to the base flow  $\mathbf{v}(x, y, z, t)$ , such that:

$$\mathbf{V}(x, y, z, t) = \tilde{\mathbf{V}}(y) + \mathbf{v}(x, y, z, t). \quad (2.2)$$

Denote  $\{u, v, w\} \in \mathbf{v}$  as the streamwise, wall-normal and spanwise perturbation velocity components respectively and  $\{\tilde{U}, \tilde{V}, \tilde{W}\} \in \tilde{\mathbf{V}}$  as the streamwise, wall-normal and spanwise velocity components of the base flow. The base flow has only a streamwise component, therefore  $\tilde{V} = \tilde{W} = 0$ . As long as it satisfies the boundary conditions, the base flow can be chosen arbitrarily. However, in the current work, the parabolic laminar mean velocity profile shall be used as the base flow. Therefore:

$$\tilde{U} = 1 - y^2. \quad (2.3)$$

The pressure scalar field can be decomposed similarly:

$$P(x, y, z, t) = \tilde{P}(y) + p(x, y, z, t). \quad (2.4)$$

Substituting (2.2) and (2.4) into (1.1) and subtracting the base flow results in the perturbation equations for a channel flow:

$$\frac{\partial u}{\partial t} = \frac{1}{\text{Re}} \nabla^2 u - \tilde{U} \frac{\partial u}{\partial x} - v \frac{\partial \tilde{U}}{\partial y} - \frac{\partial p}{\partial x} + f_x - n_x, \quad (2.5a)$$

$$\frac{\partial v}{\partial t} = \frac{1}{\text{Re}} \nabla^2 v - \tilde{U} \frac{\partial v}{\partial x} - \frac{\partial p}{\partial y} + f_y - n_y, \quad (2.5b)$$

$$\frac{\partial w}{\partial t} = \frac{1}{\text{Re}} \nabla^2 w - \tilde{U} \frac{\partial w}{\partial x} - \frac{\partial p}{\partial z} + f_z - n_z, \quad (2.5c)$$

$$0 = \frac{\partial u}{\partial x} + \frac{\partial v}{\partial y} + \frac{\partial w}{\partial z}, \quad (2.5d)$$

where  $\{f_x, f_y, f_z\} \in \mathbf{f}$  are the streamwise, wall-normal and spanwise external forcing components respectively and  $\{n_x, n_y, n_z\} \in \mathbf{n} = \mathbf{v} \cdot \nabla \mathbf{v}$  are the nonlinear terms. Neglecting nonlinear and external forcing terms, (2.5) can be represented as in (2.1a) with matrices:

$$\mathbf{x} = \begin{bmatrix} u \\ v \\ w \\ p \end{bmatrix}, \quad (2.6a)$$

$$E = \begin{bmatrix} I & 0 & 0 & 0 \\ 0 & I & 0 & 0 \\ 0 & 0 & I & 0 \\ 0 & 0 & 0 & 0 \end{bmatrix}, \quad (2.6b)$$

$$A = \begin{bmatrix} (\frac{1}{\text{Re}}\nabla^2 - \tilde{U}\frac{\partial}{\partial x}) & -\frac{\partial\tilde{U}}{\partial y} & 0 & -\frac{\partial}{\partial x} \\ 0 & (\frac{1}{\text{Re}}\nabla^2 - \tilde{U}\frac{\partial}{\partial x}) & 0 & -\frac{\partial}{\partial y} \\ 0 & 0 & (\frac{1}{\text{Re}}\nabla^2 - \tilde{U}\frac{\partial}{\partial x}) & -\frac{\partial}{\partial z} \\ \frac{\partial}{\partial x} & \frac{\partial}{\partial y} & \frac{\partial}{\partial z} & 0 \end{bmatrix}, \quad (2.6c)$$

where  $I$  is the identity. It is clear from (2.6b) that the  $E$ -matrix is singular, and therefore, the system is descriptor and not a standard state-space system. However, the pressure terms in (2.5) can be eliminated by a change of state variables, resulting in the divergence-free condition being satisfied implicitly. This is achieved by first taking the Laplacian of the linear terms in (2.5b), yielding:

$$\frac{\partial}{\partial t}\nabla^2\mathbf{v} = \frac{1}{\text{Re}}\nabla^2(\nabla^2(\mathbf{v})) - \frac{\partial^2\tilde{U}}{\partial y^2}\frac{\partial\mathbf{v}}{\partial x} - \tilde{U}\frac{\partial}{\partial x}\nabla^2\mathbf{v} - 2\frac{\partial^2\tilde{U}}{\partial y^2}\frac{\partial^2\mathbf{v}}{\partial x\partial y} - \frac{\partial}{\partial y}\nabla^2\mathbf{p}. \quad (2.7)$$

Then, summing the divergence of (2.5a)-(2.5c) and using the constraint in (2.5d) leads to:

$$\frac{\partial^2\mathbf{p}}{\partial x^2} + \frac{\partial^2\mathbf{p}}{\partial y^2} + \frac{\partial^2\mathbf{p}}{\partial z^2} = \nabla^2\mathbf{p} = -2\frac{\partial\tilde{U}}{\partial y}\frac{\partial\mathbf{v}}{\partial x}. \quad (2.8)$$

Substitution of (2.8) into (2.7) results in:

$$\frac{\partial}{\partial t}\nabla^2\mathbf{v} = \frac{1}{\text{Re}}\nabla^2(\nabla^2(\mathbf{v})) - \frac{\partial^2\tilde{U}}{\partial y^2}\frac{\partial\mathbf{v}}{\partial x} - \tilde{U}\frac{\partial}{\partial x}\nabla^2\mathbf{v}. \quad (2.9)$$

Pressure has now been eliminated. For three-dimensional channel flow, a second equation is required. Wall-normal vorticity is defined as:

$$\eta_y := \frac{\partial\mathbf{u}}{\partial z} - \frac{\partial\mathbf{w}}{\partial x}. \quad (2.10)$$

Subtracting the spanwise derivative of (2.5a) from the streamwise derivative of (2.5b) gives the following coupled wall-normal velocity - wall-normal vorticity equation:

$$\frac{\partial\eta_y}{\partial t} = -\frac{\partial\tilde{U}}{\partial y}\frac{\partial\mathbf{v}}{\partial z} + \frac{1}{\text{Re}}\nabla^2\eta_y - \tilde{U}\frac{\partial\eta_y}{\partial x}. \quad (2.11)$$

Together, (2.9) and (2.11) are known as the Orr-Sommerfeld Squire equations. When arranged into the form of (2.1a), the resulting system matrices are:

$$\mathbf{x} = \begin{bmatrix} \mathbf{v} \\ \eta_y \end{bmatrix}, \quad (2.12a)$$

$$E = \begin{bmatrix} \nabla^2 & 0 \\ 0 & I \end{bmatrix}, \quad (2.12b)$$

$$A = \begin{bmatrix} \left( \frac{1}{\text{Re}} \nabla^2 (\nabla^2(\cdot)) - \frac{\partial^2 \tilde{U}}{\partial y^2} \frac{\partial}{\partial x} - \tilde{U} \frac{\partial}{\partial x} \nabla^2 \right) & 0 \\ -\frac{\partial \tilde{U}}{\partial y} \frac{\partial}{\partial z} & \left( \frac{1}{\text{Re}} \nabla^2 - \tilde{U} \frac{\partial}{\partial x} \right) \end{bmatrix}. \quad (2.12c)$$

The  $E$ -matrix in (2.12b) is invertible (i.e. nonsingular) once appropriately discretised and with the required boundary conditions imposed. Inverting the  $E$ -matrix and bringing it over to the right-hand-side of (2.1a) results in the Orr-Sommerfeld Squire model for a channel flow:

$$\frac{\partial}{\partial t} \begin{bmatrix} \mathbf{v} \\ \eta_y \end{bmatrix} = \underbrace{\begin{bmatrix} \mathbb{L}_{\text{OS}} & 0 \\ \mathbb{L}_{\text{C}} & \mathbb{L}_{\text{Sq}} \end{bmatrix}}_{\mathbb{L}} \begin{bmatrix} \mathbf{v} \\ \eta_y \end{bmatrix}, \quad (2.13)$$

where  $\mathbb{L}_{\text{OS}} = (\nabla^2)^{-1} \left( \frac{1}{\text{Re}} \nabla^2 (\nabla^2(\cdot)) - \frac{\partial^2 \tilde{U}}{\partial y^2} \frac{\partial}{\partial x} - \tilde{U} \frac{\partial}{\partial x} \nabla^2 \right)$  is the Orr-Sommerfeld operator,  $\mathbb{L}_{\text{C}} = -\frac{\partial \tilde{U}}{\partial y} \frac{\partial}{\partial z}$  is the coupling operator, and  $\mathbb{L}_{\text{Sq}} = \left( \frac{1}{\text{Re}} \nabla^2 - \tilde{U} \frac{\partial}{\partial x} \right)$  is the Squire operator.

## 2.2 Spectral Discretisation

There are numerous methods for discretising PDAEs such as those in (2.9) and (2.11). Commonly used examples include finite difference, finite volume, finite element and spectral discretisation; each having their own advantages and disadvantages. As will be made apparent, spectral discretisation is well suited for channel flow because of its simple geometry and boundary conditions. Spectral discretisation will be used to synthesise all models in this thesis.

Given an unknown spatially one-dimensional time-dependent function  $\mathbf{u}(\mathbf{x}, t)$ , an approximation of this function can be sought from the following truncated series expansion [15]:

$$\mathbf{u}(\mathbf{x}, t) \approx \mathbf{u}_{\text{N}}(\mathbf{x}, t) = \sum_{n=0}^{\text{N}} a_n(t) \Gamma_n(\mathbf{x}), \quad (2.14)$$

where  $a_n$  is the  $n^{\text{th}}$  *spectral coefficient* and  $\Gamma_n$  is the  $n^{\text{th}}$  *basis function* of a set of  $\text{N} + 1$  basis functions. Substituting (2.14) into a standard linear equation yields:

$$L\mathbf{u}(\mathbf{x}, t) = \mathbf{f}(\mathbf{x}, t) \approx L\mathbf{u}_{\text{N}}(\mathbf{x}, t), \quad (2.15)$$

where  $L$  is a linear operator, and  $\mathbf{f}(\mathbf{x}, t)$  is a vector. A residual function can be defined as:

$$R(\mathbf{x}; a_0, a_1, \dots, a_{\text{N}}) = L\mathbf{u}_{\text{N}} - \mathbf{f}. \quad (2.16)$$

The aim of any method of discretisation is to minimise this residual function. The main advantage of spectral methods is their accuracy. The typical convergence rate of the residual for spectral methods is  $O(N^{-m})$  for every  $m$  for functions that are sufficiently smooth and  $O(c^N)$  ( $0 < c < 1$ ) for functions that are analytic [105]. This is referred to as *spectral accuracy*.

For a given set of basis functions, chosen primarily based on the boundary conditions of the problem at hand, there are a number of different spectral methods which can be used to find the corresponding spectral coefficients. Two methods that will be discussed here are Galerkin and collocation.

### 2.2.1 Streamwise and Spanwise Discretisation

Channel flow has periodic boundary conditions in both the streamwise and spanwise directions. For a channel flow with spatial dimensions  $[L_x \times 2 \times L_z]$ , this means:

$$\mathbf{v}(x, y, z, t) = \mathbf{v}(x + L_x, y, z, t), \quad (2.17a)$$

$$\mathbf{v}(x, y, z, t) = \mathbf{v}(x, y, z + L_z, t). \quad (2.17b)$$

Therefore, a natural choice of basis functions for spectral discretisation in these directions are Fourier modes. Fourier modes are periodic functions with a period of  $2\pi$  and form an orthogonal basis set. In complex form, the general Fourier series can be written as:

$$f(x) = \sum_{n=-\infty}^{\infty} c_n e^{inx}, \quad (2.18)$$

where the Fourier coefficients are found from:

$$c_n = \frac{1}{2\pi} \int_{-\pi}^{\pi} f(x) e^{-inx} dx. \quad (2.19)$$

Wall-normal velocity and wall-normal vorticity can therefore be approximated as the following truncated Fourier series:

$$v(x, y, z, t) \approx \sum_{k_x=-N_x/2+1}^{N_x/2} \sum_{k_z=-N_z/2+1}^{N_z/2} \hat{v}_{\alpha,\beta}(y, t) e^{i(\alpha x + \beta z)}, \quad (2.20a)$$

$$\eta_y(x, y, z, t) \approx \sum_{k_x=-N_x/2+1}^{N_x/2} \sum_{k_z=-N_z/2+1}^{N_z/2} \hat{\eta}_{\alpha,\beta}(y, t) e^{i(\alpha x + \beta z)}, \quad (2.20b)$$

where  $N_x$  and  $N_z$  are the number of equispaced discretisation points in the streamwise and spanwise directions respectively, and  $\alpha, \beta \in \mathbb{R}$  are the streamwise and

spanwise *wavenumbers* respectively. The wavenumbers are defined as:

$$\alpha := \frac{2\pi k_x}{L_x}, \quad (2.21a)$$

$$\beta := \frac{2\pi k_z}{L_z}, \quad (2.21b)$$

where  $k_x, k_z \in \mathbb{Z}$  are the streamwise and spanwise wavenumber *indices* respectively. Substituting (2.20) into (2.12) and simplifying notation results in the following semi-discretised system matrices for each  $(\alpha, \beta)$  pair:

$$\mathbf{x} = \begin{bmatrix} \hat{v}(y, t) \\ \hat{\eta}(y, t) \end{bmatrix}, \quad (2.22a)$$

$$E = \begin{bmatrix} E_{11} & 0 \\ 0 & E_{22} \end{bmatrix}, \quad (2.22b)$$

$$A = \begin{bmatrix} A_{11} & 0 \\ A_{21} & A_{22} \end{bmatrix}, \quad (2.22c)$$

where:

$$E_{11} := \hat{\nabla}^2, \quad (2.23a)$$

$$E_{22} := I, \quad (2.23b)$$

$$A_{11} := \frac{1}{\text{Re}} \hat{\nabla}^4 - i\alpha \frac{\partial^2 \tilde{U}}{\partial y^2} - i\alpha \tilde{U} \hat{\nabla}^2, \quad (2.23c)$$

$$A_{21} := -i\beta \frac{\partial \tilde{U}}{\partial y}, \quad (2.23d)$$

$$A_{22} := \frac{1}{\text{Re}} \hat{\nabla}^2 - i\alpha \tilde{U}, \quad (2.23e)$$

and,

$$\hat{\nabla}^2 := \frac{\partial^2}{\partial y^2} - k^2 I, \quad (2.24a)$$

$$\hat{\nabla}^4 := \frac{\partial^4}{\partial y^4} - 2k^2 \frac{\partial^2}{\partial y^2} + k^4 I, \quad (2.24b)$$

$$k^2 := \alpha^2 + \beta^2. \quad (2.24c)$$

Discretising in the manner outlined above results in spatially one-dimensional systems for each Fourier wavenumber pair  $(\alpha, \beta)$ .

### 2.2.2 Wall-Normal Discretisation

Channel flow is inhomogeneous in the wall-normal direction. This is due to the impermeability and no-slip conditions at the walls. Therefore, the following boundary conditions are imposed on wall-normal velocity and wall-normal

vorticity Fourier coefficients:

$$\hat{v}(\pm 1, t) = 0, \quad (2.25a)$$

$$\frac{\partial}{\partial y} \hat{v}(\pm 1, t) = 0, \quad (2.25b)$$

$$\hat{\eta}(\pm 1, t) = 0. \quad (2.25c)$$

Dirichlet boundary condition (2.25a) is due to the wall impermeability condition, Neumann boundary condition (2.25b) is derived from the divergence-free condition in (1.1b), and Dirichlet boundary condition (2.25c) follows from the no-slip conditions at the walls. Chebyshev polynomials are an appropriate choice of basis function for this problem. This is because they are relatively flexible in the imposition of boundary conditions and are usually defined on the same interval used in the current work -  $y \in [-1, 1]$ . Chebyshev polynomials of the first kind are defined [15]:

$$T_m(y) = \cos(m \cos^{-1}(y)) \quad \forall m \in \mathbb{Z}_+, \quad (2.26)$$

and represent an orthogonal basis set. The semi-discretised wall-normal velocity and wall-normal vorticity Fourier coefficient vectors for each wavenumber pair  $(\alpha, \beta)$  can be approximated by the following modified Chebyshev series:

$$\hat{v}_{\alpha, \beta}(y, t) \approx \sum_{n_y=0}^{N_y} a_{v, n_y}(t) \underbrace{\gamma_v(y) T_{n_y}(y)}_{\phi_{n_y}(y)} = \Phi_N \mathbf{a}_{vN}, \quad (2.27a)$$

$$\hat{\eta}_{\alpha, \beta}(y, t) \approx \sum_{n_y=0}^{N_y} a_{\eta, n_y}(t) \underbrace{\gamma_\eta(y) T_{n_y}(y)}_{\psi_{n_y}(y)} = \Psi_N \mathbf{a}_{\eta N}, \quad (2.27b)$$

where  $a_v$  and  $a_\eta$  are Chebyshev spectral coefficients for wall-normal velocity and wall-normal vorticity respectively, and  $\gamma_v$  and  $\gamma_\eta$  are weighting functions. Weighting functions are used to ensure the boundary conditions in (2.25) are satisfied. Two polynomial weighting functions which achieve this are:

$$\gamma_v = (1 - y^2)^2, \quad (2.28a)$$

$$\gamma_\eta = 1 - y^2. \quad (2.28b)$$

Multiplying these weighting functions with the Chebyshev basis function set creates two new sets of basis functions -  $\Phi$  for wall-normal velocity and  $\Psi$  for wall-normal vorticity.

Many methods exist for calculating the unknown spectral coefficients in (2.27), two of the most commonly used are collocation and Galerkin. The collocation method is easier to implement as no integration is required, but the Galerkin

method provides greater accuracy. The methods differ in how they try and minimise the residual function in (2.16).

Both methods fall under the framework of the “method of mean weighted residuals” (MWR) [15]. Within this framework, spectral coefficients are found by imposing the  $(N + 1)$  conditions:

$$\langle w_i, R(x; a_0, a_1, \dots, a_N) \rangle = 0, \quad i = 0, 1, \dots, N, \quad (2.29)$$

where  $w_i$  are suitable *test functions* and  $\langle \cdot, \cdot \rangle$  defines the following inner product:

$$\langle y, z \rangle = \int_a^b y(x)z(x)dx. \quad (2.30)$$

The choice of test function differentiates the collocation from the Galerkin method.

### Collocation Method

The collocation method, alternatively referred to as the pseudospectral method in the literature, requires test functions:

$$w_i(x) = \delta(x - x_i), \quad (2.31)$$

where  $x_i$  are a set of *collocation points* (i.e. grid points) and  $\delta(x)$  is the Dirac delta function. This choice of test function is equivalent to stating that the residual function should be zero at each collocation point, i.e.:

$$R(x_i; a_0, a_1, \dots, a_N) = 0, \quad i = 0, 1, \dots, N. \quad (2.32)$$

Therefore, evaluating the basis functions on a set of collocation points, the unknown function from (2.14) can be re-written as:

$$\mathbf{u}(x, t) \approx \mathbf{u}_N(x_i, t) = \sum_{n=0}^N a_n(t)\Gamma_n(x_i). \quad (2.33)$$

Substitution of (2.33) into (2.15) yields:

$$L\mathbf{u}(x, t) = \mathbf{f}(x, t) \approx L\mathbf{u}_N(x_i, t) = \sum_{n=0}^N a_n(t)L(\Gamma_n(x_i)) = \mathbf{f}(x_i, t). \quad (2.34)$$

Therefore, once the basis functions are evaluated at the collocation points, linear operations can be performed on them directly, making this method simple to implement. The downside of the collocation method is that the residual is only zero at the grid points and not necessarily zero between them. Many points may be needed to gain suitable accuracy. However, in practice, for sufficiently smooth

functions, this is not usually the case.

Before applying the collocation method to channel flow, a set of collocation points needs to be defined. For good accuracy and to prevent Runge phenomenon [105], a clustered grid of Gauss-Chebyshev-Lobatto points will be used. These are defined:

$$y_j = \cos(j\pi/N_y), \quad j = 0, 1, \dots, N_y. \quad (2.35)$$

Evaluating the two sets of basis functions on this grid, the following differentiation matrices can be defined for wall-normal velocity:

$$D_{v,N}^0 = \begin{bmatrix} \phi_0(y_j) & \phi_1(y_j) & \cdots & \phi_N(y_j) \end{bmatrix} = \Phi_N, \quad (2.36a)$$

$$D_{v,N}^2 = \begin{bmatrix} \phi_0''(y_j) & \phi_1''(y_j) & \cdots & \phi_N''(y_j) \end{bmatrix} = \Phi_N'', \quad (2.36b)$$

$$D_{v,N}^4 = \begin{bmatrix} \phi_0''''(y_j) & \phi_1''''(y_j) & \cdots & \phi_N''''(y_j) \end{bmatrix} = \Phi_N'''', \quad (2.36c)$$

and wall-normal vorticity:

$$D_{\eta,N}^0 = \begin{bmatrix} \psi_0(y_j) & \psi_1(y_j) & \cdots & \psi_N(y_j) \end{bmatrix} = \Psi_N, \quad (2.37a)$$

$$D_{\eta,N}^2 = \begin{bmatrix} \psi_0''(y_j) & \psi_1''(y_j) & \cdots & \psi_N''(y_j) \end{bmatrix} = \Psi_N'', \quad (2.37b)$$

where  $'$  denotes differentiation with respect to  $y$ . However, the differentiation matrices above cannot be implemented in their current form. This is because they are singular and the  $E$ -matrix in (2.22b) is required to be invertible. To remedy this, the top and bottom rows and the last two columns of each of the matrices are removed, resulting in matrices of dimension  $(N-1) \times (N-1)$ . This means that the spectral coefficients corresponding to the last two basis functions are also discarded. The system matrices in (2.22) fully discretised via Fourier and Chebyshev collocation methods are given for each Fourier wavenumber pair  $(\alpha, \beta)$  as:

$$\mathbf{x} = \begin{bmatrix} \mathbf{a}_{v,N-2}(t) \\ \mathbf{a}_{\eta,N-2}(t) \end{bmatrix}, \quad (2.38a)$$

$$E = \begin{bmatrix} \tilde{E}_{11} & 0 \\ 0 & \tilde{E}_{22} \end{bmatrix}, \quad (2.38b)$$

$$A = \begin{bmatrix} \tilde{A}_{11} & 0 \\ \tilde{A}_{21} & \tilde{A}_{22} \end{bmatrix}, \quad (2.38c)$$

where:

$$\tilde{E}_{11} := \hat{\mathbf{V}}_{v,N-2}^2, \quad (2.39a)$$

$$\tilde{E}_{22} := D_{\eta,N-2}^0, \quad (2.39b)$$

$$\tilde{A}_{11} := \frac{1}{\text{Re}} \hat{\nabla}_{v,N-2}^4 - i\alpha \frac{\partial^2 \tilde{U}}{\partial y^2} D_{v,N-2}^0 - i\alpha \tilde{U} \hat{\nabla}_{v,N-2}^2, \quad (2.39c)$$

$$\tilde{A}_{21} := -i\beta \frac{\partial \tilde{U}}{\partial y} D_{v,N-2}^0, \quad (2.39d)$$

$$\tilde{A}_{22} := \frac{1}{\text{Re}} \hat{\nabla}_{\eta,N-2}^2 - i\alpha \tilde{U} D_{\eta,N-2}^0, \quad (2.39e)$$

and,

$$\hat{\nabla}_{v,N-2}^2 := D_{v,N-2}^2 - k^2 D_{v,N-2}^0, \quad (2.40a)$$

$$\hat{\nabla}_{v,N-2}^4 := D_{v,N-2}^4 - 2k^2 D_{v,N-2}^2 + k^4 D_{v,N-2}^0, \quad (2.40b)$$

$$\hat{\nabla}_{\eta,N-2}^2 := D_{\eta,N-2}^2 - k^2 D_{\eta,N-2}^0. \quad (2.40c)$$

Note that the states,  $\mathbf{x}$ , of the system are no longer the wall-normal distribution of Fourier coefficients, but Chebyshev spectral coefficients. However, the original states can be recovered using the following substitutions:

$$\mathbf{a}_{v,N-2}(t) = \Phi_{N-2}^{-1}(y_j) \hat{v}(y_j, t), \quad (2.41a)$$

$$\mathbf{a}_{\eta,N-2}(t) = \Psi_{N-2}^{-1}(y_j) \hat{\eta}(y_j, t). \quad (2.41b)$$

Substituting (2.41) into the system matrices in (2.38), the final collocation discretised system is:

$$\mathbf{x} = \begin{bmatrix} \hat{v}(y_j, t) \\ \hat{\eta}(y_j, t) \end{bmatrix}, \quad (2.42a)$$

$$E = \begin{bmatrix} \tilde{E}_{11} & 0 \\ 0 & \tilde{E}_{22} \end{bmatrix}, \quad (2.42b)$$

$$A = \begin{bmatrix} \tilde{A}_{11} & 0 \\ \tilde{A}_{21} & \tilde{A}_{22} \end{bmatrix}, \quad (2.42c)$$

where:

$$\tilde{E}_{11} := \tilde{\nabla}_{v,N-2}^2, \quad (2.43a)$$

$$\tilde{E}_{22} := I, \quad (2.43b)$$

$$\tilde{A}_{11} := \frac{1}{\text{Re}} \tilde{\nabla}_{v,N-2}^4 - i\alpha \frac{\partial^2 \tilde{U}}{\partial y^2} I - i\alpha \tilde{U} \tilde{\nabla}_{v,N-2}^2, \quad (2.43c)$$

$$\tilde{A}_{21} := -i\beta \frac{\partial \tilde{U}}{\partial y} I, \quad (2.43d)$$

$$\tilde{A}_{22} := \frac{1}{\text{Re}} \tilde{\nabla}_{\eta,N-2}^2 - i\alpha \tilde{U} I, \quad (2.43e)$$

and,

$$\tilde{\nabla}_{v,N-2}^2 := \tilde{D}_{v,N-2}^2 - k^2 I, \quad (2.44a)$$

$$\tilde{\nabla}_{v,N-2}^4 := \tilde{D}_{v,N-2}^4 - 2k^2 \tilde{D}_{v,N-2}^2 + k^4 \mathbf{I}, \quad (2.44b)$$

$$\tilde{\nabla}_{\eta,N-2}^2 := \tilde{D}_{\eta,N-2}^2 - k^2 \mathbf{I}. \quad (2.44c)$$

The new differentiation matrices are defined:

$$\tilde{D}_{v,N-2}^2 := D_{v,N-2}^2 \Phi_{N-2}^{-1}, \quad (2.45a)$$

$$\tilde{D}_{v,N-2}^4 := D_{v,N-2}^4 \Phi_{N-2}^{-1}, \quad (2.45b)$$

$$\tilde{D}_{\eta,N-2}^2 := D_{\eta,N-2}^2 \Psi_{N-2}^{-1}. \quad (2.45c)$$

### Galerkin Method

In the Galerkin method, the basis functions are used as the test functions, i.e.:

$$w_i(\mathbf{x}) = \Gamma_i(\mathbf{x}). \quad (2.46)$$

The residual function,  $R$ , can be expressed as a truncated series like any other function of  $\mathbf{x}$ :

$$R(\mathbf{x}; a_0, a_1, \dots, a_N) = \sum_{n=0}^N r_n(a_0, a_1, \dots, a_N) \Gamma_n(\mathbf{x}), \quad (2.47)$$

where the spectral coefficients are given by:

$$r_n = \langle \Gamma_n, R \rangle. \quad (2.48)$$

The Galerkin method employs the error distribution principle. This means that  $R(\mathbf{x})$  should be small in the sense that its first  $(N + 1)$  spectral coefficients be zero, i.e.:

$$r_n = 0, \quad n = 0, 1, \dots, N. \quad (2.49)$$

Using the definition of the residual function in (2.16), the MWR condition in (2.29) and the choice of test function in (2.46), yields an equation of the form:

$$\langle \Gamma_i, L \mathbf{u}_n \rangle - \langle \Gamma_i, \mathbf{f} \rangle = 0, \quad (2.50)$$

which, when substituting in (2.14) becomes:

$$\underbrace{\langle \Gamma_i, L(\Gamma_j) \rangle}_{\tilde{L}_{i,j}} a_j = \underbrace{\langle \Gamma_i, \mathbf{f} \rangle}_{\tilde{F}_i}, \quad (2.51)$$

where  $\tilde{L}$  is the discretised linear operator matrix,  $\tilde{F}$  is the discretised vector, and subscripts  $i,j$  are matrix row and column indices respectively. Note here that unlike for the collocation method, the basis functions  $\Gamma(\mathbf{x})$  are not discretised on a

grid and are instead kept continuous. This means that the integrals in (2.51) can be evaluated analytically.

In applying the Galerkin method to the Orr-Sommerfeld Squire equations, where in this case two basis function sets are used, the basis  $\Phi$  will be used as test functions when discretising wall-normal velocity and the basis  $\Psi$  will be used as test functions when discretising wall-normal vorticity. Using the formula in (2.51), the operators from (2.23) discretised via the Galerkin method are as follows:

$$\tilde{\mathbf{E}}_{11[i,j]} = \langle \phi_i, \hat{\nabla}^2(\phi_j) \rangle = \int_{-1}^1 [\phi_i(y) \cdot \hat{\nabla}^2(\phi_j(y))] dy, \quad (2.52a)$$

$$\tilde{\mathbf{E}}_{22[i,j]} = \langle \psi_i, \psi_j \rangle = \int_{-1}^1 [\psi_i(y) \cdot \psi_j(y)] dy. \quad (2.52b)$$

$$\tilde{\mathbf{A}}_{11[i,j]} = \langle \phi_i, A_{11}(\phi_j) \rangle = \int_{-1}^1 [\phi_i(y) \cdot A_{11}(\phi_j(y))] dy, \quad (2.52c)$$

$$\tilde{\mathbf{A}}_{21[i,j]} = \langle \psi_i, A_{21}(\phi_j) \rangle = \int_{-1}^1 [\psi_i(y) \cdot A_{21}(\phi_j(y))] dy, \quad (2.52d)$$

$$\tilde{\mathbf{A}}_{22[i,j]} = \langle \psi_i, A_{22}(\psi_j) \rangle = \int_{-1}^1 [\psi_i(y) \cdot A_{22}(\psi_j(y))] dy, \quad (2.52e)$$

where integrals are evaluated on  $y \in [-1, 1]$  because these are the locations of the channel walls. In practice, the integrations are performed numerically rather than analytically, using Clenshaw-Curtis quadrature [105]. Because there is no restriction on the number of grid points used to discretise the basis functions in order to perform the integration, this does not effect the accuracy of this method. The fully discretised system matrices for this method of wall-normal discretisation are as follows:

$$\mathbf{x} = \begin{bmatrix} \mathbf{a}_{\mathbf{vN}}(t) \\ \mathbf{a}_{\eta\mathbf{N}}(t) \end{bmatrix}, \quad (2.53a)$$

$$E = \begin{bmatrix} \tilde{\mathbf{E}}_{11} & 0 \\ 0 & \tilde{\mathbf{E}}_{22} \end{bmatrix}, \quad (2.53b)$$

$$A = \begin{bmatrix} \tilde{\mathbf{A}}_{11} & 0 \\ \tilde{\mathbf{A}}_{21} & \tilde{\mathbf{A}}_{22} \end{bmatrix}. \quad (2.53c)$$

Unlike for the collocation method, rows and columns do not need to be removed from any of the system matrices in order for the  $E$ -matrix to be invertible. As for the collocation method, the states can be transformed back from Chebyshev spectral coefficients to wall-normal velocity and vorticity Fourier coefficients. However, this would mean discretising the basis functions on a set of grid points and losing the accuracy gained by keeping them continuous. For this reason, all Galerkin discretised systems will keep spectral coefficients as states.

### 2.2.3 Spectra and Pseudospectra

For LTI systems of the form shown in (2.1), the system dynamics matrix is defined as:  $E^{-1}A$ . Therefore, the dynamics matrix of the Orr-Sommerfeld Squire system from (2.13), once fully discretised, is  $\mathbb{L}$ . The eigenvalues (spectra)  $\lambda \in \mathbb{C}$  of a LTI system's dynamics matrix provide information regarding the local stability of that system for time  $t \rightarrow \infty$ . A continuous-time system is locally stable if the real part of all eigenvalues of its dynamics matrix are negative. Local stability implies that the values of the system's states  $\mathbf{x}$  will tend to zero for  $t \rightarrow \infty$ . For channel flow, all modes  $(\alpha, \beta)$  remain locally stable up until the critical Reynolds number  $\text{Re}_C = 5772.2$  [88]. At this Reynolds number, mode  $(\alpha = 1.02, \beta = 0)$  becomes locally unstable [88]. However, local instability of certain modes is not an adequate explanation for transition because flows have been observed to transition to turbulence at much lower Reynolds numbers [99].

For systems such as linear channel flow which have a highly non-normal dynamics matrix [99], large transient energy growth is possible for time  $t > 0$ . The  $\epsilon$ -*pseudospectrum* of the dynamics matrix is a way of visualising the behaviour of the system in its transient period [106]. The  $\epsilon$ -*pseudospectrum* of a matrix  $M$  is the subset of the complex plane:

$$\Lambda_\epsilon(M) = \{s \in \mathbb{C} : \|(sI - M)^{-1}\|_2 \geq \epsilon^{-1}\}, \quad (2.54)$$

where  $\|\cdot\|_2$  is the 2-norm. If the  $\epsilon$ -*pseudospectra* of a system project into the unstable right half plane, i.e.  $\Re(s) > 0$ , then transient growth is possible for time  $t > 0$ . It is thought that it is due to large transient energy growth in certain modes that subcritical Reynolds number flows transition to turbulence via bypass mechanisms [99].

Analysis of system spectra and  $\epsilon$ -*pseudospectra* is carried out in Chapter 4 in order to evaluate the performance of controllers. However, in this chapter, the spectra and  $\epsilon$ -*pseudospectra* of  $\mathbb{L}$  will be used to validate the collocation and Galerkin discretised models. Figure 2.1 contains plots of spectra and contours of  $\epsilon$ -*pseudospectra* of the dynamics matrix  $\mathbb{L}$  for wavenumber pair  $(\alpha = 1, \beta = 1)$ , Reynolds number  $\text{Re} = 1000$ , for both the collocation and Galerkin discretised models, for two wall-normal resolutions -  $N_y = 20$  and  $N_y = 50$ . At the lower resolution, it is apparent that the spectra and  $\epsilon$ -*pseudospectra* of each model are very different to each other. However, at the higher resolution it can be seen that both models have converged as the spectra and  $\epsilon$ -*pseudospectra* of both models are near identical. This suggests that the collocation and Galerkin discretised models will have similar open-loop dynamics for suitably high resolutions.

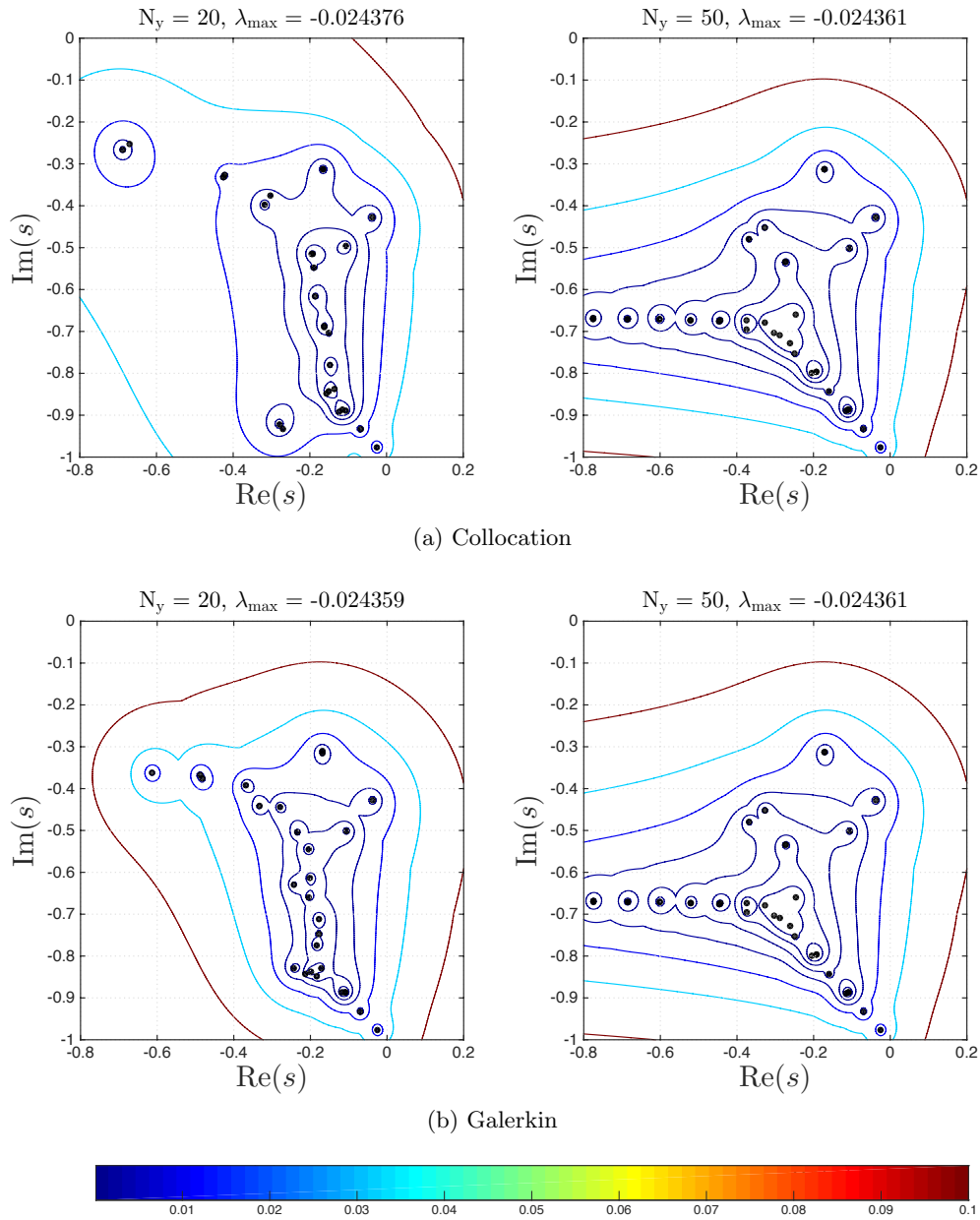


Figure 2.1: Spectra (black dots) and  $\epsilon$ -pseudospectra (coloured contours) for Orr-Sommerfeld Squire dynamics matrix  $\mathbb{L}$ , for wavenumber pair  $(\alpha = 1, \beta = 1)$ ,  $\text{Re} = 1000$ .

### 2.2.4 Incorporating Wall Actuation

All controllers novel to this thesis will use the wall-normal component of velocity at each wall as actuation. This is referred to as wall transpiration. Unfortunately it is not possible to implement this actuation directly into the state-space model developed so far due to the need to have homogenous boundary conditions at the walls in order for the  $E$ -matrix to be invertible. Instead, a lifting procedure similar to that used by McKernan et al. [87] is implemented. This transforms what would have been a homogenous equation with inhomogeneous boundary conditions into an inhomogeneous equation with homogeneous boundary conditions. Using the lifting procedure, the wall-normal velocity vector for a given Fourier mode  $(\alpha, \beta)$  is represented as:

$$\hat{v}(y, t) = \hat{v}_0(y, t) + \hat{v}_{+1}(t)f_u(y) + \hat{v}_{-1}(t)f_l(y), \quad (2.55)$$

where  $\hat{v}_0$  is the homogeneous wall-normal velocity,  $\hat{v}_{+1}$  and  $\hat{v}_{-1}$  are the values of wall-normal velocity at the upper and lower walls respectively, and  $f_u$  and  $f_l$  are lifting functions for the upper and lower walls respectively. The lifting functions can be any function of  $y$  as long as they satisfy the following boundary conditions:

$$f_u(+1) = f_l(-1) = 1, \quad (2.56a)$$

$$f_u(-1) = f_l(+1) = f'_u(\pm 1) = f'_l(\pm 1) = 0. \quad (2.56b)$$

Polynomial lifting functions which satisfy these boundary conditions and which are used throughout the current work are:

$$f_u(y) = \frac{1}{4} (2y^4 - y^3 - 4y^2 + 3y + 4), \quad (2.57a)$$

$$f_l(y) = \frac{1}{4} (2y^4 + y^3 - 4y^2 - 3y + 4). \quad (2.57b)$$

Inserting (2.55) into (2.27a), wall-normal velocity can now be approximated as:

$$\hat{v}_{\alpha, \beta}(y, t) \approx \sum_{n_y=0}^{N_y-2} a_{v_0, n_y}(t) \phi_{n_y}(y) + \hat{v}_{+1}(t)f_u(y) + \hat{v}_{-1}(t)f_l(y), \quad (2.58)$$

where two spectral coefficients/basis functions have been removed from the homogeneous part in order that the dimension of the discretised system remain  $(N_y + 1)$ . Note that if the collocation method is used for wall-normal discretisation,  $y_j$  should be used instead of  $y$ .

For the the Galerkin discretised system, the wall-normal velocity dynamics in-

cluding actuation are now:

$$\tilde{\mathbf{E}}_{11,0}\dot{\mathbf{a}}_{\mathbf{v}_0,N-2} + \tilde{\mathbf{E}}_{11,u}\dot{\hat{\mathbf{v}}}_{+1} + \tilde{\mathbf{E}}_{11,l}\dot{\hat{\mathbf{v}}}_{-1} = \tilde{\mathbf{A}}_{11,0}\mathbf{a}_{\mathbf{v}_0,N-2} + \tilde{\mathbf{A}}_{11,u}\hat{\mathbf{v}}_{+1} + \tilde{\mathbf{A}}_{11,l}\hat{\mathbf{v}}_{-1}, \quad (2.59)$$

where the subscripts 0, u and l refer to discretisation via the homogeneous, upper or lower basis functions respectively, and  $\dot{\cdot}$  denotes differentiation with respect to time. For the collocation discretised system, the wall-normal velocity dynamics are now:

$$\tilde{\nabla}_v^2 \left( \dot{\hat{\mathbf{v}}}_0 + \dot{\hat{\mathbf{v}}}_{+1}f_u + \dot{\hat{\mathbf{v}}}_{-1}f_l \right) = \tilde{\mathbf{A}}_{11} (\hat{\mathbf{v}}_0 + \hat{\mathbf{v}}_{+1}f_u + \hat{\mathbf{v}}_{-1}f_l). \quad (2.60)$$

The time-dynamics of the actuators are modelled using simple low-pass filters. In the frequency-domain, a low-pass filter for the current system is represented as a first-order transfer function from the control signal to the upper wall  $q_u$ , for example, to the wall-normal velocity at the upper wall  $\hat{\mathbf{v}}_{+1}$ , i.e.:

$$\hat{\mathbf{v}}_{+1}(s) = \frac{1}{\tau_\phi s + 1} q_u(s), \quad (2.61)$$

where  $\tau_\phi$  is the actuator time-constant. When  $\tau_\phi$  is small, the actuator has fast dynamics and conversely if  $\tau_\phi$  is large the actuator has slow dynamics. Performing an inverse-Laplace transform on (2.61), it can easily be shown that in the time-domain, the low-pass filter becomes:

$$\dot{\hat{\mathbf{v}}}_{+1}(t) = -\frac{1}{\tau_\phi}\hat{\mathbf{v}}_{+1}(t) + \frac{1}{\tau_\phi}q_u(t), \quad (2.62)$$

and similarly for the lower wall. Now that these actuator dynamics are introduced, note that the following initial conditions are always prescribed to the upper and lower walls:

$$\hat{\mathbf{v}}_{+1}(0) = \hat{\mathbf{v}}_{-1}(0) = 0. \quad (2.63)$$

Substituting (2.62) and a similar expression for the lower wall into (2.59) and inverting the homogeneous Laplacian results in the final **Galerkin** discretised wall-actuated system:

$$\begin{aligned} \dot{\mathbf{a}}_{\mathbf{v}_0,N-2} = & \underbrace{\tilde{\mathbf{E}}_{11,0}^{-1}\tilde{\mathbf{A}}_{11,0}}_{\Theta_{11}} \mathbf{a}_{\mathbf{v}_0,N-2} + \underbrace{\tilde{\mathbf{E}}_{11,0}^{-1} \left( \tilde{\mathbf{A}}_{11,u} + \frac{1}{\tau_\phi}\tilde{\mathbf{E}}_{11,u} \right)}_{\Theta_{12}} \hat{\mathbf{v}}_{+1} \\ & + \underbrace{\tilde{\mathbf{E}}_{11,0}^{-1} \left( \tilde{\mathbf{A}}_{11,l} + \frac{1}{\tau_\phi}\tilde{\mathbf{E}}_{11,l} \right)}_{\Theta_{13}} \hat{\mathbf{v}}_{-1} \\ & - \underbrace{\frac{1}{\tau_\phi}\tilde{\mathbf{E}}_{11,0}^{-1}\tilde{\mathbf{E}}_{11,u}}_{\Gamma_{11}} q_u - \underbrace{\frac{1}{\tau_\phi}\tilde{\mathbf{E}}_{11,0}^{-1}\tilde{\mathbf{E}}_{11,l}}_{\Gamma_{12}} q_l. \end{aligned} \quad (2.64)$$

These dynamical equations can be represented in matrix form as:

$$\frac{\partial}{\partial t} \underbrace{\begin{bmatrix} \mathbf{a}_{\mathbf{v}_0, N-2} \\ \hat{v}_{+1} \\ \hat{v}_{-1} \end{bmatrix}}_{\tilde{\mathbf{a}}_{\mathbf{v}, N}} = \underbrace{\begin{bmatrix} \Theta_{11} & \Theta_{12} & \Theta_{13} \\ 0 & -\frac{1}{\tau_\phi} & 0 \\ 0 & 0 & -\frac{1}{\tau_\phi} \end{bmatrix}}_{\Theta_v} \underbrace{\begin{bmatrix} \mathbf{a}_{\mathbf{v}_0, N-2} \\ \hat{v}_{+1} \\ \hat{v}_{-1} \end{bmatrix}}_{\tilde{\mathbf{a}}_{\mathbf{v}, N}} + \underbrace{\begin{bmatrix} \Gamma_{11} & \Gamma_{12} \\ \frac{1}{\tau_\phi} & 0 \\ 0 & \frac{1}{\tau_\phi} \end{bmatrix}}_{\Gamma_v} \underbrace{\begin{bmatrix} q_u \\ q_l \end{bmatrix}}_{\mathbf{u}}, \quad (2.65)$$

where the input vector  $\mathbf{u}$  is defined as the control signals to the upper and lower walls. The complete system inclusive of wall-normal vorticity can be expressed in matrix form as:

$$\frac{\partial}{\partial t} \underbrace{\begin{bmatrix} \tilde{\mathbf{a}}_{\mathbf{v}, N} \\ \mathbf{a}_{\eta, N} \end{bmatrix}}_{\mathbf{x}} = \underbrace{\begin{bmatrix} \Theta_v & 0 \\ \tilde{\mathbf{A}}_{21}^* & \tilde{\mathbf{A}}_{22} \end{bmatrix}}_A \underbrace{\begin{bmatrix} \tilde{\mathbf{a}}_{\mathbf{v}, N} \\ \mathbf{a}_{\eta, N} \end{bmatrix}}_{\mathbf{x}} + \underbrace{\begin{bmatrix} \Gamma_v \\ 0 \end{bmatrix}}_B \mathbf{u}, \quad (2.66)$$

where  $\tilde{\mathbf{A}}_{21}^*$  highlights that this operator matrix is now discretised with the set of basis functions that include the lifting functions.

Substituting (2.62) and a similar expression for the lower wall into (2.60) and inverting the homogeneous Laplacian results in the final **collocation** discretised wall-actuated system:

$$\begin{aligned} \dot{\hat{v}}_0 = & \underbrace{(\tilde{\nabla}_0^2)^{-1} \tilde{A}_{110}}_{\bar{\Theta}_{11}} \hat{v}_0 + \underbrace{(\tilde{\nabla}_0^2)^{-1} \left( \tilde{A}_{11} f_u + \frac{1}{\tau_\phi} \tilde{\nabla}^2 f_u \right)}_{\bar{\Theta}_{12}} \hat{v}_{+1} \\ & + \underbrace{(\tilde{\nabla}_0^2)^{-1} \left( \tilde{A}_{11} f_l + \frac{1}{\tau_\phi} \tilde{\nabla}^2 f_l \right)}_{\bar{\Theta}_{13}} \hat{v}_{-1} \\ & - \underbrace{\frac{1}{\tau_\phi} (\tilde{\nabla}_0^2)^{-1} \tilde{\nabla}^2 f_u}_{\bar{\Gamma}_{11}} q_u - \underbrace{\frac{1}{\tau_\phi} (\tilde{\nabla}_0^2)^{-1} \tilde{\nabla}^2 f_l}_{\bar{\Gamma}_{12}} q_l, \end{aligned} \quad (2.67a)$$

where subscript  $_0$  denotes that the operator/vector has homogeneous boundary conditions imposed. In matrix form, these dynamical equations become:

$$\frac{\partial}{\partial t} \underbrace{\begin{bmatrix} \hat{v}_0 \\ \hat{v}_{+1} \\ \hat{v}_{-1} \end{bmatrix}}_{\hat{\mathbf{v}}} = \underbrace{\begin{bmatrix} \bar{\Theta}_{11} & \bar{\Theta}_{12} & \bar{\Theta}_{13} \\ 0 & -\frac{1}{\tau_\phi} & 0 \\ 0 & 0 & -\frac{1}{\tau_\phi} \end{bmatrix}}_{\bar{\Theta}_v} \underbrace{\begin{bmatrix} \hat{v}_0 \\ \hat{v}_{+1} \\ \hat{v}_{-1} \end{bmatrix}}_{\hat{\mathbf{v}}} + \underbrace{\begin{bmatrix} \bar{\Gamma}_{11} & \bar{\Gamma}_{12} \\ \frac{1}{\tau_\phi} & 0 \\ 0 & \frac{1}{\tau_\phi} \end{bmatrix}}_{\bar{\Gamma}_v} \underbrace{\begin{bmatrix} q_u \\ q_l \end{bmatrix}}_{\mathbf{u}}. \quad (2.68)$$

The complete system inclusive of the wall-normal vorticity dynamics is then:

$$\frac{\partial}{\partial t} \underbrace{\begin{bmatrix} \hat{v} \\ \hat{\eta} \end{bmatrix}}_{\mathbf{x}} = \underbrace{\begin{bmatrix} \bar{\Theta}_v & 0 \\ \tilde{A}_{21} & \tilde{A}_{22} \end{bmatrix}}_A \underbrace{\begin{bmatrix} \hat{v} \\ \hat{\eta} \end{bmatrix}}_{\mathbf{x}} + \underbrace{\begin{bmatrix} \bar{\Gamma}_v \\ 0 \end{bmatrix}}_B \mathbf{u}. \quad (2.69)$$

The new definitions of the state vector  $\mathbf{x}$ , dynamics matrix  $A$ , input matrix  $B$  and input signal vector  $\mathbf{u}$  will be used throughout the rest of this thesis unless stated otherwise. The fully-discretised state-space models of channel flow with wall-normal forcing at the boundaries incorporated in (2.66) and (2.69) will form the basis for all novel controllers developed in this thesis.

# Chapter 3

## Simulation

### 3.1 Introduction

Computational fluid dynamics (CFD) is the field of engineering concerned with the simulation of fluid flows. As the processing power and memory capacities of computers/supercomputers has grown, CFD has been able to simulate ever more complex flows and thus is now a useful tool both in academia and industry for the study of such flows. The three main CFD methodologies used currently are:

- Reynolds-Averaged Navier Stokes (RANS)
- Large Eddy Simulation (LES)
- Direct Numerical Simulation (DNS)

These all differ on how they deal with the *turbulence closure problem* inherent in the Navier-Stokes equations [90]. The RANS method involves separating the velocity field into a Reynolds-averaged part (an ensemble average in time) and a fluctuating part, simulating only the Reynolds-averaged part and using a closure model for the un-simulated fluctuating part. The LES method separates the velocity field into large scales and small scales, simulates only the large scales and uses a closure model for the un-simulated small scales. DNS simulates all scales of the flow and therefore does not require a closure model; it is for this reason why it is the most accurate of the three. However, DNS is by far the most computationally expensive method, followed by LES, and RANS is the least computationally expensive. For anything other than simple canonical flows such as channel flow, DNS is prohibitively expensive and is rarely used. LES methods are now maturing to the extent that they are being used to simulate flows around complex geometries such as aircraft and compressible flow from supersonic jets. However, in the current work, DNS can be used to simulate low Reynolds number incompressible turbulent channel flow due to the simplicity of the geometry and boundary conditions employed. More information about all three CFD methods can be found in Pope [90]. High-fidelity DNS is used to evaluate controllers in Chapters 4 and 5, and will be discussed further in the following.

### 3.2 Direct Numerical Simulation of Channel Flow

Throughout this work there is a need to simulate turbulent channel flow with wall-actuation determined by a controller which in turn takes in flow measurements via wall sensors. To fill this need a modified version of the open-source DNS program *Channelflow* written by J. F. Gibson [41, 42] is used throughout. The code is modified by the author to allow for general inhomogeneous boundary conditions at the walls. *Channelflow* uses (Fourier  $\times$  Chebyshev-collocation  $\times$  Fourier) spectral discretisation in the streamwise, wall-normal and spanwise directions respectively. An algorithm based on the influence-matrix method [69] is used to integrate the incompressible Navier-Stokes equations forward in time using primitive variables. The code includes an array of different time-marching schemes, flow constraints and nonlinearity computation schemes, and can be used to simulate both plane channel flow and Couette flow. In this section, the procedure by which *Channelflow* integrates the Navier-Stokes equations forward in time will be outlined. It will also be shown how general inhomogeneous boundary conditions were implemented in the code.

Starting with the incompressible Navier-Stokes equations for the domain  $\Omega : [0, L_x] \times [-1, 1] \times [0, L_z]$ :

$$\frac{\partial \mathbf{V}}{\partial t} + \mathbf{V} \cdot \nabla \mathbf{V} = -\nabla P + \frac{1}{\text{Re}} \nabla^2 \mathbf{V} \quad (3.1a)$$

$$\nabla \cdot \mathbf{V} = 0, \quad (3.1b)$$

with initial and boundary conditions:

$$\mathbf{V}(\chi, 0) = \mathbf{V}_0(\chi) \quad \forall \chi \in \Omega, \quad (3.2a)$$

$$\mathbf{V}(\chi, t) = \mathbf{g}(\chi, t) \quad \forall (\chi, t) \in \partial\Omega \times [0, t_f], \quad (3.2b)$$

where  $\mathbf{V} : \Omega \times \mathbb{R}_+ \rightarrow \mathbb{R}^3$  is the total velocity vector field,  $P : \Omega \times \mathbb{R}_+ \rightarrow \mathbb{R}$  is the total pressure scalar field,  $\mathbf{V}_0 \in \mathbb{R}^3$  is an initial velocity vector for time  $t = 0$ ,  $\mathbf{g} : \partial\Omega \times \mathbb{R}_+ \rightarrow \mathbb{R}^3$  is a vector of boundary conditions, and  $\text{Re} := U_{cl}^* h^* / \nu^*$ . The endpoint of the time interval is  $t_f \in \mathbb{R}_+$ ,  $\Omega \subset \mathbb{R}^3$  is a domain in three spatial dimensions with boundary  $\partial\Omega$ , and  $\chi \in \Omega$  is a point within the domain. The boundary conditions vector  $\mathbf{g}$  is chosen such that:

$$\mathbf{V}(x, \pm 1, z, t) = 0, \quad (3.3a)$$

$$\mathbf{V}(x + L_x, y, z, t) = \mathbf{V}(x, y, z, t), \quad (3.3b)$$

$$\mathbf{V}(x, y, z + L_z, t) = \mathbf{V}(x, y, z, t), \quad (3.3c)$$

which amounts to Dirichlet boundary conditions at the walls and periodic boundary conditions in the streamwise and spanwise directions.

The total velocity and pressure fields are decomposed into constant and fluctuating parts such that:

$$\mathbf{V}(\chi, t) = \tilde{U}(y)\mathbf{e}_x + \mathbf{v}(\chi, t), \quad (3.4a)$$

$$P(\chi, t) = \frac{\partial \tilde{P}}{\partial x}(t)x + p(\chi, t), \quad (3.4b)$$

$$\nabla P(\chi, t) = \frac{\partial \tilde{P}}{\partial x}(t)\mathbf{e}_x + \nabla p(\chi, t), \quad (3.4c)$$

where  $\tilde{U}(y)$  is the time-independent base velocity field,  $\mathbf{v} : \Omega \times \mathbb{R}_+ \rightarrow \mathbb{R}^3$  is the fluctuating velocity field,  $\frac{\partial \tilde{P}}{\partial x}$  is the base pressure gradient (also referred to as the spatial mean pressure gradient),  $p : \Omega \times \mathbb{R}_+ \rightarrow \mathbb{R}$  is the fluctuating pressure field, and  $\mathbf{e}_x$  is a unit vector in the streamwise direction.

In order for the the integration of the Navier-Stokes equations be solvable for a channel flow, either the bulk velocity or mean pressure gradient must be externally constrained, with the other being a dependent variable; the choice is up to the user. This ensures that net acceleration of the flow is zero. In the current work, bulk velocity will always be kept constant and the pressure gradient will be left as a dependent variable. Bulk velocity is defined:

$$U_{\text{bulk}} := \frac{1}{2L_x L_z} \int_0^{L_x} \int_{-1}^1 \int_0^{L_z} \tilde{U}(y) + \overline{u(\chi)} dx dy dz, \quad (3.5)$$

where  $\bar{u}$  is the mean streamwise perturbation velocity profile.

Substituting (3.4a) and (3.4c) into (3.1) yields:

$$\frac{\partial \mathbf{v}}{\partial t} + \nabla p = \underbrace{\frac{1}{\text{Re}} \nabla^2 \mathbf{v}}_{\mathbf{L}\mathbf{v}} - \underbrace{\mathbf{v} \cdot \nabla \mathbf{v}}_{\mathbf{N}(\mathbf{v})} + \underbrace{\left[ \frac{1}{\text{Re}} \frac{\partial^2 \tilde{U}}{\partial y^2} - \frac{\partial \tilde{P}}{\partial x} \right]}_{\mathbf{C}} \mathbf{e}_x, \quad (3.6a)$$

$$\nabla \cdot \mathbf{v} = 0. \quad (3.6b)$$

where  $\mathbf{L}$  is the linear operator,  $\mathbf{N}(\mathbf{v})$  is the nonlinear term and  $\mathbf{C}$  is the constant term. Note that  $\mathbf{C}$  is constant in  $\mathbf{v}$  but may vary in time if the mean pressure gradient is not externally constrained. There are a number of different forms for the nonlinear term that are identical in the continuous case, but differ somewhat

when discretised. Four notable examples are:

$$\mathbf{N}(\mathbf{v}) := \begin{cases} \mathbf{V} \cdot \nabla \mathbf{V} & \text{Convection} \\ \nabla(\mathbf{V} \cdot \mathbf{V}) & \text{Divergence} \\ \frac{1}{2} \mathbf{V} \cdot \nabla \mathbf{V} + \frac{1}{2} \nabla(\mathbf{V} \cdot \mathbf{V}) & \text{Skew-symmetric} \\ \tilde{U} \frac{\partial \mathbf{v}}{\partial x} + v \frac{\partial \tilde{U}}{\partial y} \mathbf{e}_x & \text{Linearised} \end{cases} \quad (3.7)$$

The linearised case has been included in order to show what  $\mathbf{N}(\mathbf{v})$  becomes when nonlinear terms are excluded. It can be seen from (3.7) that the skew-symmetric form of the nonlinearity is the mean of the convection and divergence forms. Calculating the nonlinearity this way is expensive to compute but results in less errors at the higher spatial frequencies once discretised [114]. It is for this reason why the nonlinearity will be computed in this way for all simulations in the current thesis.

The domain is discretised using the following uniform grid in the streamwise direction:

$$x_j = \frac{jL_x}{N_x} \quad j = 0, 1, \dots, N_x - 1, \quad (3.8)$$

and similarly in the spanwise direction:

$$z_j = \frac{jL_z}{N_z} \quad j = 0, 1, \dots, N_z - 1, \quad (3.9)$$

where  $N_x$  and  $N_z$  are the number of grid points in the streamwise and spanwise directions respectively. The dependent variables have discrete Fourier representations of the form:

$$\mathbf{v}(x, y, z, t) \approx \sum_{k_x=-N_x/2}^{N_x/2-1} \sum_{k_z=-N_z/2}^{N_z/2-1} \hat{\mathbf{v}}_{\mathbf{k}_x, \mathbf{k}_z}(y, t) e^{2\pi i(k_x x/L_x + k_z z/L_z)}, \quad (3.10)$$

and similarly for pressure. The wall-normal direction is discretised using staggered grids of Chebyshev-Gauss-Lobatto points:

$$y_j = \cos \frac{\pi j}{N_y} \quad j = 0, 1, \dots, N_y, \quad (3.11a)$$

$$y_{j+1/2} = \cos \frac{\pi (j + \frac{1}{2})}{N_y} \quad j = 0, 1, \dots, N_y - 1, \quad (3.11b)$$

for velocity and pressure respectively. The continuity equation (3.1b) is enforced at the half-points given by (3.11b). If the same collocation points are used for the pressure and the continuity equation as for the velocity and momentum equation, then the linear system for the discrete dependent variables is undetermined [20].

In the wall-normal direction, velocity is represented as a truncated Chebyshev series:

$$\hat{\mathbf{v}}_{\mathbf{k}_x, \mathbf{k}_z}(y, t) \approx \sum_{m=0}^{N_y} \tilde{\mathbf{v}}_{\mathbf{k}_x, \mathbf{k}_z, m}(t) T_m(y), \quad (3.12)$$

and similarly, pressure is represented as:

$$\hat{p}_{\mathbf{k}_x, \mathbf{k}_z}(y, t) \approx \sum_{m=0}^{N_y-1} \tilde{p}_{\mathbf{k}_x, \mathbf{k}_z, m}(t) T_m(y), \quad (3.13)$$

where  $T_m$  is the  $m^{\text{th}}$  Chebyshev polynomial of the first kind.

For the time being, the wall-normal direction will be kept continuous and only the streamwise and spanwise directions of the flow shall be discretised via (3.10). Discretised in this manner, (3.6) becomes:

$$\frac{\partial \hat{\mathbf{v}}}{\partial t} + \hat{\nabla} \hat{p} = \hat{\mathbf{L}} \hat{\mathbf{v}} - \widehat{\mathbf{N}(\mathbf{v})} + \hat{\mathbf{C}}, \quad (3.14a)$$

where:

$$\hat{\nabla} := \frac{2\pi i k_x}{L_x} \mathbf{e}_x + \frac{\partial}{\partial y} \mathbf{e}_y + \frac{2\pi i k_z}{L_z} \mathbf{e}_z, \quad (3.15a)$$

$$\hat{\nabla}^2 := \frac{\partial^2}{\partial y^2} - 4\pi^2 \left( \frac{k_x^2}{L_x^2} + \frac{k_z^2}{L_z^2} \right), \quad (3.15b)$$

$$\hat{\mathbf{L}} := \frac{1}{\text{Re}} \hat{\nabla}^2, \quad (3.15c)$$

and  $_{\mathbf{k}_x, \mathbf{k}_z}$  notation is now suppressed.

### 3.2.1 Time-Stepping Algorithm

*Channelflow* offers a number of different time-stepping algorithms in order to discretise time. The scheme used in all simulations carried out for this thesis is the 3rd order Semi-implicit Backward Differentiation formula (SBDF3); alternatively named as an Adams-Bashforth/Backward differentiation scheme [89]. This scheme produces strong damping for high spatial-frequency modes and results in equally accurate pressure and velocity fields. SBDF3 treats the linear terms implicitly and the nonlinear term explicitly.

Applying SBDF3 to (3.14a) yields an update equation for each wavenumber index pair  $(\mathbf{k}_x, \mathbf{k}_z)$  of the form [89]:

$$\left( \frac{11}{16\Delta t} - \hat{\mathbf{L}} \right) \hat{\mathbf{v}}^{n+1} + \hat{\nabla} \hat{p}^{n+1} = \frac{1}{\Delta t} \left( 3\hat{\mathbf{v}}^n - \frac{3}{2}\hat{\mathbf{v}}^{n-1} + \frac{1}{3}\hat{\mathbf{v}}^{n-2} \right) - 3\hat{\mathbf{N}}^n + 3\hat{\mathbf{N}}^{n-1} - \hat{\mathbf{N}}^{n-2} + \hat{\mathbf{C}}^n, \quad (3.16)$$

where  $\hat{\mathbf{N}}^m = \widehat{\mathbf{N}(\mathbf{v}^m)}$  is the Fourier component of the calculated nonlinearity at time level  $m$ . Expanding  $\hat{\mathbf{L}}$  on the left hand side of (3.16) yields:

$$\frac{1}{\text{Re}} \hat{\mathbf{v}}'^{m+1} - \lambda \hat{\mathbf{v}}^{n+1} - \hat{\nabla} \hat{\mathbf{p}}^{n+1} = -\hat{\mathbf{R}}, \quad (3.17)$$

where:

$$\lambda = \frac{11}{16\Delta t} + \frac{4\pi^2}{\text{Re}} \left( \frac{k_x^2}{L_x^2} + \frac{k_z^2}{L_z^2} \right), \quad (3.18a)$$

$$\hat{\mathbf{R}} = \frac{1}{\Delta t} \left( 3\hat{\mathbf{v}}^n - \frac{3}{2}\hat{\mathbf{v}}^{n-1} + \frac{1}{3}\hat{\mathbf{v}}^{n-2} \right) - 3\hat{\mathbf{N}}^n + 3\hat{\mathbf{N}}^{n-1} - \hat{\mathbf{N}}^{n-2} + \hat{\mathbf{C}}^n, \quad (3.18b)$$

$$\hat{\mathbf{v}}'' = \frac{\partial}{\partial y^2} \hat{\mathbf{v}}. \quad (3.18c)$$

The above scheme requires flow fields at time levels  $n - 2$ ,  $n - 1$  and  $n$ . Therefore, another time-stepping scheme is needed initially to provide these two extra flow fields from the initial condition. In the current work, a semi-implicit 2nd-order Crank-Nicolson, Runge-Kutta algorithm [89] is used to perform the initialisation.

Therefore, dropping time level notation, the system of equations that need to be solved at each time step are as follows:

$$\frac{1}{\text{Re}} \hat{\mathbf{v}}'' - \lambda \hat{\mathbf{v}} - \hat{\nabla} \hat{\mathbf{p}} = -\hat{\mathbf{R}}, \quad (3.19a)$$

$$\hat{\nabla} \cdot \hat{\mathbf{v}} = 0, \quad (3.19b)$$

$$\hat{\mathbf{v}}(\pm 1) = 0. \quad (3.19c)$$

It can be seen that (3.19a) is a one-dimensional Helmholtz equation. This system is solved using the influence-matrix method, outlined in the following section.

### 3.2.2 The Influence-Matrix Method

In this section, the influence-matrix method of Kleiser and Schumann [69] will be derived which solves the system of equations in (3.19). The derivation is based on that by Canuto et al. [20]. Kleiser and Schumann solve the system of equations in (3.19) by solving a sequence of one-dimensional Helmholtz equations. Information on solution procedures for one-dimensional Helmholtz equations can be found in Peyret [89]. Note that the wall-normal direction will be kept continuous for the first half of this derivation.

Taking the divergence of (3.19a) gives the following equation for pressure:

$$\hat{\mathbf{p}}'' - K^2 \hat{\mathbf{p}} = \hat{\nabla} \cdot \hat{\mathbf{R}}, \quad (3.20)$$

where  $K^2 = k_x^2 + k_z^2$ , with boundary conditions:

$$\hat{\nabla} \cdot \hat{\mathbf{v}}(\pm 1) = 0, \quad \text{i.e. } \hat{v}'(\pm 1) = 0. \quad (3.21)$$

The equation and boundary conditions for  $\hat{v}$  are:

$$\frac{1}{\text{Re}} \hat{v}'' - \lambda \hat{v} - \hat{p}' = -\hat{R}_y \quad \hat{v}(\pm 1) = 0, \quad (3.22)$$

and similarly for  $\hat{u}$ :

$$\frac{1}{\text{Re}} \hat{u}'' - \lambda \hat{u} - ik_x \hat{p} = -\hat{R}_x \quad \hat{u}(\pm 1) = 0, \quad (3.23)$$

and  $\hat{w}$ :

$$\frac{1}{\text{Re}} \hat{w}'' - \lambda \hat{w} - ik_z \hat{p} = -\hat{R}_z \quad \hat{w}(\pm 1) = 0. \quad (3.24)$$

Equations (3.20) - (3.22) form a complete set for  $\hat{v}$  and  $\hat{p}$ . However, they cannot be solved directly in this form, due to the boundary conditions for (3.20) not being in terms of  $\hat{p}$ . This is termed the “*A-Problem*”. To solve this problem, the inhomogeneous “*B-Problem*” must first be considered:

$$\hat{p}'' - K^2 \hat{p} = \hat{\nabla} \cdot \hat{\mathbf{R}} \quad \hat{p}(\pm 1) = \hat{p}_{b\pm}, \quad (3.25a)$$

$$\frac{1}{\text{Re}} \hat{v}'' - \lambda \hat{v} - \hat{p}' = -\hat{R}_y \quad \hat{v}(\pm 1) = 0. \quad (3.25b)$$

The pressure at the walls  $\hat{p}_{b\pm}$  is not known *a priori*, but needs to be consistent with the boundary condition in (3.21). Define  $(\hat{p}_p, \hat{v}_p)$  as the solutions of (3.25a) and (3.25b) but with homogeneous Dirichlet boundary conditions on  $\hat{p}$ . Then define  $(\hat{p}_+, \hat{v}_+)$  and  $(\hat{p}_-, \hat{v}_-)$  as the solutions of the homogeneous *B-Problems*, i.e. (3.25a) and (3.25b) with zero on the right-hand sides, with boundary conditions:  $\hat{p}_+(-1) = \hat{p}_-(+1) = 0$ ,  $\hat{p}_+(+1) = \hat{p}_-(-1) = 1$ . The solution to the *A-Problem* can then be written:

$$\begin{pmatrix} \hat{p} \\ \hat{v} \end{pmatrix} = \begin{pmatrix} \hat{p}_p \\ \hat{v}_p \end{pmatrix} + \delta_+ \begin{pmatrix} \hat{p}_+ \\ \hat{v}_+ \end{pmatrix} + \delta_- \begin{pmatrix} \hat{p}_- \\ \hat{v}_- \end{pmatrix}. \quad (3.26)$$

The boundary conditions of the *A-Problem* require:

$$\begin{pmatrix} \hat{v}'_+(+1) & \hat{v}'_-(-1) \\ \hat{v}'_+(-1) & \hat{v}'_-(-1) \end{pmatrix} \begin{pmatrix} \delta_+ \\ \delta_- \end{pmatrix} = - \begin{pmatrix} \hat{v}'_p(+1) \\ \hat{v}'_p(-1) \end{pmatrix}. \quad (3.27)$$

Therefore, (3.27) can be solved for  $\delta_{\pm}$  which can in turn be used as the boundary condition in (3.25a), i.e.  $\hat{p}_{b\pm} = \delta_{\pm}$ . The  $(2 \times 2)$  matrix on the left-hand side of (3.27) is called the *influence matrix* and is calculated once at the start of a simulation for each wavenumber pair  $(k_x, k_z)$  and stored.

To summarise, the solution procedure for the wall-normal-continuous case is as follows:

1. Calculate the influence matrix for each wavenumber index pair  $(k_x, k_z)$  before starting the simulation.
2. Find the particular solutions  $(\hat{p}_p, \hat{v}_p)$  at each time step by solving (3.25a) and (3.25b) with homogeneous Dirichlet boundary conditions.
3. Using (3.27) calculate the correct pressure boundary conditions to solve (3.25a) for  $\hat{P}$ .
4. Now Helmholtz equations (3.22), (3.23) and (3.24) can be solved for  $\hat{v}$ ,  $\hat{u}$  and  $\hat{w}$ .

Things are complicated somewhat when solving these equations with the wall-normal direction discretised because additional terms need to be added to the right-hand side of the Helmholtz equations. The *Tau-Method* shall be used to handle the discretisation of  $y$ . Using (3.12) and (3.13) to discretise velocity and pressure respectively, the tau approximation to the system of equations in (3.19) can be written as:

$$\frac{1}{\text{Re}} \tilde{u}_m^{(2)} - \lambda \tilde{u}_m - ik_x \tilde{p}_m = -\tilde{R}_{x,m} - \tilde{\tau}_{x,m} \quad m = 0, \dots, N_y, \quad (3.28a)$$

$$\hat{u}(\pm 1) = 0, \quad (3.28b)$$

$$\frac{1}{\text{Re}} \tilde{v}_m^{(2)} - \lambda \tilde{v}_m - \tilde{p}_m^{(1)} = -\tilde{R}_{y,m} - \tilde{\tau}_{y,m} \quad m = 0, \dots, N_y, \quad (3.28c)$$

$$\hat{v}(\pm 1) = 0, \quad (3.28d)$$

$$\frac{1}{\text{Re}} \tilde{w}_m^{(2)} - \lambda \tilde{w}_m - ik_z \tilde{p}_m = -\tilde{R}_{z,m} - \tilde{\tau}_{z,m} \quad m = 0, \dots, N_y, \quad (3.28e)$$

$$\hat{w}(\pm 1) = 0, \quad (3.28f)$$

$$\tilde{d}_m \equiv ik_x \tilde{u}_m + \tilde{v}_m^{(1)} + ik_z \tilde{w}_m = 0 \quad m = 0, \dots, N_y. \quad (3.28g)$$

Note that the boundary conditions are in terms of Fourier coefficients. Superscript <sup>(1)</sup> notation is now used to represent differentials with respect to  $y$ . The tau terms  $\tilde{\tau}_{x,m}$ ,  $\tilde{\tau}_{y,m}$  and  $\tilde{\tau}_{z,m}$  are included to account for errors caused by the discretisation of  $y$ , and vanish for  $0 \leq m \leq N_y - 2$ . As for the wall-normal-continuous case, an equation for pressure can be found by taking the discrete divergence of (3.28a), (3.28c) and (3.28e) yielding:

$$\frac{1}{\text{Re}} \tilde{d}_m^{(2)} - \lambda \tilde{d}_m - \tilde{p}_m^{(2)} + K^2 \tilde{p}_m = -\tilde{r}_m - (ik_x \tilde{\tau}_{x,m} + \tilde{\tau}_{y,m}^{(1)} + ik_z \tilde{\tau}_{z,m}) \quad m = 0, \dots, N_y, \quad (3.29)$$

where:

$$\tilde{r}_m = ik_x \tilde{R}_{x,m} + \tilde{R}_{y,m}^{(1)} + ik_z \tilde{R}_{z,m} \quad m = 0, \dots, N_y. \quad (3.30)$$

However, (3.28g) is equivalent to:

$$\tilde{d}_m = 0 \quad m = 0, \dots, N_y - 2, \quad (3.31a)$$

$$\hat{d}(\pm 1) = 0. \quad (3.31b)$$

Therefore, using (3.31a), (3.29) can be re-written to create the fully discrete  $A$ -Problem:

$$\tilde{p}_m^{(2)} - K^2 \tilde{p}_m = \tilde{r}_m + \tilde{\sigma}_m^{(1)} \quad m = 0, \dots, N_y - 2, \quad (3.32a)$$

$$\hat{v}'(\pm 1) = 0, \quad (3.32b)$$

$$\frac{1}{\text{Re}} \tilde{v}_m^{(2)} - \lambda \tilde{v}_m - \tilde{p}_m^{(1)} = -\tilde{R}_{y,m} - \tilde{\sigma}_m \quad m = 0, \dots, N_y, \quad (3.32c)$$

$$\hat{v}(\pm 1) = 0, \quad (3.32d)$$

where we now use  $\tilde{\sigma}_m = \tilde{\tau}_{y,m}$ . The fully discrete  $B$ -Problem is:

$$\tilde{p}_m^{(2)} - K^2 \tilde{p}_m = \tilde{r}_m + \tilde{\sigma}_m^{(1)} \quad m = 0, \dots, N_y - 2, \quad (3.33a)$$

$$\hat{p}(\pm 1) = \hat{p}_\pm, \quad (3.33b)$$

$$\frac{1}{\text{Re}} \tilde{v}_m^{(2)} - \lambda \tilde{v}_m - \tilde{p}_m^{(1)} = -\tilde{R}_{y,m} - \tilde{\sigma}_m \quad m = 0, \dots, N_y, \quad (3.33c)$$

$$\hat{v}(\pm 1) = 0. \quad (3.33d)$$

The “tau-correction” terms,  $\tilde{\sigma}_n$  and  $\tilde{\sigma}_n^{(1)}$ , complicate the solution procedure. If not for these terms, the influence-matrix method would be a straightforward application of the Helmholtz equation techniques used for the wall-normal-continuous case. To solve the fully discrete  $B$ -Problem, first define the following  $B_1$ -Problem:

$$\tilde{p}_m^{(2)} - K^2 \tilde{p}_m = \tilde{r}_m \quad m = 0, \dots, N_y - 2, \quad (3.34a)$$

$$\hat{p}(\pm 1) = \hat{p}_{b\pm}, \quad (3.34b)$$

$$\frac{1}{\text{Re}} \tilde{v}_m^{(2)} - \lambda \tilde{v}_m - \tilde{p}_m^{(1)} = -\tilde{R}_{y,m} \quad m = 0, \dots, N_y - 2, \quad (3.34c)$$

$$\hat{v}(\pm 1) = 0, \quad (3.34d)$$

and the following  $B_0$ -Problem:

$$\tilde{p}_m^{(2)} - K^2 \tilde{p}_m = \frac{2}{\bar{c}_m} m' \quad m = 0, \dots, N_y - 2, \quad (3.35a)$$

$$\hat{p}(\pm 1) = 0, \quad (3.35b)$$

$$\frac{1}{\text{Re}} \tilde{v}_m^{(2)} - \lambda \tilde{v}_m = \tilde{p}_m^{(1)} \quad m = 0, \dots, N_y - 2, \quad (3.35c)$$

$$\hat{v}(\pm 1) = 0, \quad (3.35d)$$

where,

$$m' = \begin{cases} N_y - 1 & m \text{ even} \\ N_y & m \text{ odd} \end{cases}, \quad (3.36)$$

and

$$\bar{c}_m = \begin{cases} 2 & m = 0 \text{ or } N_y \\ 1 & 1 \leq m \leq N_y - 1 \end{cases}, \quad (3.37)$$

assuming  $N_y$  is even. Furthermore, define  $\tilde{\sigma}_{1,m}$  and  $\tilde{\sigma}_{0,m}$  for  $m = N_y - 1, N_y$  as the tau-correction terms that must be added to the v-momentum equations in (3.34c) and (3.35c) respectively, for them to hold for  $m = N_y - 1, N_y$ . It can be shown that [89]:

$$\tilde{\sigma}_m = \tilde{\sigma}_{1,m}/(1 - \tilde{\sigma}_{0,m}) \quad m = N_y - 1, N_y, \quad (3.38)$$

and:

$$\tilde{p}_m = \tilde{p}_{1,m} + \tilde{\sigma}_{m'}\tilde{p}_{0,m} \quad m = 0, \dots, N_y, \quad (3.39a)$$

$$\tilde{v}_m = \tilde{v}_{1,m} + \tilde{\sigma}_{(m+1)'}\tilde{v}_{0,m} \quad m = 0, \dots, N_y. \quad (3.39b)$$

Therefore, the solution procedure to the fully-discretised problem for each wavenumber index pair  $(k_x, k_z)$  is:

1. Calculate and store the influence matrix from the left-hand side of (3.27) by first solving for  $\hat{p}_+$  and  $\hat{p}_-$  using (3.25a) with zero on the right-hand side and the appropriate boundary conditions, then using this result, calculate  $\hat{v}_+$  and  $\hat{v}_-$  from (3.25b), again with zero on the right-hand side and with the appropriate boundary conditions.
2. Solve and store the  $B_0$ -Problem by solving (3.35a) for  $\tilde{p}_{0,m}$  and likewise (3.35c) for  $\tilde{v}_{0,m}$  for  $m = 0, \dots, N_y$ , then find  $\tilde{\sigma}_{0,m}$   $m = N_y - 1, N_y$  using (3.35c) i.e.  $\tilde{\sigma}_{0,m} = \lambda\tilde{v}_{0,m} + \tilde{p}_{0,m}^{(1)} - \nu\tilde{v}_{0,m}^{(2)}$   $m = N_y - 1, N_y$ .
3. Solve the  $B_1$ -Problem at each time step by solving (3.34a) and (3.34c) for  $\tilde{p}_{1,m}$  and  $\tilde{v}_{1,m}$  respectively for  $m = 0, \dots, N_y$ , using the stored influence matrix to do so, then find  $\tilde{\sigma}_{1,m}$   $m = N_y - 1, N_y$  using (3.34c).
4. Calculate  $\tilde{\sigma}_m$   $m = N_y - 1, N_y$  at each time step using (3.38) and the stored  $\tilde{\sigma}_{0,m}$  values.
5. Calculate  $\tilde{p}_m$  and  $\tilde{v}_m$   $m = 0, \dots, N_y$  at each time step using (3.39a) and (3.39b) respectively.
6. Find  $\tilde{u}$  and  $\tilde{w}$  using (3.28a) and (3.28e) respectively.

The influence-matrix method for integrating the Navier-Stokes equations forward in time has been derived for a channel flow with Dirichlet boundary conditions at the walls. In the next section, it shall be demonstrated how this method can be modified to allow for general inhomogeneous boundary conditions at the walls.

### 3.3 General Inhomogeneous Boundary Conditions

Define a general boundary condition matrix  $\hat{\xi}_{\pm}(\mathbf{k}_x, k_z, t)$ :

$$\hat{\xi}_{\pm}(\mathbf{k}_x, k_z, t) = \begin{bmatrix} \hat{\xi}_{u+}(\mathbf{k}_x, k_z, t) & \hat{\xi}_{v+}(\mathbf{k}_x, k_z, t) & \hat{\xi}_{w+}(\mathbf{k}_x, k_z, t) \\ \hat{\xi}_{u-}(\mathbf{k}_x, k_z, t) & \hat{\xi}_{v-}(\mathbf{k}_x, k_z, t) & \hat{\xi}_{w-}(\mathbf{k}_x, k_z, t) \end{bmatrix}, \quad (3.40)$$

where  $\hat{\xi}_+$  are boundary conditions at the upper wall and  $\hat{\xi}_-$  are boundary conditions at the lower wall for wavenumber index pair  $(\mathbf{k}_x, k_z)$  and for time  $t$  for the streamwise, wall-normal and spanwise velocity components. Using these general boundary conditions in the influence-matrix method instead of Dirichlet boundary conditions changes the solution procedure slightly. The new solution procedure is as follows:

1. Generate and store the influence matrix in exactly the same way as was done for the Dirichlet boundary condition case using (3.27); implemented boundary conditions only effect the particular solutions not the homogenous solutions.
2. Solve the  $B_0$ -Problem at each time step by solving (3.35a) for  $\tilde{p}_{0,m}$ , but now solve (3.35c) for  $\tilde{v}_{0,m}$  with boundary conditions  $\hat{v}(\pm) = \hat{\xi}_{v\pm}$  for  $m = 0, \dots, N_y$ , then calculate  $\tilde{\sigma}_{0,m}$  as before; now the  $B_0$ -Problem needs to be solved at each time step using the boundary condition imposed at that time step.
3. Solve the  $B_1$ -Problem at each time step by solving (3.34a) for  $\tilde{p}_{1,m}$ , but now solve (3.34c) for  $\tilde{v}_{1,m}$  with boundary conditions  $\hat{v}(\pm) = \hat{\xi}_{v\pm}$  for  $m = 0, \dots, N_y$  then calculate  $\tilde{\sigma}_{1,m}$  as before.
4. Calculate  $\tilde{\sigma}_m$   $m = N_y - 1, N_y$  at each time step using (3.38) and the current  $\tilde{\sigma}_{0,m}$  values (remembering that  $\tilde{\sigma}_{0,m}$  now changes at each time step).
5. Calculate  $\tilde{p}_m$  and  $\tilde{v}_m$   $m = 0, \dots, N_y$  at each time step using (3.39a) and (3.39b) respectively.
6. Solve (3.28a) for  $\tilde{u}_m$   $m = 0, \dots, N_y$  and (3.28e) for  $\tilde{w}_m$   $m = 0, \dots, N_y$  at each time step but using the boundary conditions  $\hat{u}(\pm 1) = \hat{\xi}_{u\pm}$  and  $\hat{w}(\pm 1) = \hat{\xi}_{w\pm}$  respectively.

*Channelflow* was modified to allow for generalised boundary conditions to be set at each time step by making the modifications to the influence-matrix method outlined above. To ensure that these modifications were correct, validation testing of the wall-normal boundary conditions was conducted; this is discussed in the next section.

### 3.4 Validation of Implemented Boundary Conditions

The inhomogeneous wall-normal velocity boundary conditions implemented in *Channelflow* were verified in two stages, a linear stage and a nonlinear stage. Only wall-normal boundary conditions were validated because they alone are required for controllers developed in this work. Validation of streamwise and spanwise velocity boundary conditions is an avenue of future work. In the linear stage, the velocity Fourier coefficients from a linearised Navier-Stokes *Channelflow* simulation were compared to the corresponding velocity Fourier coefficients from a linear Orr-Sommerfeld Squire simulation. Identical inhomogeneous wall-normal boundary conditions were implemented in both simulations. In the nonlinear validation stage, the energy spectra from nonlinear *Channelflow* simulations with inhomogeneous boundary conditions were analysed to check that their shapes were those expected from theory.

#### 3.4.1 Linear Validation

*Channelflow* simulations were ran with the nonlinear term computed in the linearised form shown in (3.7), with the following arbitrary inhomogeneous wall-normal boundary conditions:

$$\hat{\xi}_{v+}(\alpha, \beta, t) = \hat{\xi}_{v-}(\alpha, \beta, t) = \cos(0.05t)(0.05 - 0.01i), \quad (3.41)$$

and with zero initial condition, i.e.:

$$\mathbf{V}_0(\chi) = 0 \quad \forall \chi \in \Omega, \quad (3.42)$$

where  $\alpha = 2\pi k_x/L_x$  and  $\beta = 2\pi k_z/L_z$ . The following three wavenumber pairs were chosen for linear simulation:

1.  $\alpha = 0, \beta = 1$
2.  $\alpha = 1, \beta = 0$
3.  $\alpha = 1, \beta = 1$

These were chosen as they consist of streamwise-constant (1), spanwise-constant (2) and oblique (3) spatial modes. All simulations were ran for arbitrary centre-line Reynolds number  $Re = 10^4$ , wall-normal resolution  $N_y = 65$  and time step  $dt = 0.01$ . For comparison, the Orr-Sommerfeld Squire (OSS) model with wall-normal actuation dynamics incorporated from (2.66) was simulated with identical boundary conditions, wavenumber pairs, wall-normal resolution, time step and Reynolds number. The Galerkin method was used to discretise the wall-normal component of the OSS models. To perform the simulations of the OSS model, the `lsim()` function in `Matlab` was used. To match the actuation dynamics of the OSS model, a low-pass filter was incorporated into the *Channelflow* simulation. The

$\alpha$	$\beta$	$\bar{\mathbf{u}}_{\mathbf{E}}$	$\bar{\mathbf{v}}_{\mathbf{E}}$	$\bar{\mathbf{w}}_{\mathbf{E}}$
0	1	$3.5 \cdot 10^{-2}$	$1.3 \cdot 10^{-3}$	$3.3 \cdot 10^{-3}$
1	0	$2.7 \cdot 10^{-2}$	$9.8 \cdot 10^{-3}$	0
1	1	$3.3 \cdot 10^{-2}$	$2.3 \cdot 10^{-3}$	$2.7 \cdot 10^{-2}$

Figure 3.1: Table of error-norms between *Channelflow* and OSS simulations.

actuator time-constant used for both simulations was  $\tau_\phi = 0.05$ . Again, this was chosen arbitrarily.

Figures 3.2, 3.3 and 3.4 show profiles of both the imaginary and real parts of the velocity Fourier coefficients  $\hat{u}$ ,  $\hat{v}$  and  $\hat{w}$ , for times  $t = 0, 10, 60$ , for the three wavenumber pair selections, from both linear *Channelflow* simulations and OSS simulations. It is clear from all three figures that the profiles produced from both simulations match well qualitatively for all velocity components and wavenumber pairs. Figure 3.1 shows a table of error-norms between simulation profiles for all velocity components and wavenumber pairs. The error-norms are defined:

$$\bar{\mathbf{u}}_{\mathbf{E}} := \frac{1}{N_t} \sum_{n_t=1}^{N_t} \left( \frac{1}{N_y} \|\hat{\mathbf{u}}_{\text{CF}} - \hat{\mathbf{u}}_{\text{OSS}}\| \right), \quad (3.43a)$$

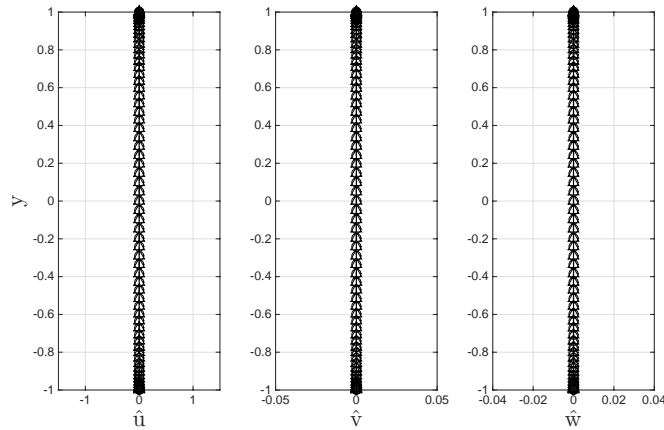
$$\bar{\mathbf{v}}_{\mathbf{E}} := \frac{1}{N_t} \sum_{n_t=1}^{N_t} \left( \frac{1}{N_y} \|\hat{\mathbf{v}}_{\text{CF}} - \hat{\mathbf{v}}_{\text{OSS}}\| \right), \quad (3.43b)$$

$$\bar{\mathbf{w}}_{\mathbf{E}} := \frac{1}{N_t} \sum_{n_t=1}^{N_t} \left( \frac{1}{N_y} \|\hat{\mathbf{w}}_{\text{CF}} - \hat{\mathbf{w}}_{\text{OSS}}\| \right), \quad (3.43c)$$

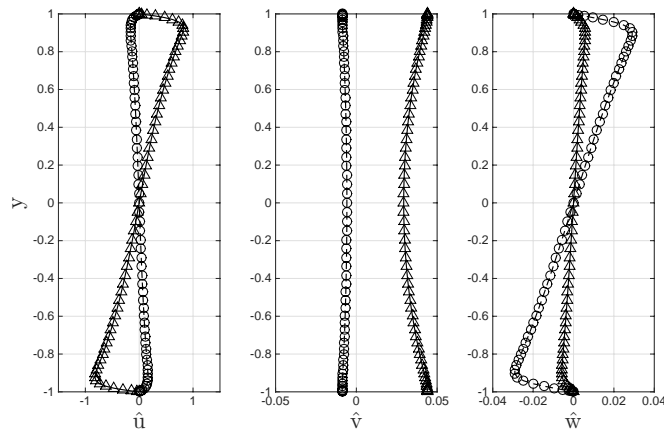
where  $N_t$  denotes the number of time steps used, subscripts  $\text{CF}$  and  $\text{OSS}$  denote velocity Fourier coefficient profiles from the *Channelflow* and OSS simulations respectively, and  $\|\cdot\|$  is the Euclidean norm. From Figure 3.1, where  $N_t = 100$ , all error-norms are shown to be satisfactorily small. This validation analysis suggests the inhomogeneous boundary conditions implemented in *Channelflow* model changes in wall-normal velocity at the wall successfully, at least for the linear case.

### 3.4.2 Nonlinear Validation

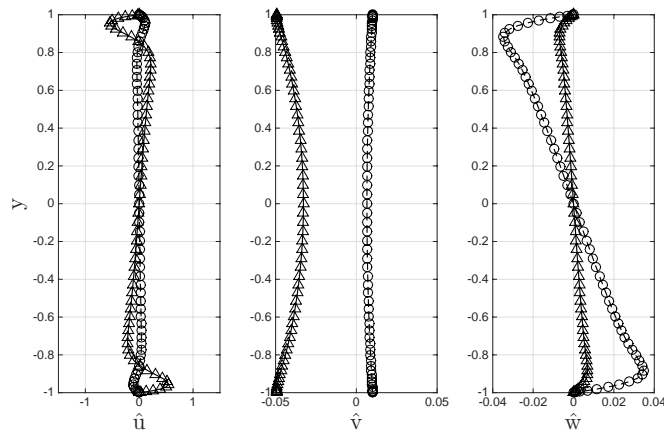
In the nonlinear validation stage, a simulation of  $\text{Re} = 10^3$  flow with a zero initial condition and validation wall-normal boundary conditions from (3.41) was performed in *Channelflow*. The boundary conditions were set for one wavenumber pair only - ( $\alpha = 0, \beta = 2$ ). The domain used for the simulation had resolution  $110 \times 65 \times 100$  in the streamwise, wall-normal and spanwise directions respectively, and corresponding spatial dimensions  $2\pi \times 2 \times 2\pi$ . The nonlinearity was computed in skew-symmetric form and the SBDF3 time-stepping algorithm was employed.



(a)  $t = 0$



(b)  $t = 10$



(c)  $t = 60$

Figure 3.2: Profiles of  $(\alpha = 0, \beta = 1)$  velocity Fourier coefficients  $\hat{u}$ ,  $\hat{v}$  and  $\hat{w}$  from *Channelflow* simulation ( $\Delta$  - real part,  $\circ$  - imaginary part) and OSS simulation (thick line - real part, dashed line - imaginary part) for  $t = 0, 10, 60$ , for  $Re = 10^4$  and validation boundary conditions (3.41).

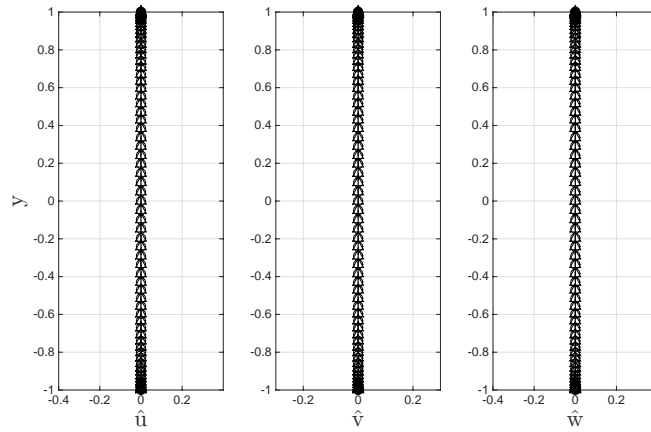
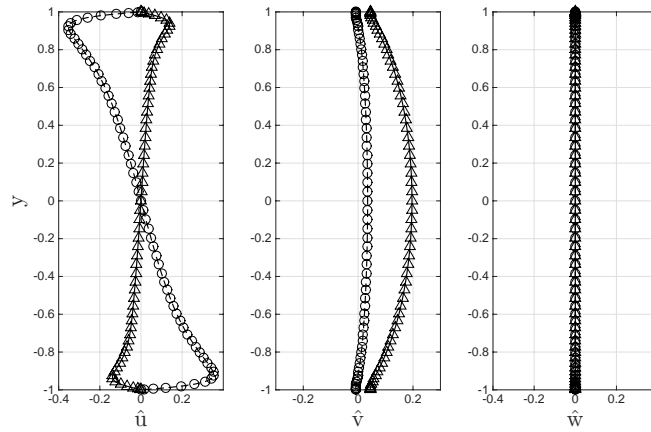
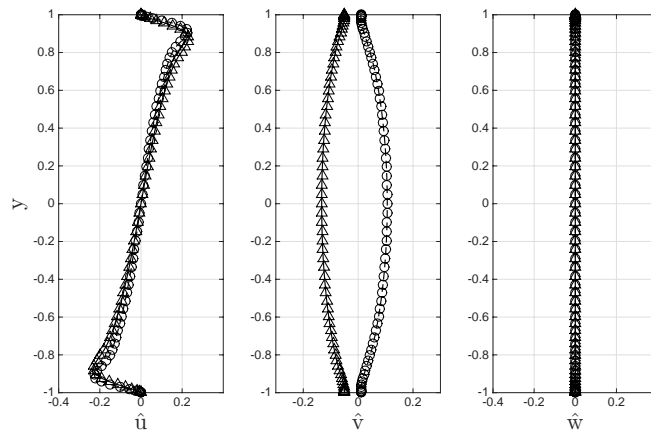
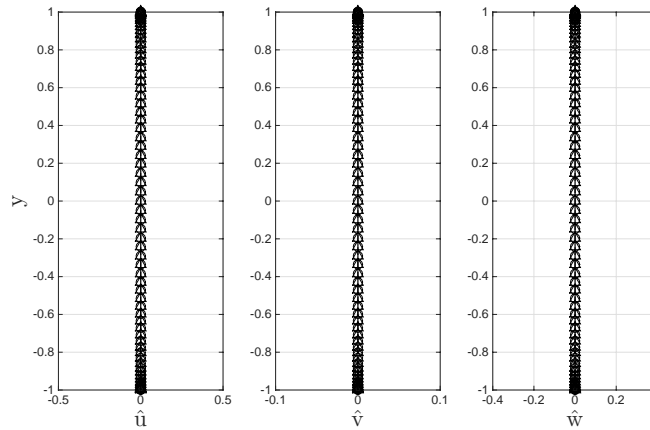
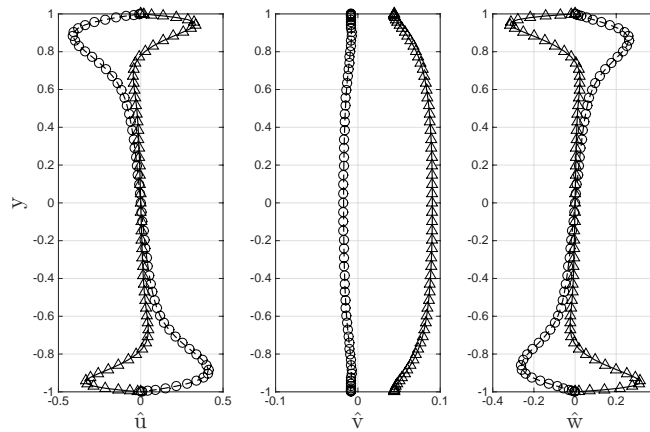
(a)  $t = 0$ (b)  $t = 10$ (c)  $t = 60$ 

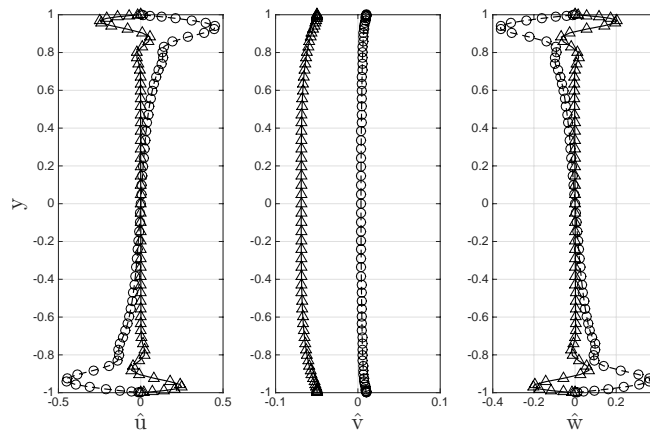
Figure 3.3: Profiles of  $(\alpha = 1, \beta = 0)$  velocity Fourier coefficients  $\hat{u}$ ,  $\hat{v}$  and  $\hat{w}$  from *Channelflow* simulation ( $\triangle$  - real part,  $\circ$  - imaginary part) and OSS simulation (thick line - real part, dashed line - imaginary part) for  $t = 0, 10, 60$ , for  $\text{Re} = 10^4$  and validation boundary conditions (3.41).



(a)  $t = 0$



(b)  $t = 10$



(c)  $t = 60$

Figure 3.4: Profiles of  $(\alpha = 1, \beta = 1)$  velocity Fourier coefficients  $\hat{u}$ ,  $\hat{v}$  and  $\hat{w}$  from *Channelflow* simulation ( $\Delta$  - real part,  $\circ$  - imaginary part) and OSS simulation (thick line - real part, dashed line - imaginary part) for  $t = 0, 10, 60$ , for  $\text{Re} = 10^4$  and validation boundary conditions (3.41).

Bulk velocity was used as the external constraint and kept constant at  $U_{\text{bulk}} = 2/3$ .

The energy spectrum from each time step of the simulation was analysed to investigate the effect of the boundary conditions on the flow. The energy spectrum of a flow field for time  $t$  is defined:

$$\hat{E}(\alpha, \beta, t) := \sqrt{\frac{1}{2} \|\hat{\mathbf{v}}_{\alpha, \beta}(y, t)\|^2}, \quad (3.44)$$

where  $\|\cdot\|$  is the Euclidean norm. Since the simulation has a zero initial condition, the boundary conditions are the only source of perturbation energy into the flow. Therefore, it is to be expected that the largest peaks in the energy spectra should be located at the wavenumber pair for which the boundary conditions are set -  $(\alpha = 0, \beta = 2)$ , with energy diffusing smoothly to wavenumber pairs in the vicinity over time. Figure 3.5 contains plots of energy spectra for  $(\alpha = 0, \beta \leq 10)$  for times  $t = 0, 2, 10$ . The energy of the boundary condition mode  $(\alpha = 0, \beta = 2)$  has the largest peak and increases over time. The energy of the other *even* streamwise-constant modes (i.e. even  $\beta$ ) also increases gradually over time as energy dissipates to these modes. It can be proven from first principles that excitation of even streamwise-constant modes will lead to energy diffusing only to other even streamwise-constant modes via triadic interactions [90]. This explains why the odd streamwise-constant modes have zero energy.

Although not as rigorous as the linear validation stage, this brief analysis suggests that the implemented boundary conditions model changes in wall-normal velocity at the walls correctly in nonlinear simulations.

### 3.5 Controller Implementation

In order to evaluate output-feedback controllers developed in later chapters, a *controller* suite is required to simulate controller dynamics and to set boundary conditions. All controllers novel to this thesis are linear time-invariant (LTI) which simplifies implementation.

A LTI controller  $\hat{\mathbf{K}}$  has the form:

$$\frac{\partial}{\partial t} \hat{\mathbf{x}}_{\mathbf{K}}(t) = \hat{A}_{\mathbf{K}} \hat{\mathbf{x}}_{\mathbf{K}}(t) + \hat{B}_{\mathbf{K}} \hat{\mathbf{y}}(t), \quad (3.45a)$$

$$\hat{\mathbf{u}}(t) = \hat{C}_{\mathbf{K}} \hat{\mathbf{x}}_{\mathbf{K}}(t) + \hat{D}_{\mathbf{K}} \hat{\mathbf{y}}(t), \quad (3.45b)$$

with initial condition:

$$\hat{\mathbf{x}}_{\mathbf{K}}(0) = \hat{\mathbf{x}}_{\mathbf{K},0}, \quad (3.46)$$

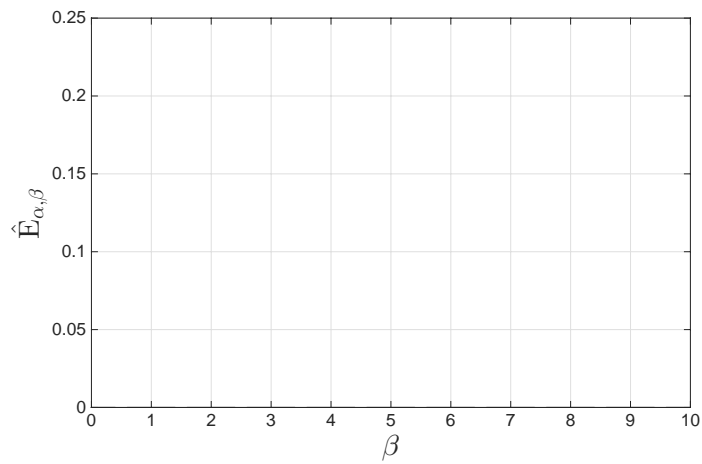
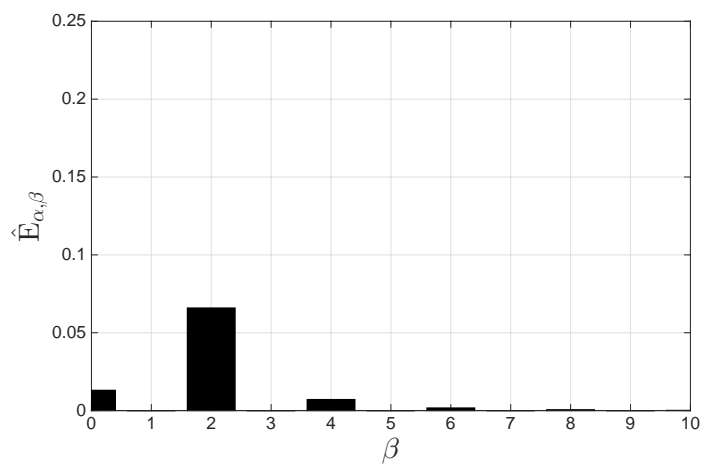
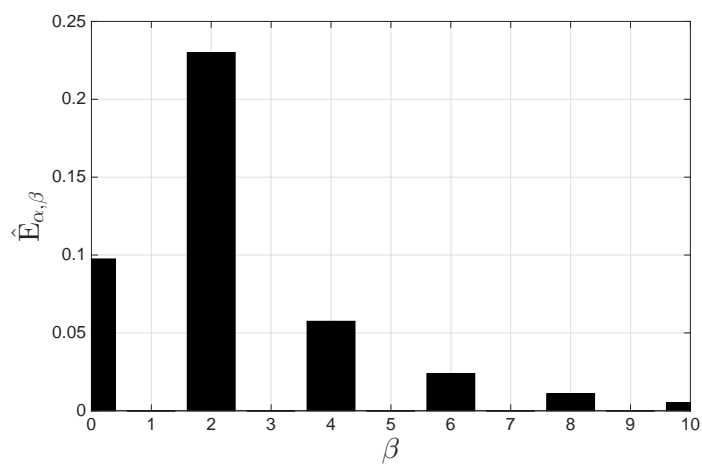
(a)  $t = 0$ (b)  $t = 2$ (c)  $t = 10$ 

Figure 3.5: Plots of energy spectra from  $\text{Re} = 10^3$  *Channelflow* simulation for times  $t = 0, 2, 10$ , and validation boundary conditions (3.41) applied to mode  $(\alpha = 0, \beta = 2)$  only. N.b. plots are symmetrical about  $\beta = 0$ , therefore, spectra only plotted for  $\beta \geq 0$ .

where  $\hat{\mathbf{x}}_{\mathbf{K}} \in \mathbb{R}^n$  is a vector of controller states,  $\hat{\mathbf{y}} \in \mathbb{R}^q$  is a vector of plant outputs,  $\hat{\mathbf{u}} \in \mathbb{R}^p$  is a vector of plant inputs, and  $\hat{A}_{\mathbf{K}} \in \mathbb{R}^{n \times n}$ ,  $\hat{B}_{\mathbf{K}} \in \mathbb{R}^{n \times q}$ ,  $\hat{C}_{\mathbf{K}} \in \mathbb{R}^{p \times n}$  and  $\hat{D}_{\mathbf{K}} \in \mathbb{R}^{p \times q}$  are time-invariant control matrices. A plant is defined as a system which one wishes to control. In the current case, the plant is a single Fourier mode  $(\alpha, \beta)$  of a nonlinear *Channelflow* simulation; hence the  $\hat{\cdot}$  notation. Therefore, the plant outputs are some linear measurement of a Fourier mode of the simulated flow:

$$\hat{\mathbf{y}}(t) = \hat{C}_s \hat{\mathbf{x}}(t), \quad (3.47)$$

where  $\hat{\mathbf{x}} \in \mathbb{R}^m$  is a vector of states from the simulation (i.e. velocity and pressure Fourier coefficients) and  $\hat{C}_s \in \mathbb{R}^{q \times m}$  is a time-invariant “sensor matrix”. The plant inputs can be any linear combination of the simulation states. However, in the current work, they will always be wall-normal velocity Fourier boundary conditions. Each LTI controller  $\hat{\mathbf{K}}$  will only control one wavenumber pair  $(\alpha, \beta)$  of the flow.

To integrate the dynamical system in (3.45) forward in time, a time-stepping algorithm needs to be employed. For the current work, an implicit Crank-Nicolson time-stepping scheme is used. This scheme is more stable than explicit schemes and yet is still very simple to implement. For a general dynamical system:

$$\frac{\partial}{\partial t} \zeta(t) = F(\zeta(t)), \quad (3.48)$$

the Crank-Nicolson method discretises time such that:

$$\frac{\zeta^{n+1} - \zeta^n}{\Delta t} \approx \frac{1}{2} [F(\zeta^{n+1}) + F(\zeta^n)], \quad (3.49)$$

where  $n$  notates time level and  $\Delta t$  represents the time between levels. Applying (3.49) to (3.45) yields:

$$\frac{\hat{\mathbf{x}}_{\mathbf{K}}^{n+1} - \hat{\mathbf{x}}_{\mathbf{K}}^n}{\Delta t} \approx \frac{1}{2} \left[ \left( \hat{A}_{\mathbf{K}} \hat{\mathbf{x}}_{\mathbf{K}}^{n+1} + \hat{B}_{\mathbf{K}} \hat{\mathbf{y}}^{n+1} \right) + \left( \hat{A}_{\mathbf{K}} \hat{\mathbf{x}}_{\mathbf{K}}^n + \hat{B}_{\mathbf{K}} \hat{\mathbf{y}}^{n+1} \right) \right], \quad (3.50a)$$

$$\hat{\mathbf{u}}^{n+1} = \hat{C}_{\mathbf{K}} \hat{\mathbf{x}}_{\mathbf{K}}^{n+1} + \hat{D}_{\mathbf{K}} \hat{\mathbf{y}}^{n+1}. \quad (3.50b)$$

After some rearranging (3.50a) becomes:

$$\hat{\mathbf{x}}_{\mathbf{K}}^{n+1} = \underbrace{\left( I - \frac{\Delta t}{2} \hat{A}_{\mathbf{K}} \right)^{-1} \left[ \left( I + \frac{\Delta t}{2} \hat{A}_{\mathbf{K}} \right) \hat{\mathbf{x}}_{\mathbf{K}}^n + \Delta t \hat{B}_{\mathbf{K}} \hat{\mathbf{y}}^{n+1} \right]}_{\hat{\mathbf{K}}(\hat{\mathbf{x}}_{\mathbf{K}}^n, \hat{\mathbf{y}}^{n+1})}. \quad (3.51)$$

Figure 3.6 shows a schematic of the control update scheme, where the cycle begins at the upper block. In the current work, all controller states will be initialised as zero, i.e.  $\hat{\mathbf{x}}_{\mathbf{K}}^0 = 0$ .

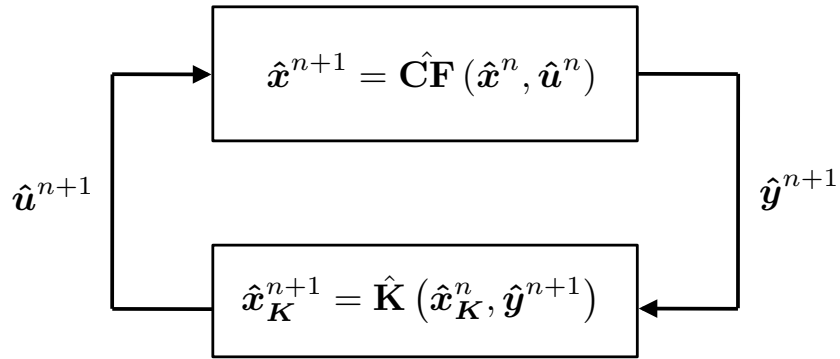


Figure 3.6: Block diagram of controller  $\hat{\mathbf{K}}$  in feedback with *Channelflow* plant  $\hat{\mathbf{C}}\mathbf{F}$  for a single Fourier mode.

To implement the control update scheme outlined above, a C++ *controller* class was incorporated into *Channelflow* by the author. The class allows as many Fourier modes to be controlled in a simulation as required and can handle both fixed and variable time-stepping. Low-pass filtering of the actuator dynamics is also implemented and modelled using a Crank-Nicolson time-stepping algorithm.

## Chapter 4

# Passivity-Based Control

### 4.1 Introduction

The framework of passive systems was first introduced for the energy-based analysis and control of electrical circuit networks. Its simplicity and effectiveness has made it a powerful tool for the analysis and control of various other systems since. In this chapter, the framework of passive systems, alternately referred to as passivity, shall be applied to turbulent channel flow with the aims of identifying the most energetic scales of the flow, and then to control these scales using passivity-based methods in order to restrict turbulent energy production and ultimately reduce skin-friction drag.

As discussed in Section 1.5, passivity-based control (PBC) has been applied to channel flow previously by Martinelli et al. [84] and Sharma et al. [101]. In the former case, PBC was used to minimise the upper bound on transient energy growth of a transitional channel flow using wall-based actuation and full flow field information. The authors did not refer to passivity in their work, but their controller can be classed as passivity-based in the author's opinion. In the latter case, PBC was used to globally stabilise a turbulent channel flow, leading to monotonic energy decay and flow relaminarisation, using body-forcing and sensing of wall-normal velocity throughout the channel. The results from both of these works are impressive. However, neither are practically implementable due to their sensing and/or actuation requirements. In the current work, all novel controllers developed will have their sensing and actuation restricted to the walls. Although this does not mean that these controllers will necessarily be practical to implement, it should give a closer indication of what drag reductions can be expected if this control method were to be practically applied.

In the following, the framework of passivity and the closely related concepts of dissipativity and positive realness will be outlined in Section 4.2, the passivity of channel flow will be evaluated in Section 4.3, and in Section 4.4, a PBC method

will be presented and the controllers evaluated through linear analyses and DNS. A brief summary is given in Section 4.5.

## 4.2 Dissipativity, Passivity and Positive Realness

In the current work, only continuous time systems will be discussed. However, the theory outlined in the following can be extended to the discrete time case.

### 4.2.1 Mathematical Preliminaries

A continuous time signal  $\gamma : \mathbb{R}_+ \rightarrow \mathbb{R}^m$  is in  $\mathcal{H}$  ( $\gamma \in \mathcal{H}$ ) if it has finite  $L_2^m$ -norm:

$$\|\gamma\|_2^2 = \int_0^\infty \gamma^\top(t)\gamma(t)dt < \infty. \quad (4.1)$$

An extended signal space,  $L_{2e}^m$ , can be defined by introducing a truncation operator:

$$\gamma_T(t) = \begin{cases} \gamma(t) & t < T \\ 0 & t \geq T \end{cases}. \quad (4.2)$$

A continuous time signal  $\gamma : \mathbb{R}_+ \rightarrow \mathbb{R}^m$  is in  $\mathcal{H}_e$  ( $\gamma \in \mathcal{H}_e$ ) if:

$$\|\gamma_T\|_2^2 = \int_0^T \gamma^\top(t)\gamma(t)dt < \infty \quad \forall T \in \mathbb{R}_+. \quad (4.3)$$

The temporal inner product of two signal vectors  $\mathbf{y}(t)$  and  $\mathbf{u}(t)$  over the time interval  $[0, T]$  is defined:

$$\langle \mathbf{y}(t), \mathbf{u}(t) \rangle_{[0, T]} = \int_0^T \mathbf{y}^\top(t)\mathbf{u}(t)dt. \quad (4.4)$$

The spatiotemporal inner product of two signal vectors  $\mathbf{y}(\chi, t)$  and  $\mathbf{u}(\chi, t)$  over the time interval  $[0, T]$  is defined:

$$\langle \mathbf{y}(\chi, t), \mathbf{u}(\chi, t) \rangle_{[0, T]} = \int_0^T \int_{\chi \in \Omega} \mathbf{y}^\top(\chi, t)\mathbf{u}(\chi, t)d\chi dt. \quad (4.5)$$

Define a system  $\Sigma$  as a relation on  $\mathcal{H}_e$ . For  $\mathbf{u} \in \mathcal{H}_e$ ,  $\Sigma\mathbf{u}$  denotes an image of  $\mathbf{u}$  under  $\Sigma$  [113], and  $\Sigma\mathbf{u}(t)$  is the value of  $\Sigma\mathbf{u}$  at time  $t$ . The continuous time system  $\Sigma : \mathcal{H}_e \rightarrow \mathcal{H}_e$  is  $L_2^m$  stable if:

$$\mathbf{u} \in L_2^m \implies \Sigma\mathbf{u} \in L_2^m. \quad (4.6)$$

The continuous time system  $\Sigma : \mathcal{H}_e \rightarrow \mathcal{H}_e$  is finite-gain  $L_2^m$  stable if there exist  $\epsilon > 0$  and  $\kappa$  such that:

$$\|(\Sigma\mathbf{u})_T\|_2 \leq \epsilon\|\mathbf{u}_T\|_2 + \kappa. \quad (4.7)$$

The symbol  $\check{\Sigma}$  shall be used if the continuous time system is LTI, otherwise the system shall be assumed general.

#### 4.2.2 Dissipativity

The theory of dissipative dynamical systems, alternately referred to as dissipativity, was first introduced by Willems [111, 112]. It can be viewed as a generalisation of passivity and is hence outlined first. Dissipativity analyses the dynamical relation between the internally stored energy of a system and the energy being supplied to that system.

For a general system  $\Sigma : \mathcal{H}_e \rightarrow \mathcal{H}_e$  with input-output relation  $\mathbf{y}(t) = \Sigma \mathbf{u}(t)$ , a locally integrable function called the *supply rate* can be defined as  $s(t) = s(\mathbf{u}(t), \mathbf{y}(t))$ . The system  $\Sigma$  is said to be dissipative with respect to its supply rate  $s(t)$ , if there exists a non-negative *storage function*  $V(\mathbf{x})$ , such that for all  $t_1 \geq t_0 \in \mathbb{R}_+$ :

$$V(\mathbf{x}(t_1)) \leq V(\mathbf{x}(t_0)) + \int_{t_0}^{t_1} s(\mathbf{u}(t), \mathbf{y}(t)) dt, \quad (4.8)$$

where  $\mathbf{x}$  is a vector of system states. The inequality in (4.8) is called the dissipation inequality, and it states “if the energy stored within the system for time  $t_1$  is less than or equal to the amount of energy stored at earlier time  $t_0$  plus the energy supplied to the system between these times, the system must either be lossless or dissipating energy”. This is intuitive. However, for many systems it is often difficult to determine the storage function uniquely [111]. This is not the case for LTI systems however, where both the storage function and supply rate can be easily defined.

For LTI system  $\check{\Sigma} \triangleq \{A, B, C, D\}$ , defined such that:

$$\frac{\partial}{\partial t} \mathbf{x}(t) = A\mathbf{x}(t) + B\mathbf{u}(t), \quad (4.9a)$$

$$\mathbf{y}(t) = C\mathbf{x}(t) + D\mathbf{u}(t), \quad (4.9b)$$

it can be assumed without loss of generality that its storage function  $V(\mathbf{x})$  has quadratic form [112]:

$$V(\mathbf{x}) = \mathbf{x}^\top Q \mathbf{x}, \quad (4.10)$$

where matrix  $Q = Q^\top > 0$ . The system  $\check{\Sigma}$  is  $(P, S, R)$ -dissipative [47] if it is dissipative with respect to the quadratic supply rate:

$$s(\mathbf{u}, \mathbf{y}) = \mathbf{y}^\top P \mathbf{y} + 2\mathbf{y}^\top S \mathbf{u} + \mathbf{u}^\top R \mathbf{u}, \quad (4.11)$$

where  $P = P^\top$  and  $R = R^\top$ .

### 4.2.3 Passivity

Passivity is a simplification of dissipativity, in that it is purely an input-output property of a system and requires no explicitly defined storage function. A passive system can only store and dissipate energy and is unable to produce energy of its own. Examples of passive systems include passive components in a circuit such as a resistor, and as will be demonstrated - the nonlinearity in the Navier-Stokes equations for a channel flow.

For the general system  $\mathbf{y}(t) = \Sigma \mathbf{u}(t)$ , the following classifications of passivity can be defined [32, 72]:

1.  $\Sigma$  is *passive* if  $\exists \kappa$  such that

$$\langle \mathbf{y}, \mathbf{u} \rangle_{[0, T]} \geq \kappa, \quad (4.12)$$

2.  $\Sigma$  is *strictly input passive* (SIP) if  $\exists \varepsilon > 0$  and  $\exists \kappa$  such that

$$\langle \mathbf{y}, \mathbf{u} \rangle_{[0, T]} \geq \varepsilon \|\mathbf{u}_T\|_2^2 + \kappa, \quad (4.13)$$

3.  $\Sigma$  is *strictly output passive* (SOP) if  $\exists \delta > 0$  and  $\exists \kappa$  such that

$$\langle \mathbf{y}, \mathbf{u} \rangle_{[0, T]} \geq \delta \|\mathbf{y}_T\|_2^2 + \kappa, \quad (4.14)$$

4.  $\Sigma$  is *very strictly passive* (VSP) if  $\exists \delta > 0, \varepsilon > 0$  and  $\exists \kappa$  such that

$$\langle \mathbf{y}, \mathbf{u} \rangle_{[0, T]} \geq \varepsilon \|\mathbf{u}_T\|_2^2 + \delta \|\mathbf{y}_T\|_2^2 + \kappa. \quad (4.15)$$

A connection can now be made between passivity and dissipativity for the LTI system case. Substituting  $P = 0$ ,  $S = (1/2)I$  and  $R = -\varepsilon I$  into the quadratic supply rate in (4.11) yields:

$$s(\mathbf{u}, \mathbf{y}) = \mathbf{y}^\top \mathbf{u} - \varepsilon \mathbf{u}^\top \mathbf{u}. \quad (4.16)$$

Then, substituting (4.16) into (4.8) results in the following dissipation inequality:

$$V(\mathbf{x}(t_1)) \leq V(\mathbf{x}(t_0)) + \langle \mathbf{y}, \mathbf{u} \rangle_{[t_0, t_1]} - \varepsilon \|\mathbf{u}_T\|_2^2, \quad (4.17)$$

which after rearranging becomes:

$$\langle \mathbf{y}, \mathbf{u} \rangle_{[t_0, t_1]} \geq \varepsilon \|\mathbf{u}_T\|_2^2 + \underbrace{(V(\mathbf{x}(t_1)) - V(\mathbf{x}(t_0)))}_{\kappa}. \quad (4.18)$$

The inequality in (4.18) is identical to the SIP inequality in (4.13). Similar results can be found for passive, SOP and VSP systems. Therefore, the passivity of a system identifies the boundedness of its supply rate.

#### 4.2.4 Positive-Realness

Both passivity and dissipativity are time-domain concepts. Passivity has a frequency-domain equivalent named positive-realness. However, this only applies to LTI systems and is therefore less general.

Taking Laplace transforms of the state vector  $\mathbf{x}(t)$ , input vector  $\mathbf{u}(t)$  and output vector  $\mathbf{y}(t)$  such that:

$$\mathbf{X}(s) = \int_0^{\infty} \mathbf{x}(t)e^{-st} dt, \quad (4.19a)$$

$$\mathbf{U}(s) = \int_0^{\infty} \mathbf{u}(t)e^{-st} dt, \quad (4.19b)$$

$$\mathbf{Y}(s) = \int_0^{\infty} \mathbf{y}(t)e^{-st} dt, \quad (4.19c)$$

where  $s = \sigma + i\omega$  denotes complex frequency, the LTI system in (4.9) can be represented by the following transfer function matrix  $\check{\Sigma}(s)$ :

$$\mathbf{Y}(s) = \underbrace{(CsI - A)^{-1}B + D}_{\check{\Sigma}(s)} \mathbf{U}(s). \quad (4.20)$$

The transfer function matrix  $\check{\Sigma}(s)$  is defined as *positive real* (PR) if the following conditions hold [72]:

1. All elements of  $\check{\Sigma}(s)$  are analytic in  $\Re(s) > 0$ .
2.  $\check{\Sigma}(i\omega) + \check{\Sigma}^{\top}(-i\omega) \geq 0$ ,  $\forall \omega \in \mathbb{R}$ , for which  $i\omega$  is not a pole for any element of  $\check{\Sigma}(s)$ .

PR systems and passive systems are equivalent.

The transfer function matrix  $\check{\Sigma}(s)$  is defined as *strictly positive real* (SPR) if the following conditions hold [72]:

1. All elements of  $\check{\Sigma}(s)$  are analytic in  $\Re(s) \geq 0$ .
2. There exists  $\varepsilon > 0$  such that  $\check{\Sigma}(i\omega) + \check{\Sigma}^{\top}(-i\omega) \geq 2\varepsilon I$ ,  $\forall \omega \in \mathbb{R}$ .

SPR systems and SIP systems are equivalent, with identical bound  $\varepsilon$ .

The following connections can be made between passivity and positive realness [72]:

1.  $\check{\Sigma}$  is passive iff  $\check{\Sigma}(s)$  is positive real.

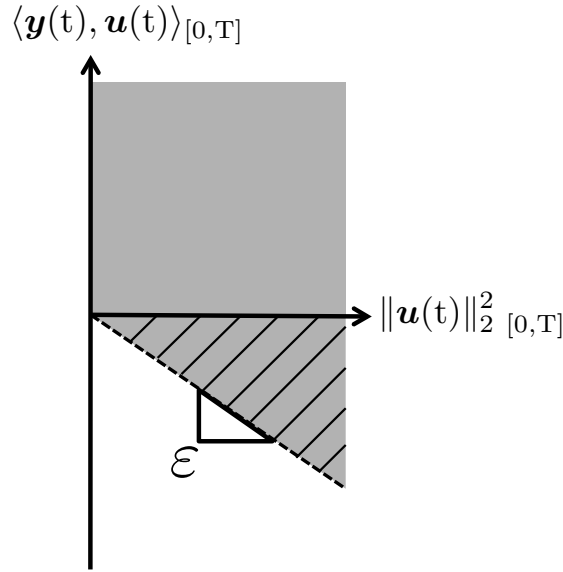


Figure 4.1: A schematic displaying the index of passivity  $\varepsilon$  of a system.

2.  $\tilde{\Sigma}$  is strictly input passive iff  $\tilde{\Sigma}(s)$  is strictly positive real.

The constant  $\varepsilon$ , which shall be referred to as a system's *index of passivity*, can be determined directly from a system's transfer function using the following formula [17]:

$$\varepsilon := \frac{1}{2} \left\{ \inf_{\omega} \lambda_{\min} (\tilde{\Sigma}(i\omega) + \tilde{\Sigma}^{\top}(-i\omega)) \right\}, \quad (4.21)$$

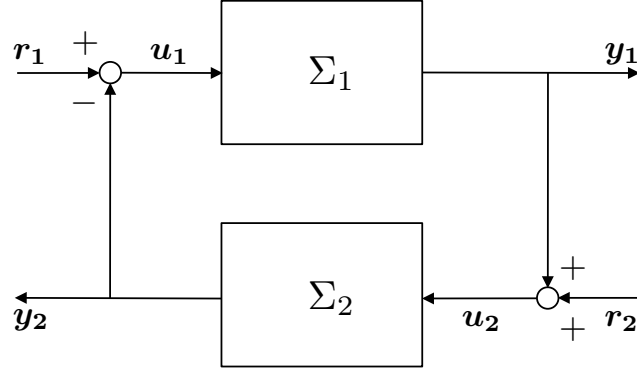
where  $\lambda_{\min}$  denotes smallest eigenvalue.

Thus far, the discussion has only been about passive systems, where  $\varepsilon \geq 0$ . In these cases,  $\varepsilon$  acts as the lower bound on a system's rate of energy dissipation. However, systems with index of passivity  $\varepsilon < 0$  will not be passive, but their index gives us information regarding how non-passive the system is -  $\varepsilon$  acts as the upper bound on a system's rate of energy production. A schematic of this is shown in Figure 4.1, where energy production can only occur in the dashed region of the graph. In later sections, feedback control will be used to make non-passive systems as close to passive as is possible by minimising  $|\varepsilon|$ .

#### 4.2.5 The Passivity Theorem

The passivity theorem determines the stability of the feedback interconnections of systems within the framework of passivity.

**Theorem** Consider the negative feedback interconnection of systems  $\Sigma_1$  and  $\Sigma_2$  in Figure 4.2, and set  $\mathbf{r}_2 \equiv 0$ . It is assumed that for any  $\mathbf{r}_1 \in \mathcal{H}$ , there exists solutions  $\mathbf{u}_1, \mathbf{u}_2 \in \mathcal{H}_e$ . Under these conditions, if  $\Sigma_1$  is *passive* and  $\Sigma_2$  is *strictly input passive*, the closed-loop system  $\mathbf{y}_1 = \Sigma_{(1 \times 2)} \mathbf{r}_1$  is passive and  $\mathbf{y}_1 \in \mathcal{H}$  [32].

Figure 4.2: The negative feedback interconnection of systems  $\Sigma_1$  and  $\Sigma_2$ .

**Proof** From Figure 4.2, signals  $\mathbf{u}_1$  and  $\mathbf{u}_2$  can be expressed as:

$$\mathbf{u}_1 = \mathbf{r}_1 - \Sigma_2 \mathbf{u}_2, \quad (4.22a)$$

$$\mathbf{u}_2 = \Sigma_1 \mathbf{u}_1. \quad (4.22b)$$

Therefore, from (4.22), and using the definitions of passivity in (4.12) and (4.13):

$$\langle \mathbf{y}_1, \mathbf{r}_1 \rangle_{[0,T]} = \langle \Sigma_1 \mathbf{u}_1, \mathbf{u}_1 \rangle_{[0,T]} + \langle \Sigma_2 \mathbf{u}_2, \mathbf{u}_2 \rangle_{[0,T]} \geq 0 + \epsilon_2 \|\mathbf{u}_{2T}\|_2^2 + \kappa, \quad (4.23)$$

where  $\epsilon_2 > 0$  since  $\Sigma_2$  is SIP. Furthermore, by the Schwarz inequality and noting that  $\mathbf{r}_1 \in \mathcal{H}$ :

$$\|\Sigma_1 \mathbf{u}_{1T}\|_2 \|\mathbf{r}_{1T}\|_2 \geq \epsilon_2 \|\Sigma_1 \mathbf{u}_{1T}\|_2^2 + \kappa \quad \forall T \in \mathbb{R}_+, \quad (4.24)$$

from which it follows  $\|\Sigma_1 \mathbf{u}_{1T}\|$  is bounded, i.e.  $\mathbf{y}_1 \in \mathcal{H}$ .

Therefore, if one knows the passivity of individual systems in a feedback arrangement, one can attain guarantees of the passivity, and hence stability, of the closed-loop system.

### 4.3 Passivity of Channel Flow

In this section, the dynamics of channel flow will be analysed using the framework of passivity outlined previously.

The perturbation equations for channel flow, previously shown in (2.5), are:

$$\frac{\partial \mathbf{v}}{\partial t} = \frac{1}{\text{Re}} \nabla^2 \mathbf{v} - \nabla p - \tilde{\mathbf{V}} \cdot \nabla \mathbf{v} - \mathbf{v} \cdot \nabla \tilde{\mathbf{V}} - \mathbf{n} + \mathbf{f}, \quad (4.25a)$$

$$\nabla \cdot \mathbf{v} = 0, \quad (4.25b)$$

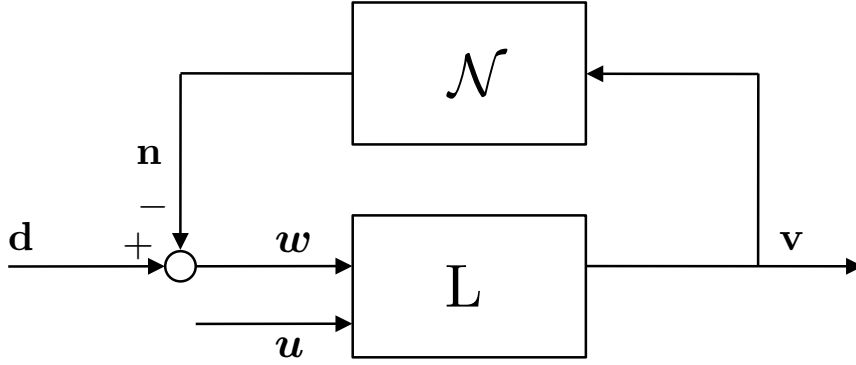


Figure 4.3: Block diagram representation of the dynamics of channel flow.

Besides the external forcing terms  $\mathbf{f}$  and nonlinear forcing terms  $\mathbf{n}$ , all other terms in (4.25) are linear in the primitive variables  $\mathbf{v}$  and  $p$ . The system of equations in (4.25) can therefore be expressed in the form:

$$\frac{\partial \mathbf{v}}{\partial t} = \mathbf{L}(\mathbf{v}, p) - \mathcal{N}(\mathbf{v}) + \mathbf{d} + \mathbf{u}, \quad (4.26a)$$

$$\nabla \cdot \mathbf{v} = 0, \quad (4.26b)$$

where  $\mathbf{L}(\cdot)$  represents the linear operations in (4.25),  $\mathcal{N}(\mathbf{v}) = \mathbf{n} = \mathbf{v} \cdot \nabla \mathbf{v}$  are the nonlinear forcing terms represented as a nonlinear operator on the velocity vector field, and  $\mathbf{f} = \mathbf{d} + \mathbf{u}$ , where  $\mathbf{d} : \Omega \times \mathbb{R}_+ \rightarrow \mathbb{R}^3$  is a vector of exogenous disturbance forces, and  $\mathbf{u} : \partial\Omega \times \mathbb{R}_+ \rightarrow \mathbb{R}^3$  is a vector of control input forcing. In this form, the nonlinearity can be viewed as a negative feedback forcing upon the linear dynamics of the flow [101]. This is illustrated in the block diagram in Figure 4.3.

With the dynamics of channel flow decomposed in such a manner, the passivity of the linear system  $\mathbf{L}$  and nonlinear system  $\mathcal{N}$  can be analysed separately. The passivity theorem can then be used to analyse the passivity of the feedback interconnection of the two systems. However, firstly, it shall be useful to outline the perturbation energy balance for a channel flow.

#### 4.3.1 Perturbation Energy Balance

Turbulence is a self-sustaining process, therefore, there must be a balance between the input energy required to feed the turbulent perturbations, and the energy that is lost due to dissipation. By multiplying (4.25a) by  $\mathbf{v}$ , setting  $\mathbf{f} = 0$  and integrating over the domain, yields, after some rearranging, the perturbation energy

balance equation for a channel flow:

$$\underbrace{\frac{D}{Dt}E(t)}_{1.} = - \underbrace{\frac{1}{V} \int_{\chi \in \Omega} \nabla \cdot \left[ \mathbf{v} \left( p + \frac{\mathbf{v} \cdot \mathbf{v}}{2} \right) \right]}_{2.} d\chi - \underbrace{\frac{1}{V} \int_{\chi \in \Omega} uv \frac{\partial \tilde{U}}{\partial y}}_{3.} d\chi \quad (4.27)$$

$$+ \underbrace{\frac{\text{Re}}{V} \int_{\chi \in \Omega} \nabla \cdot \left[ \nabla \left( \frac{\mathbf{v} \cdot \mathbf{v}}{2} \right) \right]}_{4.} d\chi - \underbrace{\frac{\text{Re}}{V} \int_{\chi \in \Omega} (\nabla \mathbf{v}) \cdot \nabla \mathbf{v}}_{5.} d\chi,$$

where  $\frac{D}{Dt} := \frac{d}{dt} + \tilde{U} \cdot \nabla$  denotes the material derivative, and  $E = \frac{1}{V} \int_{\chi \in \Omega} 1/2 (\mathbf{v} \cdot \mathbf{v}) d\chi$  is the perturbation energy density in a flow domain with volume  $V$ . The terms in (4.27) have the following physical interpretations [48]:

1. Rate of change in perturbation energy.
2. Turbulent convective diffusion.
3. Production of perturbation energy.
4. Work done by viscous stresses.
5. Viscous dissipation.

It will be shown in the following section that for an uncontrolled channel flow, terms 2. and 4. are equal to zero. For this case, the rate of change of energy depends on the balance between the energy production term, 3., which can be either negative or positive, and the dissipation term, 5., which is always positive.

#### 4.3.2 Passivity of the Nonlinear System

In order to classify the passivity of the nonlinear system, the following inner-product needs to be evaluated:

$$\langle \mathbf{n}, \mathbf{v} \rangle_{[0,T]} = \frac{1}{V} \int_0^T \int_{\chi \in \Omega} (\mathbf{v}(\chi, t) \cdot \nabla \mathbf{v}(\chi, t)) \cdot \mathbf{v}(\chi, t) d\chi dt, \quad (4.28)$$

To achieve this, first state the identity:

$$\nabla \cdot [\mathbf{v} (\mathbf{v} \cdot \mathbf{v})] \equiv 2(\mathbf{v} \cdot \nabla \mathbf{v}) \cdot \mathbf{v} + \underbrace{(\mathbf{v} \cdot \mathbf{v})(\nabla \cdot \mathbf{v})}_{=0}, \quad (4.29)$$

where the the final term on the right-hand-side is zero due to the divergence free condition. Therefore, using (4.29), the passivity statement for the nonlinearity becomes:

$$\langle \mathbf{n}, \mathbf{v} \rangle_{[0,T]} = \frac{1}{2V} \int_0^T \int_{\chi \in \Omega} \nabla \cdot [\mathbf{v}(\chi, t) (\mathbf{v}(\chi, t) \cdot \mathbf{v}(\chi, t))] d\chi dt. \quad (4.30)$$

The right-hand-side of (4.30) corresponds to the rate of work done by the dynamic pressure in term 2. of (4.27), integrated over time.

The divergence theorem states that for a continuously differentiable vector field  $\mathbf{F}$  defined on a volume  $V$ :

$$\int_V (\nabla \cdot \mathbf{F}) \, dV = \oint_S (\mathbf{F} \cdot \boldsymbol{\zeta}) \, dS, \quad (4.31)$$

where the left-hand-side is an integral over the volume, the right-hand-side is a surface integral, and  $\boldsymbol{\zeta}$  is the outward pointing unit normal field on the boundary.

Applying the divergence theorem to (4.30) yields:

$$\langle \mathbf{n}, \mathbf{v} \rangle_{[0,T]} = \frac{1}{2V} \int_0^T \oint_{\chi \in \partial\Omega} [\mathbf{v}(\chi, t) (\mathbf{v}(\chi, t) \cdot \mathbf{v}(\chi, t))] \cdot \boldsymbol{\zeta} \, d\chi dt. \quad (4.32)$$

For periodic boundary conditions in the streamwise and spanwise directions, and Dirichlet boundary conditions at the walls, the surface integral in (4.32) is necessarily zero. Therefore, the nonlinearity is passive, or more precisely, the nonlinearity is *lossless*. Applying the divergence theorem to the rate of change of work done by the static pressure in term 2. and to the work done by the viscous stresses in term 4. in (4.27), it can be shown that these must also equal zero. This amounts to a zero net flux of perturbation energy into or out of the domain.

However, for the case where wall-actuation is employed via the wall-normal component of velocity, the net flux of energy into or out of the domain due to the actuation must be taken into account. For actuated channel flow, term 2. in (4.27) corresponds to:

$$\frac{1}{V} \int_{\chi \in \Omega} \nabla \cdot \left[ \mathbf{v} \left( p + \frac{\mathbf{v} \cdot \mathbf{v}}{2} \right) \right] \, d\chi = \quad (4.33)$$

$$\begin{aligned} \frac{1}{V} \int_0^{L_x} \int_0^{L_z} [v(x, +1, z, t)p(x, +1, z, t)\zeta_y^+] + [v(x, -1, z, t)p(x, -1, z, t)\zeta_y^-] \, dz dx \\ + \frac{1}{2V} \int_0^{L_x} \int_0^{L_z} [v^3(x, +1, z, t)\zeta_y^+] + [v^3(x, -1, z, t)\zeta_y^-] \, dz dx, \end{aligned}$$

where streamwise and spanwise velocities are assumed zero at the walls, and outward pointing unit normals are defined  $\boldsymbol{\zeta}_y = \begin{bmatrix} \zeta_y^+ & \zeta_y^- \end{bmatrix}^\top$ , where positive and negative correspond to the upper and lower walls respectively. The first term on the right-hand-side of (4.33) corresponds to the rate of work done by the actuation on the static pressure, and the second term on the right-hand-side corresponds to the rate of work done on the dynamic pressure. To ensure the net flux of energy

is out of the domain, (4.33) must be greater or equal to zero for all time. This would also ensure that the nonlinearity remains passive. With wall-normal actuation, term 4. in (4.27) is still equal to zero due to the fact that  $\frac{\partial v}{\partial y} = 0$  at the walls.

The nonlinear vector field  $\mathbf{n}$  for time  $t$ , once computed from the velocity vector field  $\mathbf{v}$  for time  $t$ , can be Fourier discretised in the streamwise and spanwise directions to yield:

$$\mathbf{n}(x, y, z, t) = \sum_{\alpha=-\infty}^{\infty} \sum_{\beta=-\infty}^{\infty} \hat{\mathbf{n}}_{\alpha,\beta}(y, t) e^{i(\alpha x + \beta z)}. \quad (4.34)$$

Therefore, the passivity inner-product for the nonlinear system can be expressed as:

$$\begin{aligned} \langle \mathbf{n}, \mathbf{v} \rangle_{[0,T]} &= \int_0^T \int_{\chi \in \Omega} \sum_{\alpha=-\infty}^{\infty} \sum_{\beta=-\infty}^{\infty} \hat{\mathbf{n}}_{\alpha,\beta}^{\top}(y, t) e^{-i(\alpha x + \beta z)} \cdot \hat{\mathbf{v}}_{\alpha,\beta}(y, t) e^{i(\alpha x + \beta z)} d\chi dt \\ &= \sum_{\alpha=-\infty}^{\infty} \sum_{\beta=-\infty}^{\infty} \langle \hat{\mathbf{n}}_{\alpha,\beta}, \hat{\mathbf{v}}_{\alpha,\beta} \rangle_{[0,T]} \\ &\geq \sum_{\alpha=-\infty}^{\infty} \sum_{\beta=-\infty}^{\infty} \hat{\varepsilon}_{\mathbf{n}}(\alpha, \beta) = \varepsilon_{\mathbf{n}}, \end{aligned} \quad (4.35)$$

where  $\hat{\varepsilon}_{\mathbf{n}}$  is the index of passivity of the nonlinearity for each mode, and  $\varepsilon_{\mathbf{n}}$  is the overall index of passivity of the nonlinearity. It can be seen from (4.35) that the passivity inner-product of the nonlinear system is equal to the sum, over all wavenumber pairs  $(\alpha, \beta)$  of the passivity inner-products of each Fourier mode. Therefore, if only certain modes are controlled via wall transpiration, the net flux of energy into or out of the domain for each controlled mode would have to be taken into account in order to assess the index of passivity of the nonlinearity  $\varepsilon_{\mathbf{n}}$ .

### 4.3.3 Passivity of the Linear System

The perturbation energy production term (3.) in the energy balance equation (4.27) is driven by the linear dynamics only. This term can be positive or negative, and so can increase or reduce the rate of energy production in a flow. Analysing the passivity of the linear system will indicate the boundedness of this term.

It was demonstrated at the end of the previous section how the sum of the passivity indices over all wavenumber pairs  $(\alpha, \beta)$  of a system is equal to the passivity index of the system as a whole. Therefore, in the following, the linear system will be Fourier discretised in the periodic streamwise and spanwise directions, and the passivity of individual Fourier modes will be analysed.

Each Fourier mode of the linear system has a spatially discrete LTI state-space model of the form:

$$\underbrace{\frac{\partial}{\partial t} \begin{bmatrix} \mathbf{a}_{\mathbf{v}_N}(t) \\ \mathbf{a}_{\boldsymbol{\eta}_N}(t) \end{bmatrix}}_{\frac{\partial \mathbf{x}}{\partial t}} = \underbrace{\begin{bmatrix} \tilde{\mathbb{L}}_{\text{OS}} & 0 \\ \tilde{\mathbb{L}}_{\text{C}} & \tilde{\mathbb{L}}_{\text{Sq}} \end{bmatrix}}_A \underbrace{\begin{bmatrix} \mathbf{a}_{\mathbf{v}_N}(t) \\ \mathbf{a}_{\boldsymbol{\eta}_N}(t) \end{bmatrix}}_{\mathbf{x}} + B\mathbf{w}(t), \quad (4.36a)$$

$$\mathbf{z}(t) = C\mathbf{x}(t), \quad (4.36b)$$

where  $\mathbf{x} \in \mathbb{C}^{2N}$  is a vector of system states,  $\mathbf{w} \in \mathbb{C}^{2N}$  is a vector of exogenous disturbances including the forcing by the nonlinearity,  $\mathbf{a}_{\mathbf{v}_N}$  and  $\mathbf{a}_{\boldsymbol{\eta}_N}$  are spectral coefficients relating to wall-normal velocity and wall-normal vorticity respectively,  $\tilde{\mathbb{L}}_{\text{OS}} \equiv \tilde{\mathbf{E}}_{11}^{-1} \tilde{\mathbf{A}}_{11}$ ,  $\tilde{\mathbb{L}}_{\text{C}} \equiv \tilde{\mathbf{E}}_{22}^{-1} \tilde{\mathbf{A}}_{21}$ ,  $\tilde{\mathbb{L}}_{\text{Sq}} \equiv \tilde{\mathbf{E}}_{22}^{-1} \tilde{\mathbf{A}}_{22}$ , and  $\tilde{\mathbf{A}}$  and  $\tilde{\mathbf{E}}$  matrices are discretised using the Galerkin method and are defined in (2.52). The vector  $\mathbf{z} \in \mathbb{C}^{2N}$  is defined such that stored energy:

$$\hat{\mathbf{E}}(t) \equiv \mathbf{z}^\top(t)\mathbf{z}(t) = \mathbf{x}^\top(t)C^\top C\mathbf{x}(t) = \mathbf{x}^\top(t)Q\mathbf{x}(t), \quad (4.37)$$

where  $Q = Q^\top > 0$  is referred to as the *energy matrix*. The energy density of a single Fourier mode in terms of the primitive variables is given as [86]:

$$\hat{\mathbf{E}}(t) = \frac{1}{8} \int_{-1}^1 (\hat{\mathbf{u}}^\top \hat{\mathbf{u}} + \hat{\mathbf{v}}^\top \hat{\mathbf{v}} + \hat{\mathbf{w}}^\top \hat{\mathbf{w}}) \, dy. \quad (4.38)$$

Using the divergence free condition in (4.26b) and definition of wall-normal vorticity in (2.10), expressions for  $\hat{\mathbf{u}}$  and  $\hat{\mathbf{w}}$  in terms of the state variables can be found:

$$\hat{\mathbf{u}} = \frac{i}{k^2} \left( \alpha \frac{\partial \hat{\mathbf{v}}}{\partial y} - \beta \hat{\boldsymbol{\eta}} \right), \quad (4.39a)$$

$$\hat{\mathbf{w}} = \frac{i}{k^2} \left( \beta \frac{\partial \hat{\mathbf{v}}}{\partial y} + \alpha \hat{\boldsymbol{\eta}} \right). \quad (4.39b)$$

Substituting (4.39) into (4.38) yields:

$$\hat{\mathbf{E}}(t) = \frac{1}{8} \int_{-1}^1 \hat{\mathbf{v}}^\top \hat{\mathbf{v}} + \frac{1}{k^2} \left( \frac{\partial \hat{\mathbf{v}}^\top}{\partial y} \frac{\partial \hat{\mathbf{v}}}{\partial y} + \hat{\boldsymbol{\eta}}^\top \hat{\boldsymbol{\eta}} \right) \, dy, \quad (4.40)$$

Finally, substituting the respective Chebyshev series from (2.27) into (4.40) results in the following discrete energy matrix:

$$\hat{\mathbf{E}}(t) = \underbrace{\begin{bmatrix} \mathbf{a}_{\mathbf{v}_N}^\top(t) & \mathbf{a}_{\boldsymbol{\eta}_N}^\top(t) \end{bmatrix}}_{\mathbf{x}^\top(t)} \underbrace{\begin{bmatrix} Q_{11} & 0 \\ 0 & Q_{22} \end{bmatrix}}_Q \underbrace{\begin{bmatrix} \mathbf{a}_{\mathbf{v}_N}(t) \\ \mathbf{a}_{\boldsymbol{\eta}_N}(t) \end{bmatrix}}_{\mathbf{x}(t)}, \quad (4.41)$$

where:

$$Q_{11(i,j)} = \frac{1}{8} \int_{-1}^1 \left( \phi_i(y)\phi_j(y) + \frac{1}{k^2} \frac{\partial \phi_i}{\partial y}(y) \frac{\partial \phi_j}{\partial y}(y) \right) dy, \quad (4.42a)$$

$$Q_{22(i,j)} = \frac{1}{8k^2} \int_{-1}^1 \psi_i(y)\psi_j(y) dy, \quad (4.42b)$$

and where subscripts  $i,j$  denote matrix row and column indices. The integrals in (4.42) can be evaluated analytically. However, due to the current choice of basis functions, this is not a straightforward task. Therefore, in the current work, the integrals are evaluated numerically using Clenshaw-Curtis quadrature [105]. The  $C$ -matrix from (4.36b) can be calculated by performing a Cholesky decomposition on  $Q$ .

The  $B$ -matrix from (4.36a) remains to be defined. The exogenous forcing  $\mathbf{w}$  is required to be energy-weighted appropriately. Premultiplying (4.36a) by  $C$  gives the following dynamical energy equation:

$$\frac{\partial}{\partial t} \mathbf{z}(t) = CAC^{-1} \mathbf{z}(t) + CB\mathbf{w}(t) = \bar{A}\mathbf{z}(t) + \mathbf{w}(t). \quad (4.43)$$

Therefore, by choosing  $B = C^{-1}$ , disturbance forcing is energy-weighted appropriately. All state-space matrices have now been declared.

In order to evaluate the passivity of the linear channel flow system, the following two things need to be determined:

1. The critical energy Reynolds number for which all modes remain passive.
2. The least passive Fourier mode of the system.

#### 1. Critical energy Reynolds number

The critical energy Reynolds number, denoted  $Re_E$ , is the largest Reynolds number for which *all* Fourier modes of the linear system remain passive. This has been determined previously for a channel flow analytically by Reddy and Henningson [92] and numerically by Zhao and Duncan [115]. The critical energy Reynolds number for a channel flow was found analytically to be  $Re_E = 49.60359$ , corresponding to Fourier mode  $(\alpha = 0, \beta = 2.044)$ [92].

A search over wavenumber space was conducted to find the critical energy Reynolds number of channel flow using the index of passivity calculated from (4.21) as the test for passivity. If for a given Reynolds number  $\varepsilon \geq 0$ , the mode is passive, and non-passive otherwise. The critical energy Reynolds number for an individual mode, denoted  $Re_c$ , is the largest Reynolds number for which that mode remains passive. Therefore, the smallest modal critical energy Reynolds number

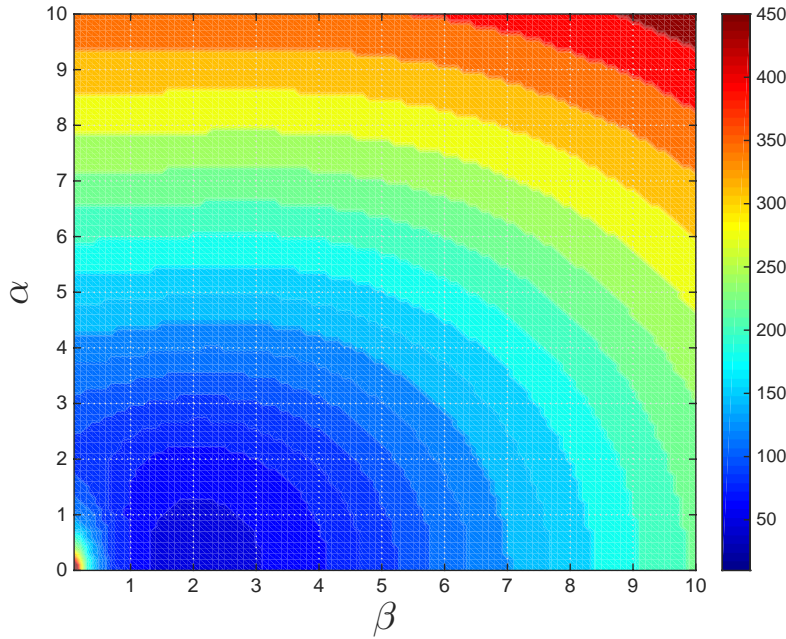


Figure 4.4: Colour map of modal critical energy Reynolds number  $Re_c$  in wavenumber space, computed using wall-normal resolution  $N_y = 60$ .

over all wavenumber space will be the global critical energy Reynolds number, i.e.  $Re_E = \inf_{\alpha, \beta}(Re_c)$ . Figure 4.4 shows a colour map of  $Re_c$  in wavenumber space. Using searches with progressively finer wall-normal resolutions, the critical energy Reynolds number was found to be  $Re_E = 49.60358$ , corresponding to mode  $(\alpha = 0, \beta = 2.044)$  which is near identical to the analytically derived solution. This proves that the index of passivity defined in (4.21) is a reliable indicator of the passivity of a system. The index of passivity as defined in (4.21) will be used throughout the remainder of this chapter to classify the passivity of systems, and to evaluate passivity-based controllers.

## 2. Least passive Fourier mode

The least passive Fourier mode of the linear system, for a given Reynolds number, is defined as the mode with minimal index of passivity  $\varepsilon$ . For  $Re \leq Re_E$  - the least passive mode dissipates energy least, and for  $Re > Re_E$  - the least passive mode is capable of producing the most energy. Figure 4.5 shows contour plots of  $\varepsilon$  in wavenumber space for  $Re = 10, 10^2, 10^3$ , in (a), (b) and (c) respectively. For mode  $(\alpha = 0, \beta = 0)$ , a passivity index cannot be calculated directly and therefore this is set to zero.

In Figure 4.5(a),  $Re = 10 < Re_E$ , therefore  $\varepsilon \geq 0$  for all Fourier modes. It can be seen that for subcritical energy Reynolds numbers, the least passive modes are those close to  $(\alpha = 0, \beta = 0)$ . Therefore, the least passive mode here will be identified as  $(\alpha = 0, \beta = 0)$ , the mean mode. This finding is not surprising because

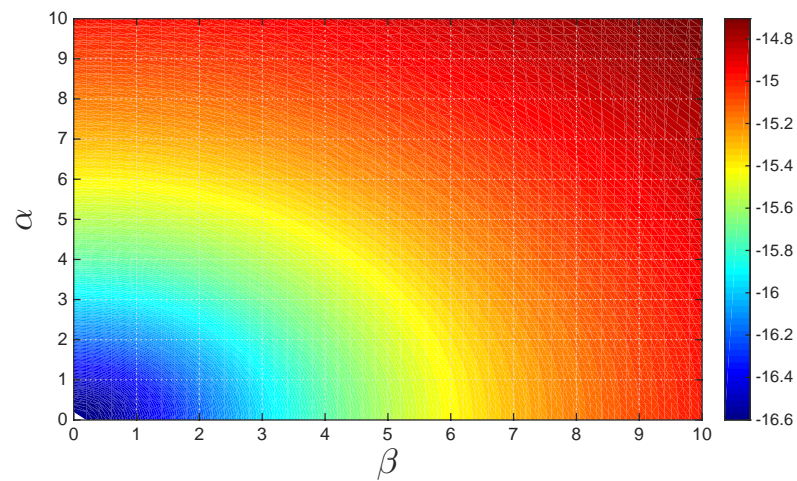
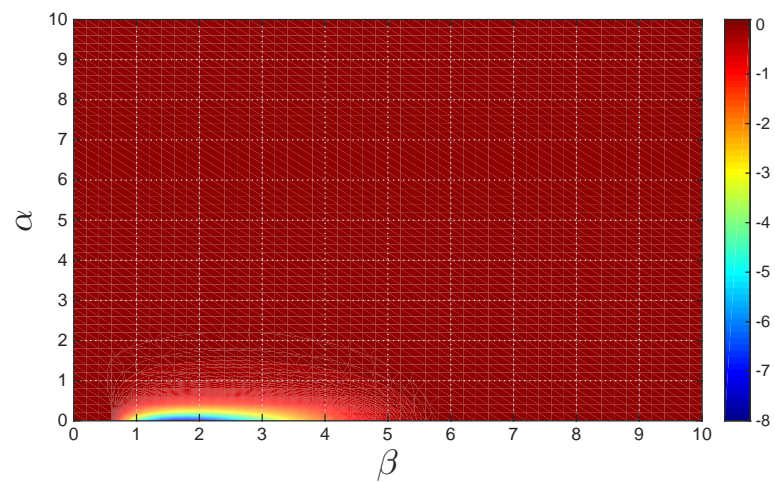
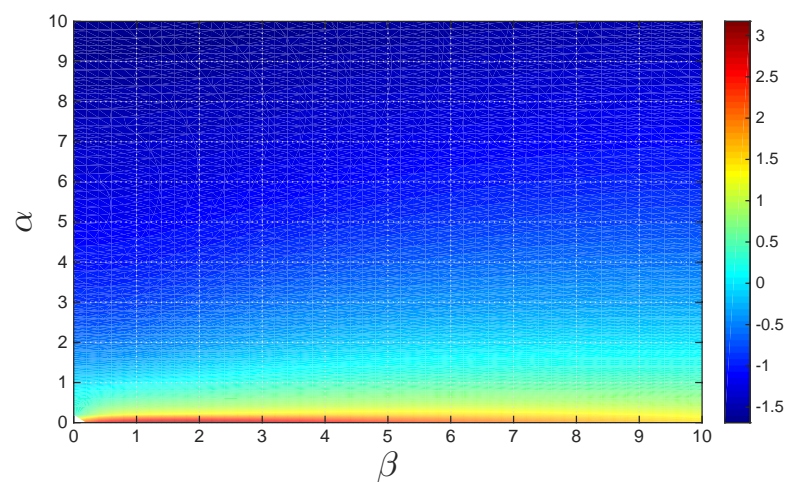
(a)  $\text{Re} = 10, \log_{10} \varepsilon$ (b)  $\text{Re} = 10^2, \varepsilon$ (c)  $\text{Re} = 10^3, \log_{10} |\varepsilon|$ 

Figure 4.5: Colour maps of  $\varepsilon$  in wavenumber space. N.b. a) and c) show contours of  $\log_{10} |\varepsilon|$ , in a) all contours represent positive  $\varepsilon$ , in c) all contours represent negative  $\varepsilon$ . Wall-normal resolution  $N_y = 80$ .

it is the smallest scales of a flow, i.e. large  $\alpha, \beta$ , which dissipate the most energy. Therefore, the larger scales of the flow, i.e. small  $\alpha, \beta$ , can be expected to dissipate the least energy.

In Figure 4.5(b),  $\text{Re} = 10^2 > \text{Re}_E$ , therefore  $\varepsilon > 0$  for a small selection of modes. However, the majority of the modes in the displayed wavenumber space remain passive. This is because local  $\text{Re}_c > 100$  for these modes, as can be seen from Figure 4.4. A plot of the  $|\varepsilon|$  distribution of the streamwise-constant modes for  $\text{Re} = 10^2$  is shown in Figure 4.6. A “bubble” of non-passive modes can be seen between  $(\alpha = 0, \beta = 0.8 - 5.9)$  which corresponds to the patch of negative contours in Figure 4.5(b). It is only these select modes which are capable of producing energy, and having relatively low magnitude indices of passivity, they are limited in the amount of energy they can produce. The least passive mode for  $\text{Re} = 10^2$  was found to be  $(\alpha = 0, \beta = 1.78)$ .

In Figure 4.5(c),  $\text{Re} = 10^3 \gg \text{Re}_E$ , and therefore  $\varepsilon < 0$  for all modes in the wavenumber space displayed. It is clear from the plot that the streamwise-constant modes are a lot less passive than other modes in the wavenumber space. In particular, low  $\beta$  streamwise-constant modes have the lowest indices of passivity, and are therefore capable of producing a relatively large amount of energy. The distribution of  $|\varepsilon|$  for these modes and Reynolds number is given in Figure 4.6. The overall least passive mode for  $\text{Re} = 10^3$  was found to be  $(\alpha = 0, \beta = 1.63)$ . Also plotted on Figure 4.6 are the streamwise-constant mode distributions of  $|\varepsilon|$  for  $\text{Re} = 10^4$  and  $\text{Re} = 10^5$ . These both have a similar shape to the  $\text{Re} = 10^3$  distribution but have higher magnitudes for higher Reynolds number. Interestingly, for both these Reynolds numbers, the least passive mode is located at  $(\alpha = 0, \beta = 1.62)$ . This suggests that for  $\text{Re} \rightarrow \infty$  the least passive mode tends to  $(\alpha = 0, \beta = 1.62)$ . Trefethen et al. [107] stated that mode  $(\alpha = 0, \beta = 1.62)$  has maximum resonance for channel flow, so perhaps this result should be expected. A summary table of least passive modes for different Reynolds number is given in Figure 4.7.

It can be assumed that most turbulent flows of interest will have Reynolds number  $\text{Re} \gg \text{Re}_E$ . Therefore, such systems will have qualitatively similar  $\varepsilon$  distributions to that shown in Figure 4.5(c) - non-passive modes close to the origin in wavenumber space, with the streamwise-constant modes being by far the least passive and therefore most capable of producing energy.

#### 4.3.4 Passivity of the Interconnected System

The passivity theorem can be used to assess the passivity of the feedback interconnection between the linear and nonlinear systems. From Figure 4.3, the following

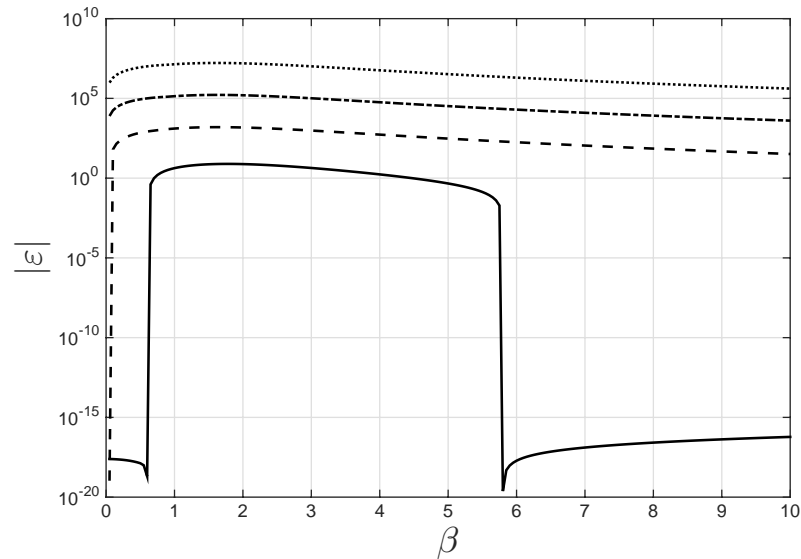


Figure 4.6: Plots of  $\beta$  vs.  $|\varepsilon|$  for  $\text{Re} = 10^2$  (—),  $\text{Re} = 10^3$  (---),  $\text{Re} = 10^4$  (-·-),  $\text{Re} = 10^5$  (··), for streamwise-constant modes ( $\alpha = 0$ ). Wall-normal resolution  $N_y = 80$ .

Re	$\alpha$	$\beta$	$\varepsilon$
10	0	0	0
$10^2$	0	1.78	-7.80
$10^3$	0	1.63	$-1.57 \cdot 10^3$
$10^4$	0	1.62	$-1.65 \cdot 10^5$
$10^5$	0	1.62	$-1.66 \cdot 10^7$

Figure 4.7: Table of least passive modes for different Reynolds numbers.

statements are true:

$$\mathbf{w} = \mathbf{d} - \mathbf{n}, \quad (4.44a)$$

$$\mathbf{v} = L\mathbf{w}. \quad (4.44b)$$

Therefore, the passivity inequality for the interconnected system from disturbance input  $\mathbf{w}$  to velocity output  $\mathbf{v}$  is:

$$\langle \mathbf{v}, \mathbf{w} \rangle_{[0,T]} = \langle L\mathbf{w}, \mathbf{d} \rangle_{[0,T]} - \langle \mathbf{v}, \mathbf{n} \rangle_{[0,T]} \geq \varepsilon \|\mathbf{d}_T\|_2^2 - 0. \quad (4.45)$$

Therefore, as the nonlinearity has been shown to be lossless when wall actuation is not employed, the index of passivity of the linear system alone determines the passivity of the interconnected system. However, as demonstrated, when wall actuation is employed, the net flux of actuation energy will affect the passivity of the nonlinearity and will have to be taken into account.

## 4.4 Passivity-Based Control of Channel Flow

The previous section demonstrated how it is only the linear dynamics which contribute to the passivity of un-actuated channel flow. It was also found that of the linear dynamics, the streamwise-constant modes are, by far, the least passive relative to all other modes in wavenumber space for supercritical energy Reynolds number flows. In this section, LTI controllers will be synthesised for streamwise-constant modes which when connected in feedback, minimise the magnitude of the index of passivity of the resulting closed-loop systems. Doing so should restrict the amount of perturbation energy these modes are able to produce, therefore reducing the total perturbation energy of the flow. This should then lead to a reduction in total skin-friction drag. However, the LTI controllers developed in this section will provide no guarantees of stability when connected in feedback with the nonlinear channel flow system. This would only be the case if each modal controller was able to enforce passivity on the mode it was controlling whilst ensuring the nonlinearity remained lossless. This was achieved by Sharma et al. [101] because their use of actuation via body-forcing ensured the net flux of energy into or out of the domain remained zero. Their LTI controllers were also capable of enforcing passivity on the modes they controlled, although they required wall-normal velocity information throughout the domain to achieve this. In the current work, all controllers have their actuation and sensing restricted to the walls. It was proven by Martinelli et al. [84] that LTI controllers with wall-restricted actuation are unable to enforce passivity on linearised channel flow for  $\text{Re} > \text{Re}_E = 49.6$ . Therefore, as controllers will be designed for and tested on  $\text{Re} = 2230$  channel flow, the objective of the current controllers is to make the linear modes they control *as close to passive as is possible*. It will be assumed that the control actuation signals will be of sufficiently small amplitude that they

have a negligible effect on the passivity of the nonlinearity which shall be assumed lossless throughout. The passivity theorem, discussed in the previous section, has been used as a guide for the current control objective rather than as a proof of closed-loop stability, which is its intended purpose.

#### 4.4.1 Positive-Real Control Method

A number of different control methods for altering the passivity index of a system exist. In the current work, the positive-real control method of Sun et al. [103] shall be used. This is a different method to that used by Sharma et al. [101] who used the method of Safonov et al. [98]. The latter approach involves transforming a positive real controller synthesis problem into a general  $\mathcal{H}_\infty$  problem, then performing loop shifting transformations, before solving two algebraic Riccati equations (AREs). Sun et al.'s approach is more direct and requires solutions to two AREs which in turn are formed from the state-space matrices of a LTI control model; no loop shifting transformations etc. are required. The resulting controller ensures the feedback interconnection between the control model and controller is SIP.

A given Fourier mode of the linear system  $\hat{\mathbf{L}}$  with wall-normal actuation incorporated has state-space representation:

$$\begin{bmatrix} \dot{\mathbf{x}} \\ \mathbf{z} \\ \mathbf{y} \end{bmatrix} = \underbrace{\begin{bmatrix} A & B_1 & B_2 \\ C_1 & 0 & 0 \\ C_2 & 0 & 0 \end{bmatrix}}_{\hat{\mathbf{L}}} \begin{bmatrix} \mathbf{x} \\ \mathbf{w} \\ \mathbf{u} \end{bmatrix}, \quad (4.46)$$

where  $\mathbf{x} \in \mathbb{C}^{2N}$  is the state vector,  $\mathbf{z} \in \mathbb{C}^{2N}$  is the energy-weighted state vector,  $\mathbf{y} \in \mathbb{C}^q$  is a vector of measured outputs,  $\mathbf{w} \in \mathbb{C}^{2N}$  is a vector of energy-weighted disturbance inputs, and  $\mathbf{u} \in \mathbb{C}^2$  is a vector of control actuation signals. Before being of use as a control model, the system model  $\hat{\mathbf{L}}$  in (4.46) needs to be augmented to include a feed-through energy term  $\bar{\epsilon} \geq 0 \in \mathbb{R}$ , control penalty term  $\epsilon_c > 0 \in \mathbb{R}$  and measurement penalty term  $\epsilon_d > 0 \in \mathbb{R}$ . Feed-through energy is the primary controller tuning constant and its importance will be made apparent later on in this section. Penalties on the control effort  $\epsilon_c$  and measurement quality  $\epsilon_d$  are needed to ensure solutions to the AREs are nonsingular. The higher the control penalty, the higher the ‘‘cost’’ of the control effort. Increasing the measurement penalty will make the controller more robust to measurement uncertainty. Including these penalty terms, the final control model for each Fourier mode is given

as:

$$\tilde{\mathbf{L}} \equiv \left[ \begin{array}{c|cc} A & \begin{bmatrix} B_1 & 0 \end{bmatrix} & B_2 \\ \hline \begin{bmatrix} C_1 \\ 0 \end{bmatrix} & \begin{bmatrix} \tilde{\epsilon}I & 0 \\ 0 & I \end{bmatrix} & \begin{bmatrix} 0 \\ \epsilon_c I \end{bmatrix} \\ \hline C_2 & \begin{bmatrix} 0 & \epsilon_d I \end{bmatrix} & 0 \end{array} \right] \equiv \left[ \begin{array}{c|cc} A & \tilde{B}_1 & B_2 \\ \hline \tilde{C}_1 & D_{11} & D_{12} \\ \hline C_2 & D_{21} & 0 \end{array} \right]. \quad (4.47)$$

The final LTI controller  $K$  will have state-space form [103]:

$$\begin{bmatrix} \dot{\mathbf{x}}_K \\ \mathbf{u} \end{bmatrix} = \underbrace{\begin{bmatrix} A_K & B_K \\ C_K & 0 \end{bmatrix}}_K \begin{bmatrix} \mathbf{x}_K \\ \mathbf{y} \end{bmatrix}, \quad (4.48)$$

where  $\mathbf{x}_K \in \mathbb{C}^{N_K}$  are the states of the controller and also estimates of the states of the control model, and matrices  $A_K$ ,  $B_K$  and  $C_K$  are formed from the solutions to the AREs yet to be given. The closed-loop system  $\Sigma_{\tilde{\mathbf{L}} \times K}$  comprised of the control model  $\tilde{\mathbf{L}}$  in feedback with controller  $K$  has state-space form [103]:

$$\Sigma_{\tilde{\mathbf{L}} \times K} \equiv \left[ \begin{array}{cc|c} A & B_2 C_K & \tilde{B}_1 \\ \hline B_K C_2 & A_K & B_K D_{21} \\ \hline \tilde{C}_1 & D_{12} C_K & D_{11} \end{array} \right] \equiv \left[ \begin{array}{c|c} A_{\tilde{\mathbf{L}},K} & B_{\tilde{\mathbf{L}},K} \\ \hline C_{\tilde{\mathbf{L}},K} & D_{11} \end{array} \right]. \quad (4.49)$$

The controller  $K$  is required to ensure two things. Firstly, that  $\Sigma_{\tilde{\mathbf{L}} \times K}$  is internally stable, i.e.  $\Re(\lambda \{A_{\tilde{\mathbf{L}},K}\}) < 0$ . Secondly, that  $\Sigma_{\tilde{\mathbf{L}} \times K}(s)$  is SPR. However, it must be stressed, that a controller capable of making the feedback interconnection between the *control* model  $\tilde{\mathbf{L}}$  and controller SPR, will not make the feedback interconnection between the actual system model  $\hat{\mathbf{L}}$  and controller SPR. This is because the control model includes a feed-through energy term  $D_{11}$  which is artificial and absent from the actual system's dynamics. The feed-through energy term included in control model  $\tilde{\mathbf{L}}$  approximates the index of passivity of the actual closed-loop system  $\Sigma_{\hat{\mathbf{L}} \times K}$ , illustrated in Figure 4.8, after the controller has been generated. This will be demonstrated below.

The transfer function of the closed-loop system comprised of control model  $\tilde{\mathbf{L}}$  and controller  $K$  is defined as:

$$\Sigma_{\tilde{\mathbf{L}},K}(s) \equiv C_{\tilde{\mathbf{L}},K} (sI - A_{\tilde{\mathbf{L}},K})^{-1} B_{\tilde{\mathbf{L}},K} + D_{11}, \quad (4.50)$$

such that  $\mathbf{Z}(s) = \Sigma_{\tilde{\mathbf{L}},K}(s)\mathbf{W}(s)$ , where  $\mathbf{Z}(s)$  and  $\mathbf{W}(s)$  are the Laplace-transformed controlled output vector  $\mathbf{z}(t)$  and disturbance input vector  $\mathbf{w}(t)$  respectively. The

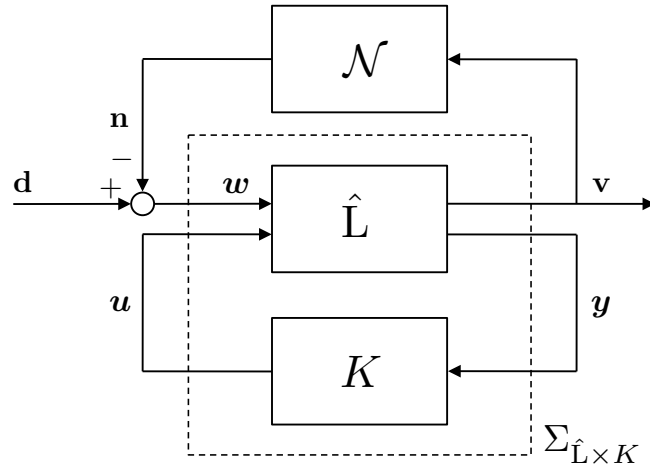


Figure 4.8: Block diagram of channel flow system in feedback with a controller.

transfer function is SPR iff for all  $\omega \in \mathbb{R}$ :

$$\frac{1}{2} \left( \Sigma_{\hat{L},K}(i\omega) + \Sigma_{\hat{L},K}^\top(-i\omega) \right) > 0. \quad (4.51)$$

Taking the feed-through terms ( $D$  matrices) to the right-hand-side of (4.51) yields:

$$\left( \Sigma_{\hat{L},K}(i\omega) + \Sigma_{\hat{L},K}^\top(-i\omega) \right) > -2\bar{\varepsilon}I \approx 2\varepsilon_{L,K}I, \quad (4.52)$$

where  $\Sigma_{\hat{L},K}(s) \equiv C_{L,K}(sI - A_{L,K})^{-1}B_{L,K}$  is the closed-loop transfer function for the feedback interconnection of system model  $\hat{L}$  and controller  $K$ , and  $\varepsilon_{L,K} < 0$  is the resulting index of passivity for the closed-loop system.

#### 4.4.2 Controller Synthesis

All controllers are designed for and tested on  $Re = 2230$  channel flow. This maximum laminar centreline velocity Reynolds number was used as it corresponds to  $Re_\tau = 100$  fully turbulent channel flow - a commonly used skin-friction Reynolds number for testing drag reducing controllers [50, 78, 101]. This Reynolds number is supercritical in terms of energy, i.e.  $Re > Re_E$ , and therefore a large area of the wavenumber space of the uncontrolled system will be non-passive. However, this Reynolds number is subcritical in terms of hydrodynamic stability, and will therefore be linear locally stable. For local stability, the critical Reynolds number for a channel flow is  $Re_C = 5772.2$  [88].

The procedure for synthesising controllers  $K$  using the positive real control method of Sun et al. [103] is provided in Appendix A. In the following, the state-space matrices of the system model  $\hat{L}$  in (4.46) will be defined for each controller. In order to investigate the effect of wall-normal discretisation on controller performance, both the collocation and Galerkin methods will be used to form control models.

All controllers will use wall transpiration as actuation. Therefore, matrices  $A$  and  $B_2$  are defined in (2.66) for the Galerkin model and (2.69) for the collocation model, where a lifting procedure is used to incorporate this type of actuation; Section 2.2.2 outlines the procedure for discretising operators using the collocation and Galerkin methods. Because a low-pass filter is used to model actuator dynamics, both of these matrices are functions of  $\tau_\phi$  - the actuator time-constant.

For the Galerkin discretised model, the energy matrix  $Q$  is calculated as in (4.41), except that the last two wall-normal velocity basis functions  $\phi_{N-1}$  and  $\phi_N$  are replaced with lifting functions  $f_u$  and  $f_l$  respectively, in order that the energy of the actuation be included. Therefore,  $Q$  is defined:

$$\hat{E}(t) = \underbrace{\begin{bmatrix} \mathbf{a}_{\mathbf{v}_{0N-2}}^\top & \hat{\mathbf{v}}^{+\top} & \hat{\mathbf{v}}^{-\top} & \mathbf{a}_{\eta_N}^\top \end{bmatrix}}_{\mathbf{x}^\top} \underbrace{\begin{bmatrix} Q_{11} & 0 & 0 & 0 \\ 0 & Q_{22} & 0 & 0 \\ 0 & 0 & Q_{33} & 0 \\ 0 & 0 & 0 & Q_{44} \end{bmatrix}}_Q \underbrace{\begin{bmatrix} \mathbf{a}_{\mathbf{v}_{0N-2}} \\ \hat{\mathbf{v}}^+ \\ \hat{\mathbf{v}}^- \\ \mathbf{a}_{\eta_N} \end{bmatrix}}_{\mathbf{x}}, \quad (4.53)$$

where,

$$Q_{11(i,j)} = \frac{1}{8} \int_{-1}^1 \left( \phi_i(y)\phi_j(y) + \frac{1}{k^2} \frac{\partial \phi_i}{\partial y}(y) \frac{\partial \phi_j}{\partial y}(y) \right) dy, \quad (4.54a)$$

$$Q_{22} = \frac{1}{8} \int_{-1}^1 \left( f_u(y)f_u(y) + \frac{1}{k^2} \frac{\partial f_u}{\partial y}(y) \frac{\partial f_u}{\partial y}(y) \right) dy, \quad (4.54b)$$

$$Q_{33} = \frac{1}{8} \int_{-1}^1 \left( f_l(y)f_l(y) + \frac{1}{k^2} \frac{\partial f_l}{\partial y}(y) \frac{\partial f_l}{\partial y}(y) \right) dy, \quad (4.54c)$$

$$Q_{44(i,j)} = \frac{1}{8k^2} \int_{-1}^1 \psi_i(y)\psi_j(y)dy. \quad (4.54d)$$

For the collocation discretised model, the energy matrix is defined:

$$\hat{E}(t) = \underbrace{\begin{bmatrix} \hat{\mathbf{v}}_0^\top & \hat{\mathbf{v}}^{+\top} & \hat{\mathbf{v}}^{-\top} & \hat{\eta}^\top \end{bmatrix}}_{\mathbf{x}^\top} \underbrace{\begin{bmatrix} Q_{11} & 0 & 0 & 0 \\ 0 & Q_{22} & 0 & 0 \\ 0 & 0 & Q_{33} & 0 \\ 0 & 0 & 0 & Q_{44} \end{bmatrix}}_Q \underbrace{\begin{bmatrix} \hat{\mathbf{v}}_0 \\ \hat{\mathbf{v}}^+ \\ \hat{\mathbf{v}}^- \\ \hat{\eta} \end{bmatrix}}_{\mathbf{x}}, \quad (4.55)$$

where,

$$Q_{11} = \frac{1}{8} \left( \mathbf{\Omega}_{N-2} + \frac{1}{k^2} (\tilde{\mathbf{D}}_{\mathbf{v}_{N-2}}^1)^\top \mathbf{\Omega}_{N-2} \tilde{\mathbf{D}}_{\mathbf{v}_{N-2}}^1 \right), \quad (4.56a)$$

$$Q_{22} = \frac{1}{8} \left( \mathbf{f}_u^\top(y_j) \mathbf{\Omega}_{N-2} \mathbf{f}_u(y_j) + \frac{1}{k^2} (\tilde{\mathbf{D}}_{\mathbf{v}_{N-2}}^1 \mathbf{f}_u(y_j))^\top \mathbf{\Omega}_{N-2} \tilde{\mathbf{D}}_{\mathbf{v}_{N-2}}^1 \mathbf{f}_u(y_j) \right), \quad (4.56b)$$

$$Q_{33} = \frac{1}{8} \left( \mathbf{f}_1^\top(y_j) \boldsymbol{\Omega}_{N-2} \mathbf{f}_1(y_j) + \frac{1}{k^2} (\tilde{D}_{v_{N-2}}^1 \mathbf{f}_1(y_j))^\top \boldsymbol{\Omega}_{N-2} \tilde{D}_{v_{N-2}}^1 \mathbf{f}_1(y_j) \right), \quad (4.56c)$$

$$Q_{44} = \frac{1}{8k^2} \boldsymbol{\Omega}_N, \quad (4.56d)$$

where  $\boldsymbol{\Omega}$  is a matrix of Clenshaw-Curtis integration weights [105], and  $\tilde{D}_v^1$  is a first Chebyshev differential matrix for wall-normal velocity.

For both cases,  $Q = C_1^\top C_1$ , and  $B_1 = C_1^{-1}$ . Note that for the collocation discretised model, the basis and lifting functions are evaluated on a set of  $N$  fixed grid points. This means that the Clenshaw-Curtis integration weighting matrix needs to be of dimension  $N$ . Zhao and Duncan [115] found that this leads to numerical errors in matrix entries  $Q_{(i,j)}$  with  $i + j > 2N - 3$ . This is not the case for the Galerkin method, where the basis and lifting functions are kept continuous, and therefore the integrals can be computed using a Clenshaw-Curtis integration weighting matrix of any dimension.

Two wall-based sensing arrangements will be investigated to ascertain their effect on controller performance. The first arrangement will include streamwise and spanwise wall-shear stress perturbations at both walls (sensing arrangement 1). The second will include streamwise and spanwise wall-shear stress perturbations *and* pressure perturbations at both walls (sensing arrangement 2). The sensing matrix,  $\mathbf{y} = C_2 \mathbf{x}$ , will be defined below for both of these arrangements.

#### Sensing Arrangement 1

Streamwise ( $\hat{\tau}_{yx}$ ) and spanwise ( $\hat{\tau}_{yz}$ ) wall-shear stress perturbations are defined:

$$\mathbf{y} = \begin{bmatrix} \hat{\tau}_{yx}|_{y=\pm 1} \\ \hat{\tau}_{yz}|_{y=\pm 1} \end{bmatrix} \equiv \frac{1}{\text{Re}} \begin{bmatrix} \left( \frac{\partial \hat{u}}{\partial y} + \frac{\partial \hat{v}}{\partial x} \right) \Big|_{y=\pm 1} \\ \left( \frac{\partial \hat{w}}{\partial y} + \frac{\partial \hat{v}}{\partial z} \right) \Big|_{y=\pm 1} \end{bmatrix}. \quad (4.57)$$

Substituting (4.39) into (4.57) yields:

$$\mathbf{y} = \frac{1}{\text{Re}} \begin{bmatrix} \left( i\alpha \left( \frac{1}{k^2} \frac{\partial^2 \hat{v}}{\partial y^2} + \hat{v} \right) - \frac{i\beta}{k^2} \frac{\partial \hat{\eta}}{\partial y} \right) \Big|_{y=\pm 1} \\ \left( i\beta \left( \frac{1}{k^2} \frac{\partial^2 \hat{v}}{\partial y^2} + \hat{v} \right) + \frac{i\alpha}{k^2} \frac{\partial \hat{\eta}}{\partial y} \right) \Big|_{y=\pm 1} \end{bmatrix}. \quad (4.58)$$

However, the  $\hat{v}$  terms are dropped because the controller sets the values of  $\hat{v}$  ( $y = \pm 1$ ), and are hence known. Therefore, for the Galerkin discretised model, the  $C_2$  matrix

for this sensing arrangement is defined:

$$\mathbf{y} = \frac{1}{k^2 \cdot \text{Re}} \underbrace{\begin{bmatrix} i\alpha\Phi_N''(+1) & i\alpha f_u''(+1) & i\alpha f_l''(+1) & -i\beta\Psi_N'(+1) \\ i\alpha\Phi_N''(-1) & i\alpha f_u''(-1) & i\alpha f_l''(-1) & -i\beta\Psi_N'(-1) \\ i\beta\Phi_N''(+1) & i\beta f_u''(+1) & i\beta f_l''(+1) & i\alpha\Psi_N'(+1) \\ i\beta\Phi_N''(-1) & i\beta f_u''(-1) & i\beta f_l''(-1) & i\alpha\Psi_N'(-1) \end{bmatrix}}_{C_2} \underbrace{\begin{bmatrix} \mathbf{a}_{v_{N-2}} \\ \hat{v}^+ \\ \hat{v}^- \\ \mathbf{a}_{\eta_N} \end{bmatrix}}_{\mathbf{x}}, \quad (4.59)$$

where ' denotes differentiation with respect to  $y$ . Likewise, for the collocation model, the  $C_2$  matrix is defined:

$$\mathbf{y} = \frac{1}{k^2 \cdot \text{Re}} \underbrace{\begin{bmatrix} i\alpha\tilde{D}_{v[1,:]}^2 & i\alpha\tilde{D}_{v[1,:]}^2 f_u(y_j) & i\alpha\tilde{D}_{v[1,:]}^2 f_l(y_j) & -i\beta\tilde{D}_{\eta[1,:]}^1 \\ i\alpha\tilde{D}_{v[N,:]}^2 & i\alpha\tilde{D}_{v[N,:]}^2 f_u(y_j) & i\alpha\tilde{D}_{v[N,:]}^2 f_l(y_j) & -i\beta\tilde{D}_{\eta[N,:]}^1 \\ i\beta\tilde{D}_{v[1,:]}^2 & i\beta\tilde{D}_{v[1,:]}^2 f_u(y_j) & i\beta\tilde{D}_{v[1,:]}^2 f_l(y_j) & i\alpha\tilde{D}_{\eta[1,:]}^1 \\ i\beta\tilde{D}_{v[N,:]}^2 & i\beta\tilde{D}_{v[N,:]}^2 f_u(y_j) & i\beta\tilde{D}_{v[N,:]}^2 f_l(y_j) & i\alpha\tilde{D}_{\eta[N,:]}^1 \end{bmatrix}}_{C_2} \underbrace{\begin{bmatrix} \hat{v}_0 \\ \hat{v}^+ \\ \hat{v}^- \\ \hat{\eta} \end{bmatrix}}_{\mathbf{x}}, \quad (4.60)$$

where subscript  $_{[i,:]}$  denotes all columns of a matrix for row index  $i$ .

### Sensing Arrangement 2

The Poisson equation in (2.8) gives a direct relation between perturbation pressure and perturbation wall-normal velocity. However, to avoid having to invert a Laplacian matrix, McKernan [86] suggested an alternative method for calculating wall pressure. The streamwise and spanwise momentum equations in (2.5a) and (2.5c), once velocity and pressure have been Fourier discretised appropriately, can be rearranged to yield:

$$i\alpha\hat{p} = \frac{1}{\text{Re}} \hat{\nabla}^2 \hat{u} - i\alpha\tilde{U}\hat{u} - \hat{v} \frac{\partial \tilde{U}}{\partial y} - \frac{\partial \hat{u}}{\partial t}, \quad (4.61a)$$

$$i\beta\hat{p} = \frac{1}{\text{Re}} \hat{\nabla}^2 \hat{w} - i\alpha\tilde{U}\hat{w} - \frac{\partial \hat{w}}{\partial t}. \quad (4.61b)$$

Therefore, adding (4.61a) and (4.61b) together, substituting in (4.39), and rearranging, gives the following equation for perturbation pressure at the walls:

$$\hat{p}|_{y=\pm 1} = \frac{1}{k^2} \frac{1}{\text{Re}} \left( \frac{\partial^3 \hat{v}}{\partial y^3} + \frac{\alpha - \beta}{\alpha + \beta} \frac{\partial^2 \hat{\eta}}{\partial y^2} \right) \Big|_{y=\pm 1} + \left( \frac{i}{\alpha + \beta} \frac{\partial \tilde{U}}{\partial y} \hat{v} \right) \Big|_{y=\pm 1}, \quad (4.62)$$

where the fact that  $\hat{u}(y = \pm 1) = \hat{w}(y = \pm 1) = 0$  has been used in the derivation. The final term on the right-hand-side of (4.62) can be dropped as was done for the first sensing arrangement. As can be seen, wall pressure measurements provide higher-order wall-normal derivatives of the states  $\hat{v}$  and  $\hat{\eta}$ . This should allow for better state estimation when the shear-stress measurements are also included.

Therefore, for the Galerkin model, the final  $C_2$  matrix for this sensing arrangement is as follows:

$$\mathbf{y} = \frac{1}{k^2 \cdot \text{Re}} \underbrace{\begin{bmatrix} i\alpha\Phi_N''(+1) & i\alpha f_u''(+1) & i\alpha f_1''(+1) & -i\beta\Psi_N'(+1) \\ i\alpha\Phi_N''(-1) & i\alpha f_u''(-1) & i\alpha f_1''(-1) & -i\beta\Psi_N'(-1) \\ i\beta\Phi_N''(+1) & i\beta f_u''(+1) & i\beta f_1''(+1) & i\alpha\Psi_N'(+1) \\ i\beta\Phi_N''(-1) & i\beta f_u''(-1) & i\beta f_1''(-1) & i\alpha\Psi_N'(-1) \\ \Phi_N'''(+1) & f_u'''(+1) & f_1'''(+1) & \frac{\alpha-\beta}{\alpha+\beta}\Psi_N''(+1) \\ \Phi_N'''(-1) & f_u'''(-1) & f_1'''(-1) & \frac{\alpha-\beta}{\alpha+\beta}\Psi_N''(-1) \end{bmatrix}}_{C_2} \underbrace{\begin{bmatrix} \mathbf{a}_{v_{N-2}} \\ \hat{v}^+ \\ \hat{v}^- \\ \mathbf{a}_{\eta_N} \end{bmatrix}}_{\mathbf{x}}, \quad (4.63)$$

where the last two rows of the  $C_2$  matrix in (4.63) correspond to the wall pressure measurements at the upper and lower walls respectively. The final  $C_2$  matrix for the collocation discretised model is defined:

$$\mathbf{y} = \frac{1}{k^2 \cdot \text{Re}} \underbrace{\begin{bmatrix} i\alpha\tilde{D}_{v[1,:]}^2 & i\alpha\tilde{D}_{v[1,:]}^2 f_u(y_j) & i\alpha\tilde{D}_{v[1,:]}^2 f_1(y_j) & -i\beta\tilde{D}_{\eta[1,:]}^1 \\ i\alpha\tilde{D}_{v[N,:]}^2 & i\alpha\tilde{D}_{v[N,:]}^2 f_u(y_j) & i\alpha\tilde{D}_{v[N,:]}^2 f_1(y_j) & -i\beta\tilde{D}_{\eta[N,:]}^1 \\ i\beta\tilde{D}_{v[1,:]}^2 & i\beta\tilde{D}_{v[1,:]}^2 f_u(y_j) & i\beta\tilde{D}_{v[1,:]}^2 f_1(y_j) & i\alpha\tilde{D}_{\eta[1,:]}^1 \\ i\beta\tilde{D}_{v[N,:]}^2 & i\beta\tilde{D}_{v[N,:]}^2 f_u(y_j) & i\beta\tilde{D}_{v[N,:]}^2 f_1(y_j) & i\alpha\tilde{D}_{\eta[N,:]}^1 \\ \tilde{D}_{v[1,:]}^3 & \tilde{D}_{v[1,:]}^3 f_u(y_j) & \tilde{D}_{v[1,:]}^3 f_1(y_j) & \frac{\alpha-\beta}{\alpha+\beta}\tilde{D}_{\eta[1,:]}^2 \\ \tilde{D}_{v[N,:]}^3 & \tilde{D}_{v[N,:]}^3 f_u(y_j) & \tilde{D}_{v[N,:]}^3 f_1(y_j) & \frac{\alpha-\beta}{\alpha+\beta}\tilde{D}_{\eta[N,:]}^2 \end{bmatrix}}_{C_2} \underbrace{\begin{bmatrix} \hat{v}_0 \\ \hat{v}^+ \\ \hat{v}^- \\ \hat{\eta} \end{bmatrix}}_{\mathbf{x}}. \quad (4.64)$$

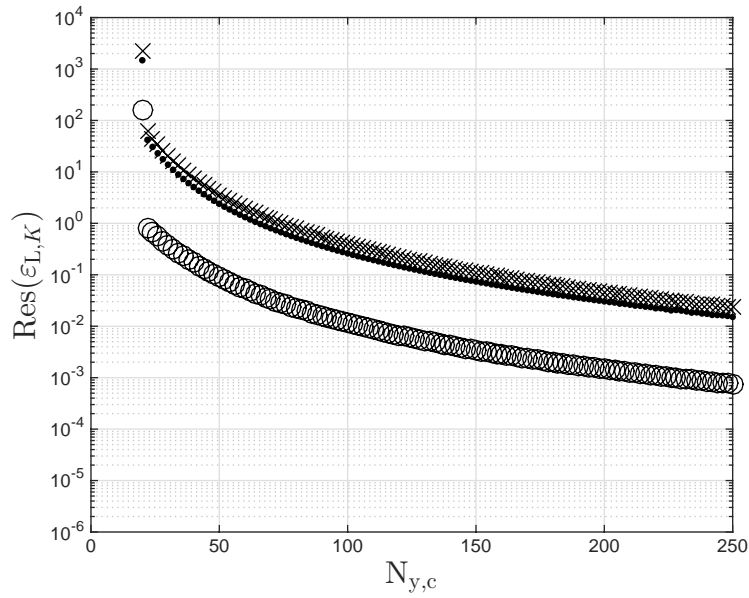
#### 4.4.3 Controller Dimension

The closed-loop index of passivity  $\varepsilon_{L,K}$  is used as an indicator of controller convergence. By evaluating the residual of the closed-loop index of passivity of controllers with increasing dimension, a controller can be deemed to have converged when this residual is suitably small. The residual of the closed-loop index of passivity is defined as:

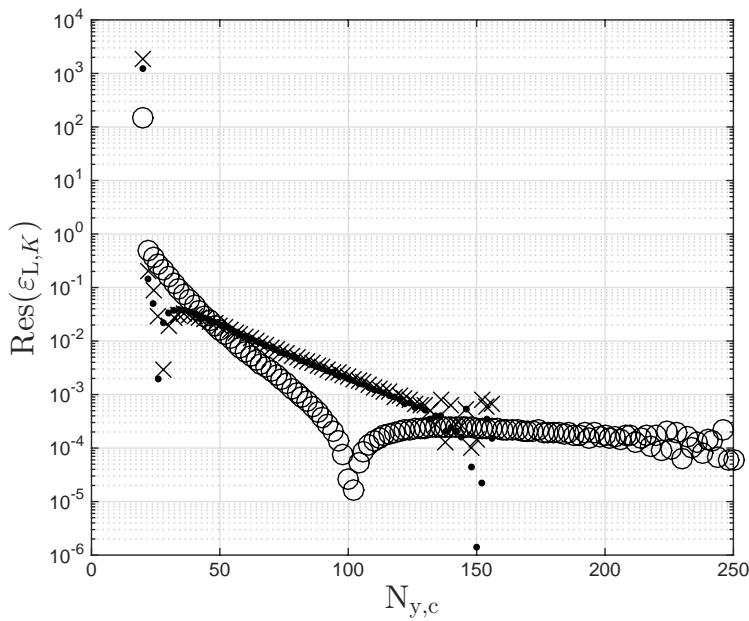
$$\text{Res}(\varepsilon_{L,K})|_{N_{y,c}} = |(\varepsilon_{N_{y,c}} - \varepsilon_{N_{y,c-1}})|. \quad (4.65)$$

Figures 4.9 and 4.10 show plots of this residual for both the collocation and Galerkin discretised controllers with sensing arrangements 1 and 2, for wavenumber pairs  $(\alpha = 0, \beta = 1, 2, 10)$ . For these plots, controllers were connected in feedback with a linear system model of fixed dimension  $N_y = 100$ , discretised in the same manner as the controllers. All controllers were generated with penalties  $\epsilon_c = \epsilon_d = 0.001$ , actuator time-constant  $\tau_\phi = 0.01$ , and constant feed-through energy  $\bar{\varepsilon} = -\varepsilon_L$ , where  $\varepsilon_L$  is the index of passivity of the open-loop system for that mode.

From the residual plots for sensing arrangement 1 in Figure 4.9, it can be seen

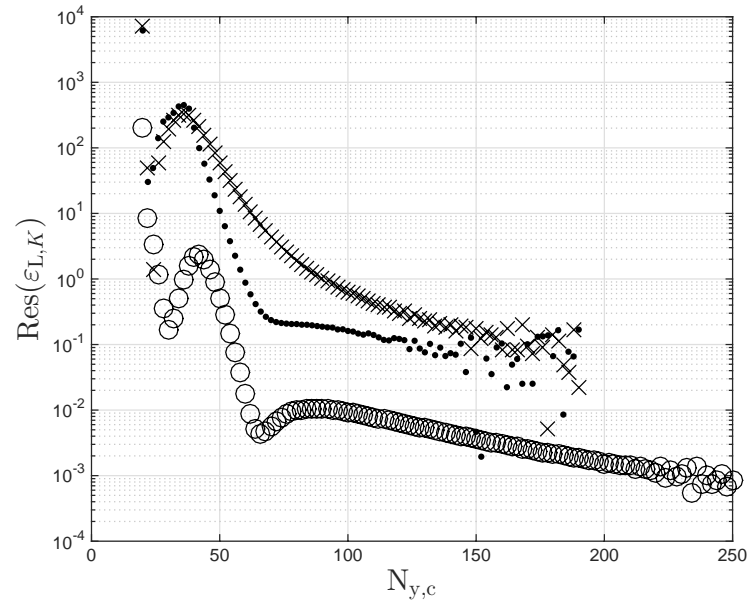


(a) Collocation Method

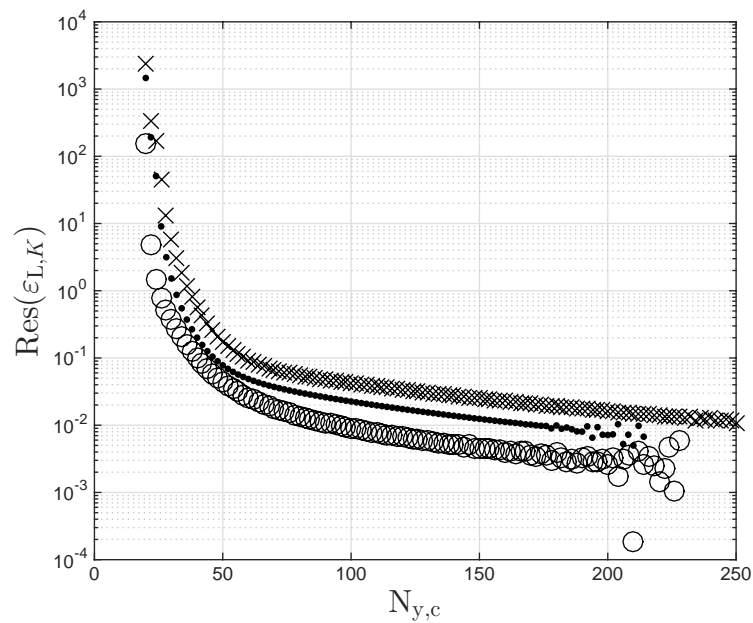


(b) Galerkin Method

Figure 4.9: Plots of residual closed-loop index of passivity for controllers generated using control models discretised via the collocation and Galerkin methods with **sensing arrangement 1**, for wavenumber pairs  $(\alpha = 0, \beta = 1)$  - ( $\cdot$ ),  $(\alpha = 0, \beta = 2)$  - ( $\times$ ), and  $(\alpha = 0, \beta = 10)$  - ( $\circ$ ).



(a) Collocation Method



(b) Galerkin Method

Figure 4.10: Plots of residual closed-loop index of passivity for controllers generated using control models discretised via the collocation and Galerkin methods with **sensing arrangement 2**, for wavenumber pairs  $(\alpha = 0, \beta = 1)$  - ( $\cdot$ ),  $(\alpha = 0, \beta = 2)$  - ( $\times$ ), and  $(\alpha = 0, \beta = 10)$  - ( $\circ$ ).

that the Galerkin discretised controllers converge relatively quickly, with modes  $(\alpha = 0, \beta = 1, 2)$  converged for  $N_{y,c} > 130$  and mode  $(\alpha = 0, \beta = 10)$  converged for  $N_{y,c} > 230$ . The collocation-discretised controllers have poor rates of convergence, with none of the modes fully converging for  $N_{y,c} < 250$ . Controllers become prohibitively expensive to compute for higher resolutions. However, for resolution  $N_{y,c} = 250$ , the residual for all controllers is sufficiently small.

Figure 4.10 shows residual plots for sensing arrangement 2. The collocation controllers converge well relative to the other sensing arrangement, with modes  $(\alpha = 0, \beta = 1, 2)$  converged for  $N_{y,c} > 160$ , and mode  $(\alpha = 0, \beta = 10)$  converged for  $N_{y,c} > 230$ . The Galerkin discretised controllers converge at much finer resolutions compared to the first sensing arrangement. Modes  $(\alpha = 0, \beta = 1, 10)$  converge for  $N_{y,c} > 200$ , and mode  $(\alpha = 0, \beta = 2)$  does not fully converge for  $N_{y,c} < 250$ . However, the residual for this mode is sufficiently small enough for resolution  $N_{y,c} = 250$ .

Because the Galerkin discretised controllers with both sensing arrangements all converge, or are close to converging, for  $N_{y,c} > 250$ , it was decided to make the resolution of all Galerkin controllers for all modes  $N_{y,c} = 250$ . As none of the collocation controllers fully converged for sensing arrangement 1, it was decided to evaluate collocation controllers of resolution  $N_{y,c} = 168$  and  $N_{y,c} = 250$ , in order to investigate how this affects controller performance. For sensing arrangement 2, the collocation controllers all converge for  $N_{y,c} > 250$ . Therefore, all collocation controllers with this sensing arrangement will have resolution  $N_{y,c} = 250$ .

#### 4.4.4 Linear Analysis

“Optimal” passivity-based controllers  $K_{\min}$  were generated for the first fifteen streamwise-constant modes of the linear system. The open-loop  $(\varepsilon_L)$  and closed-loop  $(\varepsilon_{L,K_{\min}})$  indices of passivity for these modes are plotted in Figure 4.11 for both collocation and Galerkin discretised controllers and both sensing arrangements. These represent the “best-case” controllers in terms of control and measurement penalties, because solutions to the AREs no longer exist if they are made any smaller. All controllers have control penalty  $\epsilon_c = 0.001$ , measurement penalty  $\epsilon_d = 0.001$ , and actuator time-constant  $\tau_\phi = 0.01$ .

Figure 4.11 shows that there is little difference between the performance of collocation and Galerkin controllers with either sensing arrangement. This suggests that both methods of discretisation produce similar controllers. The effect of the controllers on the lowest streamwise-constant modes is most apparent, with reductions in  $|\varepsilon|$  of  $\approx 80\%$  and  $\approx 75\%$  for  $(\alpha = 0, \beta = 1)$  and  $(\alpha = 0, \beta = 2)$  respectively. These large reductions in index of passivity will have the effect of

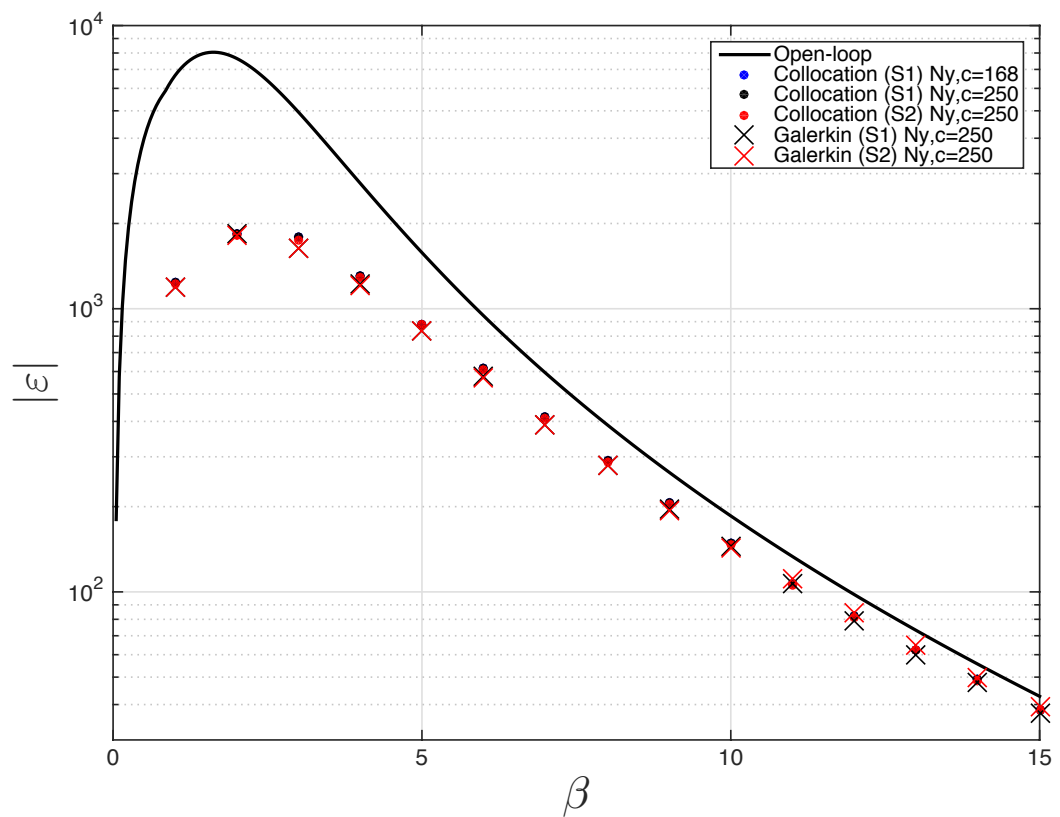


Figure 4.11: Plot of  $|\varepsilon_L|$  (thick line) and  $|\varepsilon_{L,K_{\min}}|$  for both collocation ( $\cdot$ ) and Galerkin ( $\times$ ) discretised control models, for sensing arrangement 1 (S1) and sensing arrangement 2 (S2); all controllers have penalties  $\epsilon_c = \epsilon_d = 0.001$ , and actuator time-constant  $\tau_\phi = 0.01$ .

greatly restricting the amount of energy these modes can potentially produce. The reduction in  $|\varepsilon|$  tends to zero for modes ( $\alpha = 0, \beta > 10$ ), suggesting there is little justification for trying to control them. Galerkin-discretised controllers with sensing arrangement 2 achieve marginally better reductions in  $|\varepsilon|$  for the majority of modes. The collocation-discretised controllers with sensing arrangement 1 achieve near-identical closed-loop passivity indices for both resolutions, which is to be expected.

Figures 4.12 and 4.13 show plots of spectra and  $\epsilon$ -*pseudospectra* for wavenumber pair ( $\alpha = 0, \beta = 2$ ), for the open-loop and all closed-loop cases. For the open-loop case, the projection of contours into the right-half-plane (i.e.  $\Re(s) > 0$ ) shows that the system is capable of large transient energy growth. This is shown to be the case in Figure 4.14 which shows the transient energy growth of the uncontrolled system from an “optimal” initial condition. The initial condition is optimal in the sense that it produces maximum peak transient energy growth [18]. It can be seen that this initial condition causes a peak transient energy growth of  $E(t)/E(0) \approx 960$  for  $t \approx 180$ . It is thought that it is due to these large transient amplifications in energy that subcritical Reynolds number flows transition to turbulence via nonlinear bypass mechanisms [99].

Figure 4.12 shows plots of spectra and  $\epsilon$ -*pseudospectra* for both the collocation and Galerkin controlled systems with sensing arrangement 1. There are no observable differences between them. This is not surprising, considering that controllers discretised using either method enforce a very similar closed-loop index of passivity for this mode. Both controllers pull the contours of  $\epsilon$ -*pseudospectra* tightly into the stable left-half-plane. The closed-loop spectra are also moved further into the left-half-plane. This would suggest that the transient energy growth of this mode would be greatly restricted when either controller is implemented. This prediction is confirmed in Figure 4.14. Both the collocation and Galerkin-discretised controllers achieve a reduction in peak transient energy growth of  $\approx 80\%$ .

Figure 4.12 shows plots of spectra and  $\epsilon$ -*pseudospectra* for both the collocation and Galerkin controlled systems with sensing arrangement 2. As for the first sensing arrangement, there is little difference between the spectra and  $\epsilon$ -*pseudospectra* of either closed-loop system. The only noticeable difference is that some of the spectra of the Galerkin-discretised closed-loop system appear to be pulled further into the stable left-half-plane. Both controllers pull the contours of  $\epsilon$ -*pseudospectra* slightly further into the left-half-plane than for the first sensing arrangement. This would suggest a noticeable reduction in peak transient energy growth relative to the first sensing arrangement. Figure 4.14 shows that the collocation-discretised controller with sensing arrangement 2 does reduce peak transient energy growth

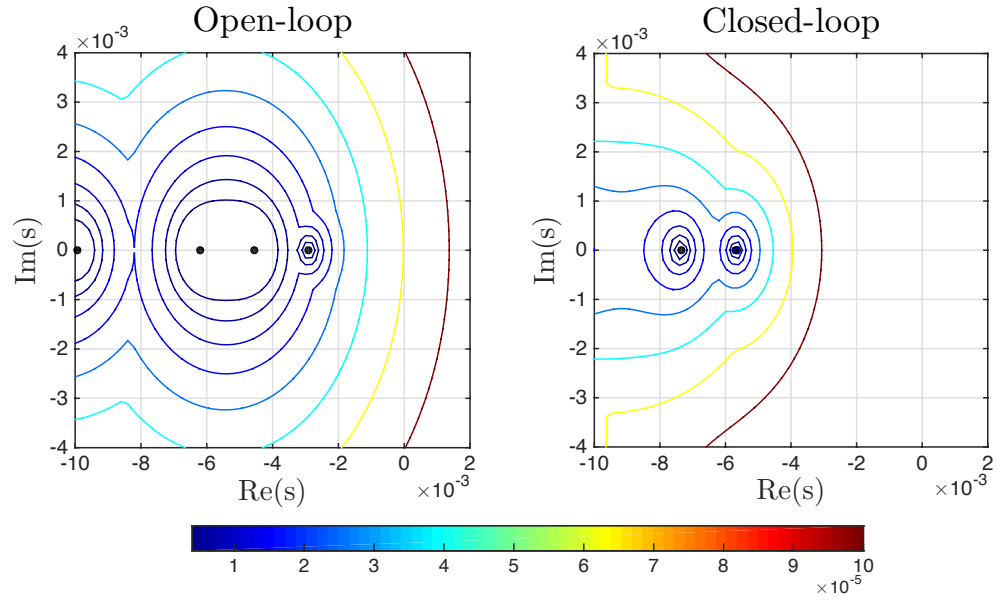
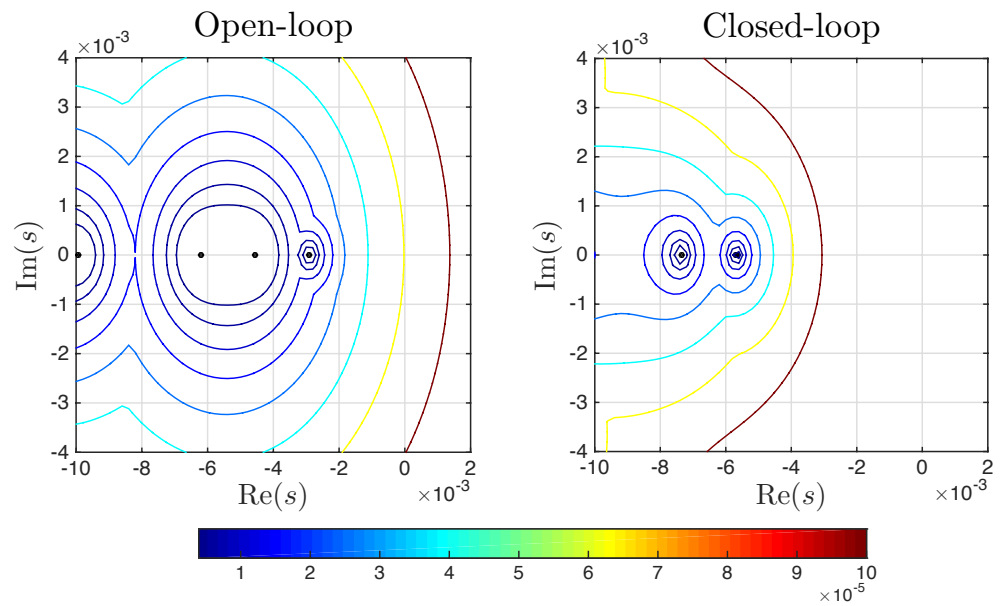
(a) Collocation,  $N_{y,c} = 250$ (b) Galerkin,  $N_{y,c} = 250$ 

Figure 4.12: Spectra (black dots) and  $\epsilon$ -pseudospectra (coloured contours) for open-loop and closed-loop ( $\alpha = 0, \beta = 2$ ) system with **sensing arrangement 1**,  $\epsilon_c = \epsilon_d = 0.001$ ,  $\tau_\phi = 0.01$ .

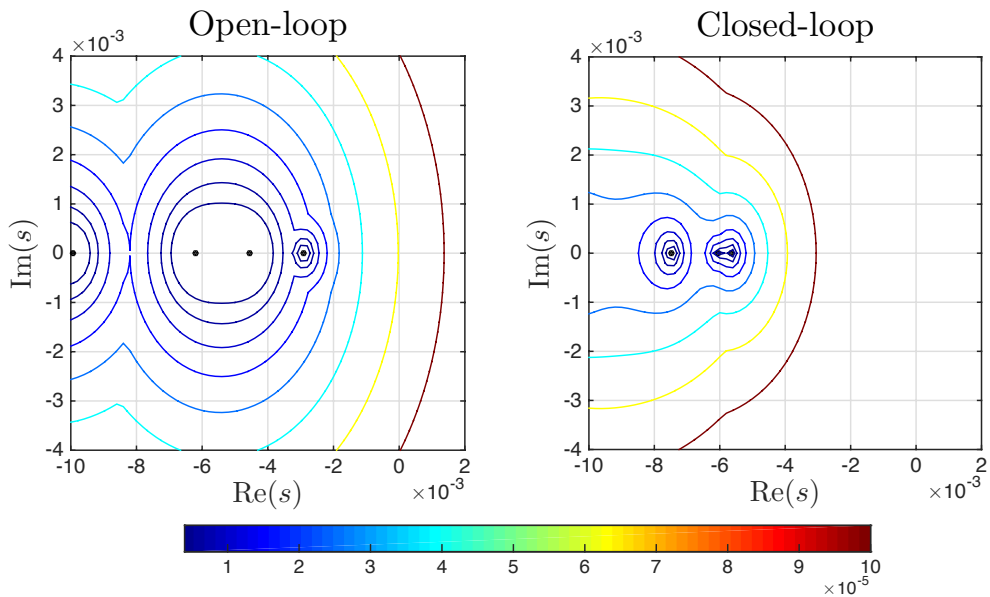
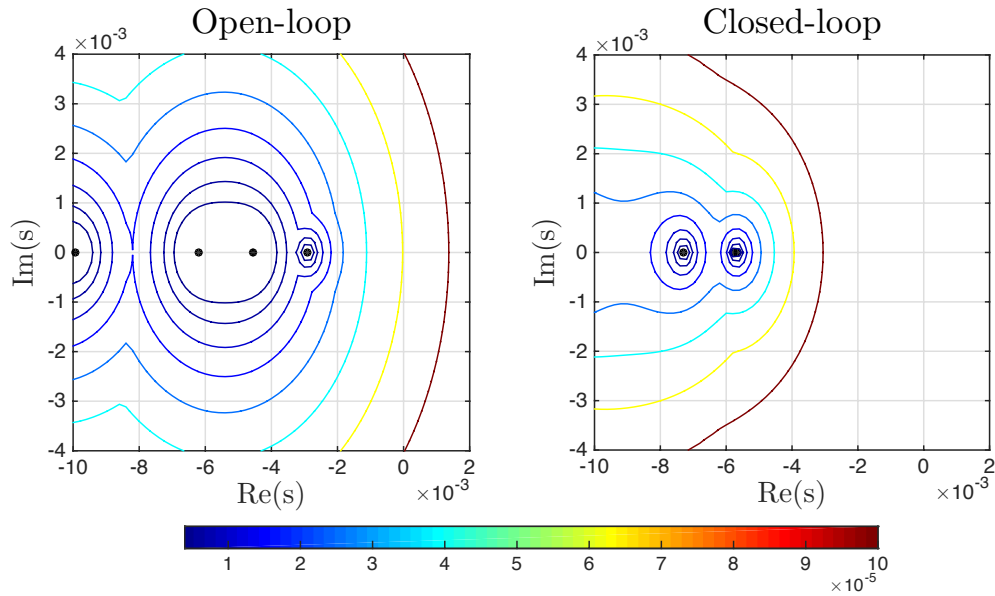


Figure 4.13: Spectra (black dots) and  $\epsilon$ -pseudospectra (coloured contours) for open-loop and closed-loop ( $\alpha = 0, \beta = 2$ ) system with **sensing arrangement 2**,  $\epsilon_c = \epsilon_d = 0.001$ ,  $\tau_\phi = 0.01$ .

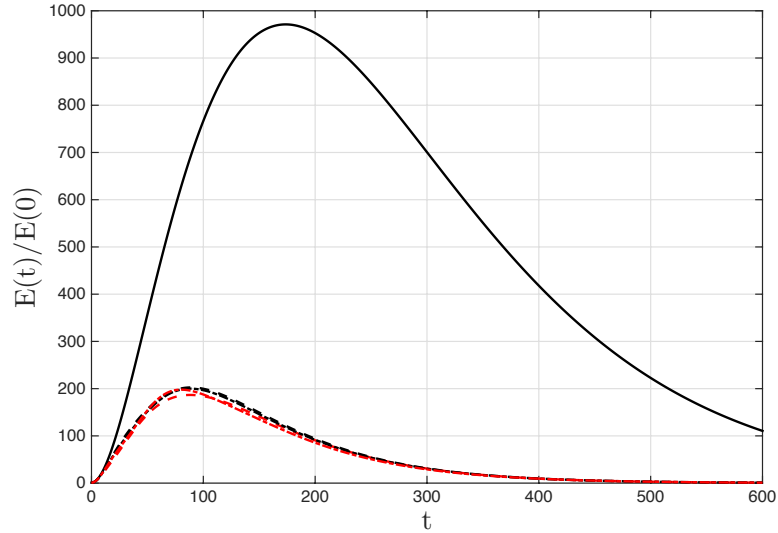


Figure 4.14: Plots of transient energy growth from linear simulations of open-loop (black solid line), and collocation (---) and Galerkin (·-) closed-loop ( $\alpha = 0, \beta = 2$ ) systems with sensing arrangement 1 (black) and sensing arrangement 2 (red), all started from “optimal” initial condition,  $\epsilon_c = \epsilon_d = 0.001$ ,  $\tau_\phi = 0.01$ ,  $N_{y,c} = 250$ .

to a greater degree. However, the Galerkin-discretised controller has a similar peak in transient energy growth as the for the first sensing arrangement, but with a higher rate of energy decay.

The linear analyses in this section have shown that there is little difference in the linear performance of controllers discretised using either the collocation or Galerkin methods. Further, the difference between sensing arrangements is almost negligible; controllers with sensing arrangement 2 perform only slightly better. However, turbulent channel flow is a highly nonlinear system and therefore linear analyses can only provide an indication of controller performance. In the following section, DNS testing will be used to evaluate the performance of collocation and Galerkin controllers with sensing arrangement 1 on fully turbulent flow.

#### 4.4.5 DNS Testing

Due to time and computing restrictions, it was decided to only conduct DNS testing on collocation- and Galerkin-discretised controllers with sensing arrangement 1. Plenty of previous research has used wall-shear stresses as sensing measurements [8, 36, 76, 78], and therefore results gained with this sensing arrangement will be more comparable. However, DNS testing of controllers with sensing arrangement 2 is an avenue for future work. Figure 4.11 indicated that there is little justification for controlling streamwise-constant modes ( $\alpha = 0, \beta > 10$ ), as the reduction in  $|\varepsilon|$  by the controllers was negligible. Therefore, it was decided to only control the ten lowest streamwise-constant modes for all DNS testing.

Initially, controllers all have penalties  $\epsilon_c = \epsilon_d = 0.001$  and actuator time-constant  $\tau_\phi = 0.01$ . However, as will be discussed further, the control and measurement penalties for the Galerkin-discretised controllers were increased to  $\epsilon_c = \epsilon_d = 0.01$ . The Galerkin discretised controllers all have resolution  $N_{y,c} = 250$  and will be denoted  $K_{G250}$ . For the collocation discretised controllers, two resolutions will be tested -  $N_{y,c} = 168$  and  $N_{y,c} = 250$ , denoted  $K_{C168}$  and  $K_{C250}$  respectively.

The controllers are evaluated on  $Re_\tau = 100$  fully turbulent channel flow using a modified version of the open-source DNS program *Channelflow*[41]. The code was modified to allow for inhomogeneous wall-normal boundary conditions at the walls; see Chapter 3. For all testing, the nonlinearity is computed in skew-symmetric form, the simulation is marched forward in time using a 3rd-order semi-implicit backward differentiation (SBDF3) algorithm, and flow bulk velocity is kept constant at  $U_{\text{bulk}} = 2/3$ . The spatial domain used for all simulations has dimensions  $4\pi \times 2 \times 2\pi$  and resolution  $182 \times 151 \times 158$  in the streamwise, wall-normal and spanwise directions respectively, which corresponds to streamwise and spanwise grid spacings of  $\Delta x^+ = 6.90$  and  $\Delta z^+ = 3.98$  respectively. This resolution is high enough to resolve the spanwise streak spacing for this Reynolds number. All controlled simulations are started from a fully developed turbulent flow field. The benchmark data of Iwamoto [53] was used to check that this flow field is statistically steady-state turbulent. To gain this initial turbulent flow field, an uncontrolled simulation was started from a random initial condition of sufficient magnitude to initiate transition and ran until a statistically steady-state was reached.

In order to ensure the validity of the DNS results, resolution checks were carried out on the uncontrolled simulation and the controlled simulation for the controller which gave the largest drag reduction; this was found to be the  $K_{C250}$  controller. The table in Figure 4.15 lists skin-friction coefficient and mean total perturbation energy results for uncontrolled simulations with different spatial resolutions. The top row of the table corresponds to the resolution used in all DNS testing:  $182 \times 151 \times 158$ . The fourth column of the table lists the sampling times used to calculate the temporal mean values. For all but the last row of the table, the percentage difference in  $C_f$  is less than 1%, and the percentage difference in mean perturbation energy is less than 2.5%. The reason for the slightly larger discrepancy in  $|\Delta C_f|$  for the last row is likely to be due to the lower value for  $Re_\tau$ . These results suggest that the uncontrolled simulation is resolved adequately. The table in Figure 4.16 lists skin-friction coefficients, mean perturbation energies, and the reduction in these values due to the control, from  $K_{C250}$ -controlled simulations with different resolutions. The percentage reductions in drag and energy listed in the final two columns of the table are with respect to the uncontrolled simulations with corresponding resolution. There is a significant variation in the percentage

$\Delta x^+$	$\Delta z^+$	$N_y$	$t_f - t_i$	$Re_\tau$	$C_f \times 10^{-3}$	$\bar{E} \times 10^{-2}$	$ \Delta C_f (\%)$	$ \Delta \bar{E} (\%)$
6.90	3.98	151	1000	101.49	9.32	3.22	—	—
11.4	3.98	151	1000	101.17	9.26	3.14	0.64	2.48
6.90	5.71	151	1000	101.47	9.32	3.16	0.00	1.86
6.90	2.99	151	1000	101.33	9.29	3.14	0.32	2.48
5.98	3.98	151	1000	101.42	9.31	3.16	0.11	1.86
6.90	3.98	129	1000	101.48	9.32	3.18	0.00	1.24
6.90	3.98	181	1000	100.93	9.22	3.21	1.07	0.31

Figure 4.15: Table detailing the resolution checks for the uncontrolled simulation. The final two columns list the percentage change in skin-friction coefficient and mean total perturbation energy with respect to the first row which corresponds to the grid spacings used for all testing.

$\Delta x^+$	$\Delta z^+$	$t_f - t_i$	$C_f \times 10^{-3}$	$\bar{E} \times 10^{-2}$	$ \Delta C_f (\%)$	$ \Delta \bar{E} (\%)$	$\bar{D}_R(\%)$	$\bar{E}_R(\%)$
6.90	3.98	1000	8.51	2.86	—	—	8.69	11.2
11.4	3.98	1000	8.60	2.85	1.04	0.35	7.13	9.24
6.90	5.71	1000	8.60	2.89	1.04	1.03	7.73	8.54
6.90	2.99	400	8.54	2.84	0.23	0.70	8.07	10.4
5.98	3.98	500	8.72	2.85	2.41	0.35	6.34	9.81

Figure 4.16: Table detailing the resolution checks for the  $K_{C250}$ -controlled simulation. Columns 6 and 7 list the percentage change in skin-friction coefficient and mean total perturbation energy with respect to the first row which corresponds to the grid spacings used for all testing. The final two columns list the percentage reductions in skin-friction drag and total perturbation energy with respect to the uncontrolled simulation with corresponding grid spacings. All reported results are for simulations with wall-normal resolution  $N_y = 151$ .

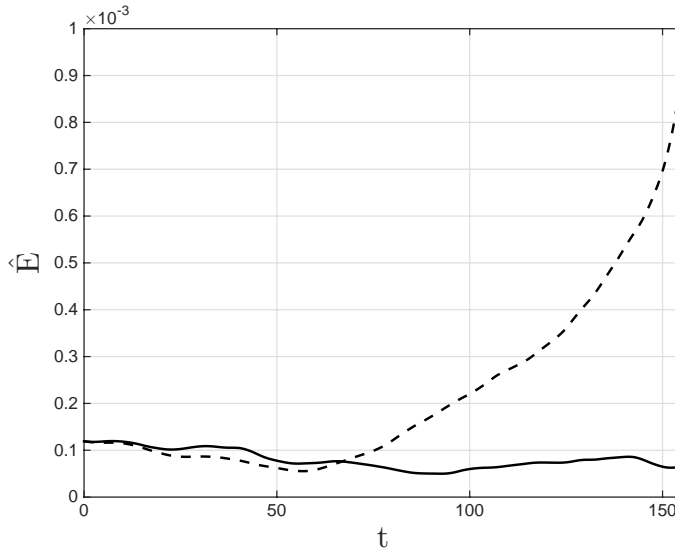


Figure 4.17: Plots of perturbation energy for mode  $(\alpha = 0, \beta = 1)$  over time for the uncontrolled (—) and  $K_{G250}$ -controlled (---) simulations, with control penalties  $\epsilon_c = \epsilon_d = 0.001$ .

reductions in both drag and energy. A conservative estimate for these reductions for the  $K_{C250}$  controller is  $\bar{D}_R = 8.7 \pm 2.5 \%$  and  $\bar{E}_R = 11.2 \pm 2 \%$ . These accuracy bounds will be applied to all energy and drag reduction results in this chapter.

#### Galerkin-Discretised Controllers

Initially, Galerkin-discretised controllers  $K_{G250}$  with control and measurement penalties  $\epsilon_c = \epsilon_d = 0.001$  were tested in DNS. However, it was found that the controllers destabilised the flow, in particular mode  $(\alpha = 0, \beta = 1)$ . Figure 4.17 shows the perturbation energy for this mode over time from uncontrolled and controlled simulations. For time  $t > 60$ , the effect of the controller on this mode is to rapidly increase perturbation energy. For time  $t > 160$ , the simulation started to become unstable in the sense that the simulation time-step needed to be continuously reduced in order for the CFL condition to be met. Therefore, the simulation was terminated. Besides this mode, all other controlled modes had large reductions in perturbation energy which is reflected in the total perturbation energy; shown in Figure 4.18. As can be seen, for the first 100 time units of the controlled simulation, the total perturbation energy is reduced significantly, with a maximum instantaneous total energy reduction of  $\approx 18\%$ . However, for time  $t > 120$ , the rapidly increasing energy of unstable mode  $(\alpha = 0, \beta = 1)$  starts to effect the flow's total perturbation energy which begins to increase. Figure 4.19 shows plots of total skin-friction drag at both walls from uncontrolled and  $K_{G250}$ -controlled simulations. It would appear from the figure, that the instability in mode  $(\alpha = 0, \beta = 1)$  is located at the upper wall. Whereas the drag at the lower wall reduces significantly, with a maximum instantaneous drag reduction

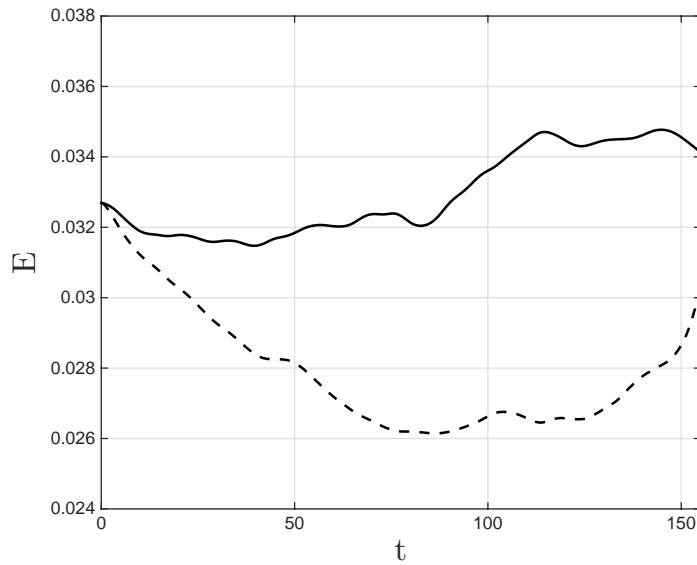


Figure 4.18: Plots of total perturbation energy over time for the uncontrolled (—) and  $K_{G250}$ -controlled (---) simulations, with control penalties  $\epsilon_c = \epsilon_d = \mathbf{0.001}$ .

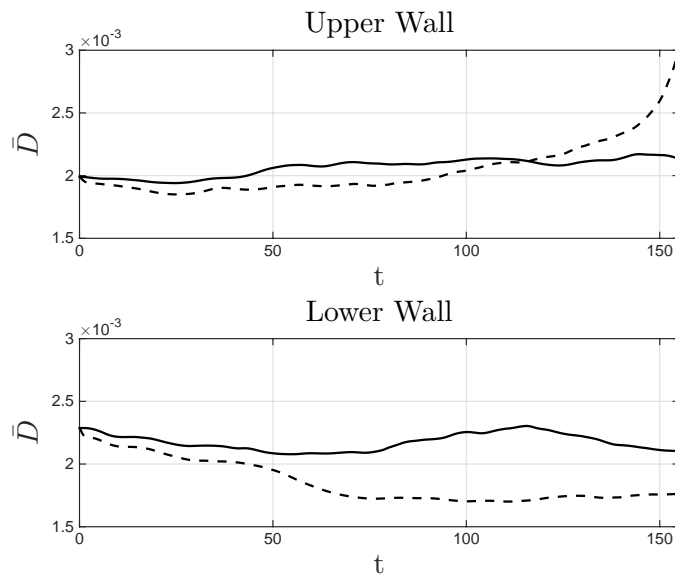


Figure 4.19: Plots of total skin-friction drag over time at the upper and lower walls for the uncontrolled (—) and  $K_{G250}$ -controlled (---) simulations, with control penalties  $\epsilon_c = \epsilon_d = \mathbf{0.001}$ .

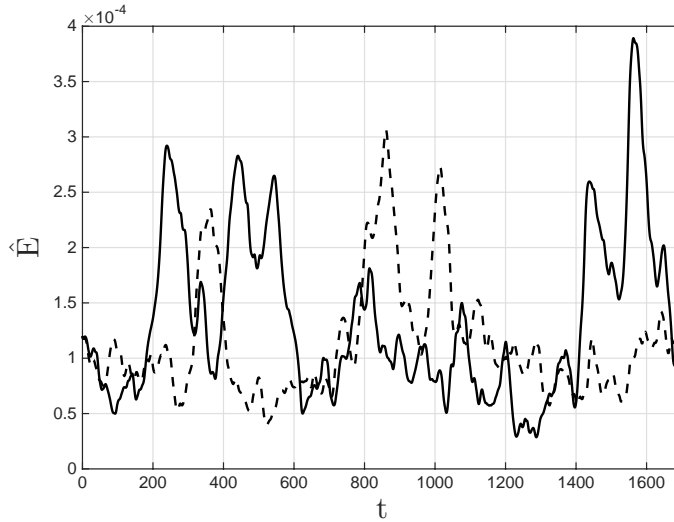


Figure 4.20: Plots of perturbation energy for mode  $(\alpha = 0, \beta = 1)$  over time for the uncontrolled (—) and  $K_{G250}^*$ -controlled (---) simulations, with control penalties  $\epsilon_c = \epsilon_d = 0.01$ .

of  $\approx 25\%$ , the drag at the upper wall increases slowly from  $t = 50$  onwards, and increases sharply from  $t = 120$  onwards.

It is unclear as to why the controller for mode  $(\alpha = 0, \beta = 1)$  causes an instability at the upper wall. The controller for this mode locally stabilises the corresponding linear system, i.e. the closed-loop system has all eigenvalues in the stable left half plane. Therefore, the two most likely explanations for the instability are - firstly, the actuation by the controller is such that the net flow of energy into the domain is very large, thus making the nonlinearity highly non-passive. Then the magnitude of the actuation signals may have been increased further by the controller to attenuate the increasing energy, making the nonlinearity even more non-passive and leading to an unstable feedback arrangement with the nonlinearity. Secondly, the measurement penalty  $\epsilon_d$  is too low and therefore small errors in the shear-stress measurements fed to the controller are making the state estimates inaccurate. For the first explanation, increasing the control penalty  $\epsilon_c$  would be one solution, because doing so would reduce the magnitude of the actuation and would reduce the net inflow of energy into the domain. Obviously, for the second explanation, increasing  $\epsilon_d$  would be the solution. Therefore, testing of  $K_{G250}$  controllers was repeated with new penalties  $\epsilon_c = \epsilon_d = 0.01$ . These new controllers will be denoted  $K_{G250}^*$ .

Figure 4.20 shows plots of perturbation energy for mode  $(\alpha = 0, \beta = 1)$  from uncontrolled and  $K_{G250}^*$ -controlled simulations. It is clear from the figure that this mode is no longer destabilised by the controller. Further, the controller has reduced mean perturbation energy for this mode by  $\approx 12\%$ . Figure 4.21 shows

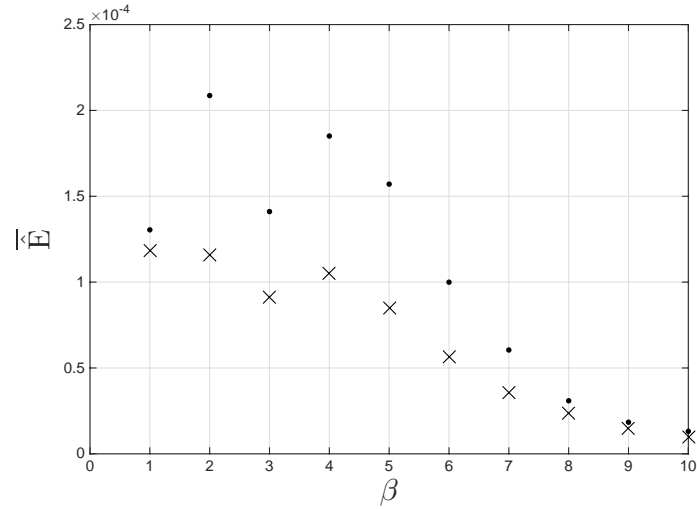


Figure 4.21: Temporal-mean perturbation energies for modes ( $\alpha = 0, \beta \leq 10$ ) from uncontrolled ( $\cdot$ ) and  $K_{G250}^*$ -controlled ( $\times$ ) simulations, with control penalties  $\epsilon_c = \epsilon_d = 0.01$ .

the mean perturbation energy for each controlled mode for the uncontrolled and  $K_{G250}^*$ -controlled simulations. The first 300 time units of controlled data have not been included in order to remove the initial transient effects of the controllers. As predicted from Figure 4.11, it is the lowest streamwise constant modes that are responsible for the largest contributions to the total perturbation energy of the flow. The controllers for the first seven streamwise-constant modes all achieve significant reductions in mean perturbation energy. For the highest three controlled modes however, the controllers seems to have had little effect. This is likely to be due to the fact that these modes are more dissipative relative to the others.

Figure 4.22 shows plots of total perturbation energy for the uncontrolled and  $K_{G250}^*$ -controlled simulations. The controllers achieve a reduction in mean total perturbation energy of  $\approx 11\%$ ; the first 300 time units of controlled data have not been included in the calculation of the mean. When the controllers are first initiated, the total energy of the flow reduces rapidly for the first 170 time units; this is the transient effect of the controllers. Thereafter, the energy of the flow recovers slightly, but with lower temporal energy peaks than the uncontrolled flow. It is these reductions in the temporal peaks of energy that ultimately brings the mean value down. Figure 4.23 shows plots of total skin-friction drag for the uncontrolled and  $K_{G250}^*$ -controlled simulations. The reduction in total perturbation energy by the controllers has led to a reduction in mean total skin-friction drag of  $\approx 6\%$  with transient effects discarded. Here, drag reduction is defined as:

$$\bar{D}_R(\%) = 100 \left( 1 - \frac{\frac{1}{2} (|\bar{D}_u| + |\bar{D}_1|)_{\text{CON}}}{\frac{1}{2} (|\bar{D}_u| + |\bar{D}_1|)_{\text{UNCON}}} \right), \quad (4.66)$$

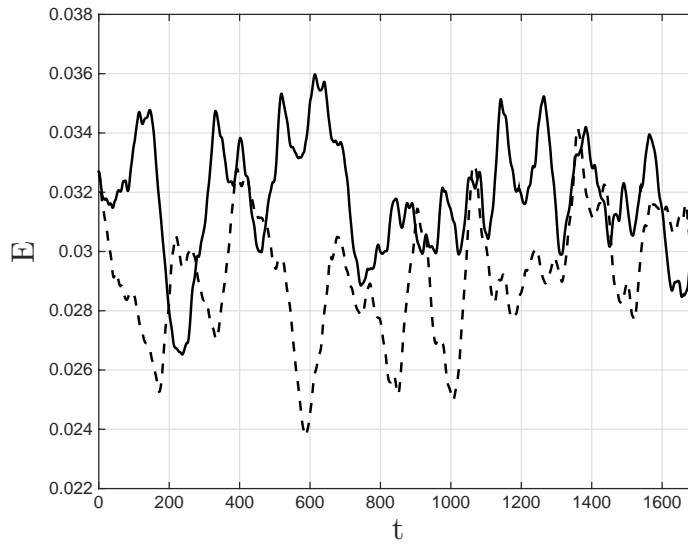


Figure 4.22: Plots of total perturbation energy over time for the uncontrolled (—) and  $K_{G250}^*$ -controlled (---) simulations, with control penalties  $\epsilon_c = \epsilon_d = \mathbf{0.01}$ .

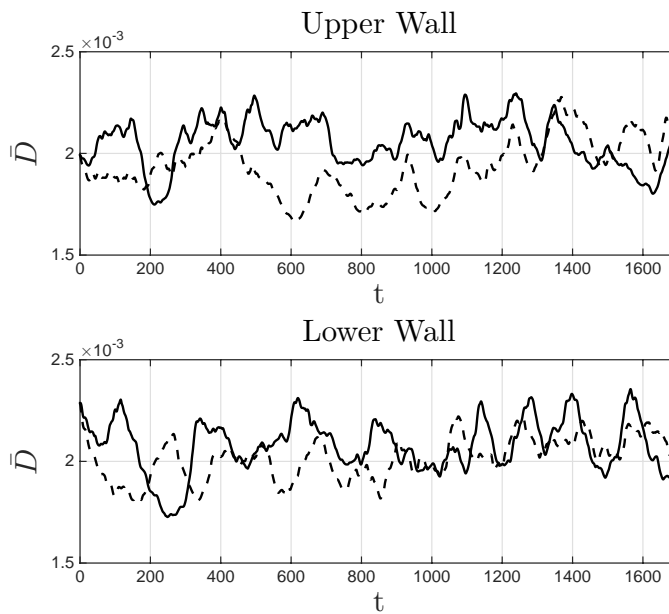


Figure 4.23: Plots of total skin-friction drag over time at the upper and lower walls for the uncontrolled (—) and  $K_{G250}^*$ -controlled (---) simulations, with control penalties  $\epsilon_c = \epsilon_d = \mathbf{0.01}$ .

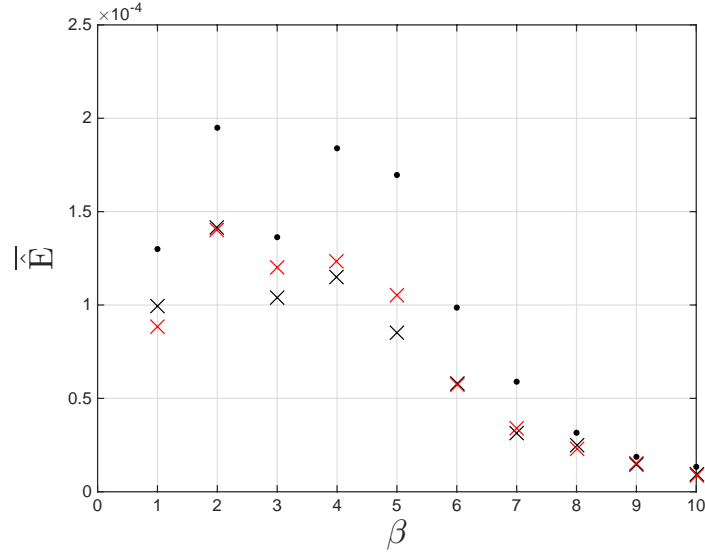


Figure 4.24: Temporal-mean perturbation energies for modes ( $\alpha = 0, \beta \leq 10$ ) from uncontrolled ( $\cdot$ ),  $K_{C168}$ -controlled ( $\times$ ), and  $K_{C250}$ -controlled ( $\times$ ) simulations.

where subscripts  $u$  and  $l$  denote the drag at the upper and lower walls respectively, and the over bar denotes temporal mean values.

#### Collocation-Discretised Controllers

The instability problems associated with the original  $K_{G250}$  controllers were not experienced when testing either the  $K_{C168}$  or  $K_{C250}$  controllers with  $\epsilon_c = \epsilon_d = 0.001$ . Therefore, results shown here are for controllers with the original choice of control and measurement penalties.

Figure 4.24 shows the uncontrolled,  $K_{C168}$ - and  $K_{C250}$ -controlled mean energies for each controlled mode; the first 300 time units of controlled data has not been included when calculating mean values. The controllers reduce mean modal energy for all modes controlled but as for the Galerkin-discretised controllers, these controllers have little effect on the three highest controlled streamwise-constant modes. Both the  $K_{C168}$  and  $K_{C250}$  controllers for wavenumber pair ( $\alpha = 0, \beta = 2$ ) have reduced mean modal energy by  $\approx 30\%$ . The reductions in energy for each mode overall is very similar for the  $K_{C168}$  and  $K_{C250}$  controllers. This may suggest the increased resolution has little effect. Figure 4.25 shows plots of perturbation energy for mode ( $\alpha = 0, \beta = 2$ ) for the uncontrolled, and  $K_{C168}$ - and  $K_{C250}$ -controlled simulations. The time histories for both controllers are of a similar magnitude to one another which explains the similar mean energies for this mode in Figure 4.24. As for the Galerkin-discretised controller, the effect of both controllers here is to reduce the size of the temporal peaks in energy for this mode. This has led to large reductions in mean perturbation energy.

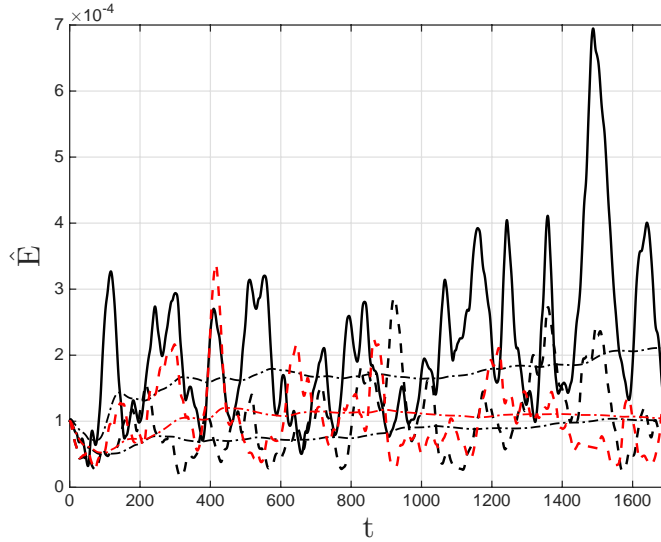


Figure 4.25: Plots of perturbation energy for Fourier mode ( $\alpha = 0, \beta = 2$ ) from uncontrolled (—),  $K_{C168}$ -controlled (---), and  $K_{C250}$ -controlled (---) simulations. Also included are dash-dot lines representing the uncontrolled (upper black),  $K_{C168}$ -controlled (lower black), and  $K_{C250}$ -controlled (red) moving mean values.

Figure 4.26 shows plots of total perturbation energy for the uncontrolled and both controlled simulations. Discarding initial transient effects, the  $K_{C168}$  controllers achieved a reduction in mean total perturbation energy of  $\approx 11\%$ , and the  $K_{C250}$  controllers have also achieved a reduction of  $\approx 11\%$ . The energy time-histories from both controlled simulations are strikingly similar to one another which is another indication that increasing the resolution of the controllers has had little effect. As for the Galerkin-discretised controllers, the effect of these controllers leads to a large reduction in energy when they are first initiated. This is an initial transient effect by the controllers. The energy of the flow then recovers slightly, but the suppression of temporal energy peaks by the controllers ensures a reduction in the mean energy of the flow. Figure 4.27 shows plots of total skin-friction drag for the uncontrolled, and both controlled simulations. The  $K_{C168}$  controllers achieved a reduction in mean total skin-friction drag of  $\approx 7\%$  and the  $K_{C250}$  controllers have achieved a reduction of  $\approx 9\%$ . The first 300 time units of controlled data has not been included when calculating these mean values. Interestingly, even though the energy time-histories for the  $K_{C168}$  and  $K_{C250}$  controllers are similar, the drag time-histories look different. This suggests that the actuation signals of each controller have different profiles but manage to achieve similar reductions in perturbation energy. Figure 4.28 contains a table summarising the reductions in mean total energy and mean skin-friction drag achieved by all controllers tested in this chapter.

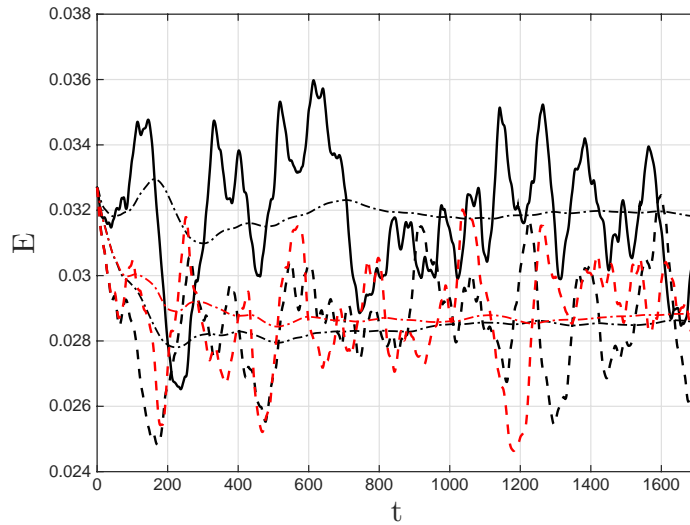


Figure 4.26: Plots of total perturbation energy over time for the uncontrolled ( $-$ ),  $K_{C168}$ -controlled ( $--$ ), and  $K_{C250}$ -controlled ( $--$ ) simulations. Also included are dash-dot lines representing the uncontrolled (upper black),  $K_{C168}$ -controlled (lower black), and  $K_{C250}$ -controlled (red) moving mean values.

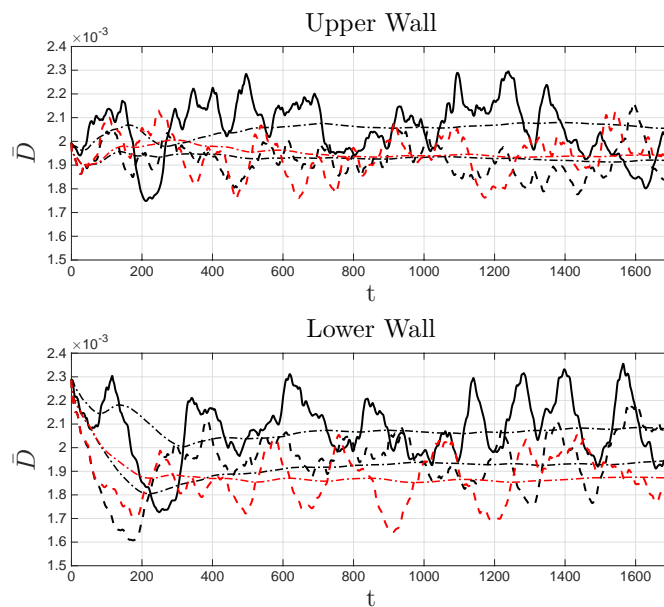


Figure 4.27: Plots of total skin-friction drag over time for the upper and lower walls for the uncontrolled flow ( $-$ ),  $K_{C168}$ -controlled flow ( $--$ ), and  $K_{C250}$ -controlled flow ( $--$ ). Also included are dash-dot lines representing the uncontrolled (upper black),  $K_{C168}$ -controlled (lower black), and  $K_{C250}$ -controlled (red) moving mean values.

$K$	$C_f \times 10^{-3}$	$\bar{E} \times 10^{-2}$	$\bar{D}_R(\%)$	$\bar{E}_R(\%)$
$K_{G250}^*$	8.74	2.87	$6.22 \pm 2.5$	$10.9 \pm 2$
$K_{C168}$	8.71	2.86	$6.55 \pm 2.5$	$11.2 \pm 2$
$K_{C250}$	8.51	2.86	$8.69 \pm 2.5$	$11.2 \pm 2$

Figure 4.28: Summary table of the % reduction in mean total energy and mean skin-friction drag achieved by each passivity-based controller tested. The first 300 time units of controlled data are not included in the calculation of these values in order to remove the transient effects of the controllers.

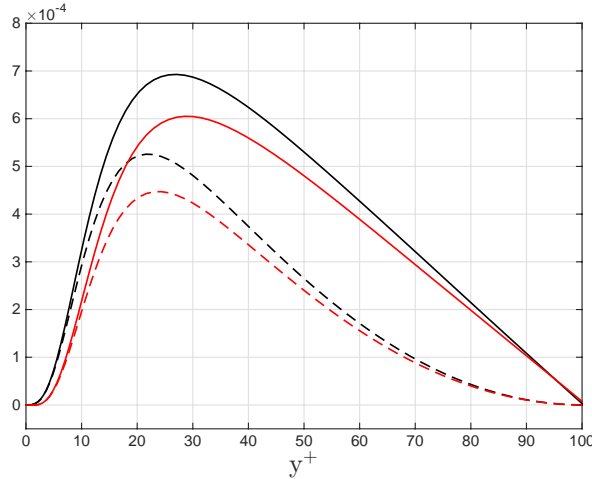


Figure 4.29: Profiles of Reynolds stress ( $-\overline{u'v'}$ ) (thick lines) and FIK-weighted Reynolds stress ( $y\overline{u'v'}$ ) (dashed lines) for the uncontrolled flow (black) and  $K_{C250}$ -controlled flow (red), displayed for the bottom half of the channel only.

The FIK identity was briefly discussed in Chapter 1 and is given in (1.11). According to this identity, the turbulent contribution to skin-friction drag in channel flow is dependent on a weighted integral of the Reynolds stress ( $-\overline{u'v'}$ ). Figure 4.29 shows the profiles of this Reynolds stress as well as the FIK-weighted Reynolds stress for both the uncontrolled and  $K_{C250}$ -controlled flows for the bottom half of the channel. The effects of the weightings is to skew the Reynolds stress profiles such that they are much larger nearer the wall than they are in the centre of the channel. This suggests that the the turbulent drag contribution near the wall is greater than away from the wall. The  $K_{C250}$  controllers have reduced the magnitude of the weighted Reynolds stresses relative to the uncontrolled flow, especially in the region  $10 \leq y^+ \leq 50$ . The FIK identity was used to calculate the skin-friction coefficient  $C_f$  for each flow. The FIK computed values and actual

	$C_{flam}$	$C_{fturb}$	$C_{ftotal}$	Actual $C_f$
Uncontrolled	$4.04 \times 10^{-3}$	$5.27 \times 10^{-3}$	$9.31 \times 10^{-3}$	$9.32 \times 10^{-3}$
$K_{C250}$ -controlled	$4.04 \times 10^{-3}$	$4.48 \times 10^{-3}$	$8.52 \times 10^{-3}$	$8.51 \times 10^{-3}$

Figure 4.30: Table of skin-friction coefficient values calculated using the FIK identity (first three columns of data) and the actual skin-friction coefficient (last column of data).

$K$	$\mathcal{P}_x$	$\Delta\mathcal{P}_x$	$\mathcal{P}_{v^3}$	$\mathcal{P}_{vp}^*$	$\mathcal{P}_\phi^*$	$\mathcal{P}_\%$
$K_{G250}^*$	-0.2098	0.0105	$1.202 \times 10^{-6}$	$3.429 \times 10^{-4}$	$3.441 \times 10^{-4}$	3.28
$K_{C168}$	-0.2039	0.0164	$8.515 \times 10^{-7}$	$3.870 \times 10^{-4}$	$3.879 \times 10^{-4}$	2.37
$K_{C250}$	-0.1992	0.0211	$4.255 \times 10^{-7}$	$3.512 \times 10^{-4}$	$3.516 \times 10^{-4}$	1.67

Figure 4.31: Table showing the power required to push the fluid  $\mathcal{P}_x$ , the power saved due to drag reduction  $\Delta\mathcal{P}_x$ , the approximate actuation power  $\mathcal{P}_\phi^*$ , and the power efficiency  $\mathcal{P}_\%$  for each controller. For the uncontrolled flow,  $\mathcal{P}_x = -0.2203$ .

calculated values are given in the table in Figure 4.30. The values for  $C_f$  calculated using the FIK identity and those found directly from the DNS data are in good agreement with one another, with an error of  $\approx 0.1\%$  for both flows.

In order to ascertain the efficiency of the three sets of passivity-based controllers outlined in this chapter, it is useful to compare the power spent on the control actuation to the power saved due to drag reduction for each case. The mean power of the actuation is calculated from (4.33) as:

$$\mathcal{P}_\phi := \int_0^{L_x} \int_0^{L_z} \frac{1}{2} \overline{(|v_+^3| + |v_-^3|)} + \overline{(|v_+p_+| + |v_-p_-|)} dz dx, \quad (4.67)$$

where  $v_+ = v(x, +1, z, t)$ ,  $v_- = v(x, -1, z, t)$ , and similarly for pressure. Absolute value signs are incorporated into (4.67) in an *ad hoc* manner, as it is unlikely that a significant amount of energy could be extracted from a flow by the actuators in reality [11]. Unfortunately, data for the static pressure variations  $p_+, p_-$  was not recorded for each time step during DNS testing. Therefore, the actuation power will be approximated as:

$$\mathcal{P}_\phi^* := \underbrace{\int_0^{L_x} \int_0^{L_z} \frac{1}{2} \overline{(|v_+^3| + |v_-^3|)} dz dx}_{\mathcal{P}_{v^3}} + \underbrace{\int_0^{L_x} \int_0^{L_z} \overline{(|v_+p_+| + |v_-p_-|)}_{T=1000} dz dx}_{\mathcal{P}_{vp}^*}, \quad (4.68)$$

where  $\mathcal{P}_{vp}^*$  is the absolute rate of work done on the static pressure by the actuation for  $T = 1000$ . This snapshot value will inform on the order of magnitude of this term assuming that it does not vary to a large degree. The power required to push the fluid along the streamwise direction of a channel is calculated from [11, 93]:

$$\mathcal{P}_x := 2L_x L_z U_b \left\langle \overline{\frac{\partial P}{\partial x}} \right\rangle, \quad (4.69)$$

where  $U_b$  is bulk velocity and  $\left\langle \overline{\frac{\partial P}{\partial x}} \right\rangle$  is the spatial and time-averaged total streamwise pressure gradient. The control power efficiency will be defined as:

$$\mathcal{P}_\% := 100 \left( \frac{\mathcal{P}_\phi^*}{\Delta\mathcal{P}_x} \right), \quad (4.70)$$

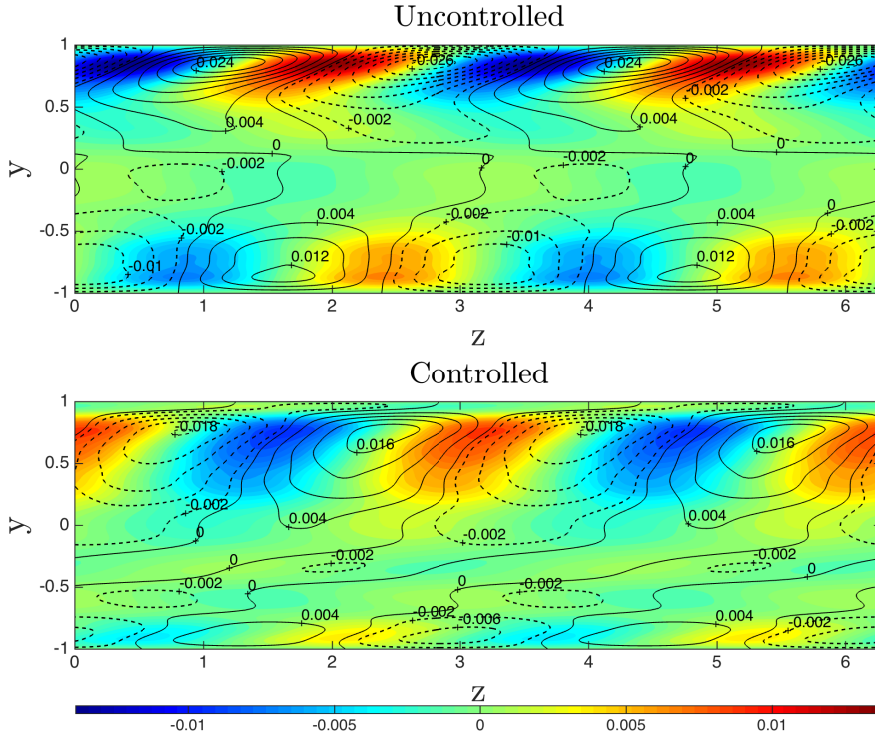


Figure 4.32: Colour maps of streamwise velocity  $\hat{u}$  overlaid with contours of streamwise vorticity  $\hat{\eta}_x$  from uncontrolled and  $K_{C168}$ -controlled simulations for wavenumber pair ( $\alpha = 0, \beta = 2$ ) and  $T = 1100$ .

where  $\Delta\mathcal{P}_x := |\mathcal{P}_{x,\text{UNCON}}| - |\mathcal{P}_{x,\text{CON}}|$  is the power saved due to drag reduction. The table in Figure 4.31 shows the control power efficiency for each of the three passivity-based controllers. It is apparent that all three controllers are highly efficient as the actuation power is only a small percentage of the power saved due to drag reduction. However, this assumes that the values of  $\mathcal{P}_{\text{vp}}^*$  reported are sufficiently close to their temporal mean values.

Insight into how the controllers reduce energy and drag in the flow can be gained from visualisation of the flow fields. Figure 4.32 shows colour maps of streamwise velocity ( $\hat{u}$ ) overlaid with contour lines of streamwise vorticity ( $\hat{\eta}_x$ ) on the  $y - z$  plane for mode ( $\alpha = 0, \beta = 2$ ), for the uncontrolled and  $K_{C168}$ -controlled simulations. Streamwise vorticity is defined as:

$$\eta_x := \frac{\partial w}{\partial y} - \frac{\partial v}{\partial z}. \quad (4.71)$$

The controller has reduced the perturbation energy for this mode by firstly, counteracting the streamwise velocity perturbations in order to reduce their magnitude. Secondly, the controller reduces the strength of streamwise vorticity close to the wall, presumably through counterrotation. The vortices are also pushed away from the wall, as can be clearly seen on the top wall of the controlled flow.

However, the effect of the controller does not appear to be drastic as there is not a large difference between the two plots.

Figure 4.33 shows isosurface plots of  $\mathbf{Q} = 0.1$  overlaid with colour maps of streamwise perturbation velocity ( $u$ ) on the  $x - z$  plane at  $y = 0.85$  for the uncontrolled and  $K_{C168}$ -controlled simulations for time  $t = 1300$ . The variable  $\mathbf{Q}$  is an identifier of local vortex strength, and comes from the  $\mathbf{Q}$ -criterion vortex identification scheme [51]. This scheme identifies vortices as regions of a flow with positive second invariant of the local velocity gradient tensor  $\nabla \mathbf{v}$ , that is, regions where  $\mathbf{Q} > 0$ .  $\mathbf{Q}$  is defined [21]:

$$\mathbf{Q} := \frac{1}{2} (\|\boldsymbol{\Omega}\|^2 - \|\mathbf{S}\|^2), \quad (4.72)$$

where  $\|\boldsymbol{\Omega}\| = \text{trace} [\boldsymbol{\Omega}\boldsymbol{\Omega}^\top]^{1/2}$ ,  $\|\mathbf{S}\| = \text{trace} [\mathbf{S}\mathbf{S}^\top]^{1/2}$ ,  $\mathbf{S} = \frac{1}{2} (\nabla \mathbf{v} + (\nabla \mathbf{v})^\top)$  is the symmetric component of  $\nabla \mathbf{v}$ , and  $\boldsymbol{\Omega} = \frac{1}{2} (\nabla \mathbf{v} - (\nabla \mathbf{v})^\top)$  is the anti-symmetric component of  $\nabla \mathbf{v}$ . Streamwise velocity was plotted on the plane perpendicular to  $y^+ = 15$  because this is the wall-normal location of maximum shear of the mean velocity profile, and is known to be an important region of the flow because of its contribution to the non-normality of the system [101]. This suggests it would be an appropriate location for visualising streaks. Sharma et al. [101] found that this was the location of maximum actuation forcing in their work. Visible on the colour maps in Figure 4.33 are sinuous bands of negative streamwise perturbation velocity. These structures are streaks and are discussed in Chapter 1. There is no noticeable difference between the two plots in Figure 4.33, with both the streaks and vortices seemingly unaffected by the  $K_{C168}$  controllers. It is likely that because the reduction in mean total perturbation energy by these controllers is only  $\approx 11\%$ , it would not be possible to visualise any noticeable effect on the total flow.

Returning back to the definitions of passivity, for a channel flow with energy-weighted disturbance inputs  $\mathbf{w}(t)$  and energy-weighted velocity outputs  $\mathbf{z}(t)$ , the system is SIP iff there exists  $\varepsilon > 0$  such that:

$$\langle \mathbf{z}(t), \mathbf{w}(t) \rangle_{[0,T]} \geq \varepsilon \langle \mathbf{w}(t), \mathbf{w}(t) \rangle_{[0,T]}, \quad (4.73)$$

for all  $T > 0$ . Neither our uncontrolled or controlled systems are SIP, but our controlled wavenumber pair systems are all closer to SIP than the uncontrolled systems. Figure 4.34 shows plots of  $\langle \mathbf{w}(t), \mathbf{w}(t) \rangle$  vs.  $\langle \mathbf{z}(t), \mathbf{w}(t) \rangle$  for modes ( $\alpha = 0, \beta \leq 2$ ), for the first 350 time units of the uncontrolled and  $K_{C168}$ -controlled simulations; initially stored energy is ignored. When  $\langle \mathbf{z}, \mathbf{w} \rangle \geq 0$  the system is only storing and dissipating energy, and when  $\langle \mathbf{z}, \mathbf{w} \rangle < 0$ , the system is also producing energy. For mode ( $\alpha = 0, \beta = 1$ ), the controlled graph is consistently above the uncontrolled graph. For mode ( $\alpha = 0, \beta = 2$ ), both uncontrolled and controlled

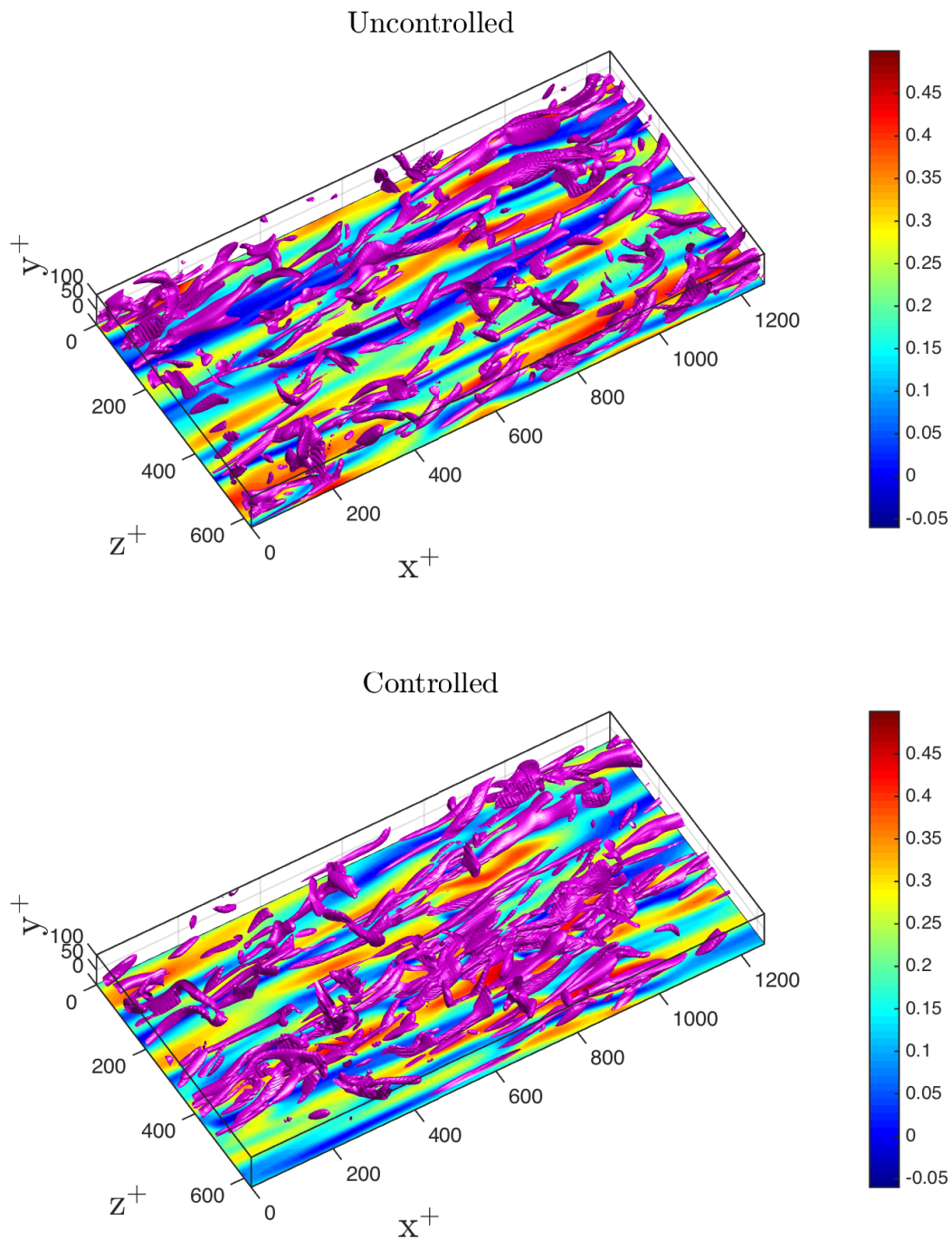


Figure 4.33: Isosurface plots of  $Q = 0.1$  at the bottom wall, underlaid with colour maps of streamwise velocity  $u$  at  $y^+ = 15$  for uncontrolled and  $K_{C168}$ -controlled simulations for time  $t = 1300$ .

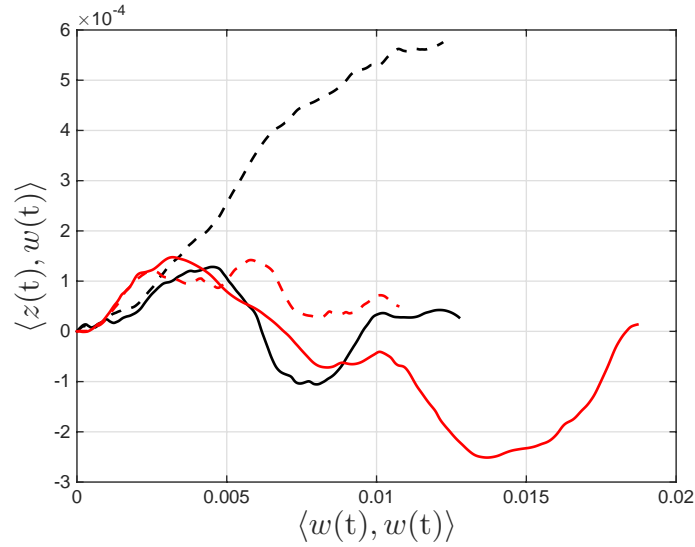


Figure 4.34: Plots of  $\langle \mathbf{w}, \mathbf{w} \rangle$  vs.  $\langle \mathbf{z}, \mathbf{w} \rangle$  for wavenumber pairs  $(\alpha = 0, \beta = 1)$  (black) and  $(\alpha = 0, \beta = 2)$  (red), from uncontrolled (—) and  $K_{C168}$ -controlled (---) simulations.

graphs are initially similar to one another, but as the inner product  $\langle \mathbf{w}, \mathbf{w} \rangle$  increases with time, the controlled graph remains above the abscissa whereas the uncontrolled graph goes well below it. This figure demonstrates that the controllers for these modes are having the desired effect - reducing their index of passivity  $|\varepsilon|$ . This in turn has restricted the production of perturbation energy in these modes.

## 4.5 Summary

This chapter has evaluated the passivity of channel flow, and investigated the use of feedback control to alter its passivity for the purposes of skin-friction drag reduction. The main findings of this chapter are as follows:

- The dynamics of channel flow can be represented as a linear system in feedback with a nonlinear system, allowing for the passivity of each system to be evaluated separately using the passivity theorem.
- The nonlinearity was found to be passive when the net flux of energy into the domain is zero. However, when wall actuation is employed, the net flux of energy introduced into the domain may effect the passivity of the nonlinearity. No analysis on the effect the controllers tested in DNS in this chapter have had on the passivity of the nonlinearity has been undertaken. This is an avenue for future work.
- For the majority of flows of interest, where Reynolds number exceeds the critical energy Reynolds number, the lower-valued Fourier modes of the linear

system are non-passive. The streamwise-constant modes are the least passive, with the largest magnitude indices of passivity, suggesting it is these modes which can potentially produce the most energy. For  $\text{Re} \rightarrow \infty$ , Fourier mode ( $\alpha = 0, \beta = 1.62$ ) is the least passive overall.

- Using the positive-real control method of Sun et al. [103], LTI controllers were generated that are capable of reducing the magnitude of the index of passivity of the linear system's streamwise-constant modes, making them closer to passive. Two sensing arrangements were investigated and both collocation- and Galerkin-discretised controllers were synthesised and tested.
- Linear analyses showed no discernible difference between the performance of controllers discretised via the collocation and Galerkin methods. Controllers with sensing arrangement 2 achieved marginally higher reductions in closed-loop index of passivity. All controllers were shown to be apt at restricting transient energy growth in linear simulations. It was shown that this was due to their effect on the pseudospectra for each controlled system.
- Collocation- and Galerkin-discretised controllers with sensing arrangement 1 (streamwise and spanwise perturbation wall-shear stresses) were evaluated upon DNS of  $\text{Re}_\tau = 100$  turbulent channel flow.
- Initial testing of the Galerkin-discretised controllers was unsuccessful as the controller for mode ( $\alpha = 0, \beta = 1$ ) was destabilising. After the control and measurement penalties of the controllers was increased, all controlled modes remained stable. The Galerkin-discretised controllers achieved reductions in mean total perturbation energy and mean total skin-friction drag of  $\approx 11\%$  and  $\approx 6\%$  respectively.
- The collocation-discretised controllers remained stable for all modes with the original control and measurement penalties. Controllers with two different resolutions,  $N_y = 168$  and  $N_y = 250$ , were tested and found to give similar energy time histories, although different drag time histories. After 1700 time units, the controllers achieved reductions in mean total perturbation energy of  $\approx 11\%$  for both resolutions tested, and reductions in mean total skin-friction drag of  $\approx 7\%$  and  $\approx 9\%$  for the  $N_y = 168$  and  $N_y = 250$  resolution controllers respectively.
- For all controllers tested, mean perturbation energy reduction was shown to occur by the controllers' mitigation of temporal peaks in energy for each controlled mode. The objective of the controllers is to reduce the magnitude of the index of passivity of a particular mode. Doing so will restrict the potential amount of energy that mode can produce. Therefore, the reduction in the temporal peaks of energy observed in DNS is confirmation that the controllers are meeting their objective.

## Chapter 5

# $\mathcal{H}_\infty$ Loop-Shaping Control

### 5.1 Introduction

The  $\mathcal{H}_\infty$  loop-shaping control method, first proposed by McFarlane and Glover [85], offers *a priori* guarantees of closed-loop robustness to uncertainty and controller performance; something not offered by many other modern control techniques. As will be demonstrated, this method is capable of dealing with various classifications of uncertainty, as well as achieving excellent multi-input disturbance rejection.  $\mathcal{H}_\infty$  loop-shaping control has been successfully applied to a wide variety of systems, including nano-positioning of a piezoelectric stage [109], autopilot design for an agile missile [83], and the development of a bio-inspired aerial navigation system [65]. With regards to controlling channel flow for the purposes of skin-friction drag reduction,  $\mathcal{H}_\infty$  loop-shaping control has been shown previously to be effective at minimising streamwise wall-shear stress perturbations for a single Fourier mode of a turbulent channel flow by Jones et al. [60]. In this chapter, this work will be extended to minimise perturbation streamwise wall-shear stress for multiple modes in DNS, with the expectation that it will lead to a reduction in total mean skin-friction drag.

In the following, sources of uncertainty in fluid flows and modelling these uncertainties will be discussed in Section 5.2, the model refinement technique will be outlined in Section 5.3, and in Section 5.4 the controller synthesis procedure will be presented and the resulting controllers evaluated using DNS. A brief summary is given in Section 5.5.

### 5.2 Uncertainty in Fluid Flows

The main purpose of feedback control is to deal with the numerous sources of uncertainty inherent in any system. However, some forms of feedback control handle uncertainty better than others. For nonlinear infinite-dimensional systems such as channel flow, approximated by discrete LTI models, Bobba [13] categorises

the various sources of uncertainty as follows:

- **Modelling uncertainty**

*Parametric uncertainty* - this arises due to the lack of knowledge of the exact parameters of a system (e.g. Reynolds number). In reality, these parameters will fluctuate. Numerical errors introduced by projecting the Navier-Stokes equations onto a divergence-free basis (e.g. forming the Orr-Sommerfeld Squire equations) are another source of parametric uncertainty because this usually involves the inversion of ill-conditioned matrices.

*Dynamic uncertainty* - this arises whenever a finite-dimensional model is used to approximate an infinite-dimensional system. A spatially discrete model is only capable of resolving a finite number of modes, and therefore higher frequency modes are neglected. The problem of identifying a suitable order of discretisation of a control model that ensures closed-loop robustness and performance is addressed later on in this chapter.

- **Disturbance uncertainty**

*Exogenous disturbances* - these disturbances arise from multiple sources, such as uncertain boundary conditions, acoustic forcing, and noise from imperfect sensors and actuators. It would be tremendously difficult to model all these effectively, other than knowing some bound on their magnitude and where they enter the system.

*Nonlinear forcing* - in the previous chapter, within the framework of passivity, the forcing from the nonlinearity could be assumed passive and therefore its influence on the system's energy dynamics could be neglected. However, in general, this nonlinear forcing appears as an uncertain disturbance acting upon the linear system. Therefore, the control objective of suppressing turbulence, a nonlinear phenomenon, can be formulated as a disturbance rejection problem.

Figure 5.1 shows a block diagram illustrating where these various disturbances enter the linear system, denoted here as  $\mathcal{P}$ . Modelling disturbances and exogenous disturbances are contained in vector  $\mathbf{w}$ , and the nonlinear forcing is denoted  $\mathbf{n}$  as previous. Control inputs are denoted  $\mathbf{u}$ . The block  $\Delta$  models the various forms of modelling and exogenous uncertainty in a feedback arrangement with the linear system. The effect of all inputs on the measured output vector  $\mathbf{y}$  is given as:

$$\mathbf{y} = \mathcal{P}_{yw}\mathbf{w} + \mathcal{P}_{yn}\mathbf{n} + \mathcal{P}_{yu}\mathbf{u}, \quad (5.1)$$

where each  $\mathcal{P}_{..}$  term on the right-hand-side of (5.1) is a transfer function and a partition of the total system. The objective of the current work is to minimise the  $\mathcal{H}_\infty$ -norm of the closed-loop transfer functions from disturbances  $\mathbf{w}$  and  $\mathbf{n}$  to

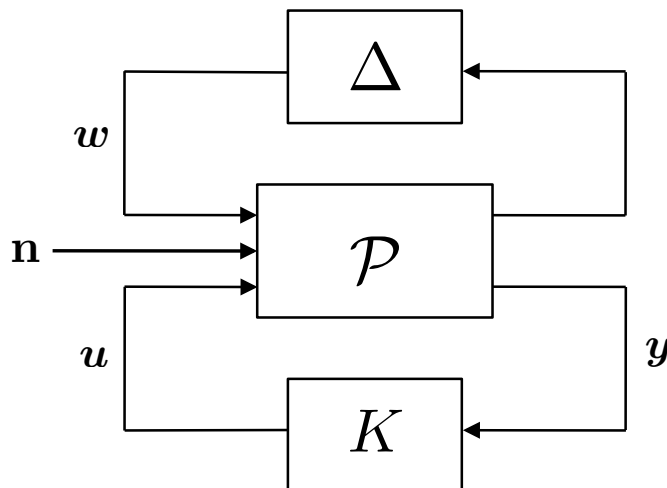


Figure 5.1: Block diagram of linear system  $\mathcal{P}$  in feedback with controller  $K$ , under forcing from nonlinearity  $\mathbf{n}$  and modelling uncertainty  $w$ .

measured output  $\mathbf{y}$ , defined:

$$\|\mathcal{P}_{yw}\|_{\infty} := \sup_{w \neq 0} \frac{\|\mathbf{y}(t)\|_2}{\|w(t)\|_2}, \quad (5.2a)$$

$$\|\mathcal{P}_{yn}\|_{\infty} := \sup_{\mathbf{n} \neq 0} \frac{\|\mathbf{y}(t)\|_2}{\|\mathbf{n}(t)\|_2}. \quad (5.2b)$$

The controller  $K$  is expected to achieve this objective in the presence of uncertainty model  $\Delta$  to ensure the robustness of this control method. The nonlinearity  $\mathbf{n}$  will be treated as a disturbance input to the linear flow dynamics throughout this chapter. The aim of the  $\mathcal{H}_{\infty}$  loop-shaping controllers will be to reject the effects of this disturbance as well as the effects of the additional disturbances  $w$ . The controllers will not be guaranteed to stabilise the fully nonlinear system because the nonlinear operator  $\mathcal{N}(\mathbf{v}) := \mathbf{v} \cdot \nabla \mathbf{v}$  has not been proven to be bounded; proving that this operator is bounded is one of the Clay Institute's 'Millennium Problems' [1]. This implies that the nonlinear operator does not necessarily have finite-incremental gain which the small gain theorem states is necessary for closed-loop stability [45]. However, by ensuring the controllers are sufficiently robust to uncertainty, the feedback interconnection of the linear systems and controllers should remain stable.

If bounds on all modelling and exogenous uncertainties entering the system were known, each uncertainty could be extracted from the system model to form a *structured* uncertainty matrix  $\Delta$ . This structure could then be exploited when designing controllers to ensure a certain level of robustness. However, it is rare that bounds on *all* uncertainties can be evaluated. A simpler and more general class of uncertainty model exists in the form of *unstructured* uncertainty. Unstructured uncertainty models include [108] - additive uncertainty, multiplicative

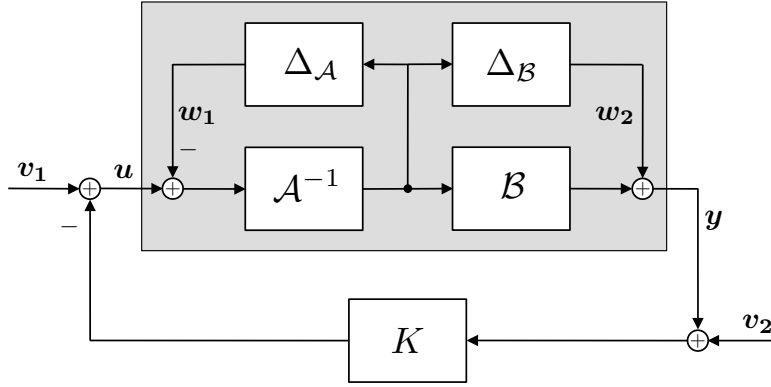


Figure 5.2: Block diagram represented the perturbed system  $\mathcal{P}_p$ , shaded box, in feedback with a controller  $K$ .  $\mathbf{v}_1$ ,  $\mathbf{v}_2$ ,  $\mathbf{w}_1$  and  $\mathbf{w}_2$  represent disturbance inputs.

input uncertainty and inverse multiplicative output uncertainty; each representing different classes of uncertainty. In the present work, for reasons that will be made apparent, a *coprime factor* uncertainty model shall be used to represent  $\Delta$ . This will be discussed in the following section.

### 5.2.1 Coprime Factor Uncertainty

Coprime factor uncertainty blends multiplicative and inverse multiplicative type uncertainties which account for dynamic and parametric uncertainty respectively [108]. Coprime factor perturbations take the form:

$$\mathcal{P}_p := \{(\mathcal{B} + \Delta_{\mathcal{B}})(\mathcal{A} + \Delta_{\mathcal{A}})^{-1}\}, \quad \text{such that} \quad \left\| \begin{bmatrix} \Delta_{\mathcal{B}} \\ \Delta_{\mathcal{A}} \end{bmatrix} \right\|_{\infty} < \frac{1}{\gamma}, \quad (5.3)$$

where  $\gamma > 1$ ,  $\mathcal{P} = \mathcal{B}\mathcal{A}^{-1}$  is a normalised right coprime factorisation of the unperturbed system  $\mathcal{P}$  such that  $\mathcal{A}^{\top}\mathcal{A} + \mathcal{B}^{\top}\mathcal{B} = I$ , and where  $\mathcal{P}_p$  is the perturbed system. Figure 5.2 shows a block diagram illustrating the effect of the coprime factor perturbations. Signal vectors  $\mathbf{v}_1$  and  $\mathbf{v}_2$  represent disturbances on the control input  $\mathbf{u}$  and measured output  $\mathbf{y}$  respectively, whereas  $\mathbf{w}_1$  and  $\mathbf{w}_2$  represent disturbances acting upon the system. The closed-loop transfer functions from the disturbance inputs to  $\mathbf{y}$  and  $\mathbf{u}$  are given as [108]:

$$\begin{bmatrix} \mathbf{y} \\ \mathbf{u} \end{bmatrix} = \begin{bmatrix} \mathcal{P} \\ I \end{bmatrix} (I - K\mathcal{P})^{-1} \begin{bmatrix} -K & I \end{bmatrix} \begin{bmatrix} \mathbf{v}_2 \\ \mathbf{v}_1 \end{bmatrix} + \begin{bmatrix} I \\ K \end{bmatrix} (I - \mathcal{P}K)^{-1} \begin{bmatrix} I & -\mathcal{P} \end{bmatrix} \begin{bmatrix} \mathbf{w}_2 \\ \mathbf{w}_1 \end{bmatrix}. \quad (5.4)$$

In order for the closed-loop system to be robust with respect to perturbations to the system's normalised coprime factors, it can be shown [108] that it is the norm of the first transfer function in (5.4) which needs to be minimised. With this in

mind, a stability margin for coprime factor perturbations  $b_{\mathcal{P},K}$  can be introduced. It is defined as follows:

$$b_{\mathcal{P},K} := \begin{cases} \left\| \left\| \begin{bmatrix} \mathcal{P} \\ I \end{bmatrix} (I - K\mathcal{P})^{-1} \begin{bmatrix} -K & I \end{bmatrix} \right\|_{\infty}^{-1} & \text{if } [\mathcal{P}, K] \text{ stable,} \\ 0 & \text{otherwise.} \end{cases} \quad (5.5)$$

It follows that  $b_{\mathcal{P},K} \geq \frac{1}{\gamma}$ , and therefore maximising  $b_{\mathcal{P},K}$  is a natural objective, subject to certain design criteria [85]. It can be proven that the  $\mathcal{H}_{\infty}$ -norm of the second transfer function in (5.4) is equal to that of the first [108], i.e.:

$$\left\| \begin{bmatrix} \mathcal{P} \\ I \end{bmatrix} (I - K\mathcal{P})^{-1} \begin{bmatrix} -K & I \end{bmatrix} \right\|_{\infty} = \left\| \begin{bmatrix} I \\ K \end{bmatrix} (I - \mathcal{P}K)^{-1} \begin{bmatrix} I & -\mathcal{P} \end{bmatrix} \right\|_{\infty}. \quad (5.6)$$

Therefore,  $b_{\mathcal{P},K}$  is a measure of both robust stability and robust performance because it bounds the gain of all eight closed-loop transfer functions between disturbance inputs and measured outputs at all points in the loop. This ability to gain *a priori* robustness guarantees on all these transfer functions is unique to the coprime factor uncertainty model, hence its use in the current work. The  $\mathcal{H}_{\infty}$  loop-shaping procedure of McFarlane and Glover [44, 85] automatically synthesises controllers which maximise the amount of coprime factor uncertainty that a closed-loop system can handle.

### 5.3 Model Refinement

Whenever a finite-dimensional model is used to approximate an infinite-dimensional system such as channel flow, the question of what degree of spatial discretisation is sufficient, is pertinent. There has been a lot of research into model reduction, and various methods exist in the literature. These methods tend to begin with high-dimensional open-loop models and use different justifications to reduce their size. Model reduction techniques include balanced proper orthogonal decomposition [96], balanced truncation [97], and eigensystem realisation [82] among others. However, these methods all produce low-order models which only match the *open-loop* systems' dynamics, and provide no guarantees on the effect the model reduction has on a closed-loop system. In this section, the model refinement procedure, first proposed by Jones and Kerrigan [58], will be outlined. Unlike most model reduction techniques, model refinement provides guarantees on the closed-loop performance of the low-order models it produces. Central to model refinement is the  $\nu$ -gap metric.

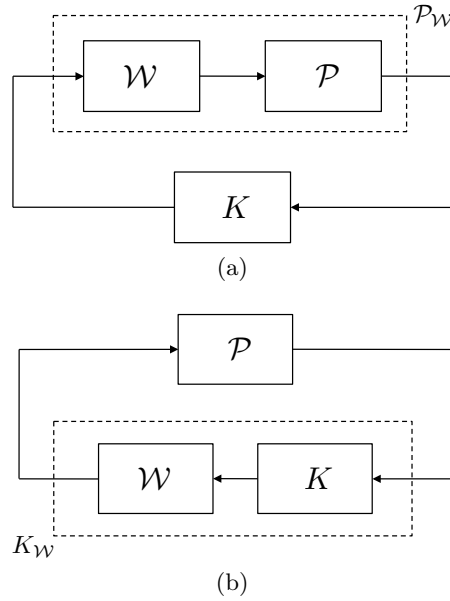


Figure 5.3: Block diagrams illustrating the loop-shaping procedure. (a) System  $\mathcal{P}$  is augmented with precompensator matrix  $\mathcal{W}$  to form shaped system  $\mathcal{P}_\mathcal{W}$  with desirable loop shape. (b) When implementing the final controller, precompensator matrix  $\mathcal{W}$  is absorbed back into  $K$  to form the weighted controller  $K_\mathcal{W}$ .

### 5.3.1 The $\nu$ -Gap Metric

In order to ascertain whether a model is suitable for feedback control, a measure of closed-loop system “closeness” is required. Such a measure exists, and it is called the  $\nu$ -gap metric [5, 108]. The  $\nu$ -gap metric between two systems, denoted  $\delta_\nu(\mathcal{P}_a, \mathcal{P}_b)$ , is a metric and thus satisfies the following properties:

$$0 \leq \delta_\nu(\mathcal{P}_a, \mathcal{P}_b) \leq 1, \quad (5.7a)$$

$$\delta_\nu(\mathcal{P}_a, \mathcal{P}_a) = 0, \quad (5.7b)$$

$$\delta_\nu(\mathcal{P}_a, \mathcal{P}_c) \leq \delta_\nu(\mathcal{P}_a, \mathcal{P}_b) + \delta_\nu(\mathcal{P}_b, \mathcal{P}_c) \quad (\text{Triangle inequality}). \quad (5.7c)$$

The  $\nu$ -gap between systems is calculated under the assumption that both systems are in feedback with a unity gain controller, i.e.  $K = I$ . Although this is a somewhat restrictive assumption, it can be overcome by shaping the systems using a precompensator matrix  $\mathcal{W}$ , such that they have desirable open-loop frequency responses - high gain at low frequency, low gain at high frequency etc.. This loop-shaping procedure is illustrated in Figure 5.3. The  $\nu$ -gap is then calculated between the shaped systems  $\delta_\nu(\mathcal{P}_{\mathcal{W}_a}, \mathcal{P}_{\mathcal{W}_b})$ . The  $\nu$ -gap is highly dependent not only on the systems  $\mathcal{P}$ , but also on the closed-loop objectives represented by the precompensator matrices  $\mathcal{W}$ . This is highly important when determining whether or not a model is suitable for feedback control.

### 5.3.2 Model Refinement Procedure

The objective of the model refinement technique is to evaluate a bound on the  $\nu$ -gap between shaped infinite-dimensional system  $\mathcal{P}_{\mathcal{W}\infty}$  and a finite dimensional approximation of the system  $\mathcal{P}_{\mathcal{W}n}$ , where  $n$  denotes order of dimension. The  $\nu$ -gap  $\delta_\nu(\mathcal{P}_{\mathcal{W}n}, \mathcal{P}_{\mathcal{W}\infty})$  is very useful for determining to what extent a spatial discretisation of an infinite-dimensional model yields a model that is suitable for feedback control. Unfortunately, this quantity can rarely be calculated directly. Instead,  $\nu$ -gaps between low-order system models of successively finer resolution are computed. The  $\nu$ -gaps calculated asymptote towards zero as resolution is increased. Once the rate of convergence of the  $\nu$ -gaps is established, an upper bound on the  $\nu$ -gap between finite-dimensional models in the computed sequence and the infinite-dimensional system can be constructed. This informs on what level of model discretisation is sufficient for robust feedback control of the infinite-dimensional system.

The model refinement procedure is as follows [58, 60]:

1. Specify closed-loop objectives by designing a precompensator matrix  $\mathcal{W}$  to form the weighted infinite-dimensional system  $\mathcal{P}_{\mathcal{W}\infty}$ .
2. Discretise this system on an initial (small) grid of  $n_i$  points, to produce spatially discrete system  $\mathcal{P}_{\mathcal{W}n_i}$ .
3. Starting from  $n = n_i$ , compute  $\nu$ -gaps  $\delta_\nu(\mathcal{P}_{\mathcal{W}n}, \mathcal{P}_{\mathcal{W}n+1})$  for progressively finer grid resolution. The  $\nu$ -gaps should asymptote towards zero with increasing  $n$ .
4. When  $\nu$ -gaps become sufficiently small for grid resolution  $n = n_0$ , construct a sequence  $\{a_n\}$ , such as a geometric progression, that upper bounds the computed  $\nu$ -gap sequence for  $n \geq n_0$ .
5. The triangle inequality property, (5.7c), can be used to bound the  $\nu$ -gap between the finite-dimensional ( $n = n_0$ ) and infinite-dimensional systems as follows:

$$\delta_\nu(\mathcal{P}_{\mathcal{W}n_0}, \mathcal{P}_{\mathcal{W}\infty}) \leq \sum_{n=n_0}^{\infty} \delta_\nu(\mathcal{P}_{\mathcal{W}n}, \mathcal{P}_{\mathcal{W}n+1}) \leq \sum_{n=n_0}^{\infty} a_n. \quad (5.8)$$

Thus a bound on  $\delta_\nu(\mathcal{P}_{\mathcal{W}n}, \mathcal{P}_{\mathcal{W}\infty})$  can be obtained by computing the series  $\{a_n\}$ . Therefore, providing the robust stability margin  $b_{\mathcal{P},K}$  of the  $\mathcal{H}_\infty$  loop-shaping controller synthesised from  $\mathcal{P}_{\mathcal{W}}, n_0$  exceeds this bound by a reasonable amount, robust closed-loop performance is guaranteed.

## 5.4 $\mathcal{H}_\infty$ Loop-Shaping Control of Channel Flow

In the previous two sections, it was shown how low-order controllers can be synthesised with *a priori* guarantees of robustness to uncertainty and performance in terms of input disturbance rejection. Therefore, in this section,  $\mathcal{H}_\infty$  loop-shaping controllers will be designed to minimise streamwise wall-shear stress perturbations in  $\text{Re} = 2230$  channel flow. This is the same Reynolds number as used for passivity-based control, and corresponds to  $\text{Re}_\tau = 100$  fully-turbulent channel flow. Controllers will be designed for a range of wavenumber pairs and tested using DNS. In the following, the controller design procedure will be demonstrated for a single wavenumber pair only - ( $\alpha = 0, \beta = 2$ ).

This control method, like the passivity-based control method, synthesises a LTI controller from a LTI control model. All controllers synthesised in this chapter will use Galerkin-discretised control models only. This is because in the previous chapter, the Galerkin-discretised controllers had better convergence properties and better linear performance. The choice of actuation via wall transpiration at each wall is the same as previous. However, for this work, only measurements of *streamwise* wall-shear stress are required by the controllers. The Galerkin-discretised LTI control model used in this chapter for each Fourier mode ( $\alpha, \beta$ ) is given as:

$$\frac{\partial}{\partial t} \mathbf{x}(t) = A\mathbf{x}(t) + B_2\mathbf{u}(t), \quad (5.9a)$$

$$\mathbf{y}(t) = C_2\mathbf{x}(t), \quad (5.9b)$$

where matrices  $A \in \mathbb{C}^{2N \times 2N}$  and  $B_2 \in \mathbb{C}^{2N \times 2}$ , state vector  $\mathbf{x} \in \mathbb{C}^{2N}$  and input vector  $\mathbf{u} \in \mathbb{C}^2$  are defined in (2.66). Vector  $\mathbf{y} \in \mathbb{C}^2$  contains measurements of streamwise wall-shear stress only at each wall. Therefore, from (4.59), the  $C_2$ -matrix is now defined as:

$$\mathbf{y} = \frac{1}{k^2 \cdot \text{Re}} \underbrace{\begin{bmatrix} i\alpha\Phi_N''(+1) & i\alpha f_u''(+1) & i\alpha f_1''(+1) & -i\beta\Psi_N'(+1) \\ i\alpha\Phi_N''(-1) & i\alpha f_u''(-1) & i\alpha f_1''(-1) & -i\beta\Psi_N'(-1) \end{bmatrix}}_{C_2} \underbrace{\begin{bmatrix} \mathbf{a}_{v_{N-2}} \\ \hat{v}^+ \\ \hat{v}^- \\ \mathbf{a}_{\eta_N} \end{bmatrix}}_{\mathbf{x}}, \quad (5.10)$$

### 5.4.1 Controller Design Procedure

The LTI state-space model in (5.9) can be transformed into the following transfer function matrix:

$$\mathcal{P}_{N_y}(s) = C_2(sI - A)^{-1}B_2, \quad (5.11)$$

where the subscript  $N_y$  denotes that the state-space system in (5.9) has been discretised on  $N_y$  grid points. Alternatively, from a Galerkin perspective, the LTI

system uses  $N_y$  spectral coefficients/basis functions. Before weighting the system, the frequency-response of the unweighted system  $\mathcal{P}_{N_y}$  needs to be analysed first. The frequency response of the maximum singular values of (5.11), denoted  $\bar{\sigma}(\mathcal{P}_{N_y})$ , is shown in Figure 5.4(a), for wall-normal resolutions  $N_y = 30$  and  $N_y = 100$ . Both responses are below unity gain for the bandwidth visible, and are similar to one another up to frequency  $\omega \approx 50$ . At higher frequencies, the two responses diverge. This is to be expected, as the lower resolution system model will have un-modelled high frequency dynamics. In order to obtain desired closed-loop performance, the system now needs to be shaped using a precompensator matrix  $\mathcal{W}$ , such that the following design criteria are met [60]:

- Loop crossover frequency at  $\omega_c \approx 1$ . This will result in good input disturbance rejection.
- Loop crossover slope of not much less than -1. This will ensure good robustness to uncertainty.
- High-gain at frequencies  $\omega < \omega_c$ . This will reduce the effects uncertain parameters and disturbances have in the low-frequency range.
- Low-gain at frequencies  $\omega > \omega_c$ . This ensures the closed-loop system is unaffected by high-frequency disturbances such as sensor noise and unmodelled dynamics.

A precompensator that achieves these objectives for this Fourier mode is found to be:

$$\mathcal{W}(s) = \frac{30}{s}I. \quad (5.12)$$

The frequency response of the maximum singular values of the shaped system, denoted  $\bar{\sigma}(\mathcal{P}_{\mathcal{W}N_y})$ , for both wall-normal resolutions, is given in Figure 5.4(b). As can be seen, all design objectives have been achieved. Note that any divergence in the responses for the two resolutions is only apparent for frequencies  $\omega \gg \omega_c$ , where the closed-loop system is insensitive to such un-modelled dynamics.

With a suitably designed precompensator  $\mathcal{W}$ , model refinement will now be used to decide what level of discretisation is required for good closed-loop robustness. The  $\nu$ -gaps between weighted system models of successively finer resolution were computed, and are plotted as black dots in Figure 5.5. As grid resolution is increased, the  $\nu$ -gaps  $\delta_\nu(\mathcal{P}_{\mathcal{W}N_y}, \mathcal{P}_{\mathcal{W}N_y+1})$  quickly asymptote towards zero as expected. The following geometric progression was found which upper bounds this computed sequence of  $\nu$ -gaps for  $5 \leq N_y \leq 40$ :

$$\{a_{N_y}\} = 1.7(0.82)^{N_y}. \quad (5.13)$$

This is plotted as black crosses in Figure 5.5. Now, assuming the series  $\{a_{N_y}\}$

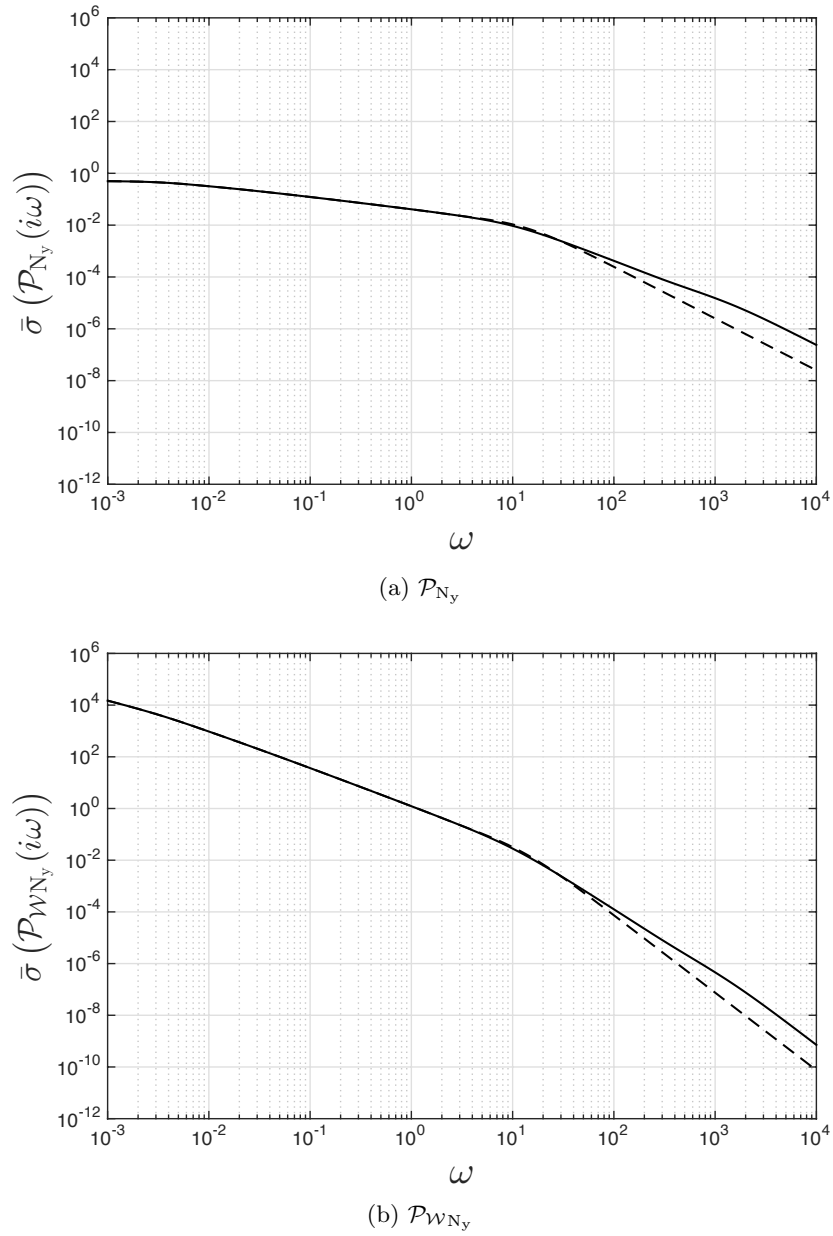


Figure 5.4: Plots of maximum singular values vs. frequency for (a) uncompensated system  $\mathcal{P}_{N_y}$ , and (b) compensated system  $\mathcal{P}_{W_{N_y}}$ , for  $N_y = 30$  (---) and  $N_y = 100$  (—), for mode  $(\alpha = 0, \beta = 2)$ .

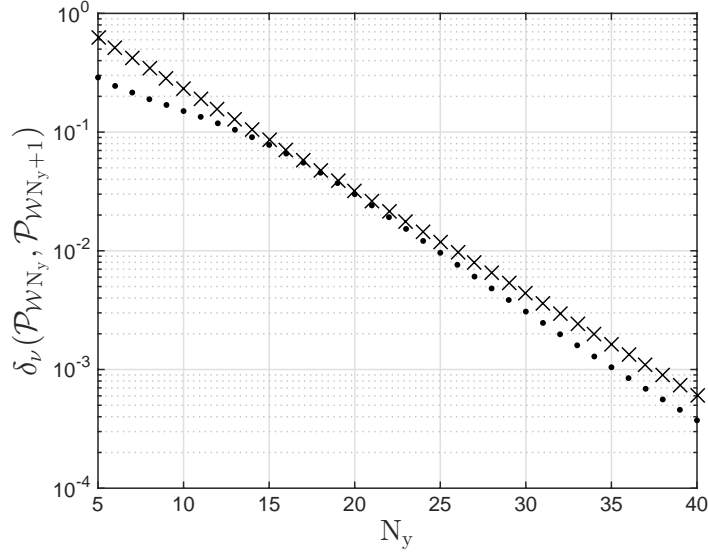


Figure 5.5: Plots of  $\delta_\nu(\mathcal{P}_{\mathcal{W}N_y}, \mathcal{P}_{\mathcal{W}N_{y+1}})$  - ( $\cdot$ ), and sequence  $\{1.7(0.82)^{N_y}\}$  - ( $\times$ ) vs. grid resolution  $N_y$ , for  $(\alpha = 0, \beta = 2)$ .

continues to upper bound the  $\nu$ -gap series  $\delta_\nu(\mathcal{P}_{\mathcal{W}N_y}, \mathcal{P}_{\mathcal{W}N_{y+1}})$  for  $N_y > 40$ , the following inequality holds:

$$\delta_\nu(\mathcal{P}_{\mathcal{W}n_0}, \mathcal{P}_{\mathcal{W}\infty}) \leq \sum_{N_y=n_0}^{\infty} 1.7(0.82)^{N_y} = \frac{1.7(0.82)^{n_0}}{1 - 0.82}. \quad (5.14)$$

Therefore, a weighted system model discretised on 20 grid points will have  $\nu$ -gap:

$$\delta_\nu(\mathcal{P}_{\mathcal{W}20}, \mathcal{P}_{\mathcal{W}\infty}) \leq 0.18. \quad (5.15)$$

The robust stability margin of a  $\mathcal{H}_\infty$  loop-shaping controller  $K_{20}$  designed using discrete system model  $\mathcal{P}_{\mathcal{W}20}$  was found to be  $b_{\text{opt}}(\mathcal{P}_{\mathcal{W}20}) = 0.50$ . The procedure for synthesising  $K$  can be found in Glover and McFarlane[44]. *A priori* guarantees of robustness are given by the fact that the robust stability margin  $b_{\text{opt}}(\mathcal{P}_{\mathcal{W}20})$  exceeds the  $\nu$ -gap  $\delta_\nu(\mathcal{P}_{\mathcal{W}20}, \mathcal{P}_{\mathcal{W}\infty})$  by a reasonable margin of 0.32. Before implementation, the controller is weighted with the precompensator matrix  $\mathcal{W}$ , as in Figure 5.3, to form the final controller  $K_{\mathcal{W}20}$ .

Controllers were synthesised for all wavenumber pairs in the range  $(\alpha \leq 2, \beta \leq 12)$ . A fixed wall-normal resolution of  $N_y = 60$  was chosen because performing the model refinement procedure on all controllers would be too time-intensive. This wall-normal resolution was deemed to be high enough for all wavenumber pairs to have sufficiently low  $\nu$ -gaps with their infinite dimensional counterparts. Future work could look at reducing the dimension of each controller using the full model

refinement procedure. Precompensators of the form:

$$\mathcal{W}(s) := \frac{X}{s}I, \quad (5.16)$$

are used for each controller, with  $X \in \mathbb{R}_+$  being varied to ensure the design criteria are met. Examples of uncompensated and compensated loop shapes for modes  $(\alpha = 1, \beta = 0)$  and  $(\alpha = 1, \beta = 1)$  are shown in Figure 5.6. Finding a precompensator matrix which achieved a desirable loop shape for mode  $(\alpha = 1, \beta = 0)$  was difficult. The final loop shape shown, has a relatively low cross-over frequency of  $\omega_c \approx 4 \cdot 10^{-2}$ , meaning the controller will only be able to reject low-frequency disturbances. Similar difficulties were found when designing loop shapes for other spanwise-constant modes. The precompensated loop shape for mode  $(\alpha = 1, \beta = 1)$  is similar to that shown for mode  $(\alpha = 0, \beta = 2)$  in Figure 5.4, and meets all the design criteria.

To ensure good robustness to uncertainty, including the nonlinear disturbance inputs, all controllers have a robustness margin of:

$$\mathcal{R} = \{b_{\text{opt}}(\mathcal{P}_{\mathcal{W}60}) - \delta_\nu(\mathcal{P}_{\mathcal{W}60}, \mathcal{P}_{\mathcal{W}\infty})\} > 0.4. \quad (5.17)$$

Each controller has an actuator time-constant  $\tau_\phi = 0.1$ . The performance of these controllers will be evaluated using DNS in the following section.

#### 5.4.2 DNS Testing

The controllers are evaluated on  $\text{Re}_\tau = 100$  fully turbulent channel flow. All simulation parameters, such as domain size, grid resolution, time-stepping algorithm etc., are exactly the same as those used to test the passivity-based controllers from the previous chapter, and so will not be repeated here. Three controlled simulations were carried out, each simulation involving different combinations of controlled modes. The modes controlled in each of the simulations are as follows:

1.  $(\alpha \leq 2, \beta \leq 4)$  - Controllers denoted  $K_{(\alpha 2, \beta 4)}$ .
2.  $(\alpha \leq 2, \beta \leq 8)$  - Controllers denoted  $K_{(\alpha 2, \beta 8)}$ .
3.  $(\alpha \leq 2, \beta \leq 12)$  - Controllers denoted  $K_{(\alpha 2, \beta 12)}$ .

The drag reductions achieved by each of the combinations of controllers will indicate which modes contribute most to the mean drag and thus need to be controlled. In the passivity-based control work, it was shown that it is the lower streamwise-constant modes of a channel flow which contribute most to the production of perturbation energy. In the current work however, the control objective is different, and therefore the spatial modes of interest may be different. It was decided to only control  $(\alpha \leq 2, \beta)$  modes and to explore the wavenumber space in the direction of increasing  $\beta$ . This is due to early pilot testing which showed relatively

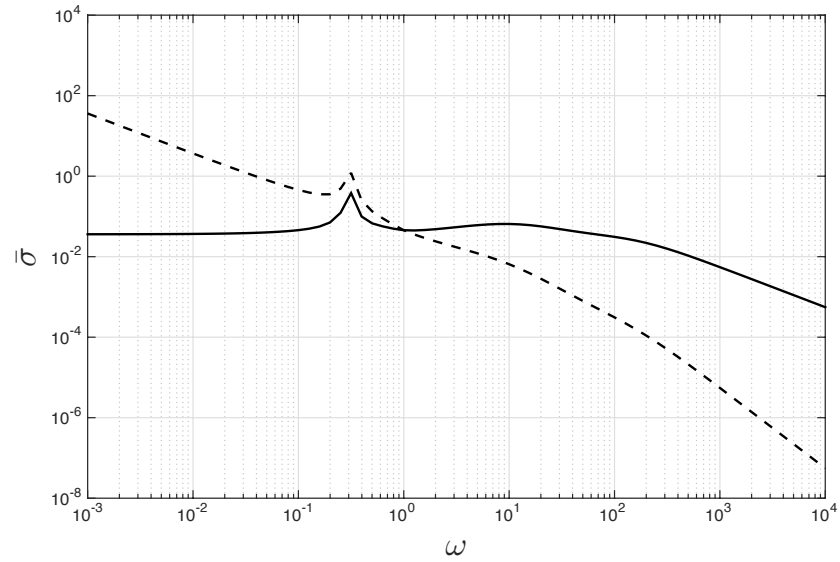
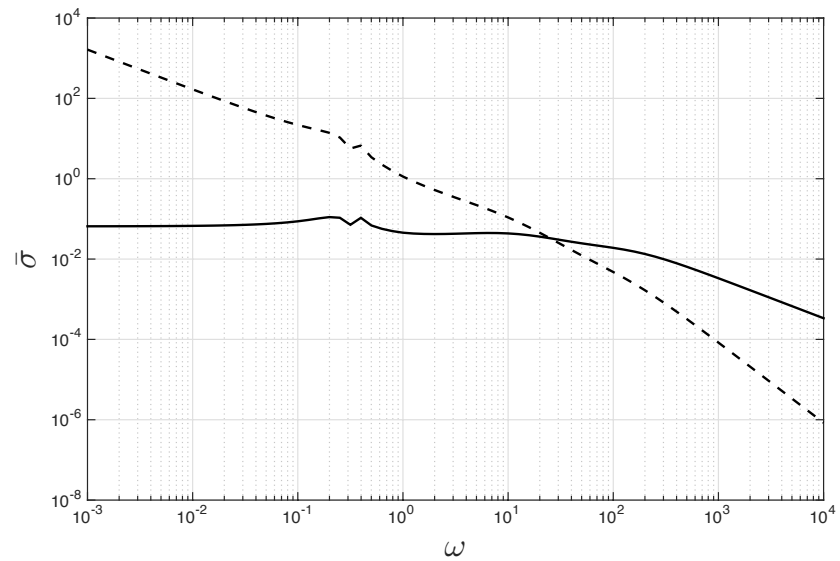
(a)  $(\alpha = 1, \beta = 0)$ ,  $\mathcal{W} = \frac{1}{s}I$ ,  $\mathcal{R} = 0.48$ (b)  $(\alpha = 1, \beta = 1)$ ,  $\mathcal{W} = \frac{25}{s}I$ ,  $\mathcal{R} = 0.46$ 

Figure 5.6: Plots of maximum singular values vs. frequency for uncompensated  $\mathcal{P}_{60}$  (—) and compensated  $\mathcal{P}_{\mathcal{W}_{60}}$  (---) systems for (a) mode  $(\alpha = 1, \beta = 0)$ , and (b) mode  $(\alpha = 1, \beta = 1)$ ,  $N_y = 60$ . Also displayed are the precompensator matrices  $\mathcal{W}$  used and the resulting robust stability margins  $\mathcal{R}$ .

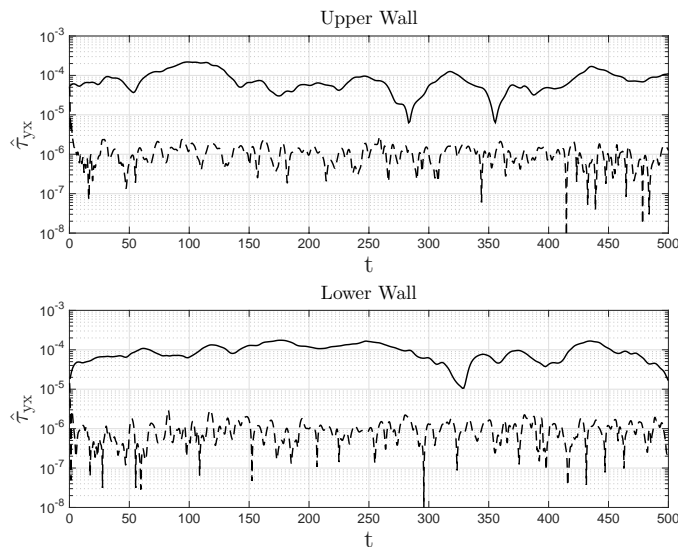


Figure 5.7: Plots of streamwise wall-shear stress  $\hat{\tau}_{yx}$  for mode  $(\alpha = 0, \beta = 2)$ , from uncontrolled (—) and controlled (---) simulations.

poor input disturbance rejection performance for wavenumber pairs  $(\alpha > 2, \beta)$ . Achieving loop-shapes which met the design criteria for these modes was difficult and this may be the reason for their poor performance.

Figure 5.7 shows plots of streamwise shear-stress for mode  $(\alpha = 0, \beta = 2)$  at the upper and lower walls from uncontrolled and controlled simulations. Of the three controlled simulations, all had very similar modal streamwise shear-stress data for the controlled modes, therefore no distinction will be made between the simulations when discussing results for individual controlled modes. The effect of the controller for this mode is striking, within five time units,  $\hat{\tau}_{yx}$  at both walls reduces by two orders of magnitude from  $\hat{\tau}_{yx} \approx 10^{-4}$  to  $\hat{\tau}_{yx} \approx 10^{-6}$ . It then remains at this level ad infinitum. This illustrates the excellent input disturbance rejection performance offered by this control method. Similar results were found for other controlled streamwise-constant modes. Figure 5.8 shows plots of streamwise wall-shear stress at both walls for spanwise-constant mode  $(\alpha = 2, \beta = 0)$  and oblique mode  $(\alpha = 2, \beta = 2)$  from uncontrolled and controlled simulations. The performance of controllers on all spanwise-constant modes was poor and had similar controlled shear stress time histories to those shown in the figure. The controllers are unable to reject disturbances for these modes effectively and hence are unable to reduce perturbation streamwise wall-shear stress to a large degree. This is likely to be due to the final loop-shapes for these controllers which, as in Figure 5.6, all have relatively low crossover frequencies. This means the controllers are limited to only rejecting very low frequency disturbances. It may be possible to improve the performance of the spanwise-constant controllers by using different weighting matrices to improve their loop shapes. The performance of

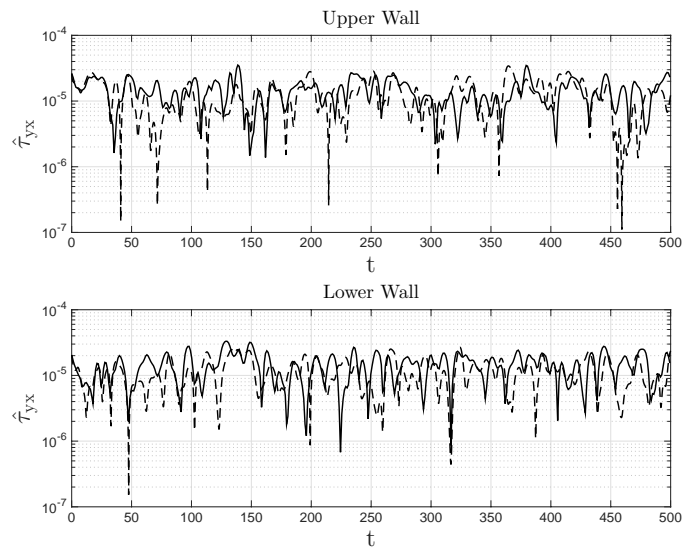
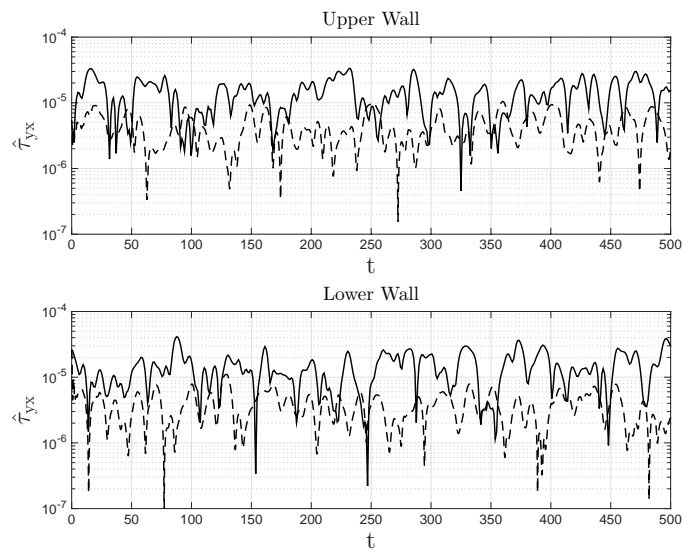
(a) ( $\alpha = 2, \beta = 0$ )(b) ( $\alpha = 2, \beta = 2$ )

Figure 5.8: Plots of streamwise wall-shear stress  $\hat{\tau}_{yx}$  for modes  $(\alpha = 2, \beta = 0)$  and  $(\alpha = 2, \beta = 2)$ , from uncontrolled (—) and controlled (---) simulations.

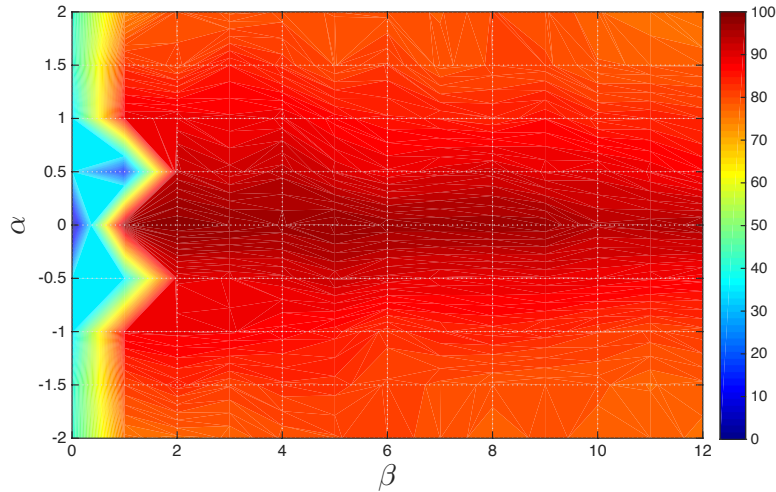


Figure 5.9: Colour map representing % rms reductions in perturbation streamwise wall-shear stress for all controlled modes from  $K_{(\alpha 2, \beta 12)}$ -controlled simulation.

controllers on oblique modes varied, but the shear stress time history in Figure 5.8 for mode  $(\alpha = 2, \beta = 2)$  is typical for these modes. The controllers are capable of significantly reducing perturbation shear stress, but not to the same degree as for the streamwise-constant modes. Again, the performance of these controllers may be improved by finding weighting matrices which lead to loop shapes with higher crossover frequencies. This will increase the bandwidth of disturbances for which the controllers can mitigate.

Figure 5.9 shows a colour map representing the %rms reductions in perturbation streamwise wall-shear stress by the controllers for all controlled modes. The streamwise-constant modes have noticeably higher reductions in streamwise wall-shear stress compared to all other modes in the wavenumber space. These modes show close to 100% reductions. Conversely, the spanwise-constant modes have the lowest reductions in shear stress, with reductions of  $\approx 40\%$ . Interestingly, the modes  $(\alpha = \pm 0.5, \beta = 1)$  have much lower shear stress reductions than the remaining oblique modes, with similar reductions to the spanwise-constant modes. This may be due to poor loop shape design for these controllers or the controllers may be unable to reject the effects of the nonlinear forcing for these modes. With the reductions in shear stress of the streamwise-constant modes so much greater than all other modes, larger drag reductions should be expected in the  $K_{(\alpha 2, \beta 12)}$ -controlled simulation as more streamwise-constant modes are controlled.

Figure 5.10 shows colour maps of streamwise velocity overlaid with contours of streamwise vorticity for mode  $(\alpha = 0, \beta = 2)$  from uncontrolled and controlled simulations for time  $t = 1100$ . The effect of the controller here is two-fold. Firstly, the controller has severely weakened the streaky structures (the alternating regions of positive and negative streamwise velocity perturbations) close to the walls and

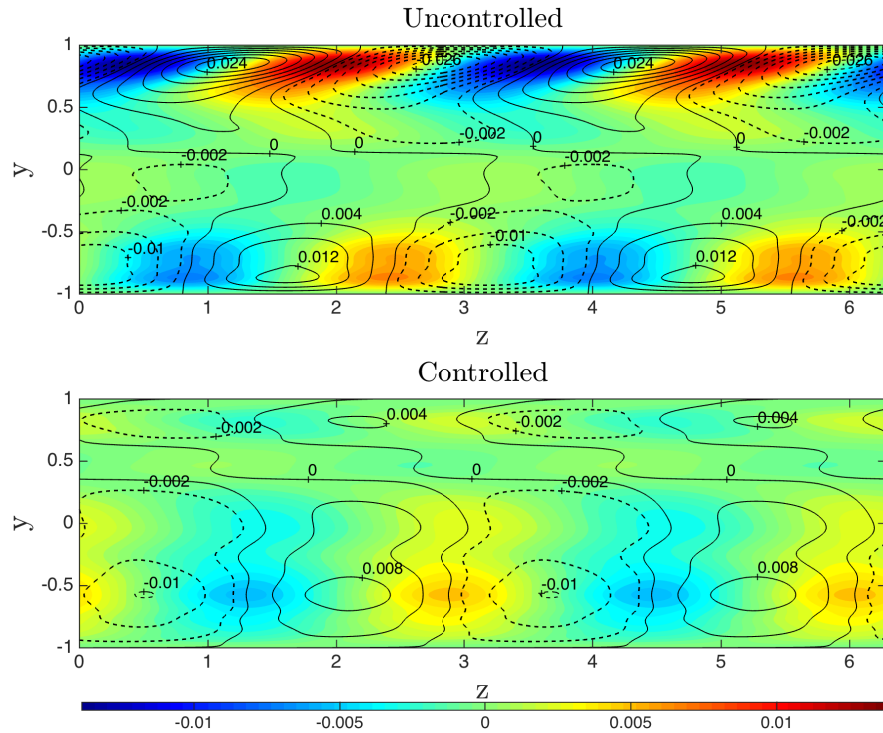


Figure 5.10: Colour maps of streamwise velocity  $\hat{u}$  overlaid with contours of streamwise vorticity  $\hat{\eta}_x$  for mode  $(\alpha = 0, \beta = 2)$ , for time  $t = 1100$ .

pushed them away from the walls. Secondly, the controller has weakened the streamwise vortices close to the walls and pushed them away from the walls. In effect, this produces “buffer zones” close to the wall with very low streamwise velocity and vorticity. Figures 5.11 and 5.12 show colour maps of streamwise velocity overlaid with arrows representing in-plane velocity at times  $t = 0, 20$  and  $50$  at the bottom wall for mode  $(\alpha = 0, \beta = 2)$  from uncontrolled and controlled simulations respectively. At  $t = 20$ , a thin buffer zone created by the controller can be seen between  $0 \leq y^+ \leq 3$ , identified by near-constant streamwise velocity  $\hat{u} \approx 0$ . This buffer zone is maintained for all  $t$ . The actuation at the wall ( $y^+ = 0$ ) can also be seen at times  $t = 20$  and  $50$ . At  $t = 20$ , there is a relatively large negative actuation signal at  $z^+ = 100$  and relatively large positive actuation signal at  $z^+ = 250$ . The effect of these actuation signals is to counterrotate a streamwise vortex centred at  $z^+ = 150, y^+ = 25$ . This is an example of how the controller weakens streamwise vorticity close to the wall. Comparing the uncontrolled and controlled plots for  $t = 50$ , it can be seen how the controller has weakened the streaks close to the wall significantly. Also, whereas in the uncontrolled case, a small streamwise vortex centred at  $z^+ = 160, y^+ = 20$  sits between the streaks, in the controlled case, all vortices have been pushed far away from the wall with no vortex centres visible in the plot.

Resolution checks were performed for the  $\mathcal{H}_\infty$  loop-shaping controllers in the same manner as for the passivity-based controllers in Chapter 4. The table in

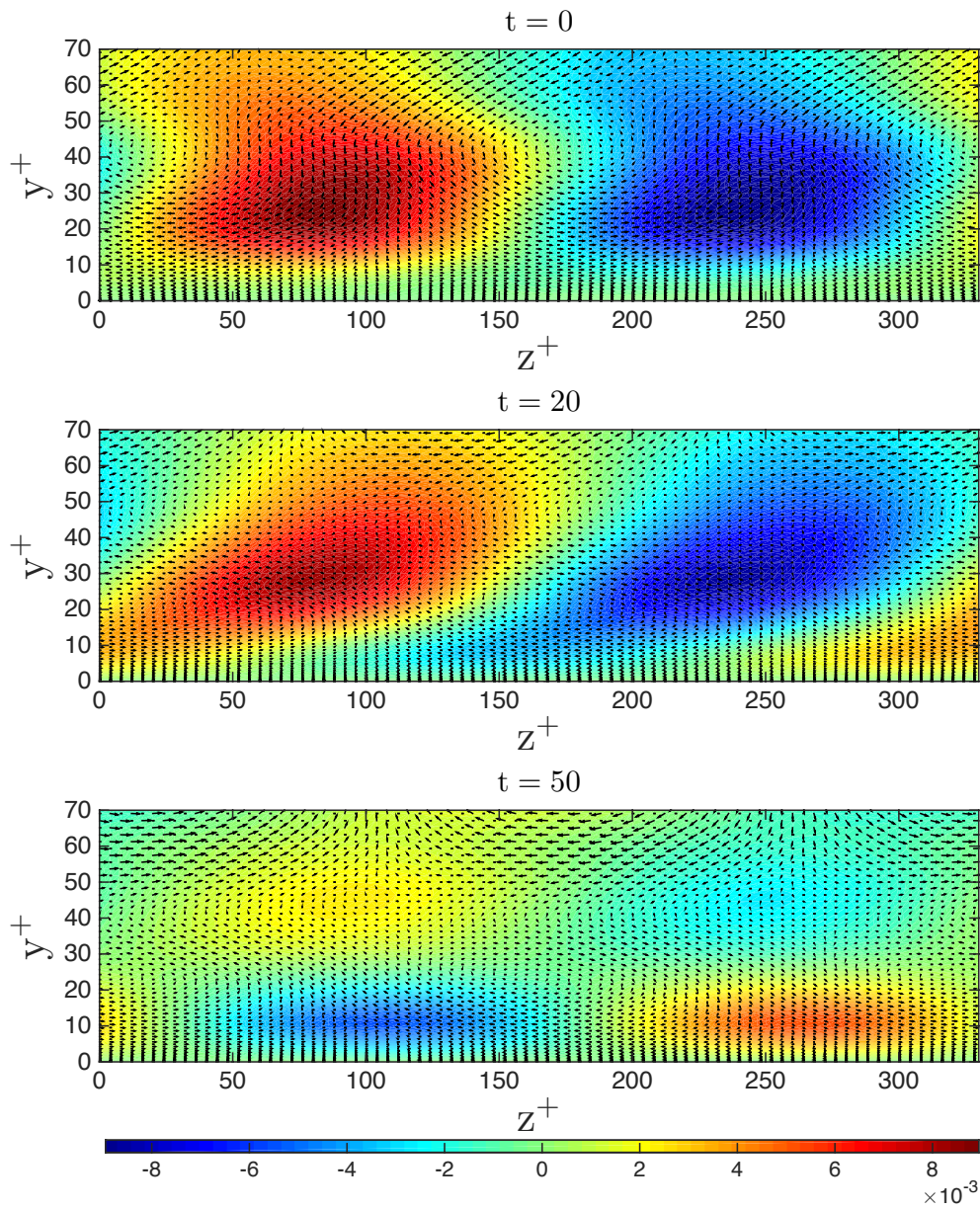


Figure 5.11: Colour maps of streamwise velocity  $\hat{u}$  overlaid with arrows representing in-plane velocity vectors at the lower wall for **uncontrolled** mode ( $\alpha = 0, \beta = 2$ ), at times  $t = 0, 20$  and  $50$ .

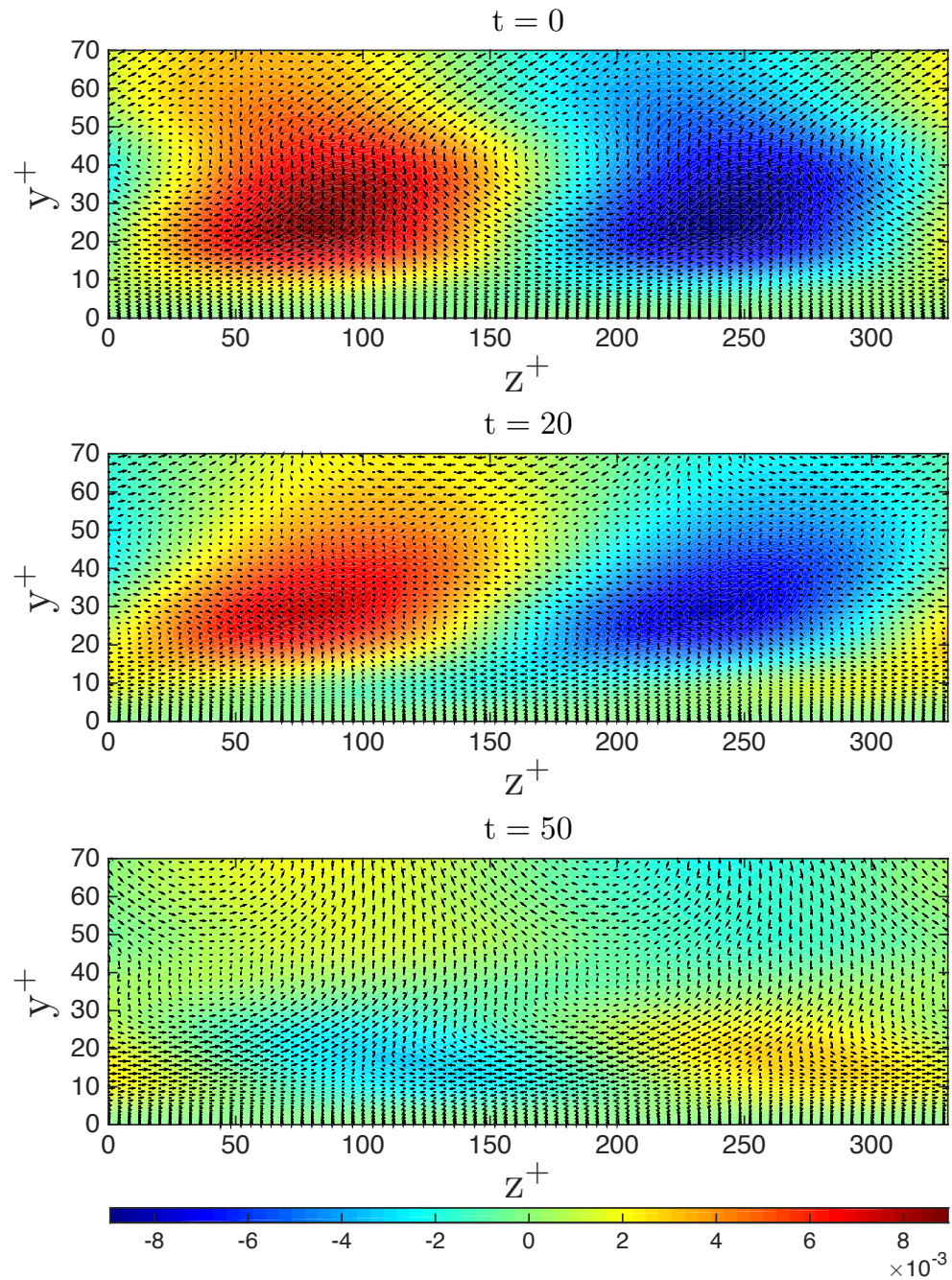


Figure 5.12: Colour maps of streamwise velocity  $\hat{u}$  overlaid with arrows representing in-plane velocity vectors at the lower wall for **controlled** mode ( $\alpha = 0, \beta = 2$ ), at times  $t = 0, 20$  and  $50$ .

$\Delta x^+$	$\Delta z^+$	$N_y$	$t_f - t_i$	$C_f \times 10^{-3}$	$ \Delta C_f (\%)$	$\bar{D}_R(\%)$
6.90	3.98	151	1000	9.04	—	3.00
11.4	3.98	151	200	9.01	0.33	2.70
6.90	5.71	151	200	9.37	3.52	-0.54
6.90	2.99	151	100	8.56	5.31	7.85
5.98	3.98	151	60	9.01	0.33	3.33
6.90	3.98	129	300	9.12	0.88	2.15

Figure 5.13: Table detailing the resolution checks for the  $K_{(\alpha 2, \beta 4)}$ -controlled simulation. Column 6 lists the percentage change in skin-friction coefficient with respect to the first row which corresponds to the grid spacings used for all testing. The final column lists the percentage reductions in skin-friction drag with respect to the uncontrolled simulation with corresponding grid spacings.

Figure 5.13 lists skin-friction coefficients and percentage drag reductions from  $K_{(\alpha 2, \beta 4)}$ -controlled simulations with different resolutions. The percentage reductions in drag listed in the final column of the table are with respect to the uncontrolled simulations with corresponding resolution; these results can be found in Figure 4.15. The data in the first row of the table pertains to the grid resolution used for all DNS testing. Unfortunately, the amount of simulation data obtained for the other resolutions is limited. Therefore, there is not enough data to obtain accurate temporal mean values for  $C_f$  and  $\bar{D}_R$  for these resolutions. This may be why the percentage drag reduction varies so wildly. Under the assumption that the data in rows 3 and 4 of the table in Figure 5.13 are anomalous due to insufficient sampling times, an estimate of the drag reduction by the  $K_{(\alpha 2, \beta 4)}$  controller is  $\bar{D}_R = 3.0 \pm 1\%$ . This accuracy bound will be applied to all results in this chapter.

Figures 5.14-5.16 show plots of total skin-friction drag at both walls for the uncontrolled and  $K_{(\alpha 2, \beta 4)}$ ,  $K_{(\alpha 2, \beta 8)}$  and  $K_{(\alpha 2, \beta 12)}$  controlled simulations respectively. A summary table of the mean total skin-friction drag reductions from each controlled simulation is provided in Figure 5.17. The  $K_{(\alpha 2, \beta 4)}$  controller achieves a modest drag reduction of  $\approx 3\%$ . This can be seen in its drag time-history in Figure 5.14 which is of a similar magnitude to the uncontrolled flow's. It would appear that the effect of these modal controllers is not enough to have a significant impact on the total drag. The  $K_{(\alpha 2, \beta 8)}$  controller achieves a higher drag reduction of  $\approx 9\%$ . This is reflected in the drag time-history from this simulation, shown in Figure 5.15. Although the controlled drag time-history does exceed that of the uncontrolled flow's at a few points in time, the controllers are capable of significantly reducing the temporal mean drag on both walls. This result indicates that wavenumber pairs ( $\alpha \leq 2, \beta > 4$ ) are important contributors to a flow's total drag. The  $K_{(\alpha 2, \beta 12)}$  controller has achieved by far the largest drag reduction of  $\approx 12\%$ . The drag time-history from this simulation in Figure 5.16, shows that besides a brief overlap at  $t \approx 250$ , the controlled total drag at both walls is consistently below that of the uncontrolled flow. The fact that the mean drag reduction is larger

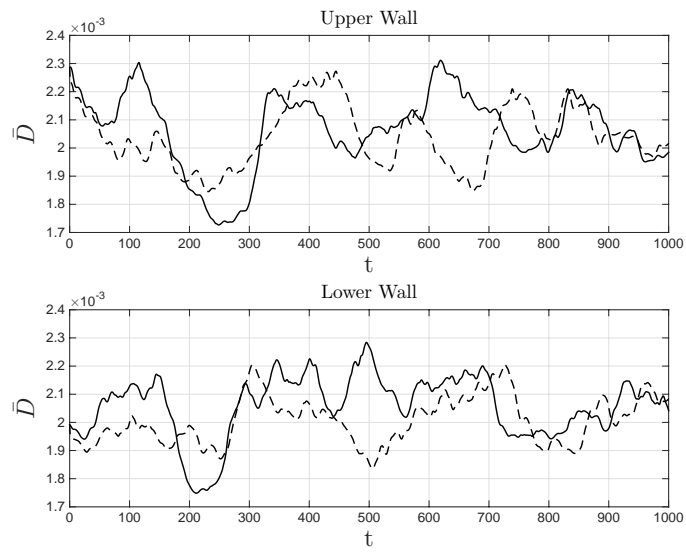


Figure 5.14: Plots of total skin-friction drag from uncontrolled (—) and  $K_{(\alpha 2, \beta 4)}$ -controlled (---) simulations.

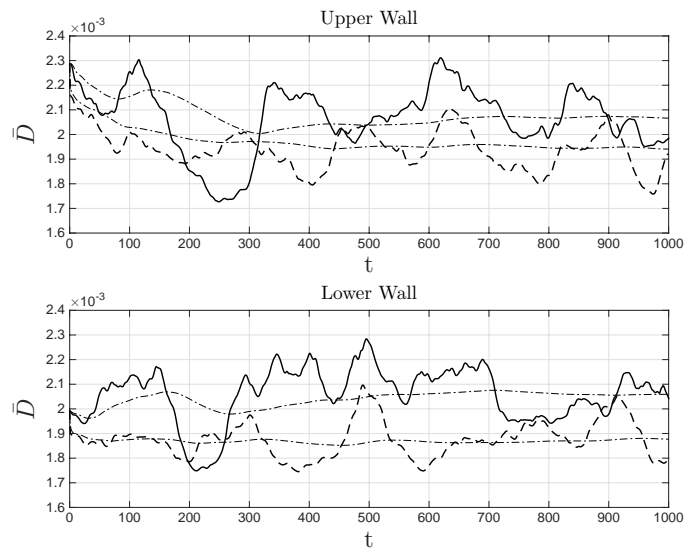


Figure 5.15: Plots of total skin-friction drag from uncontrolled (—) and  $K_{(\alpha 2, \beta 8)}$ -controlled (---) simulations, plots of the moving mean values (-·-) are also included.

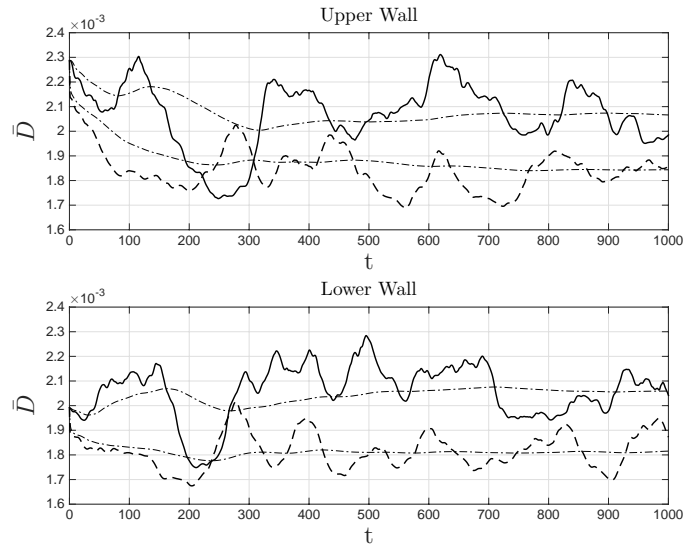


Figure 5.16: Plots of total skin-friction drag from uncontrolled (—) and  $K_{(\alpha 2, \beta 12)}$ -controlled (---) simulations, plots of the moving mean values (·-) are also included.

$\alpha$	$\beta$	$C_f \times 10^{-3}$	$\bar{D}_R(\%)$
$\leq 2$	$\leq 4$	9.04	$3.0 \pm 1$
$\leq 2$	$\leq 8$	8.47	$9.1 \pm 1$
$\leq 2$	$\leq 12$	8.21	$11.9 \pm 1$

Figure 5.17: Table of mean total drag reductions from each of the controlled simulations ran. The first 300 time units of controlled data are not included in the calculation of drag reductions so as to remove the transient effects of the controllers. N.b. that for  $K_{(\alpha 2, \beta 12)}$ , the simulation is still running.

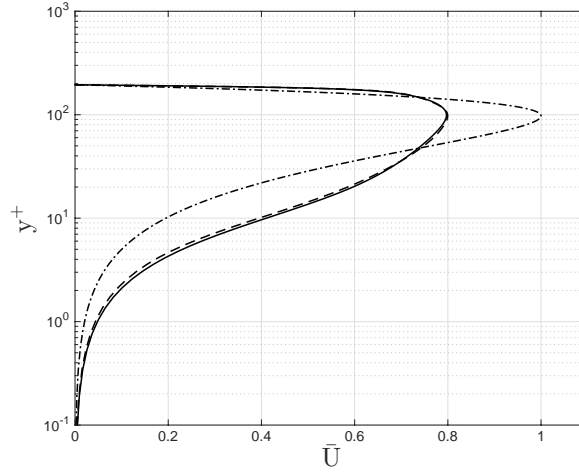


Figure 5.18: Plots of mean velocity profiles  $\overline{\langle U \rangle}$  for laminar ( $-$ ), uncontrolled turbulent ( $-$ ) and  $K_{(\alpha_4, \beta_{12})}$ -controlled ( $-$ ) turbulent flows.

for the  $K_{(\alpha_2, \beta_{12})}$  controller compared to the other two, suggests that unlike for energy production, the smaller scales (i.e. higher wavenumbers) are also important contributors to the total skin-friction drag of a flow. It is possible that even higher drag reductions could be achieved if a larger area of wavenumber space was controlled, especially in the direction of increasing  $\beta$ .

Figure 5.18 shows plots of the mean velocity profiles  $\overline{\langle U \rangle}$  for laminar, uncontrolled turbulent and  $K_{(\alpha_4, \beta_{12})}$  controlled turbulent flows. The only wall-normal region where the uncontrolled and controlled turbulent flows differ significantly is for  $1 \leq y^+ \leq 20$ . This suggests that the controller is mainly affecting the inner layer of the flow. However, there is some difference between the profiles at the centre of the channel, meaning that there is a possibility that the changes in the inner layer of the flow are having repercussions for the flow's outer layer.

Figure 5.19 shows profiles of the Reynolds stress ( $-\overline{\langle u'v' \rangle}$ ) and FIK-weighted Reynolds stress ( $y\overline{\langle u'v' \rangle}$ ) for the uncontrolled and  $K_{\alpha_2, \beta_{12}}$ -controlled flows. The controller both reduces the peak of the Reynolds stress profile and forces the profile to be negative close to the wall in the region  $0 < y^+ < 7$ . As it is the integral of the FIK-weighted profile which is directly proportional to turbulent drag, the region close to the wall has a sublaminal contribution to the total skin-friction drag. A table of skin-friction coefficients for the uncontrolled and controlled flows calculated using the FIK identity and those calculated directly from the gradient of the mean velocity profile is given in Figure 5.20. The FIK calculated values and actual values of  $C_f$  are in very good agreement, with only a 0.02% difference for the controlled flow.

The power efficiency of the three sets of controllers developed in this chapter

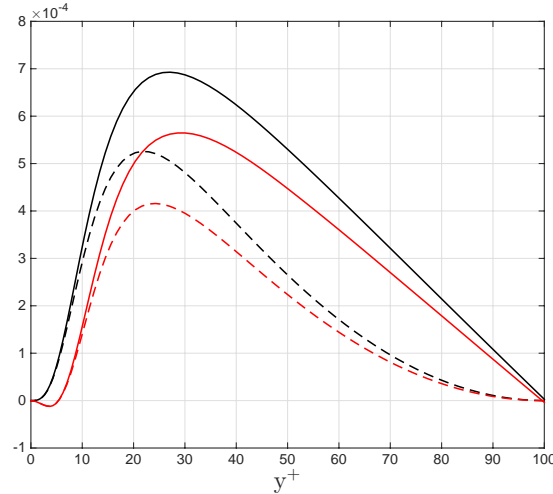


Figure 5.19: Profiles of Reynolds stress ( $-\overline{u'v'}$ ) (thick lines) and FIK-weighted Reynolds stress ( $y\overline{u'v'}$ ) (dashed lines) for the uncontrolled flow (black) and  $K_{\alpha 2, \beta 12}$ -controlled flow (red), displayed for the bottom half of the channel only.

	$C_{f\text{lam}}$	$C_{f\text{turb}}$	$C_{f\text{total}}$	Actual $C_f$
Uncontrolled	$4.04 \times 10^{-3}$	$5.27 \times 10^{-3}$	$9.31 \times 10^{-3}$	$9.32 \times 10^{-3}$
$K_{\alpha 2, \beta 12}$ -controlled	$4.04 \times 10^{-3}$	$4.17 \times 10^{-3}$	$8.21 \times 10^{-3}$	$8.21 \times 10^{-3}$

Figure 5.20: Table of skin-friction coefficient values calculated using the FIK identity (first three columns of data) and the actual skin-friction coefficient (last column of data).

was analysed using the same method as outlined in Chapter 4. The control power efficiency is defined in (4.70) and corresponds to the mean power of the actuation as a percentage of the power saved due to drag reduction. The table in Figure 5.21 lists the power efficiencies for each set of controllers. As was the case for the passivity-based controllers, the  $\mathcal{H}_\infty$  loop-shaping controllers are highly efficient with the power of their control actuation being only a small percentage of the power saved due to drag reduction.

Figure 5.22 shows isosurface plots of  $\mathbf{Q} = 0.1$  at the bottom half of the channel ( $\mathbf{Q}$  is defined in (4.72)) underlaid with colour maps of perturbation streamwise wall-shear stress for the uncontrolled and  $K_{(\alpha 2, \beta 12)}$  controlled simulations. Turning attention to the uncontrolled plots in Figure 5.22, large streamwise-elongated vortical structures are clearly visible. Looking closely, full horseshoe vortices, dis-

$K$	$\mathcal{P}_x$	$\Delta\mathcal{P}_x$	$\mathcal{P}_{v3}$	$\mathcal{P}_{vp}^*$	$\mathcal{P}_\phi^*$	$\mathcal{P}_\%$
$K_{\alpha 2, \beta 4}$	-0.2132	$7.10 \times 10^{-3}$	$2.951 \times 10^{-7}$	$2.825 \times 10^{-4}$	$2.828 \times 10^{-4}$	3.98
$K_{\alpha 2, \beta 8}$	-0.1995	0.0208	$1.140 \times 10^{-6}$	$3.888 \times 10^{-4}$	$3.899 \times 10^{-4}$	1.87
$K_{\alpha 2, \beta 12}$	-0.1927	0.0276	$1.403 \times 10^{-6}$	$4.102 \times 10^{-4}$	$4.116 \times 10^{-4}$	1.49

Figure 5.21: Table showing the power required to push the fluid  $\mathcal{P}_x$ , the power saved due to drag reduction  $\Delta\mathcal{P}_x$ , the approximate actuation power  $\mathcal{P}_\phi^*$ , and the power efficiency  $\mathcal{P}_\%$  for each controller. For the uncontrolled flow,  $\mathcal{P}_x = -0.2203$ .

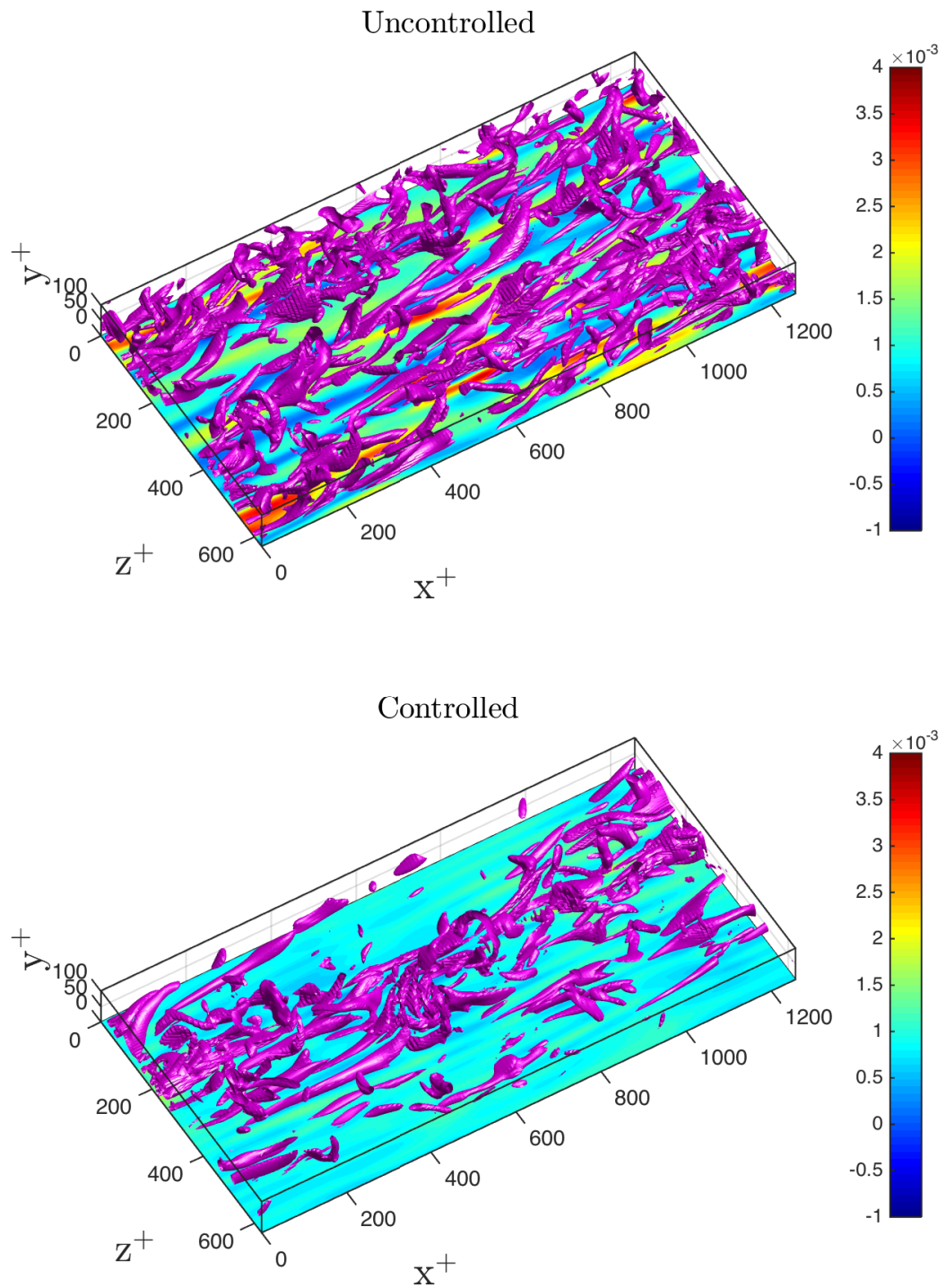


Figure 5.22: Isosurface plots of  $\mathbf{Q} = 0.1$ , overlaid with colour maps of perturbation streamwise wall-shear stress  $\frac{\partial u}{\partial y}$  at the lower wall for uncontrolled and  $K_{(\alpha_2, \beta_{12})}$  controlled simulations, for time  $t = 500$ .

cussed in Chapter 1, and the “legs” of horseshoe vortices can be seen. These vortical structures straddle the low-speed streaks as described in the literature; these are identified as regions of negative perturbation wall-shear stress. The effect of the  $K_{(\alpha 2, \beta 12)}$  controller is twofold. Firstly, perturbation streamwise shear-stress is drastically altered to the point that the bottom wall has a near uniform shear stress of  $\partial u / \partial y \approx 10^{-3}$ . This large reduction in the magnitude of the streamwise wall-shear stress is of course to be expected because of the large drag reduction achieved by this controller. However, the fact that the shear stress distribution is near uniform, suggests a buffer layer very close to the wall has formed and the streaks have been severely weakened and/or pushed away from the wall. Secondly, the controller significantly weakens wall-bounded vortices. Not only are there fewer vortices visible, but the vortices that can be seen are less elongated and thinner, especially downstream. It is unclear whether this is due to the actuation from the controller directly or if it is a consequence of the formation of the buffer region close to the wall. It was shown that for mode  $(\alpha = 0, \beta = 2)$ , the controller pushes streaks and vortices away from the wall to form a thin buffer layer. It appears that the combined action of all controllers is to form a similar buffer layer in the total flow. The formation of these buffer layers has drastically reduced skin-friction drag on both walls.

Figure 5.23 shows greyscale maps of wall-normal forcing at the lower wall from the  $K_{(\alpha 2, \beta 12)}$  controlled simulation, for times  $t = 5, 50$  and  $500$ . It is apparent from all three plots that the pattern of positive forcing is qualitatively similar to the sinuous bands of wall-bounded streaks identified by the regions of negative perturbation streamwise wall-shear stress in Figure 5.22. This may suggest that the controller may be pushing the slow-moving streaks away from the wall, perhaps in order to form a buffer zone. Alternatively, the distribution of wall-normal forcing may suggest the controller is trying to mitigate the wall-bounded vortices that are straddling the streaks. The magnitude of the forcing is greatest for  $t = 5$  and smallest for  $t = 500$ . This is to be expected as when the controllers are first initialised, large control inputs are required to reduce the modal streamwise shear stresses from their uncontrolled states. Once shear stresses in all modes are minimised by the controllers, only small control inputs are required to maintain them at their new level.

## 5.5 Summary

This chapter has outlined the  $\mathcal{H}_\infty$  loop-shaping control and model refinement methodologies, and evaluated the performance of controllers in terms of reducing modal perturbation streamwise wall-shear stress and total skin-friction drag in DNS of  $Re_\tau = 100$  turbulent channel flow. The main findings of this chapter are as follows:

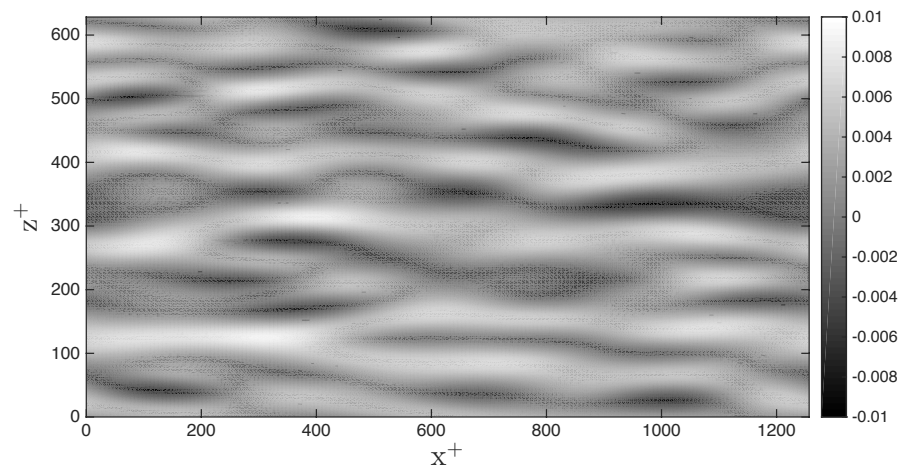
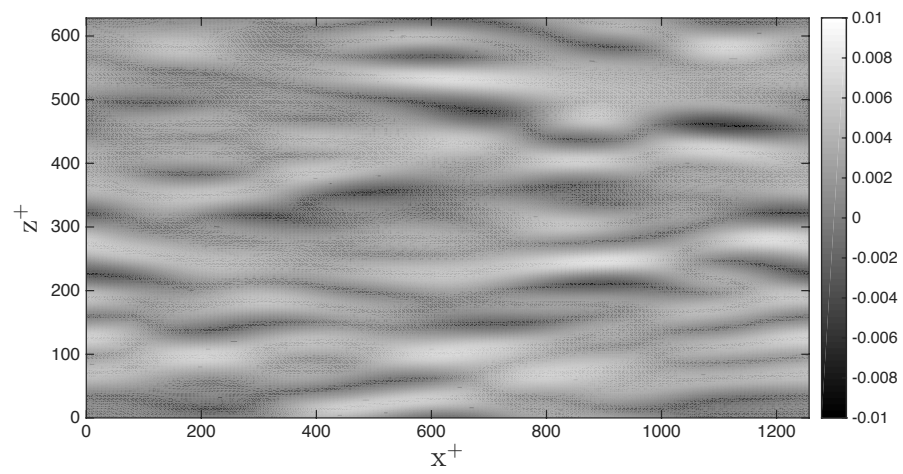
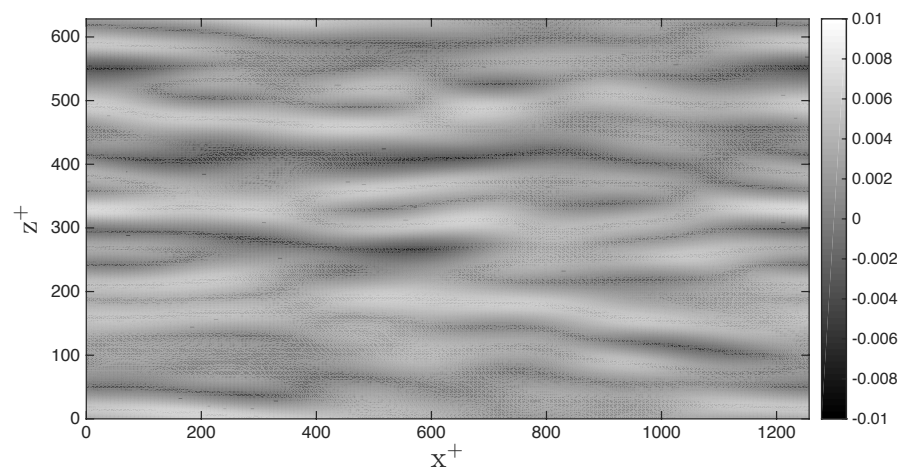
(a)  $t = 5$ (b)  $t = 50$ (c)  $t = 500$ 

Figure 5.23: Greyscale maps of wall-normal forcing at the lower wall for  $K_{(\alpha 4, \beta 12)}$  controlled flow.

- The coprime factor uncertainty model accounts for parametric and dynamic modelling uncertainties, and allows for a measure of robust stability  $b_{\mathcal{P},\mathcal{K}}$  to bound the  $\mathcal{H}_\infty$ -norm of eight closed-loop transfer functions from disturbance inputs to measured outputs. The resulting controllers offer *a priori* guarantees of robustness and performance in terms of input disturbance rejection.
- The model refinement procedure and its use of the  $\nu$ -gap metric, allows for the synthesis of low-order models with *a priori* bounds on closed-loop performance when implemented upon infinite-dimensional systems such as channel flow. Although this technique was demonstrated for mode  $(\alpha = 0, \beta = 2)$ , it was not used upon the final controllers due to time constraints. This is an avenue for future work.
- Using a precompensator matrix to shape the open-loop system allows for a high degree of flexibility in controller design. In the current work, a general precompensator matrix was used for all modes with only a single variable (the numerator of the transfer function). Future work could look at enhanced precompensator design to ensure better performance from each modal controller.
- DNS testing showed that the majority of modal controllers had excellent input disturbance rejection performance, with the streamwise-constant controllers reducing streamwise shear-stress by multiple orders of magnitude. It was shown that this was achieved by severely weakening streaks and wall-bounded streamwise vortices for these modes, which led to the formation of buffer layers adjacent to the walls. Spanwise-constant controllers performed poorly and this is likely to be due to their loop shapes.
- The combined effect of the controllers on the total flow differed greatly depending on the area of wavenumber space controlled. From  $\approx 3\%$  drag reduction for the  $K_{(\alpha 2, \beta 4)}$  controllers, to  $\approx 12\%$  for the  $K_{(\alpha 2, \beta 12)}$  controllers. This suggests that, unlike for energy production, the smaller scales of a flow are important contributors to streamwise wall-shear stress and ultimately total skin-friction drag.
- Visualisations of the total flow fields showed that the  $K_{(\alpha 2, \beta 12)}$  controller was successfully weakening both the streaks and wall-bounded vortices. Both of these coherent structures are known to be important in the turbulence regeneration process. It also appears that the controller forms buffer regions close to the channel walls because of the near-uniform perturbation streamwise wall-shear stress distributions. This may help explain the large reductions in skin-friction drag achieved via this controller.
- Future work should look at controlling larger areas of wavenumber space in DNS simulations using the  $\mathcal{H}_\infty$  loop-shaping control method, especially in

the direction of increasing  $\beta$ . The results presented in this chapter suggest that larger drag reductions could be achieved. This work could also help identify the cut-off points in wavenumber space, whereby control no longer affects a flow's total skin-friction drag.



## Chapter 6

# Discussion, Conclusions and Future Work

In this thesis, the modelling, simulation and control of turbulent channel flow has been investigated. The emphasis of this work has been on the use of feedback control for skin-friction drag reduction, with modelling and simulation being key to control model synthesis and final controller evaluation respectively. Two very different control methodologies were analysed - passivity based control and  $\mathcal{H}_\infty$  loop-shaping control. The objective of the first method is to restrict the production of perturbation energy within a flow, and the objective of the second method is to minimise perturbation streamwise wall-shear stress. Both methods differ in how they achieve their objectives and how they deal with the unmodelled non-linear dynamics. In the following, Section 6.1 presents a discussion of the main findings from this thesis and Section 6.2 presents the main conclusions from all chapters. In Section 6.3, novel contributions contained within this thesis will be presented. Avenues of future work identified within this thesis will be discussed in Section 6.4.

### 6.1 Discussion

#### 6.1.1 Passivity-Based Control V.s. $\mathcal{H}_\infty$ Loop-Shaping Control

The two control methodologies investigated in this thesis differ greatly in how they aim to reduce skin-friction drag in turbulent channel flow. The passivity-based control method aims to reduce drag indirectly, by restricting the production of perturbation energy in the flow. It has been shown previously that a reduction in perturbation energy can lead to a reduction in skin-friction drag [11, 50, 101]. The  $\mathcal{H}_\infty$  loop-shaping controllers also aims to reduce skin-friction drag indirectly. Their objective was to minimise perturbation streamwise wall-shear stress which has been shown previously to reduce the wall-normal gradient of the mean velocity profile [78] and therefore drag.

Both passivity-based and  $\mathcal{H}_\infty$  loop-shaping controllers are linear time-invariant, and therefore they are only capable of controlling a flow's linear dynamics. They differ in how they treat the nonlinear forcing. Assuming small amplitude control actuation, a flow's nonlinear dynamics can be treated as approximately passive. Therefore, in order to restrict perturbation energy production, passivity-based controllers are only required to control the linear dynamics in order to achieve their objective. However, as the passivity-based controllers developed in this thesis are unable to make the linear dynamics passive, only closer to passive, these controllers have no guarantees of stabilising the fully nonlinear system. The  $\mathcal{H}_\infty$  loop-shaping controllers treat the nonlinear forcing as an exogenous disturbance input to the linear dynamics. Therefore, the controllers aim to reject the effects of this disturbance forcing on the measured streamwise wall-shear stress perturbations. This control method does not guarantee to stabilise the fully nonlinear system either. Although,  $\mathcal{H}_\infty$  loop-shaping controllers do provide a priori guarantees of robustness via a robust stability margin. The model refinement technique can also be used to indicate a suitable level of control model resolution for the  $\mathcal{H}_\infty$  loop-shaping controllers.

The two control methods use slightly different sensing arrangements. The passivity-based controllers sense both streamwise and spanwise wall-shear stress perturbations. Using this information, they estimate the state of the flow throughout the channel in order to calculate an approximation of the perturbation energy. Wall-based measurements are unlikely to lead to accurate estimations of the state of the flow away from the wall, and therefore, the ability of these controllers to effectively reduce perturbation energy throughout the channel is restricted. Especially when wall actuation is used. The  $\mathcal{H}_\infty$  loop-shaping controllers, on the other hand, only measure streamwise wall-shear stress perturbations - the quantity which they are also trying to mitigate. These controllers only require accurate estimates of the flow in the region close to the wall because it is only the flow in this region which directly affects the wall-shear stress perturbations. Therefore, it would seem that these controllers would be more able to achieve their control objective.

The two control methods varied in their performance during DNS testing. All passivity-based controllers tested were apt at reducing mean perturbation energy, with reductions of  $\approx 11\%$ . However, the resulting drag reductions differed between 6 – 9%. This suggests that the actuation signals used differed between the three controllers tested which, although they achieved the same objective of restricting energy production, ultimately affected skin-friction drag differently. This is a problem when trying to reduce a quantity indirectly using feedback control. The  $\mathcal{H}_\infty$  loop-shaping controllers achieved drag reductions of between 3 – 12% depending on the number of modes controlled. Therefore, this control methodology has been shown to be more capable of reducing skin-friction drag compared

to passivity-based control for the chosen sensing/actuation arrangement. There is also scope for achieving higher drag reductions using the  $\mathcal{H}_\infty$  loop-shaping control method by controlling larger areas of wavenumber space and by improving the design of the controllers' loop shapes .

Overall, it is the author's opinion that, of the two control methods,  $\mathcal{H}_\infty$  loop-shaping control is a better option for reducing skin-friction drag in turbulent channel flow. These controllers achieved the highest drag reduction of  $\approx 12\%$  with scope for even higher drag reductions. Unlike for passivity-based control, this method provides a quantifiable level of robust stability and a way to choose suitable controller resolution using model refinement. Future work should look at investigating the performance of  $\mathcal{H}_\infty$  loop-shaping controllers with different sensing/actuation arrangements to see whether the results detailed in this thesis could be improved upon.

### 6.1.2 Implementation of Controllers in the Real-World

The drag reduction results presented in this thesis for both the passivity-based and  $\mathcal{H}_\infty$  loop-shaping controllers are unlikely to resemble what would be observed if these control methodologies were applied and tested in the real-world. This is due to the following:

- All controllers were designed for and tested on idealised channel flows which are periodic in both the streamwise and spanwise spatial directions. In reality, it is not possible to enforce periodic boundary conditions in a plane channel. To obtain a channel flow which is approximately homogeneous in these directions would require a wide channel and accurate enforcement of fixed mass flow. The channel would need to be wide to ensure that the testing portion of the channel was sufficiently far from the walls such that the effect of the walls was negligible. The strict enforcement of mass flow rate is necessary to ensure a constant bulk velocity.
- DNS testing of the controllers assumed sensors and actuators were infinitesimally small, collocated and densely distributed on the walls. In reality, none of these assumptions are feasible. Modern MEMS sensors and actuators have characteristic length scales up to the order of 1mm [49]. Therefore, there will be a finite number of sensors and actuators which can be arranged on the walls of a real-world channel. Finding the optimal number and arrangements of the sensors and actuators would be an additional task.
- Real-world actuators have a finite bandwidth, i.e. have a maximum frequency that they can operate at. All controllers tested in this thesis incorporate low-pass filters into their dynamics which ensures they have a finite

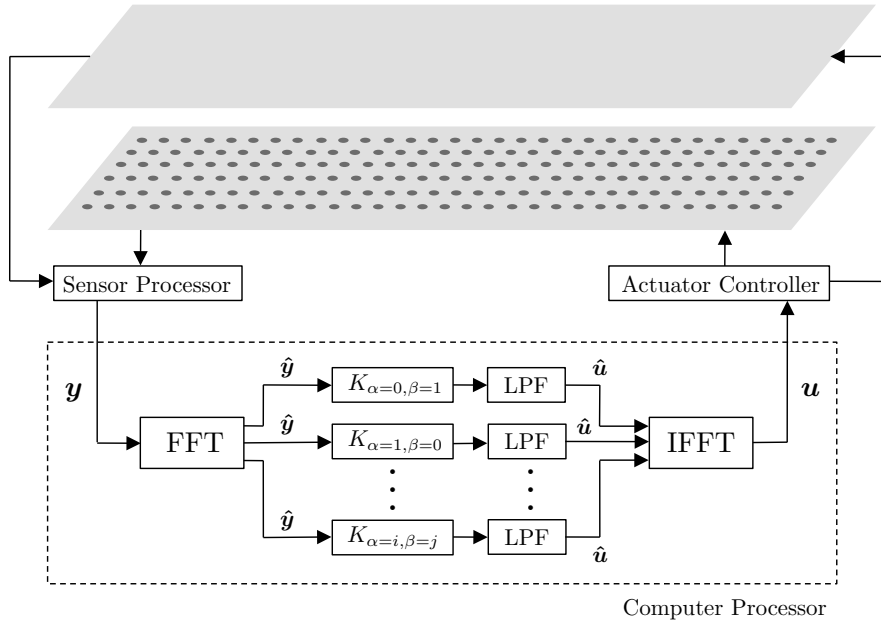


Figure 6.1: Block diagram depicting how the controllers developed in this thesis could be implemented on a real channel flow.

bandwidth. However, they all use relatively small time-constants and therefore have a large bandwidth. Depending on the actuator used, the controllers may have to use larger time-constants which could affect the performance of the controllers.

- In real-world wind tunnel and water tunnel experiments, there are many exogenous disturbances inputs affecting the flow which were absent in the DNS testing of the controllers. Examples include acoustic noise, changes in ambient temperature and noise from sensors and actuators. The advantage of using feedback control is that it can handle such exogenous uncertainty to a degree. However, only testing would show if the controllers could stabilise the flow in the presence of such uncertainty.

Figure 6.1 shows a block diagram depiction of how the controllers developed in this thesis could be implemented upon a real-world channel flow. Each wall of the channel would be densely populated with sensors and actuators; prior DNS testing could be used to find their optimal arrangement. All sensors would be connected to a sensor processor unit which would convert the analogue sensor signals to digital and using interpolation, generate an equispaced grid of measurements for each wall. This information would then be sent to a computer processor which would perform a fast Fourier transform (FFT) on the measurement grids. The measurement Fourier components would then be fed to the respective controllers, the output of which would be low-pass filtered. The computer processor would then inverse fast Fourier transform (IFFT) the low-pass filtered control signals and send these to an actuator controller unit in the form of an actuation grid for each wall. The actuation controller would then use interpolation to decide which

Control	$\alpha_{\max}$	$\beta_{\max}$	$\mathbf{k}_{\max}$	$\Delta S^*$
Passivity	0	10	10	$\frac{2\pi}{10} \frac{h^*}{N_s}$
$\mathcal{H}_\infty$ loop-shaping	$\pm 2$	12	$\approx 12$	$\frac{2\pi}{12} \frac{h^*}{N_s}$

Figure 6.2: Table of minimum dimensional sensor/actuator spacings  $\Delta S^*$  based on channel half-height  $h^*$  and sensor/actuator resolution per wavelength  $N_s$ .

actuation signals to send to each actuator and then convert the digital control signals to voltages. This process would be repeated for every control loop iteration.

The required population density of sensors and actuators is dictated by the smallest scales of the flow which are being controlled. For the passivity-based controllers the smallest controlled spatial scale is  $(\alpha = 0, \beta = 10)$ , and for the  $\mathcal{H}_\infty$  loop-shaping controllers they are  $(\alpha = \pm 2, \beta = 12)$ . The dimensionless wavelength,  $\lambda$ , corresponding to a wavenumber pair  $(\alpha, \beta)$  is found from:

$$k = \sqrt{\alpha^2 + \beta^2} = \frac{2\pi}{\lambda}. \quad (6.1)$$

The dimensional wavelength for a channel with half-height  $h^*$  is:  $\lambda^* = h^* \lambda$ . If we define  $N_s$  as the number of sensors/actuators per dimensionless wavelength, then the dimensional sensor/actuator spacing is found from:

$$\Delta S^* := \frac{2\pi}{k} \frac{h^*}{N_s}. \quad (6.2)$$

A table summarising the minimum dimensional sensor/actuator spacings can be found in Figure 6.2. For example, for a channel of total height 1 metre, and with a sensible wavelength resolution of  $N_s = 10$ , the minimum sensor/actuator spacing for the  $K_{\alpha 2, \beta 12}$   $\mathcal{H}_\infty$  loop-shaping controller would be  $\Delta S^* = 2.6$  cm. This spacing is sufficiently large enough for MEMS sensors and actuators to be implemented.

The required bandwidth of the actuators is determined by the time-constants of the low-pass filters implemented in the controllers. The passivity-based controllers use a time-constant of  $\tau_\phi = 0.01$  which corresponds to a cut-off frequency of  $\omega_{\max} = 100$  rad/T, and the  $\mathcal{H}_\infty$  loop-shaping controllers use a time-constant of  $\tau_\phi = 0.1$  which corresponds to a cut-off frequency of  $\omega_{\max} = 10$  rad/T. The cut-off frequency can be used as the maximum required bandwidth of the actuators. These frequencies are non-dimensionalised by channel half-height  $h^*$  and maximum laminar centreline velocity  $U_{cl}^*$ . Therefore, time is non-dimensionalised as  $t = t^*/T^*$ , where  $T^* = h^*/U_{cl}^*$ . Using the definition for maximum laminar centreline velocity Reynolds number  $Re$ ,  $T^*$  can also be written as:

$$T^* := \frac{h^{*2}}{Re\nu^*}. \quad (6.3)$$

Control	$\tau_\phi$	Air/Water	$\omega_{\max}^*$ (rad/s)	$F_{\max}^*$ (Hz)
Passivity	0.01	Air	$3.35(h^*)^{-2}$	$0.53(h^*)^{-2}$
Passivity	0.01	Water	$0.22(h^*)^{-2}$	$0.04(h^*)^{-2}$
$\mathcal{H}_\infty$ loop-shaping	0.1	Air	$0.33(h^*)^{-2}$	$0.05(h^*)^{-2}$
$\mathcal{H}_\infty$ loop-shaping	0.1	Water	$0.02(h^*)^{-2}$	$0.004(h^*)^{-2}$

Figure 6.3: Table of dimensional actuator bandwidths for controlling air ( $\nu = 1.5 \times 10^{-5}$ ) and water ( $\nu = 1 \times 10^{-6}$ )  $\text{Re} = 2230$  channel flows.

Therefore, the dimensional bandwidth of the actuators is found using:  $\omega_{\max}^* = \omega_{\max}/T^*$ . The table in Figure 6.3 shows a table of required dimensional actuator bandwidths for controlling  $\text{Re} = 2230$  air and water channel flows. When controlling air channel flow, the actuators need to have higher bandwidths due to the fluid having a higher kinematic viscosity. When controlling a  $\text{Re} = 2230$  air channel flow with total channel height 1 metre using passivity-based control, the maximum bandwidth of the actuators would need to be  $F_{\max}^* = 2.12$  Hz. This is relatively low and it is likely that MEMS actuators could be produced which could operate within this bandwidth.

It is unlikely that either the passivity-based or  $\mathcal{H}_\infty$  loop-shaping controllers developed in this thesis could be practically applied to reducing skin-friction drag on real-world air or marine craft. This is due to the high Reynolds numbers that most air and marine vehicles operate in. For both, Reynolds numbers of the order  $10^6$  and greater are typical. The controllers developed in this thesis were designed for and tested on relatively low Reynolds number flows. As Reynolds number increases, the required bandwidth of the actuation increases and it is unlikely that actuators with the required bandwidth exist for such high Reynolds numbers.

## 6.2 Conclusions

At the beginning of Chapter 1, previous research into the coherent structures and motions of turbulent wall-bounded flow was outlined. Although there is no generally agreed consensus on specific coherent structures, it appears that it is generally agreed that turbulence regeneration relies on wall-bounded streaks and streamwise-inclined vortices. In the current work, both of these structures were observed from visualisations of DNS flow fields. The control methods outlined in this thesis do not aim to mitigate any specific turbulent structure. However, the presence of streaks and vortices within a flow field has been used as an indicator of controller performance during DNS testing.

The review of previous research into active-closed-loop drag reduction, later in Chapter 1, showed that modern LTI  $\mathcal{H}_2$  and  $\mathcal{H}_\infty$  control methods were capable of significantly reducing skin-friction drag in turbulent flow. This proves that linear

spatially discrete control techniques are still able to perform well when applied to nonlinear infinite-dimensional systems. Many of the research discussed used wall transpiration as actuation, and this was shown to be effective. In one case wall transpiration was capable of flow relaminarisation [11]. Hence its use in the current work, although future work should look at finding better choices of flow actuation. Perturbation energy and wall-shear stress were also shown to be successful choices of flow measurement and/or control objective. These were both used as control objectives in the current work.

In Chapter 2, it was shown how the linearised Navier-Stokes equations could be projected onto a divergence-free basis via a change of state variable. This new formulation, known as the Orr-Sommerfeld Squire equations, is a suitable candidate for use as a LTI state-space control model of channel flow. Spectral discretisation was then introduced, and it was shown that because of channel flow's periodic boundary conditions, Fourier discretisation is a natural choice for streamwise and spanwise discretisation. Implementation results in spatially one-dimensional models for each Fourier mode one wishes to control. Two different spectral methods were used to discretise the inhomogeneous wall-normal direction of channel flow, namely the collocation and Galerkin methods. The Galerkin method provides higher accuracy although the collocation method is much simpler to implement because no integration is required. Analysis of the spectra and pseudospectra of models synthesised using both methods showed that there is no discernible difference for high enough resolution. It was then demonstrated how wall-normal actuation can be incorporated into the control models using a lifting procedure.

Chapter 3 outlined the DNS program *Channelflow* used to test controllers in Chapters 4 and 5. The influence matrix method, the algorithm used to integrate the Navier-Stokes equations forward in time, was presented in its original form with homogeneous wall boundary conditions. It was then shown how the influence matrix method was modified by the author to allow for general inhomogeneous boundary conditions to be set. The newly implemented boundary conditions were then validated for the wall-normal velocity case only. Both linear and nonlinear validation stages suggested that the boundary conditions had been implemented correctly. A controller class implemented in *Channelflow* by the author was presented at the end of Chapter 3. This class modelled the dynamics of LTI output-feedback controllers and enforced the required actuation during simulations.

In Chapter 4, the framework of passivity along with the closely related concepts of dissipativity and positive realness were introduced. It was demonstrated how the index of passivity ( $\varepsilon$ ) alone identifies how passive or non-passive a system is. Systems which have index of passivity  $\varepsilon > 0$  can only store and dissipate energy

and  $\varepsilon$  bounds dissipation from below. Systems which have  $\varepsilon < 0$  can also produce energy and  $\varepsilon$  bounds energy production from above. Channel flow was then analysed using this framework. It was shown how the Navier-Stokes equations can be decomposed into a linear system under feedback forcing from the nonlinearity, meaning the passivity of each system could be evaluated separately. The passivity theorem can then be used to ascertain the passivity of the feedback interconnection.

The nonlinearity in the Navier-Stokes equations was found to act as a passive operator when boundary conditions are periodic in the streamwise and spanwise directions and when there is no forcing at the walls. However, when there is forcing at the boundaries, the net flux of energy into the domain needs to be taken into account. When the net flux of energy is out of the domain, the nonlinearity becomes more passive and when the net flux of energy is into the domain, the nonlinearity becomes non-passive. When controllers using wall-based actuation were evaluated in Chapters 4 and 5, no analysis was conducted on how the actuation affected the passivity of the nonlinearity. It is possible that the instability of a Galerkin-discretised passivity-based controller was related to the nonlinearity becoming too non-passive. Future work should look at the effect of control actuation on the nonlinearity.

The passivity of the linear system was found to be heavily dependent on Reynolds number. The critical energy Reynolds number for which all Fourier modes of the linear system remain passive has previously been found analytically to be  $Re_E = 49.6$  for mode  $(\alpha = 0, \beta = 2.044)$  [92]. Using a Galerkin-discretised model and the index of passivity as an indicator, the same critical energy Reynolds number and corresponding mode were found in the current work via a numerical search over wavenumber space. The least passive modes of the linear system were then identified for subcritical and supercritical energy Reynolds numbers. For  $Re < Re_E$ , the mean mode  $(\alpha = 0, \beta = 0)$  was found to be the least passive and is thus the mode which dissipates the least energy. For  $Re > Re_E$  the streamwise-constant modes are the least passive relative to the rest of wavenumber space. For  $Re \rightarrow \infty$ , the least passive modes tends to  $(\alpha = 0, \beta = 1.62)$ .

Using the positive real control method of Sun et al. [103], passivity-based controllers were synthesised to minimise the magnitude of the closed-loop index of passivity of the ten lowest streamwise-constant modes of the linear system. Both collocation- and Galerkin-discretised controllers were generated with two different wall sensing arrangements. The first sensing arrangement included perturbation streamwise and spanwise wall-shear stresses, and the second also included wall pressure. Controllers discretised via either method and with either sensing arrangement all enforced similar reductions in closed-loop system index of passiv-

ity, with reductions of up to 80%. Controllers with sensing arrangement 2 had marginally better linear performance. These results suggest there is little difference in controllers synthesised via either method of wall-normal discretisation. They also suggest that the extra sensing measurements included in sensing arrangement 2 do little to improve closed-loop performance.

Both collocation- and Galerkin-discretised controllers with sensing arrangement 1 were tested upon DNS of  $\text{Re}_\tau = 100$  turbulent channel flow. Initial testing of the Galerkin-discretised controllers was abandoned after the controller for mode  $(\alpha = 0, \beta = 1)$  became destabilising. After the control penalties for all Galerkin-discretised controllers were increased, testing showed that the original instability no longer occurred, and reductions in total mean perturbation energy and mean skin-friction drag by the controllers of  $\approx 11\%$  and  $\approx 6\%$  respectively were observed. The collocation-discretised controllers had no instability problems with the original control penalties. They achieved reductions in total mean perturbation energy and mean skin-friction drag of  $\approx 11\%$  and up to  $\approx 9\%$  respectively. Both discretised controllers were observed to reduce the temporal peaks in perturbation energy for each mode controlled. This had the effect of significantly reducing the mean energy for each mode and resulted in reductions of total perturbation energy and ultimately drag. This demonstrates that minimising the index of passivity of these modes is having the desired effect, as these modes are no longer able to produce high magnitude peaks in energy. However, due to the limited sensing and actuation arrangements, the reductions in  $|\varepsilon|$  is not great enough to enforce large reductions in total perturbation energy. Therefore, the drag reductions achievable by this control method are limited.

In Chapter 5, the  $\mathcal{H}_\infty$  loop-shaping control method of McFarlane and Glover [85] was presented. Using a coprime factor uncertainty model, it was shown how a single robust stability margin ( $b_{\mathcal{P},K}$ ) can be used as a measure of both closed-loop robust stability and closed-loop performance in terms of input disturbance rejection. Glover and McFarlane [44] present a procedure to synthesise controllers which maximise  $b_{\mathcal{P},K}$  and this procedure was used in the current work. The model refinement method of Jones and Kerrigan [58] was also presented. Using the  $\nu$ -gap to measure the “closeness” of closed-loop systems, a bound on the  $\nu$ -gap between any finite-dimensional system and its infinite-dimensional counterpart can be deduced. This allows one to know what level of discretisation is suitable when controlling infinite-dimensional systems. Weighting matrices are used to shape the plant to ensure desirable closed-loop performance.

Low-order controllers were generated with the objective of minimising perturbation streamwise wall-shear stress. Three different combinations of controlled modes were then evaluated upon DNS of  $\text{Re}_\tau = 100$  turbulent channel flow. It

was found that the streamwise-constant mode controllers were able to minimise shear stress to a much higher degree than the other modes in wavenumber space. Conversely, the spanwise-constant mode controllers were poor at reducing shear stress. It is thought that this is due to the loop shapes for these controllers which all had much lower crossover frequencies. It is possible that with enhanced pre-compensator matrix design, the performance of these controllers could be improved. Visualisations of flow fields for streamwise-constant modes from DNS showed the effect of the controllers was to weaken and push away streamwise velocity and vorticity close to the wall. This resulted in the formation of a thin buffer layer adjacent to the wall with near-constant streamwise velocity, hence the large reductions in shear stress for these modes.

The drag reductions achieved by the three different controlled mode combinations differed greatly. The  $K_{\alpha 2, \beta 4}$ ,  $K_{\alpha 2, \beta 8}$  and  $K_{\alpha 2, \beta 12}$  controllers achieve reductions in mean skin-friction drag of  $\approx 3\%$ ,  $\approx 9\%$  and  $\approx 12\%$  respectively. The fact that drag reduction increases as more modes are controlled suggests that, unlike for perturbation energy production, the smaller scales of a flow are important contributors to skin-friction drag. It is possible that higher drag reductions could be achieved if even more modes were controlled, especially in the direction of increasing  $\beta$ . Visualisations of the total  $K_{\alpha 2, \beta 12}$ -controlled flow field showed that perturbation streamwise wall-shear stress at the bottom wall was reduced greatly and had a near-uniform distribution. This suggests that, as for the streamwise-constant modes, a thin buffer layer adjacent to the wall has formed in the total flow. The vortical structures in the  $K_{\alpha 2, \beta 12}$ -controlled flow were also severely mitigated, with both their number and size reduced. It is unclear whether this is due to the direct action from the controller, or a consequence of the formed buffer layer.

### 6.3 Novel Contributions

The novel contributions contained within this thesis are as follows:

1. Inhomogeneous general wall boundary conditions and a controller class were implemented in the open-source DNS program *Channelflow*, written by Gibson [41]. Other DNS codes have had general wall boundary conditions implemented, but to the best of the author's knowledge, this is the first time general boundary conditions have been implemented into the influence-matrix method - the algorithm used to integrate the Navier-Stokes forward in time in *Channelflow*. The code used to modify boundary conditions and model controller dynamics in *Channelflow* will be released online.
2. The index of passivity ( $\varepsilon$ ) was used to analyse the passivity of all Fourier modes of linear channel flow for different Reynolds numbers. For subcritical

- energy Reynolds numbers, it was shown how the least passive, and therefore least dissipative mode, was the mean mode ( $\alpha = 0, \beta = 0$ ). For supercritical energy Reynolds numbers, the streamwise-constant modes were shown to be least passive, and therefore capable of producing the most energy. For  $Re \rightarrow \infty$ , the least passive mode tends to ( $\alpha = 0, \beta = 1.62$ ). This is defined as the mode with maximum resonance by Trefethen et al. [107] which the author believes to be a different interpretation. Having information on which modes produce the most energy can inform on which modes to target when the objective is to minimise perturbation energy in a channel flow.
3. The positive real control method of Sun et al. [103] was used to generate passivity-based controllers using wall-based sensing *and* actuation, capable of reducing the magnitude of the index of passivity of the most energy producing modes of linear channel flow. Therefore, restricting the amount of energy these modes can produce. Controllers, discretised via two different spectral methods, were tested upon DNS of turbulent channel flow. They were shown to achieve significant reductions in mean perturbation energy and skin-friction drag. A linear analysis of this control method was presented at the UKACC 10th International Conference on Control, 2014 [46]. Results pertaining to the DNS testing of the passivity-based controllers are included in a journal article which has been accepted for publication in *Automatica*.
  4.  $\mathcal{H}_\infty$  loop-shaping controllers were generated for multiple Fourier modes of linear channel flow with the objective of minimising perturbation streamwise wall-shear stress. Jones et al. [60] previously tested this control method on a single Fourier mode. In the current work, three different combinations of modes were controlled in DNS of turbulent channel flow. This helped to identify which modes are significant contributors to skin-friction drag. Significant drag reductions were achieved when the greatest area of wavenumber space was controlled.

## 6.4 Future Work

Avenues of future work identified in this thesis are as follows:

1. Validation of general inhomogeneous boundary conditions implemented in *Channelflow* for the streamwise and spanwise velocity components. In Chapter 3, only the wall-normal velocity component boundary conditions were validated because only these were required to evaluate controllers in later chapters. However, in-plane wall actuation has shown to be effective for skin-friction drag reduction, so validating these boundary conditions may become important.

2. Evaluating passivity-based controllers with sensing arrangement 2 upon DNS of  $Re_\tau = 100$  turbulent channel flow. Due to time constraints, it was only possible to test controllers with sensing arrangement 1. However, controllers with sensing arrangement 2 achieved marginally higher reductions in the closed-loop indices of passivity of the controlled modes. Therefore, it is possible these controllers will achieve larger reductions in mean perturbation energy and skin-friction drag during DNS testing.
3. Investigating the effect of passivity-based control actuation on the passivity of the nonlinearity. It was demonstrated how the net flux of energy into or out of the domain affects the passivity of the nonlinearity. However, no analysis on how the passivity of the nonlinearity altered during DNS testing of the controllers was undertaken. It would be interesting to see whether the actuation of the controllers makes the nonlinearity more or less passive, or whether it remains lossless. It would also be important to find out whether the nonlinearity was the cause of one of the initial Galerkin-discretised controllers becoming unstable. Future work could also look at designing controllers which ensure the nonlinearity remains passive.
4. Using the full model refinement procedure on all  $\mathcal{H}_\infty$  loop-shaping controllers. This procedure was demonstrated for a single Fourier mode only. However, the order of discretisation of all controllers may be substantially reduced by using this procedure on all modes controlled - ( $\alpha \leq 2, \beta \leq 12$ ). Alternatively, the full model refinement procedure may show that the robustness margin ( $\mathcal{R}$ ) is too small for some controlled modes, and therefore the controller resolutions may need to be increased.
5. Designing enhanced precompensator weighting matrices ( $\mathcal{W}$ ) for poor performing  $\mathcal{H}_\infty$  loop-shaping controllers. It was shown that the spanwise-constant controllers were the worst performing relative to all other controlled modes. This was due to the difficulty in designing precompensators which resulted in desirable loop shapes. By using precompensator matrices of higher complexity than those used in the current work, it may be possible to improve the loop shapes for these modes. This should result in better input disturbance rejection properties for these controllers and hopefully even higher reductions in total skin-friction drag.
6. Controlling larger areas of wavenumber space using  $\mathcal{H}_\infty$  loop-shaping controllers. In the current work, the largest area of wavenumber space controlled were the modes within ( $\alpha \leq 2, \beta \leq 12$ ). Although large drag reductions were achieved for this controlled area, the results suggest that even larger drag reductions are possible if more modes are controlled, especially in the direction of increasing  $\beta$ . In fact, the streamwise-constant controllers were shown to be the most apt at reducing perturbation streamwise wall-shear stress.

Therefore, increasing the number of streamwise-constant controllers should have a noticeable effect on the flow.

7. Investigating better choices of wall sensing and actuation. In the current work, all controllers used wall transpiration as actuation and all controllers testing upon DNS used wall-shear stresses as measurements. These are commonly used actuation/sensing arrangements, however, they have not been proven to be optimal and more work needs to be done to find optimal arrangements. Further to this, the sensors and actuators in the current work are assumed to be infinitesimal and densely populated on both walls. This is an obviously impractical assumption. Future work should look at the modelling of finite-dimensional and sparsely populated sensors and actuators.
8. Evaluate the robustness of both the passivity-based controllers and  $\mathcal{H}_\infty$  loop-shaping controllers developed in the current work. Both of these methods have been claimed to be robust to uncertainty, however, this claim has not been tested in this thesis. Therefore, future work should look to test both of these control methods upon DNS of turbulent channel flows with different Reynolds numbers to those that they were designed for. Other robustness checks could include adding artificial noise of varying magnitude to flow measurements, and implementing imperfect actuation.
9. Test the performance of passivity-based controllers and  $\mathcal{H}_\infty$  loop-shaping controllers on higher Reynolds number flows. In the current work, all DNS testing was conducted on  $\text{Re}_\tau = 100$  turbulent channel flow only. Future work should investigate how reductions in perturbation energy and skin-friction drag vary as Reynolds number is increased.



# Bibliography

- [1] Navier-Stokes Equation. Online; accessed 15-January-2016 at [www.claymath.org/millennium-problems/navier-stokes-equation](http://www.claymath.org/millennium-problems/navier-stokes-equation).
- [2] Second IMO GHG study. Technical report, International Maritime Organization, 2009.
- [3] O. M. Aamo and M. Krstić. *Flow Control by Feedback*. Springer, 2003.
- [4] M. S. Acarlar and C. R. Smith. A study of hairpin vortices in a laminar boundary layer. part ii: hairpin vortices generated by fluid injection. *J. Fluid Mech.*, 175:43–83, 1987.
- [5] K. J. Aström and R. M. Murray. *Feedback Systems: An Introduction for Scientists and Engineers*. Princeton University Press, v2.10e edition, 2011.
- [6] H. Atik, C. Y. Kim, L. L. Van Dommelen, and J. D. A. Walker. Boundary-layer separation control on a thin airfoil using local suction. *Journal of Fluid Mechanics*, 535:415–443, 2005.
- [7] S. Bagheri and D. D. Henningson. Transition delay using control theory. *Philosophical Transactions of the Royal Society*, 369(1940):1365–1381, 2011.
- [8] A. Balogh, W-J. Liu, and M. Krstic. Stability enhancement by boundary control in 2-D channel flow. *IEEE Transactions on Automatic Control*, 46(11):1696–1711, 2001.
- [9] V. Barbu. *Stabilization of Navier-Stokes flows*. Springer, 2011.
- [10] T. R. Bewley and S. Liu. Optimal and robust control and estimation of linear paths to transition. *Journal of Fluid Mechanics*, 365:305–349, 1998.
- [11] T. R. Bewley, P. Moin, and R. Temam. DNS-based predictive control of turbulence: an optimal benchmark for feedback algorithms. *Journal of Fluid Mechanics*, 447:179–225, 2001.
- [12] T. J. Black. An analytical study of the measured wall pressure field under supersonic turbulent boundary layers. Technical Report CR-888, NASA, 1968.

- 
- [13] K. M. Bobba. *Robust flow stability: Theory, computations and experiments in near-wall turbulence*. PhD thesis, California Institute of Technology, Pasadena, California, USA, 2004.
- [14] A. V. Boiko, V. M. Kulik, H. H. Chun, and I. Lee. Verification of drag-reduction capabilities of stiff compliant coatings in air flow at moderate speeds. *International Journal of Naval Architecture and Ocean Engineering*, 3:242–253, 2011.
- [15] J. P. Boyd. *Chebyshev and Fourier Spectral Methods*. Dover, 2000.
- [16] K. S. Breuer, J. Park, and C. Heno. Actuation and control of a turbulent channel flow using Lorentz forces. *Physics of Fluids*, 16(4):897–907, 2004.
- [17] A. Buscarino, L. Fortuna, M. Frasca, and M. G. Xibilia. An analytical approach to one-parameter MIMO systems passivity enforcement. *International Journal of Control*, 85(9):1235–1247, 2012.
- [18] K. M. Butler and B. F. Farrell. Three-dimensional optimal perturbations in viscous shear flow. *Physics of Fluids A*, 4(8):1637–1650, 1992.
- [19] K. M. Butler and B. F. Farrell. Optimal perturbations and streak spacing in wall-bounded shear flow. *Physics of Fluids A*, 5:774–777, 1993.
- [20] C. Canuto, M. Y. Hussaini, A. Quarteroni, and T. A. Zang. *Spectral Methods in Fluid Dynamics*. Springer Series in Computational Physics. Springer-Verlag, 1988.
- [21] P. Chakraborty, S. Balachandar, and R. J. Adrian. On the relationships between local vortex identification schemes. *Journal of Fluid Mechanics*, 535:189–214, 2005.
- [22] S. I. Chernyshenko and M. F. Baig. The mechanism of streak formation in near-wall turbulence. *Journal of Fluid Mechanics*, 544:99–131, 2005.
- [23] H. Choi, P. Moin, and J. Kim. Active turbulence control for drag reduction in wall-bounded flows. *Journal of Fluid Mechanics*, 262:75–110, 1994.
- [24] K-S. Choi, T. Jukes, and R. Whalley. Turbulent boundary-layer control with plasma actuators. *Philosophical Transactions of the Royal Society*, 369:1443–1458, 2011.
- [25] K. S. Choi, X. Tang, B. R. Clayton, E. J. Glover, M. Atlar, B. N. Semenov, and V. M. Kulik. Turbulent drag reduction using compliant surfaces. *Proceedings: Mathematical, Physical and Engineering Sciences*, 453(1965):2229–2240, 1997.

- [26] S. Collis, R. D. Joslin, A. Seifert, and V. Theofilis. Issues in active flow control: theory, control, simulation, and experiment. *Progress in Aerospace Sciences*, 40(45):237 – 289, 2004.
- [27] T. C. Corke, C. L. Enloe, and S. P. Wilkinson. Dielectric barrier discharge plasma actuators for flow control. *Annual Review of Fluid Mechanics*, 42(505-529), 2010.
- [28] Cortana Corporation. Description of drag. Online; accessed 10-September-2012 at [www.cortana.com](http://www.cortana.com).
- [29] I. J. Couchman and E. C. Kerrigan. Control of mixing in a stoke’s fluid flow. *Journal of Process Control*, 20(10):1103 – 1115, 2010.
- [30] J. Cousteix. Basic concepts on boundary layers. Technical Report AGARD-R-786, Office national d’études et de recherches aérospatiales Toulouse (France), 1992.
- [31] B-Q. Deng, C-X. Xu, W-H Huang, and G-X Cui. Strengthened opposition control for skin-friction reduction in wall-bounded turbulent flows. *Journal of Turbulence*, 15(2):122–143, 2014.
- [32] C. A. Desoer and M. Vidyasagar. *Feedback Systems: Input-Output Properties*. Academic Press, 1975.
- [33] T. Endo, N. Kasagi, and Y. Suzuki. Feedback control of wall turbulence with wall deformation. *Internation Journal of Heat and Fluid Flow*, 21:568–575, 2000.
- [34] Fluent Inc., Centerra Resource Park, 10 Cavendish Court, Lebanon, NH 03766. *Fluent 6.3 User’s Guide*, September 2006.
- [35] J. Frayden. *AIP Handbook of Modern Sensors*. AIP, New York, 1993.
- [36] B. Frohnappfel, Y. Hasegawa, and N. Kasagi. Friction drag reduction through damping of the near-wall spanwise velocity fluctuation. *Internation Journal of Heat and Fluid Flow*, 31:434–441, 2010.
- [37] K. Fukagata, K. Iwamoto, and N. Kasagi. Contribution of reynolds stress distribution to the skin friction in wall-bounded flows. *Physics of Fluids*, 14(11):73–76, 2002.
- [38] K. Fukagata and N. Kasagi. Suboptimal control for drag reduction via suppression of near-wall reynolds shear stress. *Internation Journal of Heat and Fluid Flow*, 25:341–350, 2004.
- [39] M. Gad-el-Hak. *Flow control - Passive, Active and Reactive Flow Management*. Cambridge university press, 2000.

- 
- [40] R. Garcia-Mayoral and J. Jimenez. Drag reduction by riblets. *Philosophical Transactions of the Royal Society*, 369(1940):13471569, 2011.
- [41] J. F. Gibson. Channelflow: A spectral Navier-Stokes simulator in C++. Technical report, U. New Hampshire, 2012.
- [42] J. F. Gibson, J. Halcrow, and P. Cvitanovic. Visualizing the geometry of state space in plane Couette flow. *Journal of Fluid Mechanics*, 611:107–130, 2008.
- [43] A. Glezer and M. Amitay. Synthetic jets. *Annual Review of Fluid Mechanics*, 34:503–529, 2002.
- [44] K. Glover and D. McFarlane. Robust stabilization of normalised coprime factor plant descriptions with  $H_\infty$ -bounded uncertainty. *IEEE Transactions on Automatic Control*, 34(8):821–830, 1989.
- [45] M. Green and D. J. N. Limebeer. *Linear Robust Control*. Prentice Hall, 1995.
- [46] P. H. Heins, B. Ll. Jones, and A. S. Sharma. Passivity-based feedback control of a channel flow for drag reduction. In *UKACC 10th International Conference on Control (CONTROL 2014), Loughborough, U.K., 9th-11th July 2014*, pages 226–231, 2014.
- [47] D. J. Hill and P. J. Moylan. The stability of nonlinear dissipative systems. *IEEE Transactions on Automatic Control*, 21(5):708–711, 1976.
- [48] J. O. Hinze. *Turbulence*. McGraw-Hill, 1959.
- [49] C. Ho and Y. Tai. Micro-electro-mechanical-systems (MEMS) and fluid flows. *Annu. Rev. Fluid Mech.*, 30:579–612, 1998.
- [50] M. Högberg, T. R. Bewley, and D. S. Henningson. Relaminarization of  $Re_\tau = 100$  turbulence using gain scheduling and linear state-feedback control. *Physics of Fluids*, 15(11):3572–3575, 2003.
- [51] J. C. R. Hunt, A. A. Wray, and P. Moin. Eddies, stream, and convergence zones in turbulent flows. Technical Report CTR-S88, pp 193-208, Center for Turbulence Research, 1988.
- [52] IATA. Jet fuel price monitor. Online; accessed 17-May-2015 at [www.iata.org](http://www.iata.org).
- [53] K. Iwamoto. Database of fully developed channel flow. Technical Report ILR-0201, Department of Mechanical Engineering, The University of Tokyo, 2002.

- [54] K. Iwamoto and Y. Kasagi and. Reynolds number effects on wall turbulence: toward effective feedback control. *International Journal of Heat and Fluid Flow*, 23(678-689), 2002.
- [55] F. K. Jiang, Y. C. Tai, B. Gupta, R. Goodman, S. Tung, J. Huang, and C. M. Ho. A surface-micromachined shear-stress imager. In *An Investigation of Micro Structures, Sensors, Actuators, Machines and Systems*, pages 110–115, New York, 1996. IEEE.
- [56] F. K. Jiang, Y. C. Tai, C. M. Ho, and W. J. Li. A micromachined polysilicon hot-wire anemometer. In *Tech. Dig. Proc. Solid-State Sens. Actuator Workshop, Hilton, Head Isl., SC*, pages 264–267, Cleveland Heights, OH: Transd. Res. Found, 1994.
- [57] J. Jimenez and A. Pinelli. The autonomous cycle of near-wall turbulence. *Journal of Fluid Mechanics*, 389:335–359, 1999.
- [58] B. L. Jones and E. C. Kerrigan. When is the discretization of a spatially distributed system good enough for control? *Automatica*, 46:1462–1468, 2010.
- [59] B. L. Jones, E. C. Kerrigan, J. F. Morrison, and T. A. Zaki. Flow estimation of boundary layers using DNS-based wall shear information. *International Journal of Control*, 84(8):1310–1325, 2011.
- [60] B. L. Jones, P. H. Heins, E. C. Kerrigan, J. F. Morrison, and A. S. Sharma. Modelling for robust feedback control of fluid flows. *Journal of Fluid Mechanics*, 769:687–722, 2015.
- [61] P. Joseph, X. Amandolese, C. Edouard, and J-L. Aider. Flow control using MEMS pulsed micro-jets on the Ahmed body. *Experiments in Fluids*, 54(1442):1–12, 2013.
- [62] S. S. Joshi, J. L. Speyer, and J. Kim. A systems theory approach to the feedback stabilization of infinitesimal and finite-amplitude disturbances in plane poiseuille flow. *Journal of Fluid Mechanics*, 332:157–184, 1997.
- [63] R. D. Joslin, M. D. Gunzburger, R. A. Nicolaidis, G. Erlebacher, and M. Y. Hussaini. Self-contained automated methodology for optimal flow control. *AIAA Journal*, 35(5):816–824, 1997.
- [64] J. D. Anderson Jr. *Fundamentals of Aerodynamics*. McGraw-Hill, 4th edition, 2007.
- [65] J. Keshavan and J. S. Humbert. An  $H_\infty$  loopshaping approach for bio-inspired reflexive visual navigation in three-dimensional urban environments. *Robotics and Autonomous Systems*, 62(8):1085–1097, 2014.

- [66] H. T. Kim, S. J. Kline, and W. C. Reynolds. The production of turbulence near a smooth wall in a turbulent boundary layer. *Journal of Fluid Mechanics*, 50(1):133–160, 1971.
- [67] J. Kim and T. R. Bewley. A linear systems approach to flow control. *Annual Review of Fluid Mechanics*, 39(1):383–417, 2007.
- [68] J. Kim and J. Lim. A linear process in wall-bounded turbulent shear flows. *Physics of Fluids*, 12(8):1885–1888, 2000.
- [69] L. Kleiser and U. Schumann. Treatment of incompressibility and boundary conditions in 3-d numerical spectral simulations of plane channel flows. In E. Hirsch, editor, *in Proc. 3rd GAMM Conf. Numerical Methods in Fluid Mechanics*, 1980.
- [70] S. J. Kline, W. C. Reynolds, F. A. Schraub, and P. W. Runstadler. The structure of turbulent boundary layers. *Journal of Fluid Mechanics*, 30:741–773, 1967.
- [71] M. Koenig, A. V. G. Cavalieri, P. Jordan, and Y. Gervais. Jet-noise control by fluidic injection from a rotating plug: Linear and non-linear sound source mechanisms. In *19th AIAA/CEAS Aeroacoustics Conference; Berlin; Germany; 27 May 2013 through 29 May 2013; Code 99261*, 2013.
- [72] N. Kottenstette, M. J. McCourt, M. Xia, V. Gupta, and P. J. Antsaklis. On relationships among passivity, positive realness, and dissipativity in linear systems. *Automatica*, 50(4):1003–1016, 2014.
- [73] P. Koumoutsakos. Vorticity flux control for a turbulent channel flow. *Physics of Fluids*, 11(2):248–250, 1999.
- [74] G. R. Lahiji and K. D. Wise. A monolithic thermopile detector fabricated using integrated-circuit technology. In *Proc. Int. Electron Dev. Meet., Washington, DC*, pages 676–679. IEEE, 1980.
- [75] A. J. Laub. A schur method for solving algebraic Riccati equations. *IEEE Transactions on Automatic Control*, AC-24(6):913–921, 1979.
- [76] C. Lee, J. Kim, D. Babcock, and R. Goodman. Application of neural networks to turbulence control for drag reduction. *Physics of Fluids*, 9(6):1740–1747, 1997.
- [77] C. Lee, J. Kim, and H. Choi. Suboptimal control of turbulent channel flow for drag reduction. *Journal of Fluid Mechanics*, 358:245–258, 1998.
- [78] K. H. Lee, L. Cortelezzi, J. Kim, and J. Speyer. Application of reduced-order controller to turbulent flows for drag reduction. *Physics of Fluids*, 13(5):1321–1330, 2001.

- [79] J. Lim. *Control of wall-bounded turbulent shear flows using modern control theory*. PhD thesis, University of California Los Angeles, 2003.
- [80] C. R. Liu, X. G. An, and H. C. Zhang. Phase control of fluctuation aerodynamics loads with synthetic jet. *Journal of Hunan University Natural Sciences*, 41(5):65–70, 2014.
- [81] J. Lumley and P. Blossey. Control of turbulence. *Annual Review of Fluid Mechanics*, 30:311–327, 1998.
- [82] Z. Ma, S. Ahuja, and C. W. Rowley. Reduced-order models for control of fluids using the eigensystem realization algorithm. *Theoretical and Computational Fluid Dynamics*, 25:233–247, 2009.
- [83] A. Mahmood, Y. Kim, and J. Park. Robust  $H_\infty$  autopilot design for agile missile with time-varying parameters. *IEEE Transactions on Aerospace and Electronic Systems*, 50(4):3082–3089, 2014.
- [84] F. Martinelli, M. Quadrio, J. McKernan, and J. F. Whidborne. Linear feedback control of transient energy growth and control performance limitations in subcritical plane poiseuille flow. *Physics of Fluids*, 23(1):014103–014103–9, 2011.
- [85] D. McFarlane and K. Glover. A loop-shaping design procedure using  $H_\infty$  synthesis. *IEEE Transactions on Automatic Control*, 37(6):759–769, 1992.
- [86] J. McKernan. *Control of Plane Poiseuille Flow: A Theoretical and Computational Investigation*. PhD thesis, Cranfield University, 2006.
- [87] J. McKernan, G. Papadakis, and J.F. Whidborne. A linear state-space representation of plane Poiseuille flow for control design: a tutorial. *International Journal of Modelling, Identification and Control*, 1(4):272–280, 2006.
- [88] S. A. Orszag. Accurate solution of the Orr-Sommerfeld stability equation. *Journal of Fluid Mechanics*, 50(4):689–703, 1971.
- [89] R. Peyret. *Spectral Methods for Incompressible Viscous Flow*. Springer, 2002.
- [90] S. B. Pope. *Turbulent Flows*. Cambridge University Press, 2000.
- [91] M. Quadrio, P. Ricco, and C. Viotti. Streamwise-travelling waves of spanwise wall velocity for turbulent drag reduction. *Journal of Fluid Mechanics*, 627:161–178, 2009.
- [92] S. C. Reddy and D. S. Henningson. Energy growth in viscous channel flows. *Journal of Fluid Mechanics*, 252:209–238, 1993.

- [93] P. Ricco and S. Hahn. Turbulent drag reduction through rotating discs. *Journal of Fluid Mechanics*, 722:267–290, 2013.
- [94] P. Ricco, C. Ottonelli, Y. Hasegawa, and M. Quadrio. Changes in turbulent dissipation in a channel flow with oscillating walls. *Journal of Fluid Mechanics*, 2012.
- [95] S. K. Robinson. Coherent motions in the turbulent boundary layer. *Annual Review of Fluid Mechanics*, 23:601–639, 1991.
- [96] C. W. Rowley. Model reduction for fluids, using balanced proper orthogonal decomposition. *International Journal of Bifurcation and Chaos*, 15(3):997–1013, 2005.
- [97] C.W. Rowley and M. Ilak. Reduced-order models of linearized channel flow using balanced truncation. In *Control and Automation, 2006. MED '06. 14th Mediterranean Conference on*, pages 1–6, june 2006.
- [98] M. G. Safonov, E. A. Jonckheere, M. Verma, and D. J. Limebeer. Synthesis of positive real multivariable feedback systems. *International Journal of Control*, 45(3):817–842, 1987.
- [99] Peter J. Schmid. Nonmodal stability theory. *Annual Review of Fluid Mechanics*, 39(1):129–162, 2007.
- [100] A. S. Sharma and B. J. McKeon. On coherent structure in wall turbulence. *Journal of Fluid Mechanics*, 728:196–238, 2013.
- [101] A. S. Sharma, J. F. Morrison, B. J. McKeon, D. J. N. Limebeer, and W. H. Koberg et al. Relaminarisation of  $Re_\tau = 100$  channel flow with globally stabilising linear feedback control. *Physics of Fluids*, 23(125105), 2011.
- [102] C. R. Smith. A synthesized model of the near-wall behaviour in turbulent boundary layers. In *Proc. Symp. Turbul., 8th, Rolla, Mo.*, 1984.
- [103] W. Sun, P. P. Khargonekar, and D. Shim. Solution to the positive real control problem for linear time-invariant systems. *IEE Transactions on Automatic Control*, 39(10):2034–2046, 1994.
- [104] T. Theodorsen. Mechanism of turbulence. In *Proc. Midwest. Conf. Fluid Mech, 2nd, Columbus, Ohio, pp. 1–18*, 1952.
- [105] L. N. Trefethen. *Spectral Methods In Matlab*. Siam, 2000.
- [106] L. N. Trefethen and M. Embree. *Spectra and Pseudospectra*. Princeton University Press, 2005.

- [107] L. N. Trefethen, A. E. Trefethen, S. C. Reddy, and T. A. Driscoll. Hydrodynamic stability without eigenvalues. *Science*, 261:578–584, 1993.
- [108] G. Vinnicombe. *Uncertainty and feedback -  $\mathcal{H}_\infty$  loop-shaping and the  $\nu$ -gap metric*. Imperial College Press, 2001.
- [109] F. C. Wang, L. S. Chen, Y. C. Tsai, C. H. Hsieh, and J. Y. Yen. Robust loop-shaping control for a nano-positioning stage. *Journal of Vibration and Control*, 20(6):885–900, 2014.
- [110] S. Wang, B. Ma, J. Deng, H. Qu, and J. Luo. Fabrication and characterization of MEMS piezoelectric synthetic jet actuators with bulk-micromachined PZT thick film. *Microsystems Technologies*, 2014.
- [111] J. C. Willems. Dissipative dynamical systems part I: general theory. *Archive for Rational Mechanics and Analysis*, 45(5):321–351, 1972.
- [112] J. C. Willems. Dissipative dynamical systems part II: linear systems with quadratic supply rates. *Archive for Rational Mechanics and Analysis*, 45(5):352–393, 1972.
- [113] G. Zames. On the input-output stability of time-varying nonlinear feedback systems part i: Conditions derived using concepts of loop gain, conicity, and positivity. *IEEE Transactions on Automatic Control*, 11(2):228–238, 1966.
- [114] T. A. Zang. On the rotation and skew-symmetric forms for incompressible flow simulations. *Applied Numerical Mathematics*, 7(1):27–40, 1991.
- [115] S. Zhao and S. Duncan. On the accuracy of the calculation of transient growth in plane Poiseuille flow. *International Journal for Numerical Methods in Fluids*, 74:857–871, 2014.
- [116] Y. Zhou and H. Bai. Recent advances in active control of turbulent boundary layers. *Science China Physics, Mechanics and Astronomy*, 54(7):1289–1295, 2011.



## Appendix A

# Positive Real Control Method - Controller Synthesis

For a given set of system parameters, control feed-through energy, and control and measurement penalties, the following assumptions must hold for a controller to exist [103]:

**A1** The system pair  $(A, B_2)$  is stabilisable.

**A2** The system pair  $(C_2, A)$  is detectable.

**A3** The matrix  $D_{12}^\top D_{12}$  is nonsingular.

**A4** The matrix  $\begin{bmatrix} A - j\omega I & B_2 \\ \tilde{C}_1 & D_{12} \end{bmatrix}$  has full column rank for all  $\omega \in \mathbb{R}$ .

**A5** The matrix  $\begin{bmatrix} A - j\omega I & \tilde{B}_1 \\ C_2 & D_{21} \end{bmatrix}$  has full row rank for all  $\omega \in \mathbb{R}$ .

**A6** The inequality  $D_{11} + D_{11}^\top > 0$  must hold.

**A7** The ARE  $R(X) = 0$  has a stabilising solution  $X_E \geq 0$ .

**A8** The ARE  $S(Y) = 0$  has a stabilising solution  $Y_E \geq 0$ .

**A9** The spectral radius  $\rho(Y_E X_E) < 1$ .

Algebraic Riccati equations  $R(X)$  and  $S(Y)$  are defined [103]:

$$R(X) := A_R^\top X + X A_R + X B_R X + Q_R, \quad (\text{A.1a})$$

$$S(Y) := A_S^\top Y + Y A_S + Y B_S Y + Q_S, \quad (\text{A.1b})$$

where,

$$A_R \equiv A - \tilde{B}_1 (D_{11} + D_{11}^\top)^{-1} \tilde{C}_1 - (B_2 - \tilde{B}_1 (D_{11} + D_{11}^\top)^{-1} D_{12}) \cdot (D_{12}^\top (D_{11} + D_{11}^\top)^{-1} D_{12})^{-1} \cdot (D_{12}^\top (D_{11} + D_{11}^\top)^{-1} \tilde{C}_1), \quad (\text{A.2a})$$

$$\begin{aligned}
 B_R \equiv & \tilde{B}_1(D_{11} + D_{11}^\top)^{-1}\tilde{B}_1^\top - (B_2 - \tilde{B}_1(D_{11} + D_{11}^\top)^{-1}D_{12} \\
 & \cdot (D_{12}^\top(D_{11} + D_{11}^\top)^{-1}D_{12})^{-1} \cdot (B_2 - \tilde{B}_1(D_{11} + D_{11}^\top)^{-1}D_{12})^\top, \quad (\text{A.2b})
 \end{aligned}$$

$$\begin{aligned}
 Q_R \equiv & \tilde{C}_1^\top(D_{11} + D_{11}^\top)^{-1} \cdot [D_{11} + D_{11}^\top - D_{12}(D_{12}^\top(D_{11} + D_{11}^\top)^{-1}D_{12})^{-1}D_{12}^\top] \\
 & \cdot (D_{11} + D_{11}^\top)^{-1}\tilde{C}_1, \quad (\text{A.2c})
 \end{aligned}$$

$$\begin{aligned}
 A_S \equiv & [A - \tilde{B}_1(D_{11} + D_{11}^\top)^{-1}\tilde{C}_1 - \tilde{B}_1(D_{11} + D_{11}^\top)^{-1}D_{21}^\top \\
 & \cdot (D_{21}(D_{11} + D_{11}^\top)^{-1}D_{21}^\top)^{-1} \cdot (C_2 - D_{21}(D_{11} + D_{11}^\top)^{-1}\tilde{C}_1)]^\top, \quad (\text{A.2d})
 \end{aligned}$$

$$\begin{aligned}
 B_S \equiv & \tilde{C}_1^\top(D_{11} + D_{11}^\top)^{-1}\tilde{C}_1 - (C_2 - D_{21}(D_{11} + D_{11}^\top)^{-1}\tilde{C}_1)^\top \\
 & \cdot (D_{21}(D_{11} + D_{11}^\top)^{-1}D_{21}^\top)^{-1} \cdot (C_2 - D_{21}(D_{11} + D_{11}^\top)^{-1}\tilde{C}_1), \quad (\text{A.2e})
 \end{aligned}$$

$$\begin{aligned}
 Q_S \equiv & \tilde{B}_1(D_{11} + D_{11}^\top)^{-1} \cdot [D_{11} + D_{11}^\top - D_{21}^\top(D_{21}(D_{11} + D_{11}^\top)^{-1}D_{21}^\top)^{-1}D_{21}] \\
 & \cdot (D_{11} + D_{11}^\top)^{-1}\tilde{B}_1^\top. \quad (\text{A.2f})
 \end{aligned}$$

Several algorithms exist for solving AREs such as those in (A.1) [75]. Once stabilising and semi-positive definite solutions to the AREs are found, the controller  $K$  is formed from:

$$\begin{aligned}
 K \equiv & \left[ \begin{array}{c|c} A + B_2F_E + (I - Y_EX_E)^{-1}L_EC_2 + \Delta_E & -(I - Y_EX_E)^{-1}L_E \\ \hline F_E & 0 \end{array} \right] \quad (\text{A.3}) \\
 & \equiv \left[ \begin{array}{c|c} A_K & B_K \\ \hline C_K & 0 \end{array} \right],
 \end{aligned}$$

where,

$$F_E := -(D_{12}^\top(D_{11} + D_{11}^\top)^{-1}D_{12})^{-1} \cdot (B_2^\top X_E + D_{12}^\top(D_{11} + D_{11}^\top)^{-1}(\tilde{C}_1 - \tilde{B}_1^\top X_E)), \quad (\text{A.4a})$$

$$L_E := -(Y_EC_2^\top + (\tilde{B}_1 - Y_E\tilde{C}_1^\top)(D_{11} + D_{11}^\top)^{-1}D_{21}^\top) \cdot (D_{21}(D_{11} + D_{11}^\top)^{-1}D_{21}^\top)^{-1}, \quad (\text{A.4b})$$

$$\Delta_E := -(\tilde{B}_1 + (I - Y_EX_E)^{-1}L_ED_{21})(D_{11} + D_{11}^\top)^{-1} \cdot (\tilde{C}_1 - \tilde{B}_1^\top X_E + D_{12}F_E). \quad (\text{A.4c})$$

Assumptions **A7** and **A8** state that for a controller to exist, stabilising semi-

positive definite solutions to  $R(X)$  and  $S(Y)$  must exist. For a given Fourier mode and Reynolds number, whether solutions to the AREs exist or not depends primarily on the amount of feed-through energy  $\bar{\varepsilon}$  included in the control model. The amount of feed-through energy included needs to be above a certain level for the AREs to be solvable. The minimum amount of feed-through energy for which a controller exists is optimum in the sense that the resulting controller  $K_{\min}$  will ensure minimum (magnitude) closed-loop index of passivity  $\varepsilon_{L,K}$ . Control and measurement penalties  $\epsilon_c$  and  $\epsilon_d$  are a secondary consideration, although if these are set small enough, they will have little effect on the solutions to the AREs. The iterative procedure for finding  $K_{\min}$  for a given Fourier mode and supercritical energy Reynolds number is as follows:

1. Choose penalties  $\epsilon_c$  and  $\epsilon_d$ , and set actuator time-constant  $\tau_\phi \leq 1$ .
2. Find the index of passivity  $\varepsilon_L < 0$  of the uncontrolled system  $\hat{L}$  using (4.21).
3. Set feed-through energy as  $\bar{\varepsilon} = -\varepsilon_L > 0$ , form the control model  $\tilde{L}$  and solve the AREs in (A.1).
4. Reducing  $\bar{\varepsilon}$  until stabilising solutions to the AREs no longer exist, find the minimum amount of feed-through energy needed for solutions to exist.
5. Using the solutions to the AREs found with minimum feed-through energy, form “optimal” controller  $K_{\min}$  using (A.3).

The passivity index of the closed-loop system  $\Sigma_{L,K_{\min}}$  will be approximately equal in magnitude to the minimal amount of feed-through energy needed to solve the AREs. It will also be the smallest magnitude index of passivity achievable using a LTI controller.